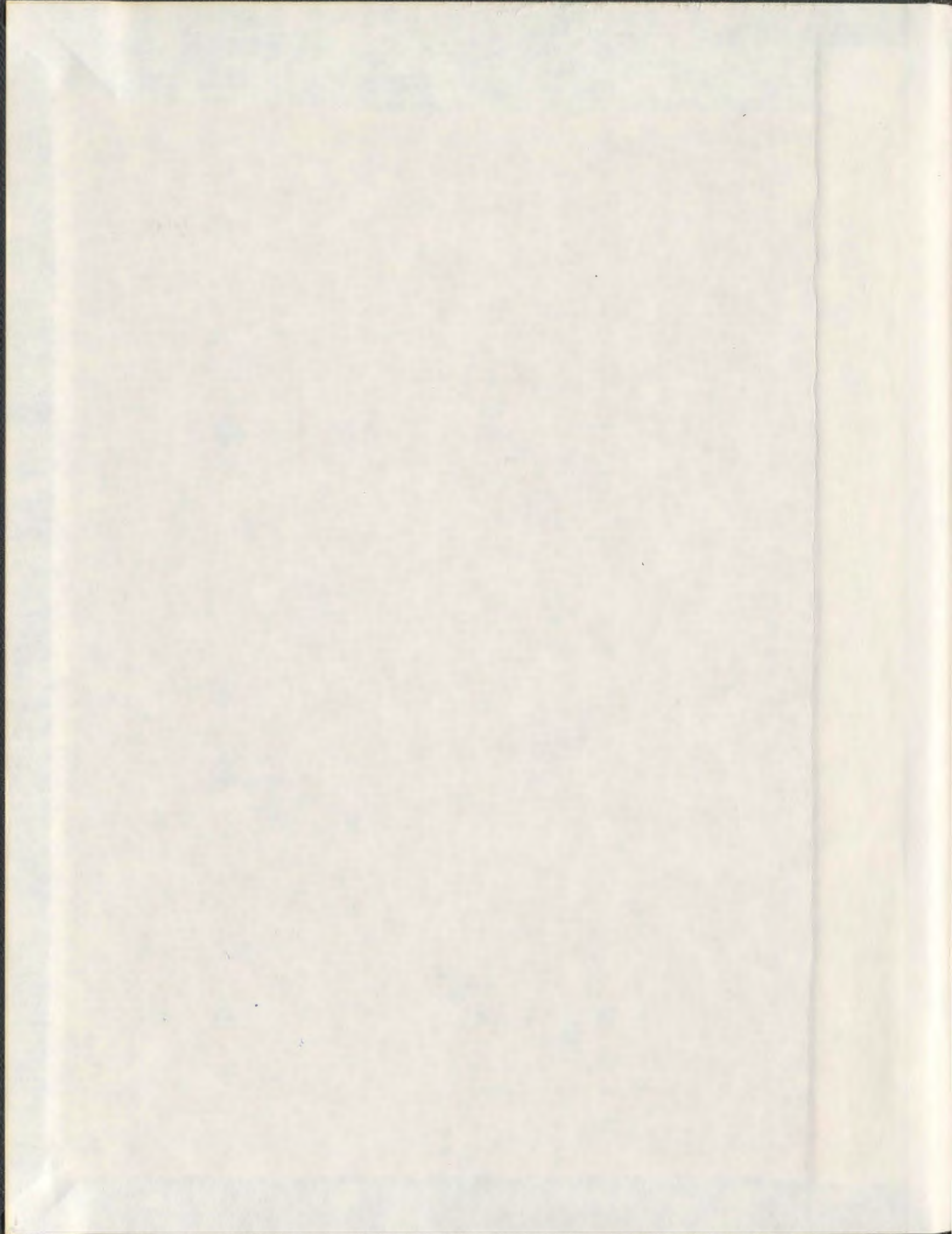
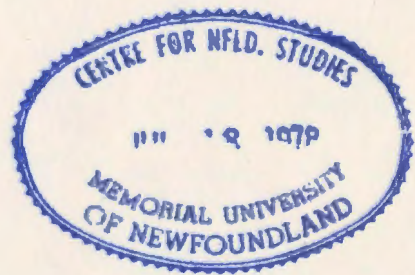


ACCURATE COMPUTATION OF FREE SURFACE FLOW  
WITH AN OSCILLATING CIRCULAR CYLINDER BASED  
ON A VISCOUS INCOMPRESSIBLE TWO-FLUID MODEL

LARISA MIRONOVA



001311





**Accurate computation of free surface flow with an  
oscillating circular cylinder based on a viscous  
incompressible two-fluid model**

by

Larisa Mironova

A thesis submitted in partial fulfillment  
of the requirements for the degree of  
Doctor of Philosophy (Mathematics)

School of Graduate Studies  
Memorial University of Newfoundland  
St. John's, Newfoundland and Labrador

July 2008

© Larisa Mironova

## Abstract

This thesis focuses on the design of a new computational model for a class of free surface flows with a moving circular cylinder based on a viscous incompressible two-fluid model. The method of solution is based on a finite volume discretization of the two-dimensional continuity and unsteady Navier-Stokes equations in their pressure-velocity formulation on a fixed Cartesian grid. The displacement of the free surface is tracked by using the volume of fluid method. The positions of both the free surface and fluid-body interfaces are determined at each time step by using the piecewise linear interface calculation algorithm. The advection of the reconstructed free surface with local velocity field is performed by the geometrical area preserving volume of fluid advection algorithm. The fractional area/volume obstacle representation method is combined with the cut cell method to improve the accuracy of the spatial discretization of a fluid-body interface. Discrete pressure and velocity fields corresponding to the successive time instants are obtained as a result of solution of a coupled sparse linear system in primitive variables using a generalized minimal residual method. This is done by making use of the Trilinos numerical solver library. The accuracy checks indicate that the resulting method is of second-order in space and first-order in time.

The numerical algorithm is applied to the problem of unsteady, laminar, two-dimensional flow of a viscous incompressible fluid past a circular cylinder undergoing forced oscillations in streamwise direction in the presence of the free surface. This is the first numerical study conducted on this problem to date. The validation of the method is presented in special cases and good comparisons with previous experimental and numerical results are obtained.

## Acknowledgments

I would like to express my gratitude to all people who have helped and inspired me during my doctoral studies at Memorial University of Newfoundland.

I am deeply indebted to my supervisor Dr. Kocabiyik for giving me the opportunity and motivation to undertake this work. Dr. Kocabiyik's perpetual energy and enthusiasm along with a guidance and encouragement during this research were a beneficial contribution to this thesis. I also appreciate Dr. Kocabiyik's total confidence and the responsibility granted me throughout this work.

I acknowledge that a financial support was provided by the School of Graduate Studies in the form of a graduate fellowship and the Natural Sciences and Engineering Research Council of Canada (NSERC) research grant received by Dr. Kocabiyik during my doctoral studies.

I am also indebted to the Department of Mathematics and Statistics for providing me a partial financial support in the form of a teaching assistanship, and for giving me the opportunity to use the departmental computing facilities which were acquired with support from Canada Foundation for Innovation (CFI), Industrial Research and Innovation Fund (IRIF) of the province of Newfoundland and Labrador and IBM. Special thanks also goes to the secretarial and computer staff members of the Department of Mathematics and Statistics.

I would like to express my appreciation to Dr. David Pike for his valuable suggestions after reading my thesis in his capacity as a member of the supervisory committee.

I also want to thank my friends and colleagues, Oleg Gubanov and Marina Tvalavadze, for all their help, support, interest and valuable discussions for which I am very grateful.

# Table of Contents

---

|  |            |
|--|------------|
| List of tables   | x          |
| List of figures  | xx         |
| <b>1 Introduction</b>  | <b>1</b>   |
| 1.1 Problem background and literature review . . . . .                                       | 2          |
| 1.1.1 Fluid boundary tracking/capturing methods . . . . .                                    | 8          |
| 1.1.2 Fluid-body interface methods . . . . .   | 18         |
| 1.1.3 Review of previous studies on free surface flows with a circular<br>cylinder . . . . . | 22         |
| 1.2 Scope of the thesis . . . . .  | 31         |
| <b>2 Viscous incompressible free surface flow model with a moving solid<br/>  body</b>       | <b>35</b>  |
| 2.1 Governing equations of viscous fluid dynamics . . . . .                                  | 38         |
| 2.2 Integral form of the FAVOR equations . . . . .   | 41         |
| 2.2.1 Generalized Reynolds transport theorem . . . . .                                       | 42         |
| 2.2.2 Continuity equation . . . . .  | 47         |
| 2.2.3 Navier-Stokes equations . . . . .  | 48         |
| 2.3 Boundary conditions . . . . .  | 51         |
| 2.4 Frame of reference and nondimensional parameters . . . . .                               | 54         |
| <b>3 Computational model and method</b>  | <b>58</b>  |
| 3.1 Discretization of the governing equations . . . . .                                      | 58         |
| 3.1.1 Computational domain geometry . . . . .  | 59         |
| 3.1.2 Discretization of the continuity equation . . . . .                                    | 64         |
| 3.1.3 Discretization of the Navier-Stokes equations . . . . .                                | 65         |
| 3.1.4 Averaging of the density . . . . .   | 83         |
| 3.2 Free surface interface capturing . . . . .   | 84         |
| 3.3 Discretization of the computational domain boundary conditions . . .                     | 92         |
| 3.4 Calculation of the lift and drag forces, and the mechanical energy transfer              | 95         |
| 3.5 Initial conditions . . . . .   | 97         |
| 3.6 Numerical simulation flowchart . . . . .   | 97         |
| <b>4 Numerical algorithm validation</b>  | <b>102</b> |
| 4.1 Spatial and temporal accuracy tests . . . . .  | 103        |
| 4.2 Choice of the computational parameters . . . . .   | 105        |
| 4.3 Uniform flow past a stationary cylinder in the absence of a free surface                 | 112        |
| 4.4 Uniform flow past an oscillating cylinder in the absence of a free surface               | 122        |

|          |   |            |
|----------|---|------------|
| 4.5      | Uniform flow past a steady rotating cylinder in the absence of a free surface   | 132        |
| 4.6      | Uniform flow past a cylinder in the presence of a free surface . . . . .  | 138        |
| <b>5</b> | <b>Forced in-line oscillations of a circular cylinder beneath a free surface: Locked-on modes and fluid forces</b>                              | <b>145</b> |
| 5.1      | Vortex shedding modes and fluid forces in the absence of the free surface ( $h = \infty$ ) . . . . .  | 147        |
| 5.2      | Vortex shedding modes and fluid forces in the presence of the free surface at $h = 0.25, 0.5, 0.75$ . . . . .                                   | 156        |
| 5.2.1    | Froude number $Fr \approx 0.0$ . . . . .  | 157        |
| 5.2.2    | Froude number $Fr = 0.2$ . . . . .  | 171        |
| 5.2.3    | Froude number $Fr = 0.4$ . . . . .  | 192        |
| <b>6</b> | <b>Summary, conclusions and recommendations for future work</b>   | <b>242</b> |
| 6.1      | Effect of the Froude number, $Fr$ , and the cylinder submergence depth, $h$ , on flow regimes, vortex shedding modes and fluid forces . . . . . | 245        |
| 6.2      | Overview of distinctive flow features and vortex shedding modes . . .   | 260        |
| 6.3      | Practical significance of the present results . . . . .   | 264        |
| 6.4      | Future work . . . . .   | 266        |
|          | <b>Bibliography</b>   | <b>268</b> |
| <b>A</b> | <b>Integral form of the FAVOR equations versus differential form of the FAVOR equations</b>   | <b>282</b> |
| <b>B</b> | <b>Generalized functions and generalized differentiation</b>  | <b>292</b> |
| <b>C</b> | <b>Surface force term in the incompressible Navier-Stokes equations</b>   | <b>295</b> |
| <b>D</b> | <b>Invariance of the governing equations in non-inertial frame of reference</b>   | <b>297</b> |
| <b>E</b> | <b>Proper orthogonal decomposition</b>  | <b>300</b> |

## List of Tables

---

|     |   |     |
|-----|---|-----|
| 4.1 | $L^2$ norm of the relative errors of the pressure, $p$ , and velocity components, $u$ , $v$ , as the time step and the number of grid cells per cylinder diameter vary for the stationary cylinder case in the absence of a free surface at $R = 10^3$ when $t = 0.1$ . . . . .   | 103 |
| 4.2 | The effect of the computational domain size on the maximum drag and lift coefficients, $C_{D,max}$ and $C_{L,max}$ ; the mean drag coefficient, $\widehat{C}_D$ ; the natural vortex shedding frequency, $f_0$ , for the case of uniform flow past a stationary cylinder in the absence of a free surface at $R = 100$ . . . . .  | 107 |
| 4.3 | The effect of the computational domain size on the maximum and minimum local heights of the free surface, $h _{L,max}$ and $h _{L,min}$ ; the RMS value of the lift coefficient, $C_{L,rms}$ ; the RMS value of the drag coefficient, $C_{D,rms}$ ; the natural vortex shedding frequency, $f _{fs}$ , for the case of uniform flow past a stationary cylinder in the presence of a free surface at $R = 200$ : $Fr = 0.3$ , $h = 0.55$ . . . . . | 108 |
| 4.4 | The effects of the near wake grid resolution and the time step, $\Delta t$ , on the maximum drag and lift coefficients, $C_{D,max}$ and $C_{L,max}$ ; the mean drag coefficient, $\widehat{C}_D$ ; the natural vortex shedding frequency, $f_0$ , for the case of uniform flow past a stationary cylinder in the absence of a free surface at $R = 100$ . . . . .   | 110 |
| 4.5 | The effects of the near wake grid resolution and the time step, $\Delta t$ , on the RMS value of the lift coefficient, $C_{L,rms}$ ; the RMS value of the drag coefficient, $C_{D,rms}$ ; the natural vortex shedding frequency, $f _{fs}$ , for the case of uniform flow past a stationary cylinder in the presence of a free surface at $R = 200$ : $Fr = 0.3$ , $h = 0.7$ . . . . .  | 111 |
| 4.6 | The comparison of the predicted natural vortex shedding frequency, $f_0$ ; the maximum lift coefficient, $C_{L,max}$ ; the mean drag coefficients, $\widehat{C}_D$ , with the previous numerical and experimental <sup>(†)</sup> results. . . . .   | 121 |
| 4.7 | The comparison of the maximum lift coefficient, $C_{L,max}$ and the mean drag coefficient, $\widehat{C}_D$ , for the case of uniform flow past a cylinder subject to in-line oscillations in the absence of a free surface at $R = 100$ : $A = 0.14$ , $f/f_0 = 2.0$ with the numerical results of Su <i>et al.</i> (2007). . . . .   | 128 |
| 4.8 | The comparison of the maximum lift coefficient, $C_{L,max}$ ; the maximum drag coefficient, $C_{D,max}$ ; the mean drag coefficient, $\widehat{C}_D$ , for the case of uniform flow past a cylinder subject to transverse oscillations in the absence of a free surface at $R = 100$ : $A = 0.2$ , $f/f_0 = 1$ with the numerical results of Karanth <i>et al.</i> (1995). . . . .  | 130 |

|      |   |     |
|------|---|-----|
| 4.9  | The comparison of the RMS lift coefficient, $C_{L,rms}$ ; the RMS drag coefficient, $C_{D,rms}$ ; the mean drag coefficient, $\widehat{C}_D$ , for the case of uniform flow past a cylinder subject to transverse oscillations in the absence of a free surface at $R = 185$ : $A = 0.2$ , $f/f_0 = 1.1$ with the numerical results of Guilmineau and Queutey (2002). . . . .   | 130 |
| 4.10 | The effect of the submergence depth, $h$ , on the local Froude number, $Fr _L$ ; the frequency ratio, $f _{fs}/f_0$ ; the average $u$ -velocity in the region directly above the cylinder, $\widehat{u}$ , for uniform flow past a stationary cylinder in the presence of a free surface at $R = 180$ : $Fr = 0.3$ , $0.1 \leq h \leq 1.0$ . Comparison with the numerical results of Reichl <i>et al.</i> (2005). . . . .  | 139 |
| 4.11 | The effect of the submergence depth, $h$ , on the local Froude number, $Fr _L$ ; the frequency ratio, $f _{fs}/f_0$ ; the average $u$ -velocity in the region directly above the cylinder, $\widehat{u}$ , for uniform flow past a stationary cylinder in the presence of a free surface at $R = 180$ : $Fr = 0.4$ , $0.16 \leq h \leq 1.0$ . Comparison with the numerical results of Reichl <i>et al.</i> (2005). . . . . | 140 |
| 5.1  | The effect of the free surface inclusion at $Fr \approx 0.0$ , $h = 0.25, 0.5, 0.75$ and the frequency ratio, $f/f_0$ , on flow regimes, vortex shedding modes and their periods, $T_0$ , at $R = 200$ , $A = 0.13$ , $1.0 \leq f/f_0 \leq 4.0$ . The superscript “*” denotes quasi-locked-on modes. . . . .  | 168 |
| 5.2  | The effect of the free surface inclusion at $Fr = 0.2$ , $h = 0.25, 0.5, 0.75$ and the frequency ratio, $f/f_0$ , on vortex shedding modes and their periods, $T_0$ , at $R = 200$ : $A = 0.13$ , $1.0 \leq f/f_0 \leq 4.0$ . The superscript “*” denotes quasi-locked-on modes. . . . .  | 188 |
| 5.3  | The effect of the free surface inclusion at $Fr = 0.2$ , $h = 0.25, 0.5, 0.75$ and the frequency ratio, $f/f_0$ , on the mean lift and drag coefficients, $\widehat{C}_L$ and $\widehat{C}_D$ , at $R = 200$ : $A = 0.13$ , $1.0 \leq f/f_0 \leq 4.0$ . . . . .   | 189 |
| 5.4  | The effect of the free surface inclusion at $Fr = 0.2$ , $h = 0.25, 0.5, 0.75$ and the frequency ratio, $f/f_0$ , on the RMS lift and drag coefficients, $C_{L,rms}$ and $C_{D,rms}$ , at $R = 200$ : $A = 0.13$ , $1.0 \leq f/f_0 \leq 4.0$ . . . . .  | 190 |
| 5.5  | The effect of the free surface inclusion at $Fr = 0.2$ , $h = 0.25, 0.5, 0.75$ and the frequency ratio, $f/f_0$ , on the total mechanical energy transfer, $E$ , at $R = 200$ : $A = 0.13$ , $1.0 \leq f/f_0 \leq 4.0$ . . . . .  | 192 |
| 5.6  | Leading eigenvalues for (a): $h = \infty$ , $f/f_0 = 2.0$ , $t = 100$ to $150$ ; (b): $Fr = 0.4$ , $h = 0.5$ , $f/f_0 = 2.0$ , $t = 20$ to $50$ (quasi-periodic state); (c): $Fr = 0.4$ , $h = 0.5$ , $f/f_0 = 2.0$ , $t = 60$ to $100$ (non-periodic state) at $R = 200$ : $A = 0.13$ . . . . .  | 212 |

|      |  |     |
|------|--|-----|
| 5.7  | The effect of the free surface inclusion at $Fr = 0.4$ , $h = 0.25, 0.5, 0.75$ , and the frequency ratio, $f/f_0$ , on flow regimes, vortex shedding modes and their periods, $T_0$ , at $R = 200$ , $A = 0.13$ , $1.0 \leq f/f_0 \leq 4.0$ . The superscript “*” denotes quasi-locked-on modes. . . . . | 232 |
| 5.8  | The effect of the free surface inclusion at $Fr = 0.4$ , $h = 0.25, 0.5, 0.75$ and the frequency ratio, $f/f_0$ , on the mean lift coefficient, $\hat{C}_L$ , at $R = 200$ : $A = 0.13$ , $1.0 \leq f/f_0 \leq 4.0$ . . . . .  | 236 |
| 5.9  | The effect of the free surface inclusion at $Fr = 0.4$ , $h = 0.25, 0.5, 0.75$ and the frequency ratio, $f/f_0$ , on the mean drag coefficient, $\hat{C}_D$ , at $R = 200$ : $A = 0.13$ , $1.0 \leq f/f_0 \leq 4.0$ . . . . .  | 237 |
| 5.10 | The effect of the free surface inclusion at $Fr = 0.4$ , $h = 0.25, 0.5, 0.75$ and the frequency ratio, $f/f_0$ , on the RMS lift coefficient, $C_{L,rms}$ , at $R = 200$ : $A = 0.13$ , $1.0 \leq f/f_0 \leq 4.0$ . . . . .   | 238 |
| 5.11 | The effect of the free surface inclusion at $Fr = 0.4$ , $h = 0.25, 0.5, 0.75$ and the frequency ratio, $f/f_0$ , on the RMS drag coefficient, $C_{D,rms}$ , at $R = 200$ : $A = 0.13$ , $1.0 \leq f/f_0 \leq 4.0$ . . . . .   | 239 |
| 5.12 | The effect of the free surface inclusion at $Fr = 0.4$ , $h = 0.25, 0.5, 0.75$ and the frequency ratio, $f/f_0$ , on the total mechanical energy transfer, $E$ , at $R = 200$ : $A = 0.13$ , $1.0 \leq f/f_0 \leq 4.0$ . . . . .   | 240 |
| 6.1  | The effect of the Froude number, $Fr$ , and the cylinder submergence depth, $h$ , on flow regimes, vortex shedding modes and their periods, $T_0$ , at $R = 200$ : $A = 0.13$ , $f/f_0 = 1.0$ . The superscript “*” denotes quasi-locked-on modes. . . . .   | 245 |
| 6.2  | The effect of the Froude number, $Fr$ , and the cylinder submergence depth, $h$ , on flow regimes, vortex shedding modes and their periods, $T_0$ , at $R = 200$ : $A = 0.13$ , $f/f_0 = 2.0$ . The superscript “*” denotes quasi-locked-on modes. . . . .   | 246 |
| 6.3  | The effect of the Froude number, $Fr$ , and the cylinder submergence depth, $h$ , on flow regimes, vortex shedding modes and their periods, $T_0$ , at $R = 200$ : $A = 0.13$ , $f/f_0 = 3.0$ . The superscript “*” denotes quasi-locked-on modes. . . . .   | 247 |
| 6.4  | The effect of the Froude number, $Fr$ , and the cylinder submergence depth, $h$ , on flow regimes, vortex shedding modes and their periods, $T_0$ , at $R = 200$ : $A = 0.13$ , $f/f_0 = 4.0$ . The superscript “*” denotes quasi-locked-on modes. . . . .   | 248 |
| 6.5  | The effect of the Froude number, $Fr$ , and the cylinder submergence depth, $h$ , on the mean lift coefficient, $\hat{C}_L$ , at $R = 200$ : $A = 0.13$ , $1.0 \leq f/f_0 \leq 4.0$ . . . . .  | 255 |

|      |  |     |
|------|--|-----|
| 6.6  | The effect of the Froude number, $Fr$ , and the cylinder submergence depth, $h$ , on the mean drag coefficient, $\hat{C}_D$ , at $R = 200$ : $A = 0.13$ , $1.0 \leq f/f_0 \leq 4.0$ . . . . .    | 256 |
| 6.7  | The effect of the Froude number, $Fr$ , and the cylinder submergence depth, $h$ , on the RMS lift coefficient, $C_{L,rms}$ , at $R = 200$ : $A = 0.13$ , $1.0 \leq f/f_0 \leq 4.0$ . . . . .     | 257 |
| 6.8  | The effect of the Froude number, $Fr$ , and the cylinder submergence depth, $h$ , on the RMS drag coefficient, $C_{D,rms}$ , at $R = 200$ : $A = 0.13$ , $1.0 \leq f/f_0 \leq 4.0$ . . . . .     | 258 |
| 6.9  | The effect of the Froude number, $Fr$ , and the cylinder submergence depth, $h$ , on the total mechanical energy transfer, $E$ , at $R = 200$ : $A = 0.13$ , $1.0 \leq f/f_0 \leq 4.0$ . . . . . | 259 |
| 6.10 | The new vortex shedding modes (and their descriptions) observed in the present thesis. . . . .   | 263 |

# List of Figures

---

|     |  |    |
|-----|--|----|
| 1.1 | Schematic of the problem. . . . .  | 1  |
| 1.2 | Kármán vortex street downstream of a circular cylinder at $R = 140$ . Retrieved from <a href="http://hmf.enseeiht.fr/">http://hmf.enseeiht.fr/</a> on October 2, 2007. . . . .   | 3  |
| 1.3 | A map of the vortex locked-on modes in the wavelength-amplitude plane near the fundamental lock-on region as observed by Williamson and Roshko (1988). The critical curve marks the transition from one mode of vortex formation to another. . . . .   | 6  |
| 1.4 | Vortex locked-on modes near the fundamental lock-on region as observed by Williamson and Roshko (1988) in the map in Figure 1.3. Each mode is defined by the number of pairs and single vortices formed per $T_0$ ; - - - encircles the vortices shed in a complete cycle. . . . .   | 7  |
| 2.1 | (a) Typical solid body surface within a Cartesian grid, (b) typical computational cell, $V^*$ , which includes areas, $A_i^*$ ( $i = 0, 1, 2, 3$ ) and volume, $V^*$ , open to flow within $V^*$ , (c) location of $\hat{A}_x^*$ , $\hat{A}_y^*$ and $\hat{V}^*$ within the computational cell, $V^*$ . The solid body is shown in gray. . . . . | 38 |
| 2.2 | The derivation of the differential and integral forms of the FAVOR equations: Hirt and Sicilian (1985), Hirt (1992), Hirt (1993), Tsukiyama <i>et al.</i> (1993), Zhu and Wu (2004), Troch <i>et al.</i> (2002) (left) and present thesis (right). . . . .   | 40 |
| 2.3 | Control volume containing a fluid-body interface. . . . .  | 42 |
| 2.4 | Regions $AB_1CB_2A$ and $A'B_1C'B_2A'$ denote material volumes at $t^* = t_0^*$ and $t^* = t_0^* + \Delta t^*$ , respectively. . . . .   | 43 |
| 2.5 | Level set function representation. . . . .   | 43 |
| 3.1 | Staggered grid arrangement: $p_{i,j}$ pressure cell. . . . .   | 60 |
| 3.2 | Staggered grid arrangement: (a) $u_{i,j}$ -velocity cell, (b) $v_{i,j}$ -velocity cell. . . . .  | 61 |
| 3.3 | An example of the calculation of the volume, $V$ , and the area, $A$ , apertures in the computational cell. The solid body is shown in gray. . . . .   | 62 |
| 3.4 | An example of the labeling of the pressure cells. The solid body is shown in dark gray. . . . .  | 63 |
| 3.5 | Discretization of the continuity equation. The solid body is shown in gray. . . . .  | 65 |
| 3.6 | An example of the situation when <b>FF</b> cell borders <b>BF</b> cell. The solid body is shown in gray. . . . .   | 67 |
| 3.7 | Discretization of the $x$ -momentum equation. The solid body is shown in gray. . . . .   | 68 |
| 3.8 | Schematic of the $B$ -spline interpolation for $u$ -velocity. The solid body is shown in gray. . . . .   | 72 |

|      |  |     |
|------|--|-----|
| 3.9  | Schematic of the discretization of the $\frac{\partial u}{\partial x}$ . The solid body is shown in gray. . . . .  | 75  |
| 3.10 | Schematic of the discretization of the $\frac{\partial u}{\partial y}$ . The solid body is shown in gray. . . . .  | 78  |
| 3.11 | Schematic of the approximation of $\frac{\partial u}{\partial \bar{n}}$ on the fluid-body interface segment. The solid body is shown in gray. . . . .  | 79  |
| 3.12 | Discretization of the pressure term. The solid body is shown in gray. . . . .  | 82  |
| 3.13 | An approximation of the free surface normal vector. The solid body is shown in gray. . . . .   | 88  |
| 3.14 | Fluid mapping algorithm. . . . .   | 90  |
| 3.15 | Fluid advection algorithm: (a) advection of the convective fluxes along the $x$ -coordinate, (b) mapping onto the image cell, (c) advection of the convective fluxes along the $y$ -coordinate. . . . .  | 91  |
| 3.16 | Computational domain boundary conditions. . . . .  | 93  |
| 3.17 | Numerical simulation flowchart. . . . .  | 99  |
| 3.18 | The structure of the matrix of the linear system, $A$ . . . . .  | 100 |
| 4.1  | An example of the computational grid (pressure cells) with $278 \times 178$ elements. . . . .  | 104 |
| 4.2  | Grid geometry parameters. The shaded region is the uniform grid region. . . . .  | 106 |
| 4.3  | The time evolution of the drag coefficient, $C_D$ , for the stationary cylinder case in the absence of a free surface at $R = 500$ : numerical results of Li <i>et al.</i> (2004) (dashed) and Ploumhans and Winckelmans (2000) (dash-dot); present results (solid). . . . .   | 113 |
| 4.4  | The time evolution of the drag coefficient, $C_D$ , (left) and the maximum vorticity, $\zeta_{max}$ , (right) for the stationary cylinder case in the absence of a free surface at $R = 10^3$ : numerical results of Anderson and Reider (1996) (dashed); present results (solid). . . . .   | 114 |
| 4.5  | The surface pressure distribution, $p_0$ , (left) and the surface vorticity distribution, $\zeta_0$ , (right) for the stationary cylinder case in the absence of a free surface at $R = 10^3$ (from top to bottom: $t = 0.5, 1.0, 1.5$ ): numerical results of Anderson and Reider (1996) (dashed); present results (solid). . . . . | 115 |

- 4.6 The equivorticity lines ((a), (b)) and the streamlines ((c), (d)) for the stationary cylinder case in the absence of a free surface at  $R = 10^3$  (from top to bottom:  $t = 0.75, 1.0, 1.25, 1.5$ ): ((a), (c)) numerical results of Anderson and Reider (1996); ((b), (d)) present results. Red colours correspond to positive vorticity (counterclockwise rotation) and green colours indicate negative vorticity (clockwise rotation). From top to bottom the values of the streamlines are: 0.683, 0.586, 0.471, 0.380, 0.280, 0.217, 0.144, 0.078, 0.008, -0.008; 0.748, 0.644, 0.538, 0.428, 0.320, 0.220, 0.112, 0.007, -0.007, -0.006; 0.633, 0.518, 0.374, 0.181, 0.109, 0.042, 0.007, 0.002, -0.080, -0.042, -0.007; 0.659, 0.556, 0.415, 0.315, 0.215, 0.148, 0.045, 0.007, -0.114, -0.074, -0.045, -0.005. . . . . 116
- 4.7 The time evolution of the  $u$ -velocity of the fluid over two periods of vortex shedding,  $t/T_0 = 2$ , for the stationary cylinder case in the absence of a free surface at  $R = 106$ : experimental results of Anagnostopoulos (1997) (circles); numerical results of Anagnostopoulos (1997) (dotted) and Al-Mdallal (2004) (dashed); present results (solid) at the locations: (a)  $(x, y) = (2.7, 0.32)$ , (b)  $(x, y) = (2.7, 0.43)$ , (c)  $(x, y) = (4.9, 0.17)$ , (d)  $(x, y) = (4.9, 0.33)$ , (e)  $(x, y) = (7.5, 0.5)$ , (f)  $(x, y) = (7.5, 0.75)$ . . . . . 117
- 4.8 The pressure distribution in the near wake region for the stationary cylinder case in the absence of a free surface at  $R = 106$  (from top to bottom:  $t/T_0 = 0, 1/8, 1/12$  ( $T_0 = 5.9$ )): numerical results of Anagnostopoulos (1997) (left) and Al-Mdallal (2004) (middle); present results (right). . . . . 119
- 4.9 The surface pressure distribution,  $p_0$ , (left) and the surface vorticity distribution,  $\zeta_0$ , (right) for the combined rotational and transverse oscillation case in the absence of a free surface at  $R = 855$ :  $A = 0.13$ ,  $A_\alpha = 30^\circ$ ,  $f/f_0 = 1$  (from top to bottom:  $t = 0.05, 0.25, 0.5$ ): analytical results of Al-Mdallal (2004) (circles); numerical results of Al-Mdallal (2004) (dashed); present results (solid). . . . . 124
- 4.10 The surface pressure distribution,  $p_0$ , (left) and the surface vorticity distribution,  $\zeta_0$ , (right) for the combined rotational and in-line oscillation case in the absence of a free surface at  $R = 855$ :  $A = 0.13$ ,  $A_\alpha = 30^\circ$ ,  $f/f_0 = 1$  (from top to bottom:  $t = 0.05, 0.25, 0.5$ ): analytical results of Al-Mdallal (2004) (circles); numerical results of Al-Mdallal (2004) (dashed); present results (solid). . . . . 125

- 4.11 The lift coefficients,  $C_L$ ,  $C_{L,f}$  and  $C_{L,p}$ , (left) and the drag coefficients,  $C_D$ ,  $C_{D,f}$  and  $C_{D,p}$ , (right) for the combined rotational and transverse oscillation case in the absence of a free surface at  $R = 855$ :  $A = 0.13$ ,  $A_\alpha = 30^\circ$ ,  $f/f_0 = 1$  (from top to bottom:  $t = 0.05, 0.25, 0.5$ ): analytical results of Al-Mdallal (2004) (circles); numerical results of Al-Mdallal (2004) (dashed); present results (solid). . . . . 126
- 4.12 The lift coefficients,  $C_L$ ,  $C_{L,f}$  and  $C_{L,p}$ , (left) and the drag coefficients,  $C_D$ ,  $C_{D,f}$  and  $C_{D,p}$ , (right) for the combined rotational and in-line oscillation case in the absence of a free surface at  $R = 855$ :  $A = 0.13$ ,  $A_\alpha = 30^\circ$ ,  $f/f_0 = 1$  (from top to bottom:  $t = 0.05, 0.25, 0.5$ ): analytical results of Al-Mdallal (2004) (circles); numerical results of Al-Mdallal (2004) (dashed); present results (solid). . . . . 127
- 4.13 The equivorticity lines for the case of uniform flow past a cylinder subject to in-line oscillations in the absence of a free surface at  $R = 100$ :  $A = 0.14$ ,  $f/f_0 = 2$  (from top to bottom:  $t/T_0 = 1/4, 1/2, 3/4, 1.0$  ( $T_0 = 5.91$ )): numerical results of Su *et al.* (2007) (left); present results (right). Red colours correspond to positive vorticity (counterclockwise rotation) and green colours indicate negative vorticity (clockwise rotation). . . . . 129
- 4.14 The equivorticity lines for the case of uniform flow past an oscillating cylinder at the angle  $\eta = 60^\circ$  in the absence of a free surface at  $R = 855$ :  $A = 0.13$  (from top to bottom:  $f/f_0 = 0.5, 1.0, 2.0, 3.0, 4.0$ ): experimental results of Ongoren and Rockwell (1988) (left); numerical results of Al-Mdallal (2004) (middle); present results (right). Red colours correspond to positive vorticity (counterclockwise rotation) and green colours indicate negative vorticity (clockwise rotation). The snapshots are taken at the instant corresponding to the maximum negative displacement of the cylinder. . . . . 133
- 4.15 The equivorticity lines for the case of uniform flow past a cylinder subject to in-line oscillations in the absence of a free surface at  $R = 855$ :  $A = 0.13$  (from top to bottom:  $f/f_0 = 0.5, 1.0, 2.0, 3.0, 4.0$ ): experimental results of Ongoren and Rockwell (1988) (left); numerical results of Al-Mdallal (2004) (middle); present results (right). Red colours correspond to positive vorticity (counterclockwise rotation) and green colours indicate negative vorticity (clockwise rotation). The snapshots are taken at the instant corresponding to the maximum negative displacement of the cylinder. . . . . 134

|      |  |     |
|------|--|-----|
| 4.16 | The streamline patterns in the near wake region for impulsively started steadily rotating cylinder in the absence of a free surface at $R = 500$ : $\alpha(t) = 1.0$ (from top to bottom: $t = 1.0, 1.5, 4.0, 5.0, 6.0$ ): numerical results of Badr and Dennis (1985) (left); Takada and Tsutahara (1998) (middle); present results (right). . . . .  | 135 |
| 4.17 | The streamline patterns in the near wake region for impulsively started steadily rotating cylinder in the absence of a free surface at $R = 200$ : $\alpha(t) = 2.0$ (from top to bottom: $t = 2.0, 3.0, 4.0, 4.5, 6.5$ ): experimental results of Coutanceau and Menard (1985) (left); numerical results of Nair <i>et al.</i> (1998) (middle); present results (right). . . . .  | 136 |
| 4.18 | The equivorticity lines and the free surface deformations for the case of uniform flow past a stationary cylinder in the presence of a free surface at $R = 180$ , $h = 0.55$ (from top to bottom: $Fr \approx 0.0$ ( $t = 19.9$ ), $Fr = 0.3$ ( $t = 19$ ), $0.4$ ( $t = 33.2$ ), $0.6$ ( $t = 20.2$ )): numerical results of Gubanov (2006) (left); Reichl <i>et al.</i> (2005) (middle); present results (right). . . . . | 137 |
| 4.19 | The equivorticity lines and the free surface deformations for the case of uniform flow past a stationary cylinder in the presence of a free surface at $R = 180$ , $h = 0.16$ (from top to bottom: $Fr \approx 0.0$ ( $t = 61.3$ ), $Fr = 0.3$ ( $t = 16$ ), $0.4$ ( $t = 50.4$ ), $0.6$ ( $t = 40$ )): numerical results of Reichl <i>et al.</i> (2005) (left); present results (right). . . . .                            | 142 |
| 4.20 | The equivorticity lines for the case of uniform flow past the cylinder subject to in-line oscillations in the presence of a free surface at $R = 917$ : $f/f_0 = 1$ , $A = 0.96$ , $h = 11.23$ , $Fr = 0.07$ : experimental results of Cetiner and Rockwell (2001) (left); present results (right). . . . .  | 143 |
| 5.1  | The time variation of the lift coefficient, $C_L$ , (black) and the in-line displacement, $x(t)$ , (gray); PSD of $C_L$ ; Lissajous patterns of $C_L$ at $R = 200$ : $A = 0.13$ , $1.0 \leq f/f_0 \leq 4.0$ , $h = \infty$ . . . . .   | 148 |
| 5.2  | The time variation of the drag coefficient, $C_D$ , (black) and the in-line displacement, $x(t)$ , (gray); PSD of $C_D$ ; Lissajous patterns of $C_D$ at $R = 200$ : $A = 0.13$ , $1.0 \leq f/f_0 \leq 4.0$ , $h = \infty$ . . . . .   | 149 |
| 5.3  | The equivorticity patterns (left), the streamline patterns (middle) and the pressure distribution in the near wake (right) over two periods of cylinder oscillation, $2T$ , at $R = 200$ : $A = 0.13$ , $f/f_0 = 2.0$ , $h = \infty$ ( $T \approx 2.525$ , $101 \leq t \leq 106$ ). The locked-on 2S mode, per $2T$ , is observed. . . . .   | 152 |

|      |  |     |
|------|--|-----|
| 5.4  | The equivorticity patterns over ten periods of cylinder oscillation, $10T$ , at $R = 200$ : $A = 0.13$ , $h = \infty$ and (a) $f/f_0 = 1.0$ ( $T \approx 5.051$ , $80.8 \leq t \leq 131.3$ ), (b) $f/f_0 = 3.0$ ( $T \approx 1.684$ , $101 \leq t \leq 118$ ), (c) $f/f_0 = 4.0$ ( $T \approx 1.263$ , $127.5 \leq t \leq 138.9$ ) (non-periodic state). . . . .   | 153 |
| 5.5  | The vortex coalescence phenomenon in the near wake of the cylinder over two periods of cylinder oscillation, $2T$ , at $R = 200$ : $A = 0.13$ , $f/f_0 = 4.0$ ( $T \approx 1.263$ , $133.8 \leq t \leq 136.3$ ), $h = \infty$ (non-periodic state).  | 155 |
| 5.6  | The equivorticity patterns ((a), (c)) and the streamline patterns ((b), (d)) over five periods of cylinder oscillation, $5T$ , at $R = 200$ : $A = 0.13$ , $f/f_0 = 4.0$ , $h = 0.25$ , $Fr \approx 0.0$ ( $T \approx 1.263$ , $30.25 \leq t \leq 36.55$ ). The quasi-locked-on <b>C(2S)</b> mode, per $5T$ , is observed. . . . .   | 158 |
| 5.7  | The equivorticity patterns ((a), (c)) and the streamline patterns ((b), (d)) over one period of cylinder oscillation, $T$ , at $R = 200$ : $A = 0.13$ , $f/f_0 = 1.0$ , $Fr \approx 0.0$ , ((a),(b)) $h = 0.5$ ( $T \approx 5.051$ , $90.85 \leq t \leq 95.95$ ); ((c),(d)) $h = 0.75$ ( $T \approx 5.051$ , $65.65 \leq t \leq 70.65$ ). The locked-on <b>2S</b> mode, per $T$ , is observed. . . . .   | 159 |
| 5.8  | The equivorticity patterns ((a), (c)) and the streamline patterns ((b), (d)) over two periods of cylinder oscillation, $2T$ , at $R = 200$ : $A = 0.13$ , $f/f_0 = 2.0$ , $Fr \approx 0.0$ , ((a),(b)) $h = 0.5$ ; ((c),(d)) $h = 0.75$ ( $T \approx 2.525$ , $95.95 \leq t \leq 100.95$ ). The locked-on <b>C(2S)</b> and <b>P+S</b> modes, per $2T$ , are observed when $h = 0.5, 0.75$ , respectively. . . . .  | 163 |
| 5.9  | The equivorticity patterns ((a), (c)) and the streamline patterns ((b), (d)) over three periods of cylinder oscillation, $3T$ , at $R = 200$ : $A = 0.13$ , $f/f_0 = 3.0$ , $Fr \approx 0.0$ , ((a),(b)) $h = 0.5$ ( $T \approx 1.684$ , $21.85 \leq t \leq 26.85$ ); ((c),(d)) $h = 0.75$ ( $T \approx 1.684$ , $57.15 \leq t \leq 62.25$ ). The quasi-locked-on <b>C(2S)</b> and <b>C(P+S)</b> modes, per $3T$ , are observed within $12T$ and $24T$ when $h = 0.5, 0.75$ , respectively. . . . .                      | 164 |
| 5.10 | The equivorticity patterns ((a), (c)) and the streamline patterns ((b), (d)) over four periods of cylinder oscillation, $4T$ , at $R = 200$ : $A = 0.13$ , $f/f_0 = 4.0$ , $Fr \approx 0.0$ , ((a),(b)) $h = 0.5$ ( $T \approx 1.263$ , $40.35 \leq t \leq 45.45$ ); ((c),(d)) $h = 0.75$ ( $T \approx 1.263$ , $78.25 \leq t \leq 83.25$ ). The quasi-locked-on <b>2P</b> mode, per $4T$ , is observed within $20T$ when $h = 0.5$ . The locked-on <b>C(P+S)</b> mode, per $4T$ , is observed when $h = 0.75$ . . . . . | 165 |
| 5.11 | The effect of the cylinder submergence depth, $h$ , and the frequency ratio, $f/f_0$ , on the equivorticity patterns at $R = 200$ : $A = 0.13$ , $Fr \approx 0.0$ . All snapshots are taken at the instant $x(t) = A$ . . . . .  | 169 |
| 5.12 | The time variation of the lift coefficient, $C_L$ , (black) and the in-line displacement, $x(t)$ , (gray); PSD of $C_L$ ; Lissajous patterns of $C_L$ at $R = 200$ : $A = 0.13$ , $1.0 \leq f/f_0 \leq 4.0$ , $Fr = 0.2$ , $h = 0.25$ . . . . .  | 171 |

|      |   |     |
|------|---|-----|
| 5.13 | The time variation of the drag coefficient, $C_D$ , (black) and the in-line displacement, $x(t)$ , (gray); PSD of $C_D$ ; Lissajous patterns of $C_D$ at $R = 200$ : $A = 0.13$ , $1.0 \leq f/f_0 \leq 4.0$ , $Fr = 0.2$ , $h = 0.25$ . . . . .   | 172 |
| 5.14 | The time variation of the lift coefficient, $C_L$ , (black) and the in-line displacement, $x(t)$ , (gray); PSD of $C_L$ ; Lissajous patterns of $C_L$ at $R = 200$ : $A = 0.13$ , $1.0 \leq f/f_0 \leq 4.0$ , $Fr = 0.2$ , $h = 0.5$ . . . . .  | 175 |
| 5.15 | The time variation of the lift coefficient, $C_L$ , (black) and the in-line displacement, $x(t)$ , (gray); PSD of $C_L$ ; Lissajous patterns of $C_L$ at $R = 200$ : $A = 0.13$ , $1.0 \leq f/f_0 \leq 4.0$ , $Fr = 0.2$ , $h = 0.75$ . . . . .   | 176 |
| 5.16 | The time variation of the drag coefficient, $C_D$ , (black) and the in-line displacement, $x(t)$ , (gray); PSD of $C_D$ ; Lissajous patterns of $C_D$ at $R = 200$ : $A = 0.13$ , $1.0 \leq f/f_0 \leq 4.0$ , $Fr = 0.2$ , $h = 0.5$ . . . . .  | 177 |
| 5.17 | The time variation of the drag coefficient, $C_D$ , (black) and the in-line displacement, $x(t)$ , (gray); PSD of $C_D$ ; Lissajous patterns of $C_D$ at $R = 200$ : $A = 0.13$ , $1.0 \leq f/f_0 \leq 4.0$ , $Fr = 0.2$ , $h = 0.75$ . . . . .   | 178 |
| 5.18 | The equivorticity patterns (left), the streamline patterns (middle) and the pressure distribution in the near wake (right) over one period of cylinder oscillation, $T$ , at $R = 200$ : $A = 0.13$ , $f/f_0 = 1.0$ , $h = 0.5$ , $Fr = 0.2$ ( $T \approx 5.051$ , $80.7 \leq t \leq 85.7$ ). The quasi-locked-on <b>2S</b> mode, per $T$ , is observed. . . . .      | 179 |
| 5.19 | The equivorticity patterns (left), the streamline patterns (middle) and the pressure distribution in the near wake (right) over one period of cylinder oscillation, $T$ , at $R = 200$ : $A = 0.13$ , $f/f_0 = 1.0$ , $h = 0.75$ , $Fr = 0.2$ ( $T \approx 5.051$ , $80.7 \leq t \leq 85.7$ ). The quasi-locked-on <b>2S</b> mode, per $T$ , is observed. . . . .     | 180 |
| 5.20 | The equivorticity patterns (left), the streamline patterns (middle) and the pressure distribution in the near wake (right) over two periods of cylinder oscillation, $2T$ , at $R = 200$ : $A = 0.13$ , $f/f_0 = 2.0$ , $Fr = 0.2$ , $h = 0.5$ ( $T \approx 2.525$ , $80.7 \leq t \leq 85.7$ ). The quasi-locked-on <b>2S</b> mode, per $2T$ , is observed. . . . .   | 182 |
| 5.21 | The equivorticity patterns (left), the streamline patterns (middle) and the pressure distribution in the near wake (right) over two periods of cylinder oscillation, $2T$ , at $R = 200$ : $A = 0.13$ , $f/f_0 = 2.0$ , $Fr = 0.2$ , $h = 0.75$ ( $T \approx 2.525$ , $70.7 \leq t \leq 75.7$ ). The quasi-locked-on <b>P+S</b> mode, per $2T$ , is observed. . . . . | 183 |
| 5.22 | The effect of the cylinder submergence depth, $h$ , and the frequency ratio, $f/f_0$ , on the equivorticity patterns at $R = 200$ : $A = 0.13$ , $Fr = 0.2$ . All snapshots are taken at the instant $x(t) = A$ . . . . .   | 186 |

|      |  |     |
|------|--|-----|
| 5.23 | The time variation of the lift coefficient, $C_L$ , (black) and the in-line displacement, $x(t)$ , (gray); PSD of $C_L$ ; Lissajous patterns of $C_L$ at $R = 200$ : $A = 0.13$ , $1.0 \leq f/f_0 \leq 4.0$ , $Fr = 0.4$ , $h = 0.25$ . . . . .  | 194 |
| 5.24 | The time variation of the drag coefficient, $C_D$ , (black) and the in-line displacement, $x(t)$ , (gray); PSD of $C_D$ ; Lissajous patterns of $C_D$ at $R = 200$ : $A = 0.13$ , $1.0 \leq f/f_0 \leq 4.0$ , $Fr = 0.4$ , $h = 0.25$ . . . . .  | 195 |
| 5.25 | The equivorticity patterns (left), the streamline patterns (middle) and the pressure distribution in the near wake (right) over four periods of cylinder oscillation, $4T$ , at $R = 200$ : $A = 0.13$ , $f/f_0 = 3.0$ , $Fr = 0.4$ , $h = 0.25$ ( $T \approx 1.684$ , $38.6 \leq t \leq 45.4$ ). The quasi-locked-on <b>C(2S)</b> mode, per $4T$ , is observed within $20T$ . . . . . | 196 |
| 5.26 | The equivorticity patterns (left), the streamline patterns (middle) and the pressure distribution in the near wake (right) over ten periods of cylinder oscillation, $10T$ , at $R = 200$ : $A = 0.13$ , $f/f_0 = 3.0$ , $Fr = 0.4$ , $h = 0.25$ ( $T \approx 1.684$ , $69 \leq t \leq 85.8$ ) (non-periodic state). . . . .   | 197 |
| 5.27 | The equivorticity patterns (left), the streamline patterns (middle) and the pressure distribution in the near wake (right) over five periods of cylinder oscillation, $5T$ , at $R = 200$ : $A = 0.13$ , $f/f_0 = 4.0$ , $Fr = 0.4$ , $h = 0.25$ ( $T \approx 1.263$ , $25.2 \leq t \leq 31.5$ ). The quasi-locked-on <b>C(2S)</b> mode, per $5T$ , is observed within $20T$ . . . . . | 198 |
| 5.28 | The time variation of the lift coefficient, $C_L$ , (black) and the in-line displacement, $x(t)$ , (gray); PSD of $C_L$ ; Lissajous patterns of $C_L$ at $R = 200$ : $A = 0.13$ , $1.0 \leq f/f_0 \leq 4.0$ , $Fr = 0.4$ , $h = 0.5$ . . . . .   | 199 |
| 5.29 | The time variation of the drag coefficient, $C_D$ , (black) and the in-line displacement, $x(t)$ , (gray); PSD of $C_D$ ; Lissajous patterns of $C_D$ at $R = 200$ : $A = 0.13$ , $1.0 \leq f/f_0 \leq 4.0$ , $Fr = 0.4$ , $h = 0.5$ . . . . .   | 200 |
| 5.30 | The equivorticity patterns (left), the streamline patterns (middle) and the pressure distribution in the near wake (right) over one period of cylinder oscillation, $T$ , at $R = 200$ : $A = 0.13$ , $f/f_0 = 1.0$ , $Fr = 0.4$ , $h = 0.5$ ( $T \approx 5.051$ , $35.3 \leq t \leq 40.4$ ). The quasi-locked-on <b>C(2S)</b> mode, per $T$ , is observed within $5T$ . . . . .       | 210 |
| 5.31 | The equivorticity patterns (left), the streamline patterns (middle) and the pressure distribution in the near wake (right) over two periods of cylinder oscillation, $2T$ , at $R = 200$ : $A = 0.13$ , $f/f_0 = 2.0$ , $Fr = 0.4$ , $h = 0.5$ ( $T \approx 2.525$ , $30.3 \leq t \leq 35.3$ ). The quasi-locked-on <b>C(2S)</b> mode, per $2T$ , is observed within $14T$ . . . . .   | 211 |

|      |   |     |
|------|---|-----|
| 5.32 | POD eigen-modes for (a): $h = \infty$ , $f/f_0 = 2.0$ , $t = 100$ to $150$ ; (b): $Fr = 0.4$ , $h = 0.5$ , $f/f_0 = 2.0$ , $t = 20$ to $50$ (quasi-periodic state); (c): $Fr = 0.4$ , $h = 0.5$ , $f/f_0 = 2.0$ , $t = 60$ to $100$ (non-periodic state) at $R = 200$ : $A = 0.13$ . . . . .  | 213 |
| 5.33 | The equivorticity patterns (left), the streamline patterns (middle) and the pressure distribution in the near wake (right) over three periods of cylinder oscillation, $3T$ , at $R = 200$ : $A = 0.13$ , $f/f_0 = 3.0$ , $Fr = 0.4$ , $h = 0.5$ ( $T \approx 1.684$ , $33.6 \leq t \leq 38.6$ ). The quasi-locked-on <b>C(P+S)+S</b> mode, per $3T$ , is observed within $18T$ . . . . . | 216 |
| 5.34 | The equivorticity patterns (left), the streamline patterns (middle) and the pressure distribution in the near wake (right) over four periods of cylinder oscillation, $4T$ , at $R = 200$ : $A = 0.13$ , $f/f_0 = 4.0$ , $Fr = 0.4$ , $h = 0.5$ ( $T \approx 1.263$ , $17.6 \leq t \leq 22.7$ ). The quasi-locked-on <b>C(P+S)+S</b> mode, per $4T$ , is observed within $28T$ . . . . .  | 217 |
| 5.35 | The vortex coalescence phenomenon in the quasi-locked-on <b>C(P+S)+S</b> mode over two periods of cylinder oscillation, $2T$ , at $R = 200$ : $A = 0.13$ , $f/f_0 = 4.0$ , $h = 0.5$ , $Fr = 0.4$ ( $T \approx 1.263$ , $20.15 \leq t \leq 22.7$ ). . . . .   | 218 |
| 5.36 | The time variation of the lift coefficient, $C_L$ , (black) and the in-line displacement, $x(t)$ , (gray); PSD of $C_L$ ; Lissajous patterns of $C_L$ at $R = 200$ : $A = 0.13$ , $1.0 \leq f/f_0 \leq 4.0$ , $Fr = 0.4$ , $h = 0.75$ . . . . .   | 219 |
| 5.37 | The time variation of the drag coefficient, $C_D$ , (black) and the in-line displacement, $x(t)$ , (gray); PSD of $C_D$ ; Lissajous patterns of $C_D$ at $R = 200$ : $A = 0.13$ , $1.0 \leq f/f_0 \leq 4.0$ , $Fr = 0.4$ , $h = 0.75$ . . . . .   | 220 |
| 5.38 | The equivorticity patterns (left), the streamline patterns (middle) and the pressure distribution in the near wake (right) over two periods of cylinder oscillation, $2T$ , at $R = 200$ : $A = 0.13$ , $f/f_0 = 2.0$ , $Fr = 0.4$ , $h = 0.75$ ( $T \approx 2.525$ , $17.6 \leq t \leq 22.8$ ). The quasi-locked-on <b>P+S</b> mode, per $2T$ , is observed within $14T$ . . . . .       | 227 |
| 5.39 | The equivorticity patterns (left), the streamline patterns (middle) and the pressure distribution in the near wake (right) over three periods of cylinder oscillation, $3T$ , at $R = 200$ : $A = 0.13$ , $f/f_0 = 3.0$ , $Fr = 0.4$ , $h = 0.75$ ( $T \approx 1.684$ , $20.2 \leq t \leq 25.2$ ). The quasi-locked-on <b>C(2S)+S</b> mode, per $3T$ , is observed within $18T$ . . . . . | 228 |
| 5.40 | The equivorticity patterns (left), the streamline patterns (middle) and the pressure distribution in the near wake (right) over four periods of cylinder oscillation, $4T$ , at $R = 200$ : $A = 0.13$ , $f/f_0 = 4.0$ , $Fr = 0.4$ , $h = 0.75$ ( $T \approx 1.263$ , $22.7 \leq t \leq 27.7$ ). The quasi-locked-on <b>C(2S)+S</b> mode, per $4T$ , is observed within $12T$ . . . . .  | 229 |

|      |  |     |
|------|--|-----|
| 5.41 | The effect of the cylinder submergence depth, $h$ , and the frequency ratio, $f/f_0$ , on the equivorticity patterns at $R = 200$ : $A = 0.13$ , $Fr = 0.4$ . All snapshots are taken at the instant $x(t) = A$ . . . . .                                  | 233 |
| 6.1  | The effect of the Froude number, $Fr$ , and the cylinder submergence depth, $h$ , on the equivorticity patterns at $R = 200$ : $A = 0.13$ , $f/f_0 = 1.0$ . All snapshots are taken at the instant $x(t) = A$ . . . . .                                    | 249 |
| 6.2  | The effect of the Froude number, $Fr$ , and the cylinder submergence depth, $h$ , on the equivorticity patterns at $R = 200$ : $A = 0.13$ , $f/f_0 = 2.0$ . All snapshots are taken at the instant $x(t) = A$ . . . . .                                    | 250 |
| 6.3  | The effect of the Froude number, $Fr$ , and the cylinder submergence depth, $h$ , on the equivorticity patterns at $R = 200$ : $A = 0.13$ , $f/f_0 = 3.0$ . All snapshots are taken at the instant $x(t) = A$ . . . . .                                    | 252 |
| 6.4  | The effect of the Froude number, $Fr$ , and the cylinder submergence depth, $h$ , on the equivorticity patterns at $R = 200$ : $A = 0.13$ , $f/f_0 = 4.0$ . All snapshots are taken at the instant $x(t) = A$ . . . . .                                    | 254 |
| A.1  | Location of $\hat{A}_x^*$ , $\hat{A}_y^*$ and $\hat{V}^*$ within the computational cell, $V^*$ . The solid body is shown in gray. . . . .  | 283 |
| A.2  | Typical computational cell, $V^*$ , containing a fluid-body interface, (b) typical computational cell, $V^*$ , which includes areas, $A_i^*$ ( $i = 0, 1, 2, 3$ ) and volume, $V^*$ , open to flow within $V^*$ . The solid body is shown in gray. . . . . | 285 |

## Nomenclature

|               |  |
|---------------|--|
| $\bar{A}$     | fractional area open to flow   |
| $A$           | area open to flow (area aperture)  |
| $\hat{A}_x^*$ | dimensional fractional area porosity function in $x^*$ -direction                  |
| $\hat{A}_y^*$ | dimensional fractional area porosity function in $y^*$ -direction                  |
| $\vec{a}$     | acceleration of non-inertial frame of reference, $\hat{X}$ , ( $= (a_1, a_2, 0)$ ) |
| $A$           | forcing amplitude of the recti-linear cylinder oscillation ( $= A^*/d$ )           |
| $A_\alpha$    | forcing amplitude of the rotational cylinder oscillation ( $= A_\alpha^*/d$ )      |
| $C_L$         | lift coefficient ( $= 2L/\rho U^2 d$ )   |
| $C_{L,max}$   | maximum lift coefficient   |
| $C_{L,min}$   | minimum lift coefficient   |
| $\hat{C}_L$   | mean lift coefficient  |
| $C_{L,rms}$   | RMS lift coefficient   |
| $C_D$         | drag coefficient ( $= 2D/\rho U^2 d$ )   |
| $C_{D,max}$   | maximum drag coefficient   |
| $C_{D,min}$   | minimum drag coefficient   |
| $\hat{C}_D$   | mean drag coefficient  |
| $C_{D,rms}$   | RMS drag coefficient   |
| $d$           | cylinder diameter  |
| $\bar{d}$     | line distance from the origin in equation (3.57)                                   |

|                |  |
|----------------|--|
| $D$            | drag force per unit length   |
| $f$            | forcing frequency of the recti-linear cylinder oscillation ( $= df^*/U$ )                        |
| $f_\alpha$     | forcing frequency of the rotational cylinder oscillation ( $= df_\alpha^*/U$ )                   |
| $f_0$          | natural vortex shedding frequency<br>in the absence of a free surface ( $= df_0/U$ )             |
| $f _{fs}$      | natural vortex shedding frequency<br>in the presence of a free surface ( $= df^* _{fs}/U$ )      |
| $Fr$           | Froude number ( $= U/\sqrt{dg^*}$ )  |
| $Fr _L$        | local Froude number ( $= U/\sqrt{h^* _L g^*}$ )  |
| $F_{\Omega_1}$ | fraction of the fluid in the region $\Omega_1$ in a computational cell (VOF function)            |
| $F_{\Omega_2}$ | fraction of the fluid in the region $\Omega_2$ in a computational cell                           |
| $F_b$          | fraction of the body in a computational cell   |
| $\vec{F}_s^*$  | dimensional external surface force   |
| $\vec{F}^*$    | dimensional external force ( $= (F_1^*, F_2^*, 0)$ )   |
| $\vec{g}^*$    | dimensional gravitational acceleration in inertial<br>frame of reference, X, ( $= (0, g^*, 0)$ ) |
| $h$            | depth of cylinder submergence ( $= h^*/d$ )  |
| $\Delta h$     | spatial uniform grid step size   |
| $\bar{h}$      | height of the fluid at the outflow boundary  |
| $h _L$         | local free surface height  |

|              |  |
|--------------|--|
| $H$          | Heaviside unit step function   |
| $\mathbb{L}$ | length of a fluid-body interface open to flow                                    |
| $L$          | lift force per unit length   |
| $\vec{n}$    | outward unit normal vector ( $= (n_1, n_2, 0)$ )                                 |
| $P$          | fluid property   |
| $p$          | fluid pressure   |
| $p_0$        | surface pressure   |
| $p_h$        | hydrostatic pressure   |
| $\delta p$   | hydrodynamic pressure  |
| $p_a^*$      | dimensional constant atmospheric pressure  |
| $R$          | Reynolds number ( $= \rho U d / \mu$ )   |
| $S$          | control volume boundary  |
| $t$          | time ( $= t^* U / d$ )   |
| $\Delta t$   | time step  |
| $T$          | period of forced cylinder oscillation ( $= 1/f$ )                                |
| $T_0$        | period of natural vortex shedding in the absence of a free surface ( $= 1/f_0$ ) |
| $\vec{u}$    | fluid velocity ( $= (u, v, 0)$ )   |
| $U$          | uniform flow velocity  |
| $\bar{u}$    | maximum $u$ -velocity of the fluid in the region directly above the cylinder     |
| $\hat{u}$    | average $u$ -velocity of the fluid in the region directly above the cylinder     |

|                 |   |
|-----------------|---|
| $\vec{u}_n$     | normal fluid velocity   |
| $\vec{u}_c$     | velocity of a fluid-body interface  |
| $\bar{V}$       | fractional volume open to flow  |
| $V$             | control volume  |
| $V(t)$          | material volume   |
| $\mathbb{V}$    | volume open to flow (volume aperture)   |
| $\hat{V}^*$     | dimensional fractional volume porosity function                                     |
| $\partial V(t)$ | material volume boundary  |
| $v_j^*$         | dimensional velocity of an arbitrary time dependent fluid domain $\Omega(t)$        |
| $\vec{v}$       | velocity of non-inertial frame of reference, $\hat{X}$ , $(= (v_1, v_2, 0))$        |
| $\vec{x}$       | vector of spatial coordinates in inertial frame of reference, $X$ , $(= (x, y, 0))$ |
| $X$             | inertial frame of reference $(= \{\vec{x}^*, t^*\})$                                |
| $\hat{X}$       | non-inertial frame of reference $(= \{\vec{\hat{x}}^*, \hat{t}^*\})$                |
| $\tilde{X}$     | frame of reference which moves with the uniform flow                                |

### Greek Symbols

|               |                                      |
|---------------|--------------------------------------|
| $\alpha(t)$   | angular displacement of the cylinder |
| $\delta$      | Dirac delta function                 |
| $\zeta$       | vorticity                            |
| $\zeta_{max}$ | maximum vorticity                    |
| $\zeta_0$     | surface vorticity                    |

|                      |   |
|----------------------|---|
| $\eta$               | angle of cylinder oscillation with respect to the uniform free stream |
| $\kappa$             | surface curvature ( $= 1/r$ ), $r$ : radius of curvature              |
| $\mu$                | dynamic viscosity of the fluid  |
| $\nu$                | kinematic viscosity of the fluid ( $= \mu/\rho$ )                     |
| $\rho$               | fluid density   |
| $\sigma$             | surface tension coefficient   |
| $\bar{\sigma}$       | stress tensor   |
| $\bar{\tau}$         | outward unit tangential vector ( $= (\tau_1, \tau_2, 0)$ )            |
| $\phi(x, t)$         | level set function  |
| $\hat{\phi}$         | test function   |
| $\psi$               | stream function   |
| $\omega^*$           | dimensional frequency of the cylinder oscillation ( $= 2\pi f^*$ )    |
| $\Omega$             | arbitrary fluid domain  |
| $\Omega_i, i = 1, 2$ | computational domain occupied by the fluid                            |
| $\partial\Omega$     | arbitrary fluid domain boundary                                       |
| $\nabla$             | vector differential operator  |
| $\nabla^2$           | Laplace operator  |

### Superscripts

|   |                         |
|---|-------------------------|
| * | dimensional quantity    |
| · | differentiation by time |

## Abbreviations

|       |  |
|-------|--|
| CFD   | computational fluid dynamics                   |
| FAVOR | fractional area/volume obstacle representation |
| PSD   | power spectral density                         |
| PLIC  | piecewise linear interface calculation         |
| POD   | proper orthogonal decomposition                |
| SLIC  | simple line interface calculation              |
| VOF   | volume of fluid                                |
| RMS   | root mean square                               |



$d$  is submerged in the fluid in  $\Omega_2$  at the dimensional distance  $h^*$  below undisturbed free surface;  $g^*$  is the dimensional acceleration due to gravity,  $\vec{g}^* = (0, g^*, 0)$ ;  $U$  is the uniform stream velocity;  $f^*$  is the dimensional oscillating frequency of the cylinder. At time  $t^* = 0$  ( $t^*$  is the dimensional time), the cylinder is abruptly forced to perform recti-linear oscillations in the in-line direction to that of uniform flow. The imposed translational oscillatory motion of the center of the cylinder along the translation axis is assigned by

$$x^*(t^*) = A^* \cos(2\pi f^* t^*), \quad (1.1)$$

where  $A^*$  is the dimensional forcing amplitude of the cylinder oscillation. The governing equations and boundary conditions which describe the problem are presented in Chapter 2.

In what follows, a brief discussion of flow past a stationary cylinder and an oscillating cylinder in the absence of a free surface is presented due to its relevance to the problem under consideration.

## 1.1 Problem background and literature review

Kármán (1911, 1912) experimentally observed that the wake of a stationary bluff body in an unbounded uniform free stream in the absence of a free surface has a natural self sustained instability resulting in formation of the double rows of vortices being shed alternately from either side of the body as shown in Figure 1.2. Earlier, Strouhal (1878) observed this type of the vortex formation and shedding while examining the

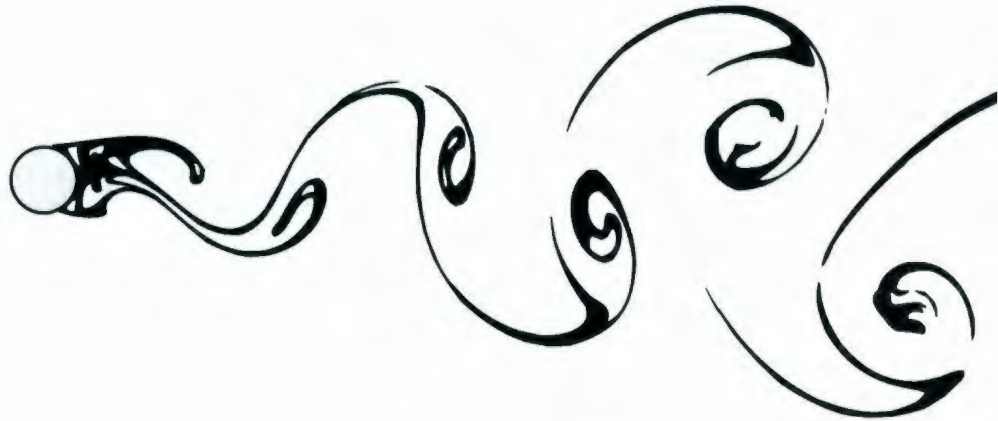


Figure 1.2: Kármán vortex street downstream of a circular cylinder at  $R = 140$ . Retrieved from <http://hmf.enseeiht.fr/> on October 2, 2007.

frequency response of wind blowing over a wire or a string in an Aeolian harp. This type of vortex shedding, called the Kármán vortex street, is widely observed both in the laboratory and in nature for a wide range of Reynolds numbers,  $R$ . In the case of a stationary circular cylinder,  $R = \rho U d / \mu$  ( $\rho$  is the density of the fluid;  $\mu$  is the dynamic viscosity of the fluid), the vortex shedding only occurs when the Reynolds number exceeds a critical value, which is somewhere between 40 and 50. Bénard (1908a,b) was the first to sketch the alternate procession of eddies observed behind a towed circular cylinder in water. The vortex street remains periodic and essentially two-dimensional for the Reynolds number of  $180 \sim 200$ . The vortices are shed with the dimensionless natural Kármán vortex shedding frequency,  $f_0 = d f_0^* / U$  ( $f_0^*$  is the dimensional natural vortex shedding frequency), or the Strouhal number,  $S_0 (= f_0)$ .

A regular vortex shedding from the cylinder excites a periodic resulting force on its surface with transverse and in-line components known as lift and drag forces, respectively. For the stationary cylinder, the lift force oscillates with the Kármán vortex

shedding frequency,  $f_0$ , and the drag force oscillates with twice the Kármán vortex shedding frequency,  $2f_0$ . The variations of regimes of the wake of a circular cylinder and fluid forces with the Reynolds number have been reviewed extensively [see, for example, Norberg (2003), Thompson *et al.* (2001), Posdziech and Grundmann (2001), Henderson (1995), Kravchenko *et al.* (1999), Park *et al.* (1998), Anagnostopoulos (1997), Zdravkovich (1997), Gerrard (1997), Sumer and Fredsøe (1997), Williamson (1996), Wu *et al.* (1996), Zhang and Dalton (1998), Braza *et al.* (1986) and Farrell (1981)].

When the cylinder is subject to forced oscillations in a uniform flow, there might be a situation when the dimensionless oscillatory frequency of the cylinder,  $f = df^*/U$ , passes through  $f_0$  or  $2f_0$ , i.e.,  $f/f_0 \approx 1$  or  $f/f_0 \approx 2$ . At these conditions the vortex shedding becomes *locked-on* to the cylinder motion depending on the oscillation type and may result in a noise and even a structural failure. A striking example is the Cormorant-Sullom Voe oil line in the North Sea which surfaced in 1975 after losing 60% of its concrete coating. The lock-on has been recognized as the response to oscillatory cylinder motions in the absence of a free surface. The conditions of lock-on have been studied previously in hundreds of papers [see, for example, Al-Mdallal *et al.* (2007), Sarpkaya (2004), Anagnostopoulos (2002), Cetiner and Rockwell (2001), Meneghini and Bearman (1995), Griffin and Hall (1991), Ongoren and Rockwell (1988a, 1988b), Williamson and Roshko (1988) and Bearman (1984)]. For transverse or rotational oscillations of the cylinder, the range near  $f/f_0 \approx 1$  constitutes the fundamental lock-on regime; for in-line oscillations of the cylinder the lock-on is observed at  $f/f_0 \approx 2$ . The classical definition of the lock-on is based on the existence of a strong spectral peak of the wake frequency. However, lock-on phe-

nomenon cannot be identified, clearly, from the spectral analysis in all the types of motions (for example, in-line oscillations case). In this case, lock-on can be defined through the Lissajous trajectories, i.e., the phase diagrams of the lift and drag forces versus the displacement of the cylinder [see, for example, Al-Mdallal *et al.* (2007) and Cetiner and Rockwell (2001)]. The bounds of lock-on generally include all the cases where the dominant frequency becomes close to the Kármán vortex shedding frequency,  $f_0$ .

The general form of the vortices shed into the near wake of the cylinder is often described in terms of the mode of vortex shedding. Williamson and Roshko (1988) classified the modes of vortex shedding for the case of transversely oscillating cylinder in the absence of a free surface. The extensive mapping of Williamson and Roshko (1988), shown in Figure 1.3, is obtained over the range of Reynolds numbers,  $300 < R < 10^3$ , in the range of amplitude of the cylinder oscillation,  $0 < A(= A^*/d) \leq 1.8$ , for the frequency ratios  $f/f_0 \geq 0.3$ . The wavelength ratio is defined as  $\lambda/d = UT^*/d$  ( $T^*(= 1/f^*)$  is the dimensional period of cylinder oscillation). It should be noted, that the Reynolds number,  $R$ , is never held fixed and the observed vortex locked-on modes are expected to persist over the range of Reynolds numbers beyond  $300 < R < 10^3$  and for different types of cylinder oscillations.

The vortex locked-on modes observed by Williamson and Roshko (1988) are shown in Figure 1.4. The most commonly observed modes near the fundamental lock-on region are **2S**, **2P** and **P+S**. For the **2S** mode, two single vortices of opposite sign are shed per the dimensionless period of natural vortex shedding,  $T_0(= 1/f_0)$ , forming the classical von Kármán street. The **2P** mode corresponds to the shedding of two

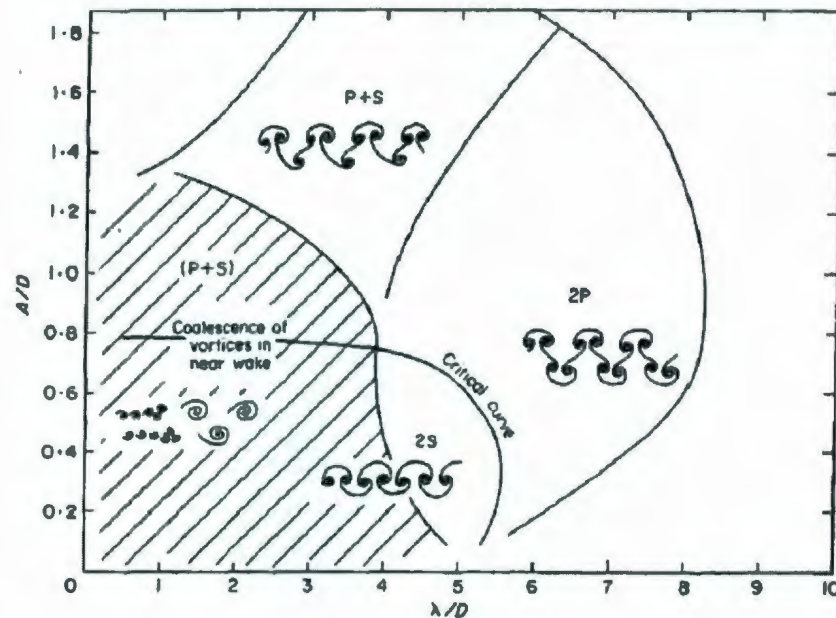


Figure 1.3: A map of the vortex locked-on modes in the wavelength-amplitude plane near the fundamental lock-on region as observed by Williamson and Roshko (1988). The critical curve marks the transition from one mode of vortex formation to another.

counter-rotating pairs per  $T_0$ . For the **P+S** mode, one single and a pair of co-rotating vortices are shed per  $T_0$ . The patterns marked as **P** and **2P\*** take the appearance of a jet rather than a wake. For **P** mode, a single pair of co-rotating vortices are shed from the one side of the cylinder. Mode **2P\*** is similar to **2P** except that vortex pairs in one half of period of vortex shedding convect downstream of cylinder wake. Finally, **2P + 2S** mode comprises two vortex pairs forming at both sides of the cylinder as in **2P** mode, but with the inclusion of single vortices between each vortex pair. The most interesting mode of vortex shedding is a coalescence (or merging) of vortices. Williamson and Roshko (1988) denote the two modes as **C(2S)** and **C(P+S)**. In

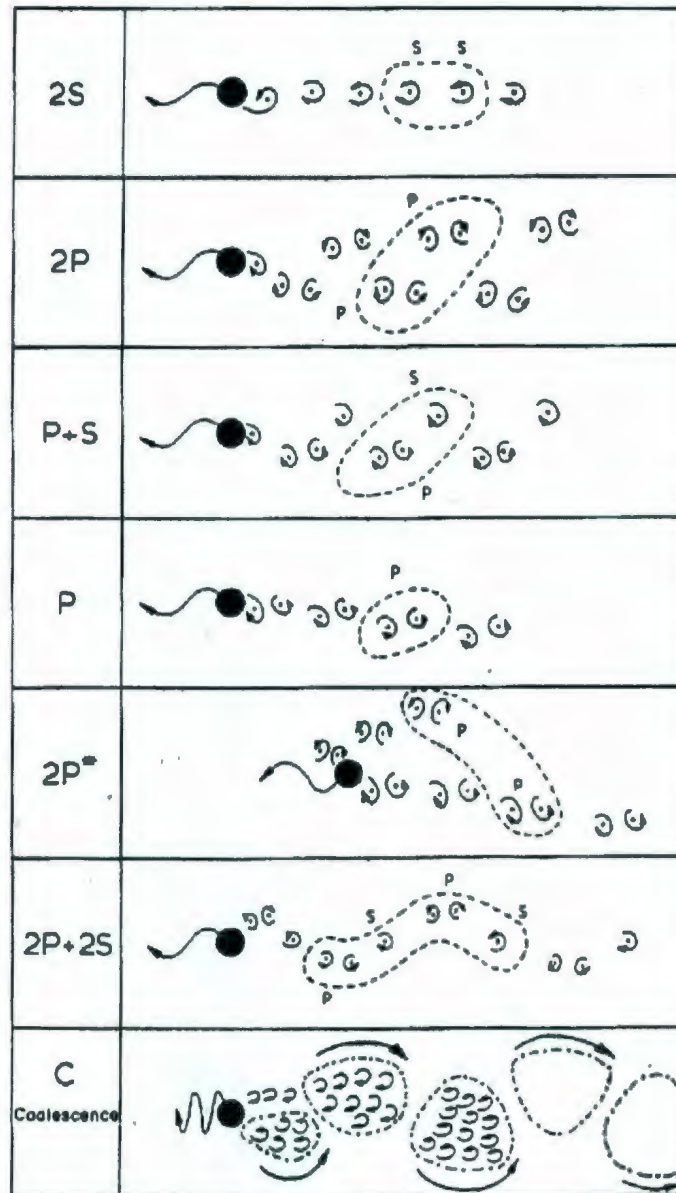


Figure 1.4: Vortex locked-on modes near the fundamental lock-on region as observed by Williamson and Roshko (1988) in the map in Figure 1.3. Each mode is defined by the number of pairs and single vortices formed per  $T_0$ ; - - - encircles the vortices shed in a complete cycle.

**C(2S)** mode, the smaller vortices coalesce either immediately behind the cylinder forming **2S** mode near the cylinder or **2S** mode persists near the cylinder but smaller vortices coalesce in the downstream of the cylinder. Similarly, in **C(P+S)** mode the smaller vortices coalesce either immediately behind the cylinder forming **P+S** mode near cylinder or **P+S** mode persists near the cylinder but smaller vortices coalesce in the downstream of the cylinder. Figure 1.4 shows examples of the vortex coalescence phenomenon.

One of the mechanisms which affects the Kármán instability is the presence of a free surface. When the flow past a cylinder is bounded in part by the free surface, both the structure of the near wake and the hydrodynamic forces on the cylinder can be significantly altered. For this type of flow two important controlling parameters are the dimensionless cylinder submergence depth below a free surface,  $h = h^*/d$ , and the Froude number,  $Fr = U/\sqrt{g^*d}$ , which vary the level of free surface deformation.

### 1.1.1 Fluid boundary tracking/capturing methods

In nature, a fluid boundary represents an interface between two fluids of different physical properties. The special type of the fluid boundary which separates two homogeneous fluids, for example water and the air in the Earth's atmosphere, is known as a *free surface*. A comprehensive introduction to free surface flows can be found, for example, in Floryan and Rasmussen (1989), Rood (1995) and Sarpkaya (1996). The free surface is free to deform during the interaction with vortices and thus, its position in space evolves with time. The deformation of the free surface is characterized by a

surface curvature,  $\kappa = 1/r$  ( $r$  is the radius of curvature). Hence, the free surface can actually be viewed as the fluid boundary which contains the vorticity field; the effect of the dynamic evolution of the fluid on the external side of the surface is negligible. The free surface has a major impact on the fluid interactions since its deformation results in the generation and flux of secondary vorticity and produces gravity and capillary waves. This secondary vorticity interacts with the initial vorticity field to produce complex flows. The generation of the secondary vorticity near the free surface interface is due to two important effects: free surface curvature,  $\kappa$ , and surface tension gradients,  $\nabla\sigma$  ( $\sigma$  is the surface tension coefficient) [see Rood (1995) and Sarpkaya (1996) for details]. The curvature induced secondary vorticity depends on the radius of curvature,  $r$ . In some cases, vortices rising toward the free surface can induce a secondary vorticity which is larger than their own vorticity. Longuet-Higgins (1992) has shown that for a steady viscous flow case in which the tangential stress vanishes (no surface tension gradients) the vorticity at the free surface,  $\zeta_{fs}$ , is given by

$$\zeta_{fs} = -2\kappa q, \quad (1.2)$$

where  $q$  is the tangential velocity of a fluid particle. On the other hand, surface tension gradients drive a flow that tends to diminish concentration gradient. Sarpkaya (1996) has shown that for the free surface of negligible curvature the secondary vorticity induced by the presence of surface tension gradients is given by

$$\zeta_{fs} = \frac{1}{\mu} \frac{\partial \sigma}{\partial x}. \quad (1.3)$$

The free surface can also be deformed (and generate secondary vorticity) by an irrotational (potential) flow. The free surface deforms to satisfy stress balance condition which is usually split into normal stress and tangential stress conditions. In Cartesian

coordinates, the free surface normal and tangential stress conditions are

$$2\mu \left( n_1 n_1 \frac{\partial u^*}{\partial x^*} + n_1 n_2 \left( \frac{\partial u^*}{\partial y^*} + \frac{\partial v^*}{\partial x^*} \right) + n_2 n_2 \frac{\partial v^*}{\partial y^*} \right) = p^* - p_a^* + \sigma \kappa, \quad (1.4)$$

$$2n_1 \tau_1 \frac{\partial u^*}{\partial x^*} + (n_1 \tau_2 + n_2 \tau_1) \left( \frac{\partial u^*}{\partial y^*} + \frac{\partial v^*}{\partial x^*} \right) + 2n_2 \tau_2 \frac{\partial v^*}{\partial y^*} = \frac{\partial \sigma}{\partial x}, \quad (1.5)$$

respectively [see, for example, Griebel *et al.* (1998)]. Here,  $p^*$  is the dimensional fluid pressure;  $p_a^*$  is the constant atmospheric pressure;  $\vec{u}^* = (u^*, v^*, 0)$  is the dimensional fluid velocity;  $\vec{n} = (n_1, n_2, 0)$  and  $\vec{\tau} = (\tau_1, \tau_2, 0)$  are the outward unit normal and tangential vectors, respectively;  $\vec{x}^* = (x^*, y^*, 0)$  is the vector of spatial coordinates. It is noted that the kinematic motion of the fluid interface has to match the fluid velocity field and thus, in addition to the boundary conditions (1.4) and (1.5), the continuity of the velocity needs to be satisfied at the free surface interface. For small deformations of the free surface, the term  $\sigma \kappa$  does not play an important role; however, it becomes critical as wave steepness increases. The free surface is free to move due to its interaction with the initial vorticity field and its position unknown a priori is a function of the fluid itself.

The modeling of the free surface is a challenging task. In the past decades, there has been a growing interest in developing accurate and robust numerical methods for solving the free surface flows. A number of numerical methods have been proposed in an effort to study the dynamics of the fluid interface. Basically, these methods can be classified in three categories: Lagrangian methods, Eulerian methods and arbitrary Lagrangian-Eulerian methods. In the Lagrangian methods (also known as the interface tracking techniques), the grid moves together with the fluid particles and thus conforms to the shape of the free surface interface. The Lagrangian methods

maintain the interface as a discontinuity and explicitly track its evolution. The main advantage of these schemes is that the boundary conditions can be applied at the exact position of the free surface interface. However, these methods are not suitable for the problems where moving boundaries can have large deformations and topological changes as it is dictated by the dynamics of the fluid. This is mainly due to the break down of the structured grid arrangement and the need for redistribution of the grid points and values of the field variables in the neighbourhood of the interface for unstructured grid. Therefore, the Lagrangian methods found their wide application in the problems with non-deforming boundaries. The Eulerian methods (also known as the interface capturing techniques) employ a fixed grid formulation. In these methods, the free surface interface is not explicitly tracked but is reconstructed from the properties of the appropriate field variables. In these schemes, the solution of an advection equation is required to satisfy boundary conditions at the free surface since the position of the free surface interface is not known a priori. The advection equation governs the evolution of an interface function that marks the location of the interface. This leads to smearing of boundary information, and thus the detailed physical features may not be fully captured. On the other hand, the Eulerian methods have an advantage in handling the topological changes of the fluid domain automatically. Recently, the advantages of both the Eulerian and Lagrangian methods have been utilized in so called arbitrary Lagrangian-Eulerian technique, in which computational grid moves independently of the fluid motion. These methods are particularly suitable for solution to free surface problems assuming that free surface does not break up. A number of moving boundary methods under the broad categories of the Lagrangian and Eulerian schemes have been developed by the researches so far. A comprehensive

review of the methods can be found in the book by Shyy *et al.* (1996).

According to their abilities, the Eulerian methods are of more interest in free surface modeling, especially when complex interface topologies such as wave breaking are included. In this thesis, the Eulerian method is used to model the free surface due to the specifications of the physical problem under current consideration. In the context of general free surface flow problems, the popular Eulerian free surface modeling techniques include the level set methods and the volume of fluid (VOF) methods. In the original level set method [Osher and Sethian (1988)], a level set function,  $\phi(\vec{x}^*, t^*)$ , is introduced to define the distance from the point  $\vec{x}^*$  to the initial interface location. Therefore, the interface can be represented by the contour,  $\phi = 0$ , at any time, which is evolved in time by

$$\frac{\partial \phi}{\partial t^*} + \vec{u}_n^* |\nabla \phi| = 0, \quad (1.6)$$

where  $\vec{u}_n^*$  is the dimensional normal velocity to the interface. The level set methods are capable to handle large free surface distortions and topology changes. However, these methods have serious problems with respect to the mass conservation. Recently, the level set method by Osher and Sethian (1988) is combined with the VOF method in order to overcome the problem with the mass conservation [see, for example, Sussman and Puckett (2000)]. Reviews of the level set methods can be found in Sethian and Smereka (2003) and Osher and Fedkiw (2003).

The VOF method is an interface capturing algorithm that has proven to be a robust tool since its development [Hirt and Nichols (1981)]. This method is incorporated in the commercial CFD packages FLOW-3D (Flow Science, Inc.) and Fluent which are applicable to a broad range of industrial problems including the simulation of free

surface flows. The VOF algorithm has been applied to solve the complex interfacial phenomena, including green water loading [Fekken (2004)], tank sloshing [Akyildiz and Ünal (2006)], capillary motion [Taha and Cui (2004)], hydrodynamic stability [Pan *et al.* (2006)] and many others. The VOF method is an example of volume fraction methods. The essential features of this method are as follows. First, a VOF function,  $F_{\Omega_2}$  (with values between zero and one), is computed from the known fluid interface geometry. The VOF function indicates the fractional volume of the computational cell that is filled with the fluid in  $\Omega_2$ . It is noted that the computational cell is defined as a two-dimensional object that represents an element of a computational grid. Second, the fluid interface is subsequently “captured” by evolving  $F_{\Omega_2}$  in time with the solution of the advection equation

$$\frac{\partial F_{\Omega_2}}{\partial t^*} + \vec{u}^* \cdot \nabla F_{\Omega_2} = 0. \quad (1.7)$$

Equation (1.7) states the conservation of the volume fraction in the computational cell. The exact location of the fluid interface is not known and is reconstructed from the local  $F_{\Omega_2}$  data at any time step. The interface location is then used to compute the convective fluxes necessary for the convective term in the advection equation.

Based on the features of the interface reconstruction algorithm and the advection of the interface, the different VOF methods can be distinguished. For the interface reconstruction two main methods are the simple line interface calculation (SLIC) [Noh and Woodward (1976)] and the piecewise linear interface calculation (PLIC) [Youngs (1987)]. In the two-dimensional Cartesian grid geometry, the SLIC approximates the fluid interface in the computational cell by a segment aligned with one of the coordinate axes [see, for example, Hirt and Nichols (1981), Kothe and Mjolsness (1992)].

On the other hand, the PLIC represents the fluid interface in the computational cell by a portion of the straight line defined as

$$\vec{n} \cdot \vec{x} + \bar{d} = 0, \quad (1.8)$$

where  $\bar{d}$  is the line distance from the origin [see, for example, Pilliod and Puckett (2004), Scardovelli and Zaleski (2003)]. The PLIC algorithms are more accurate since they reconstruct interface more exactly and, in particular, do not produce “flotsam” and “jetsam” which appear in the SLIC techniques. The flotsam and the jetsam represent small bits of material (about the size of the grid spacing) separated from the main body of the fluid. The accuracy of the PLIC method depends on a precise choice of the normal vector. The normal vector to the interface,  $\vec{n}$ , can be calculated using  $F_{\Omega_2}$  data in the neighbour computational cells while the line distance,  $\bar{d}$ , is determined, using the calculated normal vector,  $\vec{n}$ , and the  $F_{\Omega_2}$  data in the computational cell under consideration. A number of numerical methods have been developed to compute the normal vector to the interface,  $\vec{n}$ , and the line distance,  $\bar{d}$  [see, for example, Pilliod and Puckett (2004), Gerrits (2001), Sussman and Puckett (2000), Rider and Kothe (1998)].

The advection of the fluid interface requires the calculation of computational cell boundary fluxes necessary for the convective term in (1.7). For the calculation of fluxes, a number of different methods exist. Some methods are Lagrangian in the sense that the fluid interface is advected by means of markers placed on the reconstructed interface [Aulisa *et al.* (2003a), Biausser *et al.* (2004)]. In other methods, the fluid is not advected at all and thus the redistribution algorithms are used to conserve the mass in the computational cell [Rider and Kothe (1998), Harvie and Fletcher (2000)]. The VOF advection methods compute the fluxes geometrically based on the

reconstructed fluid interface. That is, the amount of fluid that should be advected is calculated geometrically by defining a region for each computational cell boundary from which the fluid is fluxed through the boundary. The strength of the geometrical VOF advection methods is that the natural sharpness of the fluid interface is preserved. The VOF advection techniques are mainly divided in two categories: one-dimensional (operator split) and multi-dimensional (unsplit) schemes. In the operator split schemes, the advection is done independently along each coordinate direction [Rider and Kothe (1998), Pilliod and Puckett (2004), Scardovelli and Zaleski (2003)] while the unsplit methods perform the advection in all coordinate directions simultaneously [Harvie and Fletcher (2000), Aulisa *et al.* (2003b)]. The main disadvantage of the VOF advection schemes is that the mass is not always conserved in the computational cell and as a result the volume fractions do not satisfy  $0 \leq F_{\Omega_2} \leq 1$ . This leads to the generation of little holes in the fluid body, so-called “wisp”. The wisp should not be confused with the flotsam or the jetsam, which are bigger in nature and mainly due to low-order reconstruction algorithms. Recently, Aulisa *et al.* (2003b) developed the advection scheme that amounts to piecewise linear, area preserving mappings of tessellations of the plane. Aulisa *et al.*'s work demonstrated that their advection algorithm preserves the mass exactly for two-dimensional incompressible flows on a Cartesian grid.

The strength of the VOF methods is that the large distortions of the free surface can be easily handled. Moreover, comparing to the level set methods, the VOF methods do not have serious problems with respect to the mass conservation. The most striking disadvantage of the VOF method is that it cannot be treated with precision. This is mainly due to considerable logical and algorithmic complexity reconstruction and

advection of the free surface interface. Comprehensive reviews of the modern VOF methods are given in Rider and Kothe (1998) and Rudman (1997). The VOF method forms a basis for the computational method presented in this thesis.

In the numerical modeling of free surface flows, the main computational difficulty arises from the implementation of the boundary conditions at the free surface interface. In general, there are two models which can be used to satisfy boundary conditions at the free surface: the single-phase flow approach and the two-phase flow approach. In the single-phase flow method, the fluid in  $\Omega_1$  is assumed to be much lighter than the fluid in  $\Omega_2$ . Thus, the fluid in  $\Omega_1$  can be neglected, and the governing equations are solved in the region  $\Omega_2$  only. Consequently, the free surface is modeled explicitly as the computational boundary, i.e., the free surface boundary conditions (1.4) and (1.5) are solved. A potential constraint in this case is that the free surface may form a breaking wave at high Froude numbers and the single-phase flow methods may have computational difficulties. Therefore, these methods are very limited to certain types of fluids where the free surface does not break up. A number of numerical schemes have been developed to discretize the boundary conditions at the free surface [see, for example, Gubanov (2006), Kleefsman (2005), Fekken (2004) and Gerrits (2001)].

In the two-phase flow methods, one set of governing equations is solved for the whole domain treating different fluid phases as one fluid with variable material properties such as  $\rho$  and  $\mu$ . Interfacial terms are accounted for by adding the appropriate sources as Delta functions at the phase boundary. Although efforts to compute the motion of two-phase flows are as old as CFD, the difficulty in solving the continuity and

Navier-Stokes equations in the presence of a deforming phase boundary has proven to be considerably more difficult. The main challenge in using these methods is the maintenance of a sharp boundary between the phases and the computation of the terms concentrated at the interface such as surface tension. A number of recent developments are summarized in the books by Prosperetti and Tryggvason (2007) and Levy (1999). The most popular approach for computing two-phase flows is to capture the phase boundary on a Cartesian grid and then identify the different phases by markers or a marker function. The VOF method is the best known example. The VOF method determines the degree of mixing between the phases using the VOF fractions of each of the phases in the computational cell. The other methods include the marker and cell method of Harlow and Welsh (1965), the level set method of Sussman and Puckett (2000), the constrained interpolated propagation method of Takewaki and Yabe (1987) and the phase field method of Jacqmin (1999). The attraction of the two-phase flow methods on a Cartesian grid is due to their simplicity and efficiency. However, in these methods the interface is represented on the grid as a rapid change in the material properties and has a finite width in the order of the grid size. Consequently, the formal accuracy of these methods is generally limited to first-order.

In this thesis, the two-phase flow approach is used. The reason is that the single-phase flow model, although being more computationally appealing, is shown to have numerical difficulties which arise due to complexity of application of boundary conditions at the free surface on the non-boundary-fitted Cartesian grid [Gubanov (2006)]. The two-phase flow model enables implicit application of boundary conditions at the free surface, which makes numerical simulations of free surface flows more accurate

even in the case of large deformations of the free surface [Reichl (2001)].

### **1.1.2 Fluid-body interface methods**

There are two types of interfaces in the present problem: the free surface and the fluid-body interface. The choice of the fluid-body boundary modeling method depends on the choice of the numerical grid. Basically, a computational grid has two characteristics: the grid is either structured or unstructured. In addition, the structured/unstructured grid can be either boundary-fitted or non-boundary-fitted. In the structured grid, grid cells have the same shape and size. The grid is called unstructured, otherwise. In the boundary-fitted grid, the boundary of the flow domain coincides with the cell faces of the grid. The grid is called non-boundary-fitted, otherwise. The structured non-boundary-fitted grid is commonly called a Cartesian grid. There are two important advantages in using the boundary-fitted grids: the ability to generate grids for very complex shaped flow domains and direct application of the boundary conditions at the boundary of the flow domain. However, it is extremely difficult to generate this type of grid for flow domains which undergo topological changes. In the latter case, a constant remeshing is required at every time step to conform the shape of the computational domain, which involves considerable logical and algorithmic complexity and is often more time consuming than the flow simulation itself. In contrast, the use of the non-boundary-fitted grids takes negligible time with respect to the flow simulation time. The non-boundary-fitted grids are easy to generate and there is no need to remesh the grid. In this thesis, the VOF method is chosen to capture the free surface. Since the VOF reconstruction and advection algo-

rithms are based on the geometrical procedures, the Cartesian grid is more practical for this type of simulation.

The popular fluid-body interface modeling techniques which allow modeling interface on Cartesian grids include the immersed boundary method, the fictitious domain method, the cut cell method and the fractional area/volume representation (FAVOR) method. In the original immersed boundary method [Peskin (2002)], the fluid-body interface is represented by a set of markers. The interface force which acts on the markers is incorporated in the Navier-Stokes equations by means of an integral source term. The Heaviside step function and the Dirac delta function which will be introduced in Chapter 2 are used to smooth the distribution of the fluid properties over the fluid-body interface and to spread the interface force to the nearby grid points, respectively. As a result, the fluid-body interface has a finite thickness which is usually of the same order as the local grid spacing. The advection of the fluid-body interface is performed by displacing the markers following

$$(\vec{x}^*)^{n+1} = (\vec{x}^*)^n + \Delta t^* (\vec{u}^*)^n, \quad (1.9)$$

where  $\Delta t^*$  is the dimensional time step. The improved immersed boundary methods are given, for example, in Tseng and Ferziger (2003) and Kim *et al.* (2001). Glowinski *et al.* (1997) developed the fictitious domain method also known as the domain embedding method. The idea behind the fictitious domain method is to extend the solution inside the solid body, i.e., the complete computational domain is assumed to be filled with the fluid and the influence of the fluid-body interface is acquired by the body forces. The fictitious domain method utilizes the boundary or distributed Lagrange multipliers to force the solid body motion. The many modifications of this

method have been also developed [see, for example, Glowinski and Kuznetsov (2007), Ramière *et al.* (2007), Veeramani *et al.* (2007) and Wan and Turek (2007)].

The above mentioned type of immersed boundary methods as well as fictitious domain methods represent the diffuse interface techniques. In the diffuse interface methods, the interface is treated as a special region in one fluid, which occupies the entire computational domain, and the discontinuities across the interface are somewhat smoothed. The influence of the boundary in these methods is transmitted to the fluid through source terms in the Navier-Stokes equations. The main problem with the diffusive interface techniques is that the fluid-body boundary is represented as the diffuse interface of a finite thickness. In the convection dominated flow, like the one considered in this thesis, the interface between the solid body and the fluid should be treated as a sharp interface without smearing the information in the neighbourhood of the interface. The popular sharp interface methods are the cut cell method by Udaykumar *et al.* (1997) and the FAVOR method by Hirt and Sicilian (1985). In these methods, the fluid-body boundary is represented either explicitly as curves or as level sets and remains sharp irrespective of the grid resolution. As a result, the interface clearly divides two regions in the computational domain and retains the jumps in fluid properties as sharp discontinuities.

In the cut cell method [Udaykumar *et al.* (1997)], the solid boundary is represented by marker particles. The geometry of the solid body cuts through the Cartesian grid cells and the intersections with the grid are determined. Rectangular cells that are cut by the fluid-body interface are reshaped by discarding the part occupied by the solid body. The fluid-body interface is assumed to be built of piecewise linear

segments. Cut cells for which centers are located in the solid body are merged with neighbouring cells to form trapezoidal shaped control volumes. This way, small cut cells are avoided and the global second-order accuracy of the flow solver is preserved when evaluating mass, convective and diffusive fluxes, and the pressure on the edges of the trapezoidal cells with the sufficient accuracy [see Udaykumar *et al.* (1997) and Udaykumar *et al.* (2001), for details]. The modifications of cut cell method can be found, for example, in Lin (2007), Hu *et al.* (2006), Fekken (2004), Kirkpatrick *et al.* (2003) and Udaykumar *et al.* (2001).

The FAVOR method is used in the commercial CFD package FLOW-3D developed by Flow Science, Inc. The FAVOR method is an another example of volume fraction methods. In this method, solid boundaries are accounted for by a porosity function (Heaviside function) which changes abruptly from unity to zero across the solid boundary. The numerical representation of the variable porosity function is defined in terms of fractional areas and volumes open to flow in the computational cells. These numerical values represent volumetric averages of the quantities in cells that are partially occupied by the solid body, and are retained for each flow variable such as pressure and velocity in these cells. The same technique used in the VOF method can be used to define solid boundaries that cut the computational grid. This is the fraction of the body,  $F_b$ , (with values between zero and one) which indicates the volume of the cell that is occupied by the body. For cells with  $0 < F_b < 1$ , areas and volumes open to flow are computed and the fluid-body interface is reconstructed as a piecewise linear segment.

In this thesis, the FAVOR method has been initially chosen due to its simplicity

as well as the easy programming features. It is noted that the formulation of the FAVOR method assumes that there are no special considerations that are needed at the solid boundary. However, the preliminary experiments have shown that when a finite volume discretization is used, the method results in low accuracy. In the present computational model, it is found effective to combine the FAVOR method and the cut cell method. It is shown that the resulting method is of second-order accuracy.

### 1.1.3 Review of previous studies on free surface flows with a circular cylinder

The circular cylinder and other similar geometries are common both in nature and in engineering structures and the study of flow past a circular cylinder is of obvious practical significance. The large body of literature is attributed to the features of uniform flow past the cylinder placed in a fluid flow of an infinite extent. The practical significance of this problem has led to a large number of fundamental studies, many of which are discussed in the comprehensive reviews of King (1977), Bearman (1984), Griffin and Hall (1991), Williamson (1996), Rockwell (1998), Williamson and Govardhan (2004), Sarpkaya (2004) and in book chapters by Naudascher and Rockwell (1993), Sumer and Fredsøe (1997), Zdravkovich (1997), Anagnostopoulos (2002). To the author's knowledge, little research has been undertaken to determine effects of the presence of a free surface on the development of vortex shedding modes. This problem has been principally investigated in the experimental studies by Carberry *et al.* (2004), Carberry (2002), Carberry *et al.* (2001), Cetiner and Rockwell (2001), Zhu *et al.* (2000) and Sheridan *et al.* (1997).

The case of steady viscous flow past a stationary cylinder beneath the free surface is addressed in the experimental studies by Carberry *et al.* (2004), Carberry (2002), Carberry *et al.* (2001) and Sheridan *et al.* (1997). Quantitative particle image velocimetry measurements by Carberry *et al.* (2004), Carberry (2002) and Carberry *et al.* (2001) identified three possible wake states in the range of cylinder submergence depths  $0.079 < h < 3.0$ . These studies reported (i) the suppression of vortex shedding at  $h < 0.125$ ; (ii) the formation of a jet flow at  $0.125 \leq h \leq 0.5$  and (iii) the modified von Kármán vortex street at  $0.5 < h \leq 3.0$  when the Reynolds and Froude numbers are fixed at  $R = 2100$  and  $Fr = 0.166$ , respectively.

Sheridan *et al.* (1997) studied the possible states of the near wake and corresponding distortions of the free surface for  $0 < h \leq 0.75$ ,  $5990 \leq R \leq 9120$  and  $0.47 \leq Fr \leq 0.72$ . The particle image velocimetry measurements by Sheridan *et al.* (1997) identified two distinctly different wake states which occur when the cylinder is close to the free surface: (i) a jet-like flow at  $h \leq 0.16$  and (ii) a jet flow at  $0.16 < h \leq 0.75$  for the considered ranges of the Reynolds and Froude numbers. Such possibilities are foreshadowed by the observation of Sheridan *et al.* (1995), who characterized a structure of the near wake for a single set of parameters. Sheridan *et al.* (1997) describe the jet-like flow as the flow formed by a vorticity layer from the free surface which is adjacent to a layer from the surface of the cylinder. The vorticity layer from the free surface is generated due to the localized separation (in the form of small scale breaking of a free surface wave) or complete separation from the free surface. On the other hand, in the jet flow the well defined layers of positive and negative vorticity from the free surface and top surface of the cylinder merge with the positive layer from the lower surface of the cylinder. In the work by Sheridan

*et al.* (1997), the significant surface deformations are reported at Froude numbers  $0.47 \leq Fr \leq 0.72$ .

The vortex shedding modes near the fundamental lock-on region and the resulting fluid forces for the case of an oscillating circular cylinder beneath the free surface have been addressed in the experimental works by Carberry *et al.* (2004), Carberry *et al.* (2001), Cetiner and Rockwell (2001) and Zhu *et al.* (2000). Carberry *et al.* (2004) and Carberry *et al.* (2001) considered transverse oscillations of the cylinder in a steady flow at  $R = 2100$ ,  $Fr = 0.166$ ,  $A = 0.5$ ,  $0.76 \leq f/f_0 \leq 1.05$  and  $h = 3/16$ ,  $3/8$ . It is shown that the presence of a free surface appears to inhibit, but not eliminate, periodic vortex shedding from the oscillating cylinder. For both  $h = 3/16$  and  $h = 3/8$  the near wake structure is reported as **2S**. However, the vortices shed into the wake appear to be less well defined and the vorticity is more widely distributed throughout the wake when compared to the corresponding case of a transversely oscillating cylinder in the absence of a free surface.

In the work by Cetiner and Rockwell (2001), the uniform flow past the cylinder subject to in-line oscillations is considered at  $R = 917, 2075$ ,  $Fr = 0.07, 0.158$ ,  $A = 0.96$ ,  $f/f_0 = 0.44, 1.0$  and  $h = 0.06, 0.19, 11.23$ . It is shown that the effect of the free surface is to generate distinctly different patterns of vorticity in the near wake from those corresponding to the classical case of the Kármán vortex formation from a transversely oscillating cylinder. Moreover, the observed patterns are shown to be different from the ordered patterns of vortex formation from a cylinder undergoing in-line oscillations in the absence of a free surface. Cetiner and Rockwell (2001) showed that the presence of an adjacent free surface provides the possibility for locked-on

vortex formation not only from the cylinder, but also from the free surface at locations both upstream and downstream of the cylinder. It was shown that in the case when a finite gap exists between the cylinder and the free surface ( $h = 0.19$ ), jet-like flow through the gap acts to destabilize such locked-on states by inducing a negative vortex from the cylinder surface. In the work by Cetiner and Rockwell (2001), the experiments have been conducted over more than a hundred cylinder oscillation cycles and it was observed that for certain cases the flow is locked-on over several cycles of cylinder oscillation and then the transition to the non-locked state occurs. It was also shown that localized distortions of the free surface appear due to vortical structures shed from both the cylinder and the free surface.

Zhu *et al.* (2000) investigated the effect of cylinder submergence depth on the vortex shedding modes and streamline topology for a cylinder undergoing combined translatory and vertically-accelerating motion at  $R = 1041$ , where the Reynolds number is based on the maximum velocity of the cylinder,  $A = 0.4$  and  $h = 0.76, 4.23$ . Zhu *et al.* (2000) have shown that the proximity of the free surface speeds up the process of vortex shedding from the upper surface of the cylinder. As a consequence, the shed vorticity exhibits a remarkable distribution of the vorticity in the near wake. The end consequence of this is substantially larger magnitudes of the negative lift force and the drag force relative to the case when the free surface is absent.

There are only a few numerical studies which consider the viscous free surface flows with a circular cylinder. To the author's knowledge, only four numerical studies [Reichl *et al.* (2005), Reichl *et al.* (2003), Reichl (2001) and Warburton and Karniadakis (1997)] and two numerical studies [Gubanov (2006) and Yan (2000)] discuss stationary

and oscillating circular cylinders, respectively. Reichl *et al.* (2005) and Reichl (2001) numerically investigated the level of free surface deformations, the structure of the near wake and the variation of the Strouhal number for the stationary cylinder case at  $R = 180$ ,  $0 \leq Fr \leq 0.7$  and  $0.1 \leq h \leq 0.5$ . The two-dimensional flow is calculated using the computational fluid dynamics commercial software package FLUENT 5. The method of solution is based on a finite volume discretization of the continuity and Navier-Stokes equations which are solved on an unstructured boundary-fitted grid. The two-phase flow model is chosen to capture the free surface using the modified VOF method as incorporated within FLUENT 5. The spatial discretization is performed by a quadratic upstream interpolation for convective kinematics method of Leonard (1979). The discretization scheme used produces results which are second-order accurate in space and first-order accurate in time. The system setup simply involves the two fluid phases (the fluids in the regions  $\Omega_1$  and  $\Omega_2$ ) entering into the domain with a uniform velocity at the inlet and leaving through the outlet boundary where the pressure gradient is prescribed. The properties of the two phases are set as follows: density ratio  $\rho_2/\rho_1 = 100$  and viscosity ratio  $\mu_2/\mu_1 = 100$  ( $\nu_2/\nu_1 = 1$ ). Here,  $\rho_1$  is the density of the fluid in  $\Omega_1$ ;  $\rho_2$  is the density of the fluid in  $\Omega_2$ ;  $\mu_1$  is the dynamic viscosity of the fluid in  $\Omega_1$ ;  $\mu_2$  is the dynamic viscosity of the fluid in  $\Omega_2$ ;  $\nu_1$  is the kinematic viscosity of the fluid in  $\Omega_1$ ;  $\nu_2$  is the kinematic viscosity of the fluid in  $\Omega_2$ . It is shown that at low values of the Froude number ( $Fr < 0.3$ ), the free surface shares many features with the case of flow past cylinder close to the non-deformable surface. However, for moderate values of the Froude numbers ( $0.3 \leq Fr \leq 0.4$ ), the free surface deformation becomes substantial which leads to localized free surface sharpening and wave breaking. The free surface vorticity diffuses and then convects

to the main flow, altering the development of Strouhal vortices from the top shear layer, affecting wake skewness and suppressing the absolute instability. At larger Froude numbers ( $Fr > 0.4$ ), there is a suppression of the absolute instability in the wake. At very small cylinder submergence depths ( $0.1 \leq h \leq 0.2$ ), shedding ceases and the flow becomes more two-dimensional. The results for the case of flow past a stationary cylinder submerged under the free surface at  $R = 180$ ,  $Fr = 0.0, 0.2$ ,  $0.1 \leq h \leq 0.5$  and  $Fr = 0.55$ ,  $h = 0.4$  are addressed in the numerical study by Reichl *et al.* (2003). Reichl *et al.*'s work demonstrated that for  $Fr = 0.0, 0.2$  a weak form of shedding is still observed down to  $h = 0.16$  (no shedding observed at smaller depths of submergence) while a jet flow is observed for  $Fr = 0.55$ ,  $h = 0.4$ .

Warburton and Karniadakis (1997) studied the vorticity generation mechanisms for the case of flow past a circular cylinder close to the free surface at  $R = 100$ ,  $Fr = 0.3$  and  $h = 0.3, 1$ . The flow is sustained by moving the bottom boundary of the computational domain with a constant velocity  $\bar{U}$ . The motion starts impulsively and the Reynolds number is defined by  $R = \rho \bar{U} d / \mu$ . The full incompressible continuity and Navier-Stokes equations in primitive variables are formulated in their variational form. This is done following the work by Ho (1989). To this end, the test functions,  $\hat{\phi}_i$ , are defined in the space where all functions and their derivatives are square-integrable, i.e.,  $\hat{\phi}_i \in H^1[\Omega(t^*)]$ . Here,  $\Omega(t^*)$  is a time-dependent domain, where the governing equations are stated. Next, the Navier-Stokes equations are multiplied by the test functions and then integration by parts is performed. The reference system on which time differentiation takes place is defined by use of the Reynolds transport theorem and using the fact that the test function  $\hat{\phi}_i$  follows the material points and its time

derivative is zero in the same reference frame, i.e.,

$$\frac{d\hat{\phi}_i}{dt^*} = \hat{\phi}_{i,t^*} + v_j^* \hat{\phi}_{i,j} = 0, \quad (1.10)$$

where  $v_j^*$  is the dimensional velocity of the time-dependent domain  $\Omega(t^*)$ . The governing equations are solved in space using the spectral discretization which is based on the arbitrary triangulizations and a hybrid Lagrangian-Eulerian scheme. Following the work by Karniadakis *et al.* (1991), the governing equations are discretized in time using a splitting scheme and stiffly stable integration of third-order. The free surface is modeled explicitly by solving the stress balance conditions (1.4) and (1.5). These equations are discretized using an arbitrary Lagrangian-Eulerian scheme. The periodic conditions are assumed at the inflow and outflow boundaries while sliding plate conditions are applied to the bottom boundary of the computational domain. The no-slip conditions are imposed on the surface of a cylinder. Warburton and Karniadakis's work demonstrated that at  $h = 0.3$  the free surface is strongly influenced by the vorticity generated at the cylinder even at the start up. At a later time, a steep cusp is generated on the free surface with large concentrations of opposite vorticity around the cusp. The magnitude of the vorticity around the cusp is as large as the maximum positive vorticity shed off the lower side of the cylinder. This study also showed that when  $h = 1.0$  the mean drag has increased somewhat compared to the case when the free surface is absent. Moreover, the mean lift becomes non-zero with its direction towards the bottom wall.

Yan (2000) investigated the influence of imposed steady current on the resulting steady streaming due to either recti-linear oscillations or purely orbital motion of a circular cylinder. In Yan's work, the vorticity/stream function formulation of the

continuity and the Navier-Stokes equations is employed. These equations are solved in a frame of reference fixed to the moving cylinder, with the polar coordinate system. The computational grid of a hybrid type is used. In the neighbourhood of the cylinder, the grid is based on polar coordinates, elsewhere the grid is based on Cartesian coordinates. The numerical scheme employs a fully implicit Crank-Nicholson scheme of second-order and, in the overlap domain, flow variables are interpolated between the grids using techniques that maintain second-order accuracy. The method of solution is based on a perturbation scheme in which the magnitude of the steady current is chosen as  $O(\epsilon)$ , where  $\epsilon = A^*/a \ll 1$  and the Reynolds number,  $R_b = a^2\omega^*/\nu$ , is 50. Here,  $a$  is the cylinder radius and  $\omega^*(= 2\pi f)$  is the dimensional cylinder oscillation frequency. The inviscid flow solutions are used to provide boundary conditions at the free surface, and the inlet and outlet boundaries, for the viscous flow calculations. The inviscid flow solutions are obtained by expanding the velocity potential in powers of  $\epsilon$ . Each term of the velocity expansion satisfies Laplace's equation, with the appropriate free surface boundary conditions derived from equations (1.4) and (1.5). The boundary element method is then used to calculate the unknown velocity potentials by following the works of Yan (1998) and Yan and Riley (1996). It is demonstrated that when the magnitude of the steady current is relatively large, the induced steady streaming for recti-linear oscillations is largely independent of the type of oscillations. On the other hand, for small magnitudes of steady current, the Reynolds stresses, produced by the oscillation become significant in the neighbourhood of the cylinder and hence the induced steady streaming has a classic four-cell structure. It is interesting to note that when the cylinder performs uniform orbital motion, the circulation around the cylinder is almost independent of the magnitude of the steady current.

The work of Gubanov (2006) is the first comprehensive numerical study conducted on the uniform two-dimensional flow past a transversely oscillating circular cylinder in the presence of a free surface. The numerical simulations are conducted at the lock-on conditions for the circular cylinder placed in unbounded fluid at  $R = 200$ ,  $A = 0.25$ ,  $0.5$  and  $f/f_0 = 0.95, 1.0, 2.0, 3.0, 4.0$ . The depth of cylinder submergence is fixed at  $h = 1.25$  and the Froude number is fixed at  $0.3$ . In Gubanov's work, the integral form of the governing equations is used to solve the incompressible viscous free surface flow problems using the pressure-velocity form of the unsteady incompressible continuity and the Navier-Stokes equations on a fixed Cartesian grid. In his work, the motion of the fluid in  $\Omega_1$  is neglected and the effect of the ambient pressure exerted on the fluid in  $\Omega_1$  by the fluid in  $\Omega_2$  is taken into consideration. At the free surface, the boundary conditions (1.4) and (1.5) are solved after making use of the fact that in gravity dominated flows viscous and surface tension effects play a minor role and thus the terms  $2\mu \frac{\partial \bar{u}_n^*}{\partial \bar{n}}$ ,  $\sigma \kappa$  and  $\partial \sigma / \partial x$  in (1.4) and (1.5) can be ignored. This is done following the works of Gerrits (2001) and Fekken (2004). The free surface is captured by use of the VOF method. The PLIC algorithm of Gerrits (2001) is utilized at each time step for determining the position of both the free surface and fluid-body interfaces. The reconstructed free surface is then advected using computed local velocity field based on the geometrical area preserving VOF advection algorithm of Aulisa *et al.* (2003b). Well-posed boundary conditions due to Gresho and Sani (1998) are used at the inflow and outflow boundaries. The no-slip boundary conditions are prescribed at the surface of the cylinder. For the treatment of the no-slip boundary, the cut cell method of Gerrits (2001) and Fekken (2004) is used. Gubanov's work demonstrated that for small amplitude oscillation,  $A = 0.25$ , the presence of a free surface has a slight

effect on the dynamics of vortex shedding process. However, at  $A = 0.5$  the effect of transverse oscillation becomes significant which leads to pronounced disturbance of the free surface and a change over from one mode of vortex formation to another is observed as  $f/f_0$  increases from 0.95 to 4.0. The observed vortex shedding modes are **2S** per  $T$ , **C(4S)** per  $5T$ , **C(2S)** per  $3T$  and **C(4S)** per  $4T$  when  $h = 1.25$ . In the vortex shedding mode **C(2S)**, per  $3T$ , the cylinder alternately sheds a single vortex from each side over  $3T$ , in which the development of each vortex is a result of coalescence of two weak vortices in the shear layer. Similarly, in the vortex shedding modes **C(4S)**, per  $4T$ , and **C(4S)**, per  $5T$ , the cylinder alternately sheds a single vortex from each side over  $4T$  and  $5T$ , respectively, in which the development of each vortex is a result of coalescence of two weak vortices in the shear layer. It is also shown that the presence of a free surface has a great influence on the unsteady and mean fluid forces acting on the cylinder as well as the mechanical energy transfer.

## 1.2 Scope of the thesis

In this thesis, an accurate computational method is presented for the solution of the problem of uniform flow of a viscous incompressible fluid past an oscillating horizontal rigid circular cylinder of infinite length located beneath the free surface. The method of solution is based on a finite volume discretization of the special integral form of the two-dimensional unsteady continuity and Navier-Stokes equations in their pressure-velocity formulation on a fixed Cartesian grid. The two-phase fluid model based VOF method is used to discretize the free surface interface. The combined FAVOR

and cut cell method is used to approximate the fluid-body interface on the Cartesian grid. The computational model is implemented into computer program written in C++ programming language. The method is applied to study the problem of unsteady, laminar, two-dimensional flow of a viscous incompressible fluid past a cylinder subject to recti-linear oscillations in the in-line direction to that of uniform flow in the presence of a free surface.

The content of the remainder of this thesis is organized as follows. In Chapter 2, the detailed derivation of governing equations for the numerical simulation of the present viscous flow with a moving solid body is given. A special integral form of the governing equations is derived by extending the Reynolds transport theorem and then applying it to control volumes containing a fluid-body interface. This is done by utilizing, mainly, generalized differentiation. In this derivation, the Heaviside unit step function (defined as zero within the solid body and one within the fluid) is used to represent the fluid property over entire control volume (computational cell). The integration of the Heaviside unit step function over the computational cell occupied by the solid body geometry results in the introduction of the areas and volume open to flow in this cell. This allows one to represent the fluid-body interface within the grid by computing the areas and volume open to flow for each computational cell occupied by the static or moving solid body.

In Chapter 3, the computational model and method are presented. The governing equations derived in Chapter 2 are discretized using a finite volume approximation on a staggered grid. The no-slip conditions are implemented on the surface of the cylinder. Well-posed boundary conditions are enforced at the inflow and outflow

boundaries since they ensure correct physical development of the flow near the computational domain boundaries. The free slip boundaries are assumed at the top and the bottom of the computational domain. The free surface boundary conditions are applied implicitly using the two-phase flow technique which treats the fluids in regions  $\Omega_1$  and  $\Omega_2$  as one fluid with variable material properties. The free surface is discretized with the VOF method in which the volume fraction is used to distinguish between two different phases, the fluid in  $\Omega_1$  and the fluid in  $\Omega_2$ , in the computational domain. The positions of both the free surface and fluid-body interfaces are determined at each time step using the PLIC algorithm. The advection of the reconstructed free surface with local velocity field is performed by the geometrical area preserving VOF advection algorithm. The combination of the FAVOR and cut cell methods is used to model the motion of the fluid-body interface.

In Chapter 4, the ability of the present numerical model to approximate free surface flows with moving bluff bodies and other relevant viscous flows is discussed. Specifically, the test problems are restricted to the two-dimensional, unsteady, laminar flow of a viscous incompressible fluid around circular cylinders. The validation of numerical algorithm is presented for uniform flow past (i) a stationary cylinder; (ii) a cylinder undergoing forced recti-linear oscillations (oscillations at an angle  $\eta = 60^\circ$  with respect to the free stream, transverse, in-line oscillations); (iii) a cylinder undergoing forced combined transverse and rotational, and combined in-line and rotational oscillations; (iv) a steadily rotating cylinder in the absence of a free surface. The validation of the present numerical model is also presented for uniform flow past (i) a stationary cylinder and (ii) a cylinder undergoing forced translational oscillations in the in-line direction in the presence of a free surface.

In Chapter 5, the present computational method is applied to study the problem of unsteady, laminar, two-dimensional flow of a viscous incompressible fluid past a cylinder subject to recti-linear oscillations in the in-line direction to that of uniform flow in the presence of a free surface. The fluid flow is calculated at the Reynolds number of  $R = 200$  and the forcing amplitude  $A = 0.13$  for the range of frequency ratios  $1.0 \leq f/f_0 \leq 4.0$ . The flow characteristics for the Froude numbers  $Fr = 0.0, 0.2, 0.4$  and for the depths of cylinder submergence  $h = 0.25, 0.5, 0.75$  are examined. The results are analyzed by means of equivorticity patterns, streamlines and pressure contours in the near wake region as well as the fluid forces. The PSD analysis of the lift coefficient, the near wake vorticity contours and the Lissajous patterns of the lift coefficient are used to define the lock-on modes. The Lissajous representations of the lift and drag coefficients are also used to demonstrate the mechanism of mechanical energy transfer between the fluid and the cylinder, degree of phase-locking or a loss of lock-on and associated phase shift. The effect of the free surface on the mechanical energy transfer is also explained using the energy transfer equation. For selected cases, POD analysis of the vorticity field is used to interpret unsteady near wake structures in terms of POD eigen-modes.

Summary and conclusions, and recommendations for future work can be found in Chapter 6.

## 2. Viscous incompressible free surface flow model with a moving solid body

In this chapter, the detailed derivation of governing equations for the numerical simulation of viscous free surface flow with a moving solid body and appropriate boundary conditions are presented. A special integral form of the governing equations is derived by extending the Reynolds transport theorem and then applying it to control volumes containing a fluid-body interface. This is done following the works by Hirt and Sicilian (1985) and Farassat (1996) and by utilizing, mainly, generalized differentiation. The resulting governing equations are the integral form of the well-known FAVOR equations. The FAVOR equations were originally introduced in the works of Hirt (1992) and Hirt (1993). Their derivation is based on the FAVOR technique of Hirt and Sicilian (1985). In the work by Hirt and Sicilian (1985), a grid porosity technique for computing flows bounded by complicated geometric shapes is described. Solid bodies are defined within a grid composed of rectangular control volumes (computational cells) with a porosity value between zero and one as the solid body fills in the control volumes. The grid porosity value is zero within solid bodies and one for cells without the solid body. Cells only partially filled with a solid body have a value between zero and one, based on the percent volume that is solid. Therefore, the solid body interface is defined by cells within the grid that have a porosity between zero and one. The location of the solid body interface in each cell is defined as a straight line in two dimensions and a plane in three dimensions and is determined by the points where the solid body intersects the cell faces. The slicing plane not

only defines the volume fraction that can contain fluid but also determines the area fraction on each cell surface through which flux (fluid flow) can occur. Geometries are embedded in the mesh by setting the area fractions on the control volume faces along with the volume fraction open to flow. This makes the geometry and the grid completely independent of each other, and, as a result, complex solid body can be generated. Geometry of the solid body is defined within the fluid grid by computing the fractional areas and volumes of each element that is blocked by static or moving solid body. Thus, this technique is known as the FAVOR method (also known as fluid flow aperture technique). The differential form of the FAVOR equations for treating two-dimensional incompressible Newtonian viscous fluid flows with solid bodies of arbitrary configuration can be written in a Cartesian coordinate system as follows.

The two-dimensional porosity equations,

$$\frac{\partial H}{\partial t^*} + \nabla \cdot (H\vec{u}^*) = 0, \quad (2.1)$$

$$\frac{\partial(H\vec{u}^*)}{\partial t^*} + \nabla \cdot (H\vec{u}^*\vec{u}^*) = -\frac{1}{\rho}H\nabla p^* + \nu\nabla \cdot H\nabla\vec{u}^* + H\vec{F}^*, \quad (2.2)$$

can be reformulated using fractional area and volume porosity functions based on the FAVOR method as

$$\frac{\partial\hat{V}^*}{\partial t^*} + \frac{\partial(u^*\hat{A}_x^*)}{\partial x^*} + \frac{\partial(v^*\hat{A}_y^*)}{\partial y^*} = 0, \quad (2.3)$$

$$\frac{\partial u^*}{\partial t^*} + \frac{1}{\hat{V}^*} \left( u^*\hat{A}_x^* \frac{\partial u^*}{\partial x^*} + v^*\hat{A}_y^* \frac{\partial u^*}{\partial y^*} \right) = F_1^* - \frac{1}{\rho} \frac{\partial p^*}{\partial x^*} + \nu \nabla^2 u^*, \quad (2.4)$$

$$\frac{\partial v^*}{\partial t^*} + \frac{1}{\hat{V}^*} \left( u^*\hat{A}_x^* \frac{\partial v^*}{\partial x^*} + v^*\hat{A}_y^* \frac{\partial v^*}{\partial y^*} \right) = F_2^* - \frac{1}{\rho} \frac{\partial p^*}{\partial y^*} + \nu \nabla^2 v^* \quad (2.5)$$

[see, for example, Hirt (1992), Hirt (1993), Tsukiyama *et al.* (1993) and Zhu and Wu (2004), Hirt and Sicilian (1985), Troch *et al.* (2002)]. In equations (2.1)-(2.5),

$H(\vec{x}^*)$  is the porosity (Heaviside) function that is equal to unity if  $\vec{x}^*$  is in the fluid region and zero if  $\vec{x}^*$  is in the solid body;  $\nabla = \left( \frac{\partial}{\partial x}, \frac{\partial}{\partial y}, 0 \right)$ ;  $\vec{F}^* = (F_1^*, F_2^*, 0)$  is the dimensional external force;  $\widehat{V}^*$  is the fractional volume (fractional volume porosity function) open to flow within the computational cell,  $V^*$ ;  $\widehat{A}_x^*$  and  $\widehat{A}_y^*$  are the fractional areas (fractional area porosity functions) open to flow within the computational cell,  $V^*$ , in  $x^*$ - and  $y^*$ -directions, respectively. It is noted that  $\widehat{V}^*$  and  $\widehat{A}_x^*$ ,  $\widehat{A}_y^*$  are located in the centre and in face centers of the boundaries of each computational cell, respectively, as shown in Figure 2.1(c). They are defined as the limit of the average of the porosity function over the computational cell itself,  $V^*$ , and the computational cell boundary,  $S^*$ ,

$$\widehat{V}^* = \lim_{V^* \rightarrow 0} \bar{V}^*, \quad \widehat{A}_x^* = \lim_{S_x^* \rightarrow 0} \bar{A}_x^*, \quad \widehat{A}_y^* = \lim_{S_y^* \rightarrow 0} \bar{A}_y^*$$

where

$$\bar{V}^* = \frac{1}{V^*} \int_{V^*} H dV^*, \quad \bar{A}_x^* = \frac{1}{S_x^*} \int_{S_x^*} H dS^*, \quad \bar{A}_y^* = \frac{1}{S_y^*} \int_{S_y^*} H dS^*.$$

Here,  $\bar{V}^*$  and  $\bar{A}_x^*$ ,  $\bar{A}_y^*$  are the fractional volume and areas, respectively, open to flow within the computational cell,  $V^*$  [see Hirt and Sicilian (1985) for details]. Equations (2.3)-(2.5) are known as the differential form of the FAVOR equations. These equations are identical to the special differential form of the continuity and Navier-Stokes equations (when a solid body is present). Figure 2.2 summarizes the derivation of the differential and integral forms of the FAVOR equations. In Appendix A, their derivation is presented.

In what follows, the special integral form of governing equations for two-dimensional flow of an incompressible Newtonian fluid with moving solid bodies of arbitrary config-

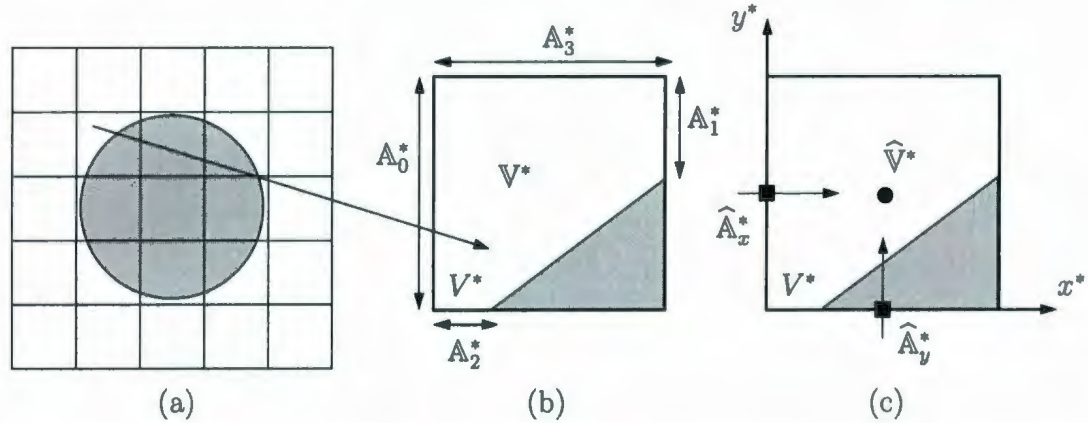


Figure 2.1: (a) Typical solid body surface within a Cartesian grid, (b) typical computational cell,  $V^*$ , which includes areas,  $A_i^*$  ( $i = 0, 1, 2, 3$ ) and volume,  $V^*$ , open to flow within  $V^*$ , (c) location of  $\hat{A}_x^*$ ,  $\hat{A}_y^*$  and  $\hat{V}^*$  within the computational cell,  $V^*$ . The solid body is shown in gray.

uration is presented. The governing equations are derived by extending the Reynolds transport theorem and then applying it to control volumes containing a fluid-body interface. In the process, a new model for a class of flows including free surface flows with moving bodies is constructed based on the FAVOR technique and the generalized functions theory. The properties of the generalized functions used in deriving these equations are given in Appendix B.

## 2.1 Governing equations of viscous fluid dynamics

Many numerical models developed for the study of viscous fluid flow dynamics are based on the differential form of the continuity and Navier-Stokes equations. The general differential form of governing equations can be stated as

$$\frac{\partial \rho}{\partial t^*} + \nabla \cdot \rho \vec{u}^* = 0, \quad (2.6)$$

$$\frac{\partial \rho \bar{u}^*}{\partial t^*} + (\rho \bar{u}^* \cdot \nabla) \bar{u}^* = -\nabla p^* + \nabla \cdot (\mu \nabla \bar{u}^*) + \rho \bar{F}^*, \quad (2.7)$$

where equations (2.6) and (2.7) represent the conservation of mass and momentum, respectively;  $\rho = \rho(p, t, T^\circ)$ , where  $T^\circ$  is the absolute temperature of the fluid. It is noted that for incompressible Newtonian fluid ( $\rho$  is constant), equations (2.6) and (2.7) coincide with the porosity equations (2.1) and (2.2) when no solid body is present. In a finite volume discretization, the conservation laws are transformed into discrete conservation laws. Therefore, the integral form of the governing equations of viscous fluid flow dynamics yields advantages with respect to conservation of the analytical properties and forms a basis for the discretization used in the present thesis. The conservation of mass (also known as the continuity equation), considering an arbitrary *control volume*,  $V^*$ , with boundary  $S^*$ , can be written in the integral form as

$$\int_{V^*} \frac{\partial \rho}{\partial t^*} dV^* + \int_{S^*} (\rho \bar{u}^* \cdot \bar{n}) dS^* = 0. \quad (2.8)$$

The conservation of momentum (also known as the Navier-Stokes equations), with respect to control volume,  $V^*$ , takes the form

$$\int_{V^*} \frac{\partial \rho \bar{u}^*}{\partial t^*} dV^* + \int_{S^*} \rho \bar{u}^* (\bar{u}^* \cdot \bar{n}) dS^* = - \int_{S^*} p^* \bar{n} dS^* + \int_{S^*} \mu \nabla \bar{u}^* \cdot \bar{n} dS^* + \int_{V^*} \rho \bar{F}^* dV^*. \quad (2.9)$$

Here, the control volume,  $V^*$ , is defined as an imaginary boundary used to identify the system and in particular locate all the inlets, outlets and energy sources. It is noted that the differential equations (2.6) and (2.7) can be derived from the integral equations (2.8) and (2.9) by making use of the divergence theorem [see, for example, Versteeg and Malalasekera (1995)].

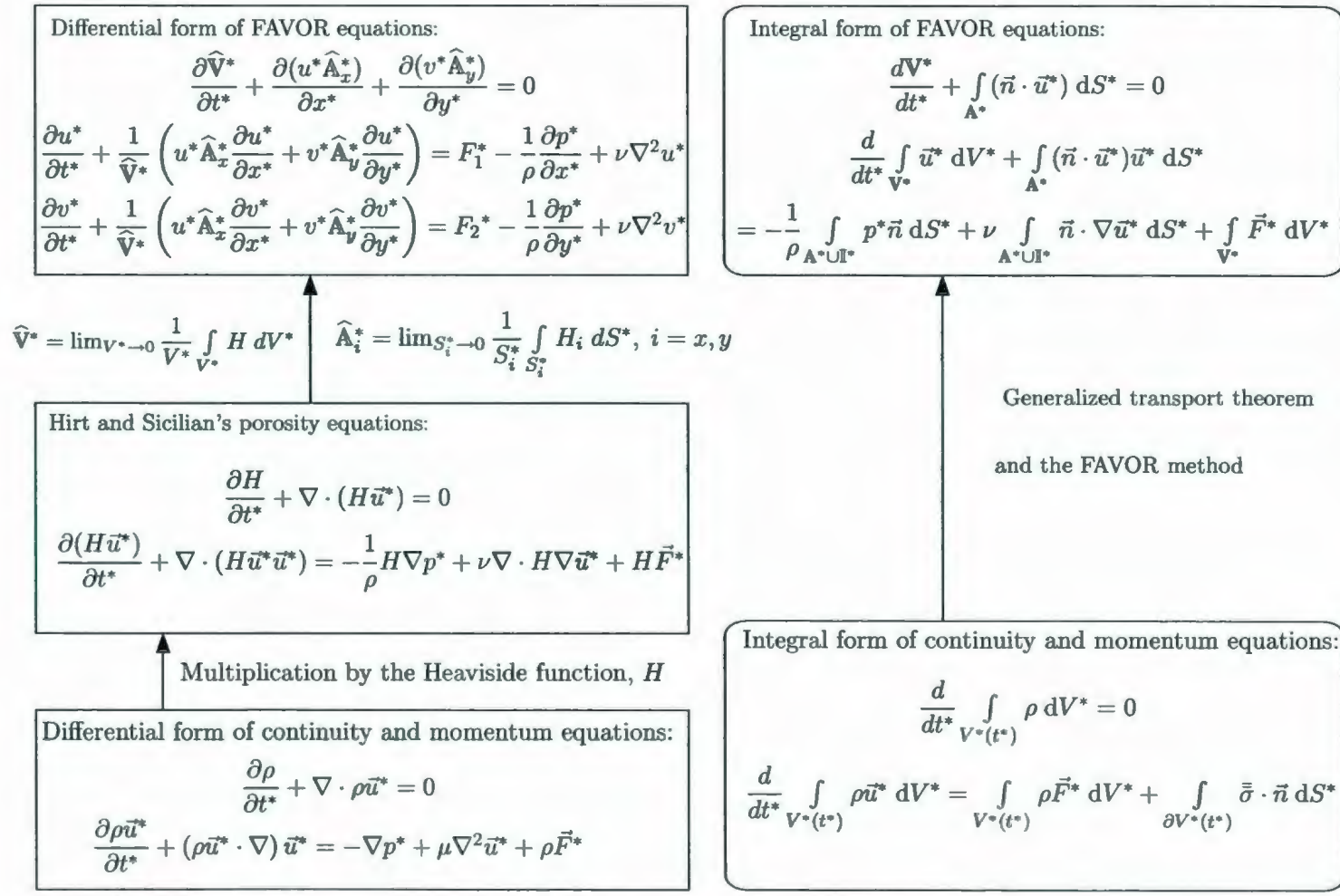


Figure 2.2: The derivation of the differential and integral forms of the FAVOR equations: Hirt and Sicilian (1985), Hirt (1992), Hirt (1993), Tsukiyama *et al.* (1993), Zhu and Wu (2004), Troch *et al.* (2002) (left) and present thesis (right).

Equations (2.8) and (2.9) can be derived by applying the Reynolds transport theorem to the law of conservation of mass and Newton's second law of motion, respectively [see, for example, White (1998)]. The Reynolds transport theorem states that at  $t^* = t_0^*$  the time rate of change of the continuously differentiable fluid property,  $P$  (such as  $\rho$  and  $\rho\vec{u}$ ), within the *material volume*,  $V^*(t^*)$ , equals the sum of the time rate of change of this property within the control volume,  $V^*$ , and its flux through the control volume boundary,  $S^*$ ,

$$\frac{d}{dt^*} \int_{V^*(t^*)} P dV^* = \frac{\partial}{\partial t^*} \int_{V^*} P dV^* + \int_{S^*} P(\vec{u}^* \cdot \vec{n}) dS^*, \quad (2.10)$$

where the material volume,  $V^*(t^*)$ , is defined as the time dependent volume of fluid consisting of identical fluid particles. The Reynolds transport theorem (2.10) only holds for the control volume which contains no fluid-body interface. In this thesis, the governing equations are discretized using a non-boundary-fitted Cartesian grid. Consequently, to be able to model the problems with a stationary or moving solid body using this type of the grid, it is necessary to extend the Reynolds transport theorem over the control volume containing a fluid-body interface.

## 2.2 Integral form of the FAVOR equations

In this section, the integral form of the continuity and Navier-Stokes equations when a solid body is present are derived based on the FAVOR technique and the generalized function theory after making use of the generalized Reynolds transport theorem.

### 2.2.1 Generalized Reynolds transport theorem

A typical rectangular control volume,  $V^*$ , which is partly occupied with the fluid is considered as shown in Figure 2.3. The material volume,  $V^*(t^*)$ , is the part of an arbitrary material volume,  $\Omega$ , which consists of all the fluid particles located within control volume,  $V^*$ , at  $t^* = t_0^*$ . Since the material volume,  $V^*(t^*)$ , is moving, at

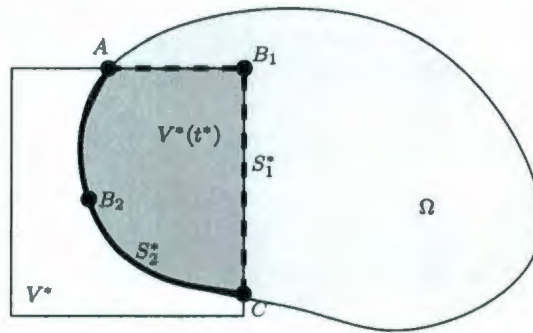


Figure 2.3: Control volume containing a fluid-body interface.

$t^* = t_0^* + \Delta t^*$  it occupies another region  $A'B_1'C'B_2'A'$  as shown in Figure 2.4. The determination of how the fluid property,  $P$ , changes with time within the material volume,  $V^*(t^*)$ , is of interest. In order to calculate the time rate of change of fluid property,  $P$ , within the material volume,  $V^*(t^*)$ ,

$$\frac{d}{dt^*} \int_{V^*(t^*)} P dV^*, \quad (2.11)$$

only very small values of  $\Delta t^*$  are considered, so that the topology of the control volume boundary,  $\partial V^*(t^*)$ , is not changed. The boundary of the material volume,  $\partial V^*(t^*)$ , is piecewise smooth and consists of two parts:  $S_1^*(= AB_1C)$  is the part which coincides with the control volume boundary;  $S_2^*(= AB_2C)$  is the fluid-body boundary located within the control volume,  $V^*(t^*)$ . Farassat (1996) has shown that

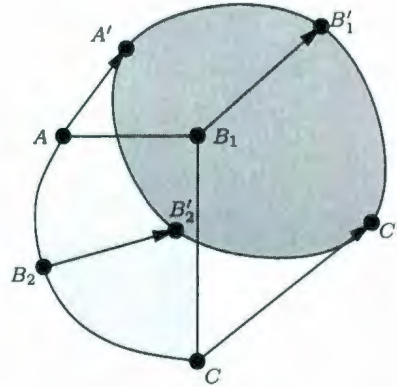


Figure 2.4: Regions  $AB_1CB_2A$  and  $A'B'_1C'B'_2A'$  denote material volumes at  $t^* = t_0^*$  and  $t^* = t_0^* + \Delta t^*$ , respectively.

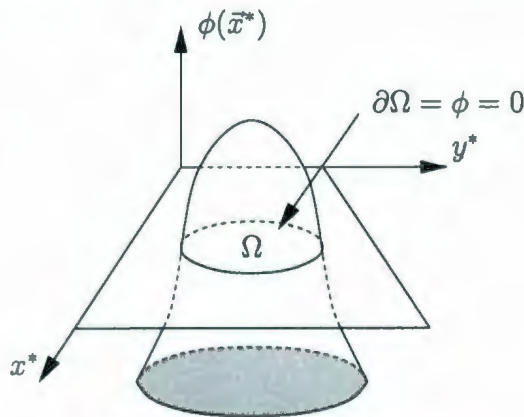


Figure 2.5: Level set function representation.

any arbitrary domain  $\Omega$  with the boundary  $\partial\Omega$  can be conveniently represented by the level set function  $\phi(\vec{x}^*)$  as shown in Figure 2.5, whose zero level set coincides with the domain boundary,  $\partial\Omega$ . The function  $\phi(\vec{x}^*)$  can be chosen such that

$$\phi(\vec{x}^*) = \begin{cases} > 0, & \vec{x}^* \in \Omega, \\ < 0, & \vec{x}^* \notin \Omega, \\ = 0, & \vec{x}^* \in \partial\Omega, \end{cases} \quad (2.12)$$

and

$$\nabla\phi(\vec{x}^*) = \vec{n}, \quad (2.13)$$

where  $\vec{n}$  denotes an inward unit normal vector. Following the work of Farassat (1996), the boundaries  $S_1$  and  $S_2$  are represented by the level set functions  $\phi_1(\vec{x}^*)$  and  $\phi_2(\vec{x}^*)$ , respectively. The Heaviside unit step function,  $H(\phi)$ , is used to represent the fluid property,  $P$ , over three-dimensional real space,  $\mathbb{R}$ , as

$$\Phi = H(\phi(\vec{x}^*)) P, \quad (2.14)$$

where

$$H(\phi) = \begin{cases} 1, & \phi > 0, \\ 0, & \phi < 0 \end{cases} \quad \text{and} \quad \Phi = \begin{cases} P, & \vec{x}^* \in \Omega, \\ 0, & \vec{x}^* \notin \Omega. \end{cases} \quad (2.15)$$

It is noted that  $\Phi = 0$  at all  $\vec{x}^* \notin \Omega$  since  $\phi(\vec{x}^*) < 0$  ( $H(\phi) = 0$ ) at all  $\vec{x}^* \notin \Omega$ . Consequently, the fluid property,  $P$ , can be represented as an integral of  $\Phi$  over  $\mathbb{R}$  by

$$\int_{\Omega} P dV^* = \int_{\mathbb{R}} \Phi dV^* = \int_{\mathbb{R}} H(\phi(\vec{x}^*)) P dV^*. \quad (2.16)$$

The time rate of change of the fluid property,  $P$ , within material volume can be then expressed as

$$\frac{d}{dt^*} \int_{V^*(t^*)} P dV^* = \frac{\bar{d}}{dt^*} \int_{\mathbb{R}} H(\phi_1)H(\phi_2)P dV^*. \quad (2.17)$$

Since  $\Phi$  is a discontinuous function,  $\frac{\bar{d}}{dt^*}$  represents the generalized time derivative in the integral on the right hand side of equation (2.17). Equation (2.17) can be written as

$$\frac{\bar{d}}{dt^*} \int_{\mathbb{R}} H(\phi_1)H(\phi_2)P dV^* = \int_{\mathbb{R}} \frac{\bar{d}}{dt^*} \left( H(\phi_1)H(\phi_2)P \right) dV^*, \quad (2.18)$$

after making use of the fact that the generalized time derivative,  $\frac{\bar{d}}{dt^*}$ , can be moved inside the integral over  $\mathbb{R}$ . It is noted that since  $H(\phi_1)$  and  $H(\phi_2)$  are discontinuous in different points then its generalized derivative can be calculated by

$$\begin{aligned} \int_{\mathbb{R}} \frac{\bar{d}}{dt^*} (H(\phi_1)H(\phi_2)P) dV^* &= \int_{\mathbb{R}} H(\phi_1(t_0^*)) \frac{\bar{d}}{dt^*} H(\phi_2)P dV^* \\ &+ \int_{\mathbb{R}} H(\phi_2(t_0^*))P(t_0^*) \frac{\bar{d}}{dt^*} H(\phi_1) dV^*. \end{aligned} \quad (2.19)$$

Consider the integrals on the right hand side of equation (2.19). In the first integral,  $H(\phi_1(t_0^*))$  is constant and the generalized time derivative,  $\frac{\bar{d}}{dt^*}$ , can be taken outside the integral directly since  $\mathbb{R}$  is independent of time. Thus,

$$\int_{\mathbb{R}} H(\phi_1(t_0^*)) \frac{\bar{d}}{dt^*} H(\phi_2)P dV^* = \frac{\bar{d}}{dt^*} \int_{\mathbb{R}} H(\phi_1(t_0^*))H(\phi_2)P dV^*. \quad (2.20)$$

The product  $H(\phi_1(t_0^*))H(\phi_2)$  in the above integrand is not zero at all  $\bar{x}^* \in V^* \cap \Omega$ , which is the part of the control volume open to flow. Following the work of Hirt and Sicilian (1985), the *volume open to flow* is defined, for arbitrary  $V^*$ , as

$$V^* = \int_{V^*} H(\phi_1)H(\phi_2) dV^*. \quad (2.21)$$

A typical example of the volume open to flow,  $V^*$ , within the computational cell is shown in Figure 2.1(b). The fluid property,  $P$ , is a continuously differentiable function in  $V^*$  and  $H(\phi_1(t_0^*))H(\phi_2) = 1$  at all  $\bar{x}^* \in V^*$ . Thus, equation (2.20) can be written as

$$\frac{\bar{d}}{dt^*} \int_{\mathbb{R}} H(\phi_1(t_0^*))H(\phi_2)P dV^* = \frac{d}{dt^*} \int_{V^*} P dV^*, \quad (2.22)$$

where  $\frac{d}{dt^*}$  is the time derivative.

The generalized time derivative of  $H(\phi_1) = H(\phi_1(x^*(t^*)))$  is

$$\frac{\bar{d}H(\phi_1)}{dt^*} = \frac{\bar{d}H(\phi_1)}{d\phi_1} \left( \frac{\bar{\partial}\phi_1}{\partial\vec{x}^*} \frac{d\vec{x}^*}{dt^*} \right), \quad (2.23)$$

where the time rate of change of a fluid particle at point  $\vec{x}^*$ ,  $\frac{d\vec{x}^*}{dt^*}$ , is the fluid velocity at point  $\vec{x}^*$ ,  $\vec{u}_c^*$ , i.e.,

$$\frac{d\vec{x}^*}{dt^*} = \vec{u}_c^*. \quad (2.24)$$

In addition,

$$\nabla H(\phi_1) = \vec{n}\delta(\phi_1) \quad \text{and} \quad \nabla\phi_1 = \vec{n}, \quad (2.25)$$

where  $\delta$  is the Dirac function. Thus, the second integral on the right hand side of equation (2.19) can be written as

$$\int_{\mathbf{R}} H(\phi_2(t_0^*))P(t_0^*) \frac{\bar{d}}{dt^*} H(\phi_1) dV^* = \int_{\mathbf{R}} H(\phi_2(t_0^*))P(t_0^*)(\vec{n} \cdot \vec{u}^*)\delta(\phi_1) dV^*, \quad (2.26)$$

after making use of equations (2.23), (2.24) and (2.25). The integral on the right hand side of equation (2.26) can be written as

$$\int_{\mathbf{R}} H(\phi_2(t_0^*))P(t_0^*)(\vec{n} \cdot \vec{u}^*)\delta(\phi_1) dV^* = \int_{\mathbf{A}^*} P(t_0^*)(\vec{n} \cdot \vec{u}^*) dS^*, \quad (2.27)$$

after making use of equation (B.5) and the fact that  $H(\phi_2(t_0^*))$  is not zero at all  $\vec{x}^* \in \Omega$  and  $H(\phi_2(t_0^*)) = 1$  at all  $\vec{x}^* \in \mathbf{V}^*$ . Here,

$$\mathbf{A}^* = \int_{S^*} H(\phi_2) dS^* \quad (2.28)$$

is defined as the *area open to flow* across the computational cell boundary  $S^*$ . The areas  $\mathbf{A}_0^*$  (left),  $\mathbf{A}_1^*$  (right),  $\mathbf{A}_2^*$  (bottom) and  $\mathbf{A}_3^*$  (top) are either completely open to flow within a computational cell or blocked as are the right,  $\mathbf{A}_1^*$ , and bottom,  $\mathbf{A}_2^*$ , areas shown in Figure 2.1. It is noted that in the present thesis the values of  $\mathbf{V}^*$  and  $\mathbf{A}^*$  are not normalized unlike in the study by Hirt and Sicilian (1985). This greatly

simplifies the discretization of the governing equations as will be shown later.

Finally, equation (2.17) can be rewritten as

$$\frac{d}{dt^*} \int_{V^*(t^*)} P dV^* = \frac{d}{dt^*} \int_{V^*} P dV^* + \int_{A^*} (\vec{n} \cdot \vec{u}^*) P dS^*, \quad (2.29)$$

after making use of equations (2.18)-(2.20), (2.22), (2.26) and (2.27). This yields the generalized form of the Reynolds transport theorem which states that at  $t^* = t_0^*$  the rate of change of the fluid property,  $P$ , within the material volume,  $V^*(t^*)$ , equals the sum of the rate of change of this property within the part of the control volume open to flow,  $V^*$ , and its flux through the control volume boundary open to flow,  $A^*$ . The fluid is assumed to be incompressible and Newtonian in the subsequent sections.

### 2.2.2 Continuity equation

The conservation of mass,

$$\frac{d}{dt^*} \int_{V^*(t^*)} \rho dV^* = 0, \quad (2.30)$$

states that the mass of material volume,  $V^*(t^*)$ , is constant if there are no sources or sinks of mass. Equation (2.30) can be written for the control volume,  $V^*$ , containing a fluid-body interface as

$$\frac{d}{dt^*} \int_{V^*} \rho dV^* + \int_{A^*} (\rho \vec{u}^* \cdot \vec{n}) dS^* = 0, \quad (2.31)$$

after making use of the generalized Reynolds transport theorem (2.29) and taking  $P = \rho$ . For the incompressible Newtonian fluid case ( $\rho$  is constant), the continuity

equation takes the form

$$\frac{dV^*}{dt^*} + \int_{A^*} (\vec{n} \cdot \vec{u}^*) dS^* = 0. \quad (2.32)$$

### 2.2.3 Navier-Stokes equations

Newton's second law of motion states that the rate of change of momentum in the material volume,  $V^*(t^*)$ , is equal to the resulting external force acting on its boundary,  $V^*(t^*)$ , i.e.,

$$\frac{d}{dt^*} \int_{V^*(t^*)} \rho \vec{u}^* dV^* = \vec{F}^*. \quad (2.33)$$

There are two types of external forces which act on the fluid particle in the material volume. The volume forces act on the material volume,  $V^*(t^*)$ , and surface forces act on the boundary of the material volume,  $\partial V^*(t^*)$ ,

$$\vec{F}^* = \int_{V^*(t^*)} \rho \vec{F}^* dV^* + \int_{\partial V^*(t^*)} \vec{\sigma} \cdot \vec{n} dS^*. \quad (2.34)$$

It is noted that at the considered moment of time,  $t = t_0$ , control volume  $V^*$  coincides with the material volume  $V^*(t^*)$ . Thus, equation (2.34) can be written as

$$\vec{F}^* = \int_{V^*} \rho \vec{F}^* dV^* + \int_{S^*} \vec{\sigma} \cdot \vec{n} dS^*. \quad (2.35)$$

Equation (2.33) can be rewritten, after making use of equation (2.35) and applying the generalized Reynolds transport theorem (2.29) (where  $P = \rho \vec{u}^*$ ) as

$$\frac{d}{dt^*} \int_{V^*} \rho \vec{u}^* dV^* + \int_{A^*} (\vec{n} \cdot \vec{u}^*) \rho \vec{u}^* dS^* = \int_{V^*} \rho \vec{F}^* dV^* + \int_{S^*} \vec{\sigma} \cdot \vec{n} dS^*. \quad (2.36)$$

For the Newtonian fluids the stress tensor,  $\bar{\sigma}$ , has the form

$$\bar{\sigma} = -p^* \bar{I} + \mu (\nabla \bar{u}^* + (\nabla \bar{u}^*)^T). \quad (2.37)$$

For the continuous double differentiable velocity fields, the stress tensor,  $\bar{\sigma}$ , takes the form

$$\bar{\sigma}' = -p^* \bar{I} + \mu \nabla \bar{u}^* \quad (2.38)$$

as shown in Appendix C. The stress tensor form (2.38) is more convenient for numerical approximation of the Navier-Stokes equations since it eliminates the unknowns  $\frac{\partial u^*}{\partial y^*}$  and  $\frac{\partial v^*}{\partial x^*}$  from the  $x^*$ - and  $y^*$ -momentum equations, respectively, and thus greatly simplifies the discretization.

Consider the integrals on the right hand side of equation (2.36). The volume integral can be rewritten as

$$\int_{V^*} \rho \bar{F}^* dV^* = \int_{V^*} \rho \bar{F}^* dV^*. \quad (2.39)$$

Similarly, the surface integral can be rewritten as

$$\begin{aligned} \int_{S^*} \bar{\sigma} \cdot \bar{n} dS^* &= - \int_{S^*} p^* \bar{n} dS^* + \int_{S^*} \bar{n} \cdot \mu \nabla \bar{u}^* dS^* \\ &= - \int_{A^* \cup \Gamma^*} p^* \bar{n} dS^* + \int_{A^* \cup \Gamma^*} \bar{n} \cdot \mu \nabla \bar{u}^* dS^*, \end{aligned} \quad (2.40)$$

after making use of equation (2.38). Here,  $\Gamma^*$  denotes the length of a fluid-body interface open to flow within the control volume,  $V^*$ . Substitution of equations (2.39) and (2.40) into equation (2.36) yields the Navier-Stokes equations for the Newtonian fluids, formulated for the control volume containing a fluid-body interface

$$\frac{d}{dt^*} \int_{V^*} \rho \vec{u}^* dV^* + \int_{A^*} (\vec{n} \cdot \vec{u}^*) \rho \vec{u}^* dS^* = - \int_{A^* \cup \Gamma^*} p^* \vec{n} dS^* + \int_{A^* \cup \Gamma^*} \vec{n} \cdot \mu \nabla \vec{u}^* dS^* + \int_{V^*} \rho \vec{F}^* dV^*. \quad (2.41)$$

Equation (2.41) can then be written as

$$\frac{d}{dt^*} \int_{V^*} \vec{u}^* dV^* + \int_{A^*} (\vec{n} \cdot \vec{u}^*) \vec{u}^* dS^* = - \frac{1}{\rho} \int_{A^* \cup \Gamma^*} p^* \vec{n} dS^* + \nu \int_{A^* \cup \Gamma^*} \vec{n} \cdot \nabla \vec{u}^* dS^* + \int_{V^*} \vec{F}^* dV^*, \quad (2.42)$$

after making use of the fact that incompressible fluid density,  $\rho$ , and dynamic fluid viscosity,  $\mu$ , are constant.

Equations (2.32) and (2.42) are the integral form of the continuity and Navier-Stokes equations:

$$\begin{aligned} \frac{dV^*}{dt^*} + \int_{A^*} (\vec{n} \cdot \vec{u}^*) dS^* &= 0, \\ \frac{d}{dt^*} \int_{V^*} \vec{u}^* dV^* + \int_{A^*} (\vec{n} \cdot \vec{u}^*) \vec{u}^* dS^* &= - \frac{1}{\rho} \int_{A^* \cup \Gamma^*} p^* \vec{n} dS^* + \nu \int_{A^* \cup \Gamma^*} \vec{n} \cdot \nabla \vec{u}^* dS^* + \int_{V^*} \vec{F}^* dV^*, \end{aligned}$$

which are valid for control volumes containing a fluid-body interface. In this thesis, these equations are named as the integral form of the FAVOR equations. These equations are identical to the special integral form of the continuity and Navier-Stokes equations (when a solid body is present). It is important to note that equations (2.32) and (2.42) can be derived from the differential form of the FAVOR equations (2.1) and (2.2) after making use of

$$\int_{V^*} \hat{V}^* dV^* = \frac{V^*}{V^*}, \quad \int_{S^*} \hat{A}_x^* dS^* = \frac{A_0^*}{S_0^*}, \quad \int_{S^*} \hat{A}_y^* dS^* = \frac{A_2^*}{S_2^*}. \quad (2.43)$$

This derivation is given in Appendix A.

It is noted that two-phase Navier-Stokes flow models generally include interface ef-

fects such as surface tension. However, this study deals with the gravity dominated flow in which surface tension plays a minor role and thus can be ignored [see, for example, Reichl *et al.* (2005), Fekken (2004), Armenio (1997)]. The finite volume formulation of the governing equations (2.32) and (2.42) permits discontinuities in material properties and the fluids in  $\Omega_1$  and  $\Omega_2$  are assumed to be incompressible. Thus, the governing equations remain valid for the present two-phase flow model in which surface tension effects are ignored [see Prosperetti and Tryggvason (2007) for details].

## 2.3 Boundary conditions

In this section, the boundary conditions for the problem under consideration are stated. These conditions are the no-slip of the fluid on the cylinder surface, the uniform stream at the inflow, the zero shear stress (free slip) at the top and bottom boundaries of the computational domain and the outflow boundary conditions based on the balance of surface forces (also known as the open boundary conditions [Gresho and Sani (1998)]). It is noted that in two-phase models there are no explicit boundary conditions at the free surface interface. Instead, a single set of the governing equations is solved in the flow domain  $\Omega = \Omega_1 \cup \Omega_2$  (see Figure 1.1). The free surface is then defined in the grid cells where a rapid change in density,  $\rho$ , and viscosity,  $\mu$ , occurs.

### Fluid-body interface

At the surface of the cylinder, the no-slip boundary conditions for a viscous fluid,

$$u^* = u_c^*, \quad v^* = v_c^*, \quad (2.44)$$

are applied. The no-slip conditions state that a solid boundary is impermeable and

the flow sticks to the surface of a solid body due to the viscous effects.

### Inflow and outflow

Uniform flow conditions apply at the infinity. Due to the bounded computational domain, the following inflow and outflow boundary conditions have been chosen. At the inflow boundary, the uniform free stream conditions,

$$u^* = U, \quad v^* = 0 \quad (2.45)$$

are prescribed.

The outflow part of the computational domain boundary is the hardest one to model since, due to the development of an unsteady cylinder wake, the non-uniform velocity field at the outflow is expected. The most commonly used outflow boundary conditions are that of zero normal and tangential derivatives of fluid velocity,

$$\frac{\partial u_n^*}{\partial \vec{n}} = 0, \quad \frac{\partial u_\tau^*}{\partial \vec{n}} = 0, \quad (2.46)$$

which may be supplemented with prescribed pressure at the outflow [see, for example, Versteeg and Malalasekera (1995)]. Gresho and Sani (1998) have shown that the boundary conditions (2.46) are mathematically ill posed. In their work, the open boundary conditions based on the balance of surface forces at the outflow are suggested. In what follows, the derivation of the open boundary conditions due to Gresho and Sani (1998) is given.

The external surface force,  $\vec{F}_s^*$ , acting on the outflow boundary is balanced by the fluid surface force

$$\vec{F}_s^* = \int_{S^*} \vec{n} \cdot \vec{\sigma} \, dS^*. \quad (2.47)$$

Equation (2.47) can be written in the component form as

$$F_{s,1}^* = \int_{S^*} \left( -p^* + \mu \frac{\partial u^*}{\partial x^*} \right) dS^*, \quad F_{s,2}^* = \int_{S^*} \frac{\partial v^*}{\partial x^*} dS^*, \quad (2.48)$$

after making use of the fact that the normal vector at the outflow boundary is  $\vec{n} = (1, 0, 0)$ . The normal component of external force,  $F_{s,1}^*$ , includes the pressure which consists of the hydrostatic,  $p_h^*$ , and hydrodynamic,  $\delta p^*$ , components

$$p^* = p_h^* + \delta p^*. \quad (2.49)$$

The external force  $F_{s,1}^*$  can be represented as

$$F_{s,1}^* + \int_{S^*} p_h^* dS^* = \int_{S^*} \left( -\delta p^* + \mu \frac{\partial u^*}{\partial x^*} \right) dS^*, \quad (2.50)$$

after making use of equation (2.49). Equation (2.50) can be rewritten as

$$F_{s,1}^* + \int_{S^*} p_h^* dS^* = 0. \quad (2.51)$$

This is done based on the fact that in equation (2.50) the hydrostatic pressure is dominant and the hydrodynamic pressure,  $\delta p^*$ , and the viscous term,  $\mu \frac{\partial u^*}{\partial x^*}$ , can be ignored. The hydrostatic pressure,  $p_h^*$ , can be defined as

$$p_h^* = \rho g^* \bar{h}^*, \quad (2.52)$$

where  $\bar{h}^*$  is the height of the fluid at the outflow boundary. Substitution of equation (2.52) into equation (2.51) yields

$$F_{s,1}^* = - \int_{S^*} \rho g^* \bar{h}^* dS^*. \quad (2.53)$$

Finally, the normal velocity open boundary condition can be written as

$$\int_{S^*} \left( -p^* + \mu \frac{\partial u^*}{\partial x^*} \right) dS^* = - \int_{S^*} \rho g^* \bar{h}^* dS^*, \quad (2.54)$$

after making use of equations (2.48) and (2.53). Equation (2.54) can be then written

in the differential form as

$$\nu \frac{\partial u^*}{\partial x^*} + g^* \bar{h}^* = \frac{p^*}{\rho}. \quad (2.55)$$

This is done by making use of the fact that the incompressible fluid density,  $\rho$ , is constant. The tangential velocity boundary condition

$$\int_{S^*} \frac{\partial v^*}{\partial x^*} dS^* = 0 \quad (2.56)$$

follows from equation (2.48) after making use of the fact that  $F_{s,2}^* = 0$ . This equation can be written in the differential form as

$$\frac{\partial v^*}{\partial x^*} = 0. \quad (2.57)$$

Thus, boundary conditions (2.55) and (2.57) are prescribed at the outflow.

### Free slip

At the top and bottom boundaries of the computational domain, the free slip boundary conditions which state that the shear stress is zero at the boundary,

$$\frac{\partial u^*}{\partial x^*} = 0, \quad v^* = 0, \quad (2.58)$$

are prescribed.

## 2.4 Frame of reference and nondimensional parameters

The preliminary numerical experiments conducted in the present study show that when the cylinder moves through the fixed staggered grid, the pressure cell which

belongs to the cylinder at time  $t = t^n$  may become the fluid cell at time  $t = t^{n+1}$ . The continuity equation (2.32) needs to be discretized in this pressure cell. Since at time  $t = t^n$  the velocities in the pressure cell do not satisfy the mass balance exactly, the pressure field has to do extra work to restore the mass balance in the pressure cell at time  $t = t^{n+1}$ . This extra work seems to reflect as a spike in the pressure. Fekken (2004) and Kleefsman (2005) attempted to overcome this difficulty but they failed to eliminate these pressure spikes. In the present computational model, the pressure spikes are eliminated by using a non-inertial frame of reference (symbolically denoted by  $\hat{X}$ ) which translates with the cylinder. In Appendix D, it is shown that the governing equations (2.32) and (2.42) are invariant in the non-inertial frame of reference,  $\hat{X}$ .

The governing equations and boundary conditions for the problem under consideration can be summarized as follows

$$\frac{dV^*}{dt^*} + \int_{\Lambda^*} (\vec{n} \cdot \vec{u}^*) dS^* = 0, \quad (2.59)$$

$$\frac{d}{dt^*} \int_{V^*} \vec{u}^* dV^* + \int_{\Lambda^*} (\vec{n} \cdot \vec{u}^*) \vec{u}^* dS^* = -\frac{1}{\rho} \int_{\Lambda^* \cup \Gamma^*} p^* \vec{n} dS^* + \nu \int_{\Lambda^* \cup \Gamma^*} \vec{n} \cdot \nabla \vec{u}^* dS^* + \int_{V^*} \vec{F}^* dV^* \quad (2.60)$$

and

$$u^* = 0, \quad v^* = 0 \quad \text{at the cylinder boundary,} \quad (2.61)$$

$$u^* = U - v_1^*, \quad v^* = -v_2^* \quad \text{at the inflow boundary,} \quad (2.62)$$

$$\nu \frac{\partial u^*}{\partial x^*} + g^* \bar{h}^* = \frac{p^*}{\rho}, \quad \frac{\partial v^*}{\partial x^*} = 0 \quad \text{at the outflow boundary,} \quad (2.63)$$

$$\frac{\partial u^*}{\partial x^*} = 0, \quad v^* = -v_2^* \quad \text{at the top and the bottom boundaries.} \quad (2.64)$$

It is noted that equations (2.59)-(2.64) are stated in the non-inertial frame of reference,  $\widehat{\mathbf{X}}$ ;  $\widehat{\mathbf{v}}^* = (v_1^*, v_2^*, 0)$  is the dimensional velocity of the non-inertial frame of reference,  $\widehat{\mathbf{X}}$ .

All the quantities in equations (2.59)-(2.64) are stated in their dimensional form. The dimensionless counterparts of these quantities are given by

$$x = \frac{x^*}{d}, \quad y = \frac{y^*}{d}, \quad u = \frac{u^*}{U}, \quad v = \frac{v^*}{U}, \quad t = \frac{t^*U}{d},$$

$$V = \frac{V^*}{d^2}, \quad A = \frac{A^*}{d}, \quad S = \frac{S^*}{d}, \quad \mathbf{V} = \frac{\mathbf{V}^*}{d^2}, \quad \mathbf{A} = \frac{\mathbf{A}^*}{d}, \quad \mathbf{I} = \frac{\mathbf{I}^*}{d},$$

where  $U$  and  $d$  are the unit characteristic parameters. The pressure,  $p^*$ , in equation (2.60) is divided by  $\rho_1$  when this equation is solved in the region  $\Omega_1$  and by  $\rho_2$  when this equation is solved in the region  $\Omega_2$ . Thus, the dimensionless pressure,  $p$ , becomes

$$\frac{p}{\varepsilon} = \frac{p^*}{\rho_2 U^2}, \quad \text{where } \varepsilon = \begin{cases} \gamma, & \vec{x} \in \Omega_1, \\ 1, & \vec{x} \in \Omega_2, \end{cases} \quad (2.65)$$

where  $\gamma = \rho_1/\rho_2$ . In this thesis, the fluid properties are set to  $\rho_1/\rho_2 = 1/100$  and  $\mu_1/\mu_2 = 1/100$  or  $\nu_1/\nu_2 = 1$ . This is done following the work of Reichl *et al.* (2005). Therefore, the Reynolds numbers in the fluids in  $\Omega_1$  and  $\Omega_2$  are the same and are defined by

$$R = \frac{Ud}{\nu_2}. \quad (2.66)$$

Finally, the Froude number is

$$Fr = \frac{U}{\sqrt{dg^*}}. \quad (2.67)$$

The governing equations in their dimensionless form become

$$\frac{d\mathbf{V}}{dt} + \int_{\Lambda} (\vec{u} \cdot \vec{n}) dS = 0, \quad (2.68)$$

$$\frac{d}{dt} \int_{\mathcal{V}} \vec{u} \, dV + \int_{\mathcal{A}} (\vec{n} \cdot \vec{u}) \vec{u} \, dS = -\frac{1}{\varepsilon} \int_{\mathcal{A} \cup \mathcal{I}} p \vec{n} \, dS + \frac{1}{R} \int_{\mathcal{A} \cup \mathcal{I}} \vec{n} \cdot \nabla \vec{u} \, dS + \int_{\mathcal{V}} \vec{F} \, dV. \quad (2.69)$$

In equation (2.69),  $\varepsilon = \rho_2/\rho_1$  when this equation is solved for the fluid in  $\Omega_1$  and  $\varepsilon = 1$  when it is solved for the fluid in  $\Omega_2$ . The external force,  $\vec{F}$ , is due to the dimensionless gravity force,  $\vec{g} = (0, 1/Fr^2, 0)$ , and due to the dimensionless acceleration of the non-inertial frame of reference,  $\hat{X}$ ,  $\vec{a} = (a_1^*d/U^2, a_2^*d/U^2, 0)$ . This yields

$$\vec{F} = (-a_1, \frac{1}{Fr^2} - a_2, 0). \quad (2.70)$$

The dimensionless boundary conditions can be written as

$$u = 0, \quad v = 0 \quad \text{at the cylinder boundary,} \quad (2.71)$$

$$u = 1 - v_1, \quad v = -v_2 \quad \text{at the inflow boundary,} \quad (2.72)$$

$$\frac{1}{R} \frac{\partial u}{\partial x} + \frac{\bar{h}}{Fr^2} = p, \quad \frac{\partial v}{\partial x} = 0 \quad \text{at the outflow boundary,} \quad (2.73)$$

$$\frac{\partial u}{\partial x} = 0, \quad v = -v_2 \quad \text{at the top and the bottom boundaries.} \quad (2.74)$$

The corresponding dimensionless parameters of the problem shown in Figure 1.1 are given by

$$h = \frac{h^*}{d}, \quad f = \frac{f^*d}{U}, \quad A = \frac{A^*}{d}, \quad T = \frac{T^*U}{d},$$

where  $T(= 1/f)$  is the period of cylinder oscillation.

### 3. Computational model and method

In this chapter, the computational method for the numerical simulation of viscous flows with both a moving solid body and a free surface is presented. The continuity and Navier-Stokes equations are discretized using a finite volume approximation on a fixed Cartesian grid. The computational domain boundary conditions are discretized using a finite difference approximation. The Cartesian grid in combination with the discretization of the solid body geometry results in the computational cells containing the fluid-body interface. The volume and area apertures are used to define the region of the computational cell which is not occupied by the solid body geometry. A labeling system is introduced to distinguish the cells of different type. The free surface is discretized with the VOF method in which the volume fraction,  $F_{\Omega_2}$ , is used to distinguish between two different phases, the fluid in  $\Omega_1$  and the fluid in  $\Omega_2$ , in the computational domain. At any time in the solution, the interface is reconstructed using the PLIC algorithm. The advection of the free surface in time is performed after the new velocity field has been calculated from the governing equations, using area-preserving VOF unsplit advection algorithm of Aulisa *et al.* (2003b).

#### 3.1 Discretization of the governing equations

The governing equations (2.68) and (2.69) are solved in the flow part of the computational domain,  $\Omega = \Omega_1 \cup \Omega_2$ , shown in Figure 1.1. In this section, the discretization of the governing equations is presented. The method of solution is based on a Carte-

sian grid finite volume scheme. A second-order accurate central-difference scheme is used to discretize the governing equations in space in conjunction with the first-order explicit forward Euler scheme to advance numerical solutions in time. A cell merging procedure is used to preserve a global second-order accuracy of the spatial discretization. That is, the velocity cells cut by the fluid-body interface are merged with the appropriate neighbour fluid cells to form trapezoidal cells near the surface of the cylinder. A combination of  $B$ -spline and polynomial interpolations is then used to evaluate convective and diffusive fluxes through the edges of the resulting trapezoidal cells.

### 3.1.1 Computational domain geometry

#### Computational grid

The governing equations are discretized on a staggered grid introduced by Harlow and Welsh (1965). In the staggered grid arrangement, the values of the pressure are stored at the centers of the pressure control volumes, while the values of the horizontal and vertical velocity components are stored at the centers of the vertical and horizontal edges of the pressure control volumes, respectively (see Figure 3.1). The staggered arrangement of the pressure and velocity knots is more complicated than the collocated arrangement, where the pressure and velocity values are stored at the centers of the pressure control volumes. However, it is shown that the straightforward discretization on collocated grid leads to pressure spikes and wavy velocity field [see Patankar (1980), Harlow and Welsh (1965) for details]. In contrast, in the stag-

gered grid arrangement, the difference between adjacent knots is used for pressure and velocity discretizations. Thus, no pressure spikes and wavy velocity field occur.

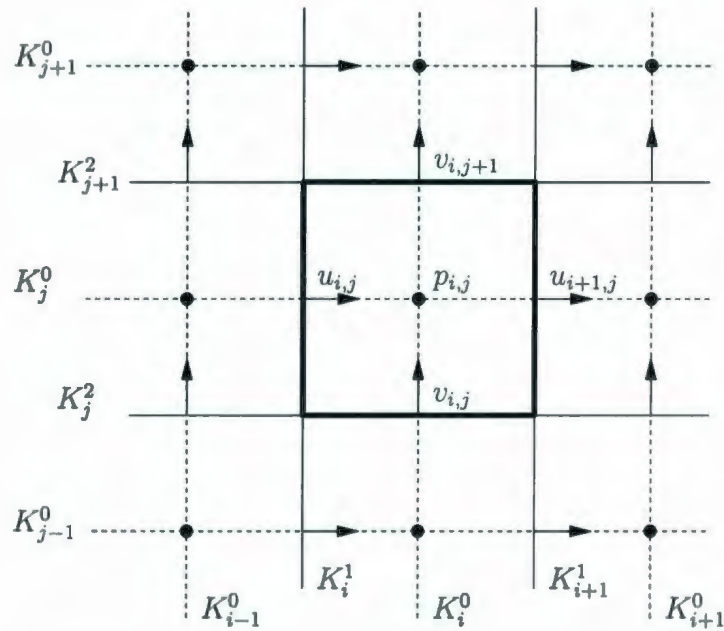


Figure 3.1: Staggered grid arrangement:  $p_{i,j}$  pressure cell.

In the staggered grid arrangement, the pressure knots,  $p_{i,j}$ , are located at the centers of the pressure cells and are defined by the Cartesian coordinates  $(K_i^0, K_j^0)$ , where  $i = 0, \dots, N - 1$ ,  $j = 0, \dots, M - 1$ . Here,  $N$  and  $M$  denote the number of pressure knots in  $x$ - and  $y$ -directions, respectively. An example of the pressure cell  $p_{i,j}$  is shown in Figure 3.1. In this figure,  $p_{i,j}$  is shown by the solid rectangle. The  $u_{i,j}$  and  $v_{i,j}$  velocity knots are located at the centers of the corresponding velocity cells. The examples of  $u_{i,j}$  and  $v_{i,j}$  velocity cells are shown in Figures 3.2(a) and 3.2(b), respectively. In these figures, solid rectangles indicate pressure cells; dashed rectangles indicate velocity cells. The  $u_{i,j}$  knots are defined by the Cartesian coordinates

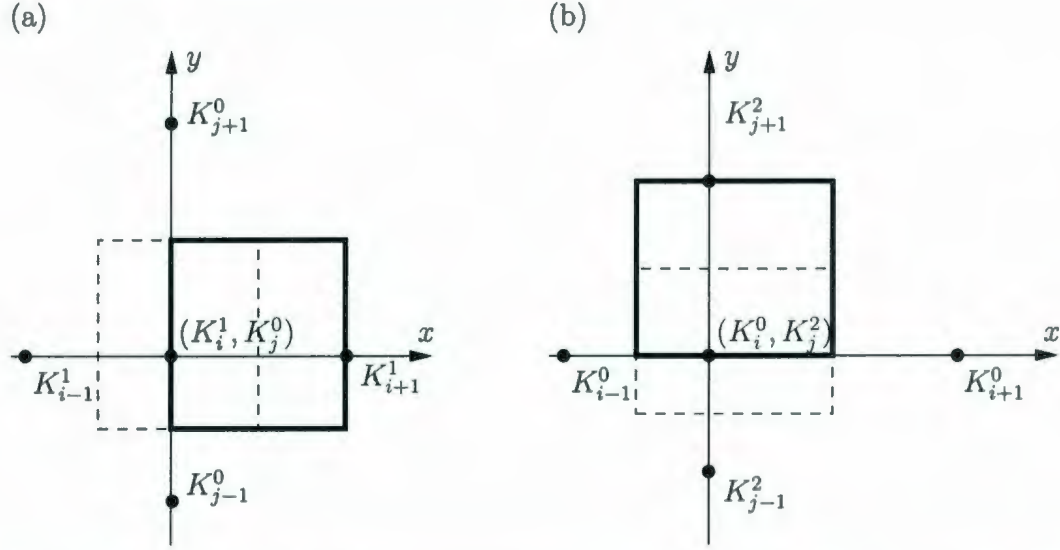


Figure 3.2: Staggered grid arrangement: (a)  $u_{i,j}$ -velocity cell, (b)  $v_{i,j}$ -velocity cell.

$(K_i^1, K_j^0)$ , where  $i = 0, \dots, N$ ,  $j = 0, \dots, M - 1$ . Similarly, the  $v_{i,j}$  knots are defined by the Cartesian coordinates  $(K_i^0, K_j^2)$ , where  $i = 0, \dots, N - 1$ ,  $j = 0, \dots, M$ .

In addition,

$$K_i^1 = \frac{K_{i-1}^0 + K_i^0}{2}, \quad K_j^1 = K_j^0, \quad \text{where } i = 0, \dots, N, \quad j = 0, \dots, M - 1. \quad (3.1)$$

$$K_i^2 = K_i^0, \quad K_j^2 = \frac{K_{j-1}^0 + K_j^0}{2}, \quad \text{where } i = 0, \dots, N - 1, \quad j = 0, \dots, M. \quad (3.2)$$

It is noted that in equations (3.1) and (3.2), coordinates of the ghost pressure knots  $p_{-1,j}, p_{N,j}$ ,  $j = 0, \dots, M - 1$ , and  $p_{i,-1}, p_{i,M}$ ,  $i = 0, \dots, N - 1$  are used. The coordinates of the ghost knots  $p_{-1,j}, p_{N,j}$  are defined, respectively, by

$$K_0^0 - K_{-1}^0 = K_1^0 - K_0^0, \quad K_N^0 - K_{N-1}^0 = K_{N-1}^0 - K_{N-2}^0. \quad (3.3)$$

Similarly, the coordinates of the ghost knots  $p_{i,-1}, p_{i,M}$ , are defined, respectively, by

$$K_0^0 - K_{-1}^0 = K_1^0 - K_0^0, \quad K_M^0 - K_{M-1}^0 = K_{M-1}^0 - K_{M-2}^0. \quad (3.4)$$

### Geometry labeling

For the definition of the geometry on the Cartesian grid, the volume,  $V$ , and the areas,  $A$ , open to flow (also called apertures) are used. It is recalled that the volume aperture,  $V$ , and the area apertures,  $A$ , indicate the part of the computational cell cut by the body geometry which is open to flow. In Figure 3.3, an example of the calculation of the apertures in the computational cell is given. In this figure,  $A_0$ ,  $A_1$ ,

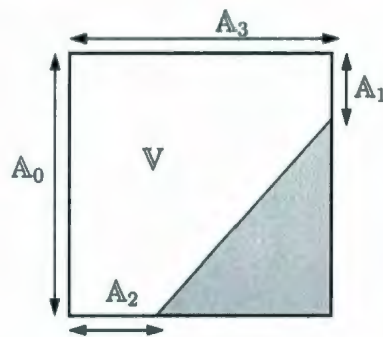


Figure 3.3: An example of the calculation of the volume,  $V$ , and the area,  $A$ , apertures in the computational cell. The solid body is shown in gray.

$A_2$  and  $A_3$  define the left, right, top and bottom apertures in the computational cell, respectively. The apertures are computed geometrically for each computational cell from the solid body geometry. Based on the values of the volume apertures a cell labeling is introduced. The cell labeling is used to identify the cells in which (i) the governing equations are solved and (ii) the boundary conditions are satisfied. For pressure cells four different cell types are distinguished:

- F**(luid) : Cells for which the fluid occupies more than a half cell.
- B**(oundary) : Cells located in the vicinity of fluid-body interface.
- D**(omain) : Cells located at the computational domain boundary.

(e) **X**(cluded) : Cells occupied by the body.

The labeling of pressure cells is performed in three steps. First, consider the pressure cell  $p_{i,j}$ , where  $i = 0, \dots, N - 1, j = 0, \dots, M - 1$ . Let  $\bar{V} = V/V$  be the fractional volume open to flow within the computational cell ( $V$  is the volume of the cell). If the fractional volume open to flow within the cell is greater than half, i.e.,  $\bar{V} \geq 0.5$ ,  $p_{i,j}$  is labeled as **F**. Otherwise,  $p_{i,j}$  is labeled as **X**. Second, consider pressure cells  $p_{i,j}$ , where  $i = 1, \dots, N - 2, j = 1, \dots, M - 2$  which were labeled as **X** during the previous step. If at least one of the neighbour cells  $p_{i-1,j}, p_{i+1,j}, p_{i,j-1}, p_{i,j+1}$  is **F** cell,  $p_{i,j}$  is labeled as **B**. Finally, cells  $p_{i,0}, p_{i,M-1}, p_{0,j}, p_{N-1,j}$ , where  $i = 0, \dots, N - 1, j = 0, \dots, M - 1$  are labeled as **D**.

|   |   |   |   |   |   |
|---|---|---|---|---|---|
| D | D | D | D | D | D |
| D | F | F | F | F | F |
| D | F | F | F | F | F |
| D | F | F | F | F | B |
| D | F | F | F | B | X |
| D | F | F | B | X | X |

Figure 3.4: An example of the labeling of the pressure cells. The solid body is shown in dark gray.

The continuity equation is discretized in all the **F** cells. The value of pressure is set to zero in **B**, **D** and **X** knots. An example of pressure cells labeling is shown in Figure

3.4. Next, velocity cells are labeled in the following manner: the edge of pressure cell on which  $u$ - or  $v$ -velocity knot is located is labeled according to the types of pressure cells this edge belongs to. For example, the edge between two **F** cells is denoted as **FF** edge. As a result, seven types of velocity cells can be distinguished: **FF**, **BF**, **BX**, **DF**, **BB**, **DD** and **XX**. The Navier-Stokes equations are discretized in all the **FF** cells. The values of velocities **BF**, **BB**, **BX** and **XX** are set to zeros. **DF** and **DD** velocities are used to apply boundary conditions at the computation domain boundary.

### 3.1.2 Discretization of the continuity equation

Figure 3.5 shows an example of the pressure cell,  $p_{i,j}$ , in which the continuity equation (2.68) is discretized. In the inertial frame of reference, **X**, the time rate of change of the volume aperture is not zero when body moves as this term becomes a source or sink of volume of the fluid displaced by the body in that cell. On the other hand, equation (2.68) is solved in the non-inertial frame of reference fixed to the cylinder,  $\hat{\mathbf{X}}$ . Therefore, the rate of change of the volume aperture in the cell  $p_{i,j}$ ,  $\frac{dV_{p_{i,j}}}{dt}$ , is identically zero.

The convective term in equation (2.68) is written as the sum of convective fluxes,  $f_{A_k}$ , through each edge aperture,  $A_k$ ,

$$\int_A \vec{n} \cdot \vec{u} dS = \sum_{k=0}^3 f_{A_k}, \quad f_{A_k} = \int_{A_k} \vec{n} \cdot \vec{u} dS. \quad (3.5)$$

In the finite volume discretization,  $u$ - and  $v$ -velocities are assumed to be constant and characteristic for the entire edges these velocities belong to. Thus, the convective

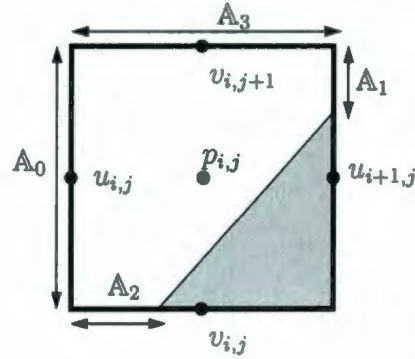


Figure 3.5: Discretization of the continuity equation. The solid body is shown in gray.

flux through each of the edge apertures is approximated as the product of the normal component, the edge aperture and the corresponding velocity component as

$$\begin{aligned} f_{A_0} &= -(u_{i,j} A_0)^{n+1}, & f_{A_1} &= (u_{i+1,j} A_1)^{n+1}, \\ f_{A_2} &= -(v_{i,j} A_2)^{n+1}, & f_{A_3} &= (v_{i,j+1} A_3)^{n+1}. \end{aligned} \quad (3.6)$$

Substitution of (3.6) into equation (2.68) yields the discrete continuity equation per pressure cell,  $p_{i,j}$ ,

$$-(u_{i,j} A_0)^{n+1} + (u_{i+1,j} A_1)^{n+1} - (v_{i,j} A_2)^{n+1} + (v_{i,j+1} A_3)^{n+1} = 0. \quad (3.7)$$

### 3.1.3 Discretization of the Navier-Stokes equations

Equation (2.69) can be rewritten in the componentwise form as

$$\frac{d}{dt} \int_{\mathcal{V}} u \, dV + \int_{\mathcal{A}} (\vec{n} \cdot \vec{u}) u \, dS = -\frac{1}{\varepsilon} \int_{\mathcal{A}} p m_1 \, dS + \frac{1}{R} \int_{\mathcal{A}} \vec{n} \cdot \nabla u \, dS + \int_{\mathcal{V}} F_1 \, dV, \quad (3.8)$$

$$\frac{d}{dt} \int_{\mathcal{V}} v \, dV + \int_{\mathcal{A}} (\vec{n} \cdot \vec{u}) v \, dS = -\frac{1}{\varepsilon} \int_{\mathcal{A}} p m_2 \, dS + \frac{1}{R} \int_{\mathcal{A}} \vec{n} \cdot \nabla v \, dS + \int_{\mathcal{V}} F_2 \, dV. \quad (3.9)$$

In what follows, only the discretization of equation (3.8) is discussed; the discretization of equation (3.9) follows a similar approach. If **FF** cell is not in the vicinity of the fluid-body interface, its neighbour velocity cells will be one of the following types: **FF**, **DF** or **DD**. In this situation, a standard discretization is used to discretize equation (3.8). The standard discretization of the momentum equation on a Cartesian grid approximates velocities and their normal derivatives at the edges of velocity cells by using a linear interpolation between fluid neighbour velocity knots which results in a second-order accurate approximation [see, for example, Versteeg and Malalasekera (1995)]. However, when **FF** cell borders at least one cell of **BF** type, it indicates that this **FF** knot is in the vicinity of the fluid-body interface. In this case, the neighbour velocity may be located in the region occupied by the solid body. For such **FF** cell, the standard discretization of equation (3.8) will result in the loss of accuracy. The typical situation when **FF** cell borders **BF** cell is shown in Figure 3.6. Many studies exclude **BF** cells from consideration and apply the no-slip condition to calculate **BF**-velocity [see, for example, Gubanov (2006), Kleefsman (2005), Fekken (2004) and Gerrits (2001)]. This thesis deals with viscous flows at moderately high Reynolds numbers. In such flows, relatively thin boundary layers will form in the vicinity of the fluid-body interface. These boundary layers are not only regions of high gradients but they are also the most important features of the flow field. Therefore, accurate discretization of the governing equations is important within the boundary layers. Obviously, in viscous flows ignoring **BF** cells will lead to inadequate resolution of boundary layers since these cells are located in the vicinity of the fluid-body interface. In fact, Gubanov (2006) pointed out that the loss of accuracy in the vicinity of the fluid-body interface due to excluding **BF** cells greatly

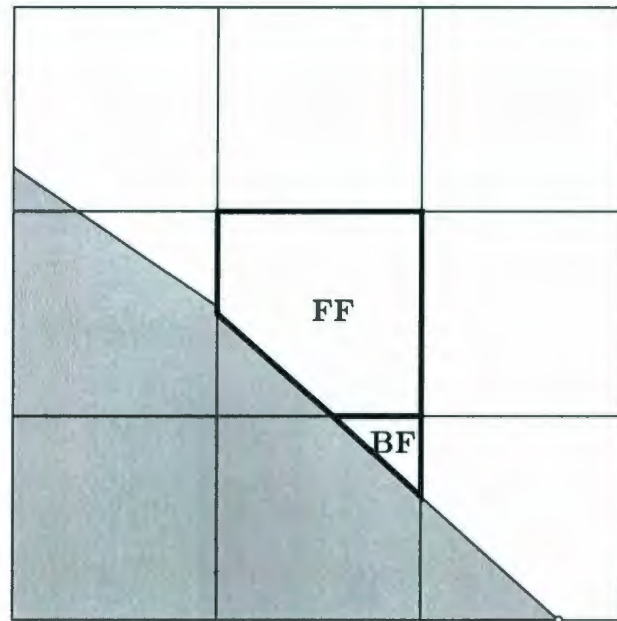


Figure 3.6: An example of the situation when **FF** cell borders **BF** cell. The solid body is shown in gray.

affects computed hydrodynamic forces imposed on this interface. In this thesis, the cell merging technique is used to discretize the Navier-Stokes equations in such **FF** cells to ensure that global second-order accuracy is preserved. The algorithm of the cell merging is described below. In what follows, the **BF** cell is denoted as the “*slave*” cell. The “*master*” cell is the corresponding **FF** cell to which the slave cell is merged.

*Cell merging algorithm.* In general, the **BF** cell can border more than one **FF** cell. For such **BF** cell, the master cell is chosen to be the neighbour **FF** cell with the largest common area aperture. It is noted that this choice of master cells guarantees that the slave cell may have only one master cell. On the other hand, each master cell can have from one to four slave cells. Let **FF** be the cell for which equation (3.8) is discretized. If this cell is the master cell for neighbouring **BF** cell, the slave cell

becomes attached to this master cell. This results in the reshaping of the master cell as shown in Figure 3.6. Depending on the location and the local orientation of the fluid-body interface, cells of a wide variety of shapes can be formed.

### Unsteady term.

An example of  $u$ -cell in which equation (3.8) is discretized is shown in Figure 3.7.

The time derivative is approximated by using the midpoint rule as

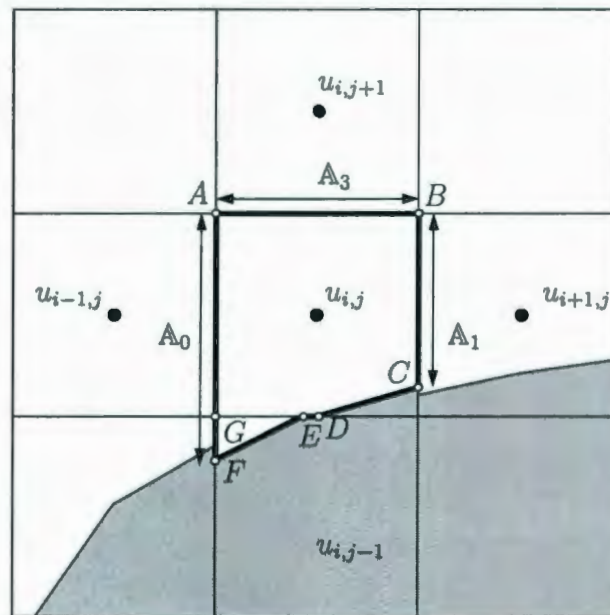


Figure 3.7: Discretization of the  $x$ -momentum equation. The solid body is shown in gray.

$$\frac{d}{dt} \int_V u \, dV \approx \frac{d(u_{i,j} \nabla u_{i,j})}{dt}, \quad (3.10)$$

where, in general,

$$\mathbb{V}_{u_{i,j}} = \mathbb{V}_{\mathbf{FF}} + \sum_{i=0}^{N'} \mathbb{V}_{\mathbf{BF}}, \quad N' = 0, \dots, 3. \quad (3.11)$$

Here,  $\mathbb{V}_{\mathbf{FF}}$  and  $\mathbb{V}_{\mathbf{BF}}$  are the volume apertures of the master cell and the slave cell, respectively. The number of slaves merged with the master cell is denoted by  $N'$ . In Figure 3.7, the master cell is cut by the cylinder geometry. In addition, this cell has the only slave. Therefore, its total volume aperture can be calculated as the sum of volumes bounded by the polygons  $ABCDEG$  and  $GEF$  as

$$\mathbb{V}_{u_{i,j}} = \mathbb{V}_{ABCDEG} + \mathbb{V}_{GEF}. \quad (3.12)$$

Finally, using an explicit forward Euler method, the temporal discretization of equation (3.10) follows

$$\frac{d(u_{i,j} \mathbb{V}_{u_{i,j}})}{dt} \approx \frac{u_{i,j}^{n+1} \mathbb{V}_{u_{i,j}}^{n+1} - u_{i,j}^n \mathbb{V}_{u_{i,j}}^n}{\Delta t}, \quad (3.13)$$

where  $\Delta t$  is the time step.

### Convection and diffusion.

A finite volume approximation of the convection and diffusion to the second-order requires accurate evaluation of the integrands in convective and diffusive terms in equation (3.8). For  $\mathbf{FF}$  cells which are away from the fluid-body interface, the velocities, convective and diffusive fluxes can be approximated at each edge center to second-order accuracy in a straightforward manner by using the standard discretization on a Cartesian grid [see, for example, Versteeg and Malalasekera (1995)]. This is not the case for  $\mathbf{FF}$  cells which lie in the vicinity of the fluid-body interface and therefore, they are either reshaped by merging with the neighbouring  $\mathbf{BF}$  cells or cut by

the cylinder geometry. The key issue here is to perform the discretization separately for each edge of such **FF** cells: one has to define the edges to which the standard discretization can be applied and those which require a special consideration.

The convective term in equation (3.8) is discretized on the Cartesian grid using the midpoint rule as

$$\int_{\mathbf{A}} (\vec{n} \cdot \vec{u}) u \, dS = \int_{\mathbf{A}} u(n_1 u + n_2 v) \, dS \approx \sum_{k=0}^{N'} u_{\mathbf{A}_k}^{n+1} f_{\mathbf{A}_k}^n, \quad N = 2, \dots, 8, \quad (3.14)$$

where  $f_{\mathbf{A}_k}^n$  is the convective flux through an edge  $\mathbf{A}_k$  at time  $t = t^n$ ,  $N'$  denotes a number of edges of  $u$ -cell cell for which the velocity and convective flux are evaluated. It is noted that  $f_{\mathbf{A}_k}^n$  is evaluated at time  $t^n$  using known velocity field,  $u_{\mathbf{A}_k}^n$ . Thus, the discretization of the convective term yields a linear equation. Consider an example “master and slave” cell in Figure 3.7. The edge  $\mathbf{A}_0$  of this cell is composed of two pieces:  $AG$  and  $GF$  coming from the master cell and the slave cell, respectively. Consequently, the integration of the velocity and convective flux through this edge is decomposed as

$$\int_{\mathbf{A}_0} u(n_1 u + n_2 v) \, dS = \int_{AG} u(n_1 u + n_2 v) \, dS + \int_{GF} u(n_1 u + n_2 v) \, dS, \quad (3.15)$$

where the integrals are then approximated by

$$\int_{AG} u(n_1 u + n_2 v) \, dS \approx u_{AG}^{n+1} f_{AG}^n \quad \text{and} \quad \int_{GF} u(n_1 u + n_2 v) \, dS \approx u_{GF}^{n+1} f_{GF}^n. \quad (3.16)$$

The next step is to check if the standard discretization is applicable to the edge under consideration. It is noted that the check is made separately for each edge  $AG$  and  $GF$ . If, for a considered edge, the  $u$ -cells at both sides of this edge are of **FF** type, and the pressure cell corresponding to the edge is not cut by the cylinder geometry, then the standard discretization at the edge can be performed. This is the case for

the edge  $AG$  in Figure 3.7. Thus, the velocity  $u_{AG}^{n+1}$  is approximated at the center of the edge  $AG$  by the linear interpolation as

$$u_{AG}^{n+1} = (1 - \bar{\alpha}) u_{i-1,j}^{n+1} + \bar{\alpha} u_{i,j}^{n+1}, \quad (3.17)$$

where the linear interpolation factor  $\bar{\alpha}$  is defined by

$$\bar{\alpha} = \frac{K_{i-1}^0 - K_{i-1}^1}{K_i^1 - K_{i-1}^1}. \quad (3.18)$$

It is noted that in the case of a uniform grid equation (3.18) yields  $\bar{\alpha} = 1/2$ . The standard approximation of the convective flux through the edge  $AG$  results in

$$f_{AG}^n = -|AG|^n u_{AG}^n, \quad u_{AG}^n = (1 - \bar{\alpha}) u_{i-1,j}^n + \bar{\alpha} u_{i,j}^n, \quad (3.19)$$

where  $|AG|^n$  denotes the length of the edge  $AG$  at time  $t = t^n$  and the linear interpolation factor  $\bar{\alpha}$  is defined by equation (3.18). A second-order approximation to  $u_{GF}^{n+1}$  and  $f_{GF}^n$  is obtained by using a two-dimensional spline interpolating function implemented in SINTEF multilevel  $B$ -spline approximation library [available at [www.sintef.no](http://www.sintef.no)]. The  $B$ -spline interpolation allows a second-order approximation of the velocity and convective flux from available neighbouring values. The algorithm of the  $B$ -spline interpolation is described below. This algorithm illustrates the  $u$ -velocity interpolation. A similar algorithm is applied to interpolate the  $v$ -velocity.

*Algorithm of the B-spline interpolation.* Let  $(x_0, y_0)$  be the point at which the  $u$ -velocity must be interpolated. Consider a  $3 \times 3$  block of the neighbouring cells as shown in Figure 3.8. In this figure, the points of intersection of the grid with the fluid-body interface denoted by letters from  $A$  to  $F$  are used to define the locations of the fluid-body interface velocities. The values of velocities at the points of intersection are calculated using the no-slip boundary condition: these velocities are set to the velocities of the cylinder calculated at points  $A, \dots, F$ . These interface veloc-

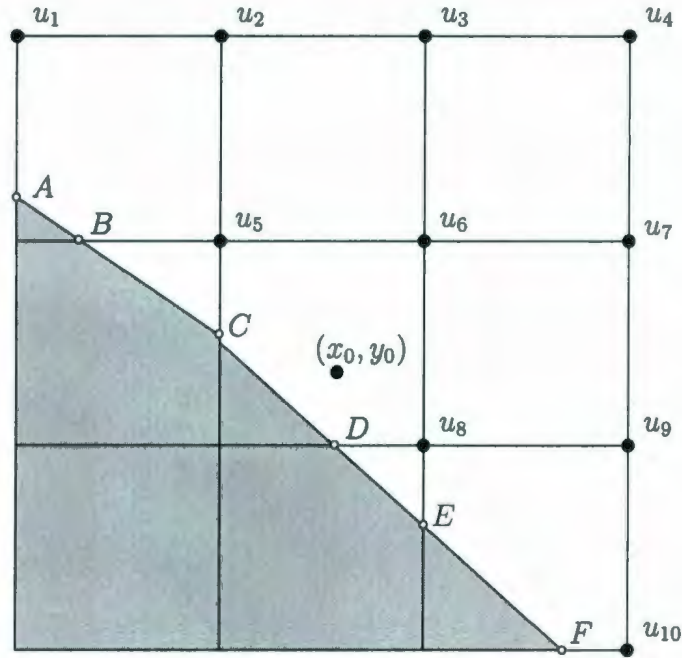


Figure 3.8: Schematic of the  $B$ -spline interpolation for  $u$ -velocity. The solid body is shown in gray.

ities together with the neighbouring **FF** velocities ( $u_1, \dots, u_{10}$  in an example case in Figure 3.8) calculated at time  $t = t^n$  are used to reconstruct the  $B$ -spline surface and then to calculate the value of the  $u$ -velocity in the point  $(x_0, y_0)$ .

Using the algorithm of the  $B$ -spline interpolation, the velocity  $u_{GF}^n$  is interpolated to the center of the edge  $GF$ . It is noted that since the velocities at time  $t = t^n$  are used in the  $B$ -spline approximation, the discretization of the convective term at the edge  $GF$  at time  $t = t^{n+1}$  becomes

$$\int_{GF} u(n_1 u + n_2 v) dS \approx -|GF|^n u_{GF}^n u_{GF}^n. \quad (3.20)$$

A similar procedure is used to approximate the velocity at and convective flux through the edge  $A_1$ . For the situation shown in Figure 3.7, the convective term at the edge

$A_1$  is discretized at time  $t = t^{n+1}$  by the  $B$ -spline approximation yielding

$$\int_{BC} u(n_1u + n_2v) dS \approx |BC|^n u_{BC}^n u_{BC}^n. \quad (3.21)$$

The approximation of the convective flux through the horizontal edges  $A_2$  and  $A_3$  involves the interpolation of the  $v$ -velocity in the centers of the edge apertures. This is due to the fact that in a staggered grid arrangement  $v$ -cells are shifted with respect to the  $u$ -cells and thus,  $v$ -velocities are located at the corners of the  $u$ -cells. In Figure 3.7, the standard discretization for the edge  $A_3$  can be performed. Consequently, the discretization of the convective term for this edge becomes

$$\int_{AB} u(n_1u + n_2v) dS \approx u_{AB}^{n+1} f_{AB}^n, \quad (3.22)$$

where the velocity  $u_{AB}^{n+1}$  is approximated at the center of the edge  $AB$  by the linear interpolation as

$$u_{AB}^{n+1} = (1 - \bar{\alpha}) u_{i,j}^{n+1} + \bar{\alpha} u_{i+1,j}^{n+1}, \quad \text{where} \quad \bar{\alpha} = \frac{K_{j+1}^2 - K_j^1}{K_{j+1}^1 - K_j^1}. \quad (3.23)$$

The discretization of the convective flux through the edge  $A_3$  involves the evaluation of the  $v$ -velocity at time  $t = t^n$ ,

$$f_{AB}^n = |AB|^n v_{AB}^n. \quad (3.24)$$

The linear interpolation is also used to approximate velocity  $v_{AB}^n$  at the center of the edge  $AB$

$$v_{AB}^n = (1 - \bar{\alpha}) v_{i-1,j+1}^n + \bar{\alpha} v_{i,j+1}^n, \quad \text{where} \quad \bar{\alpha} = \frac{K_i^1 - K_{i-1}^2}{K_i^2 - K_{i-1}^2}. \quad (3.25)$$

When the standard discretization for the horizontal edge is not possible the following two-step approach is used:

1. First, the point  $(x_0, y_0)$  is located at the center of the area aperture of the con-

sidered edge.

2. After that, the velocities  $u(x_0, y_0)$ ,  $v(x_0, y_0)$  are found from the known neighbouring **FF** velocities using the *B*-spline interpolation.

It is noted that in Figure 3.7, there is no approximation of the convective term for the aperture  $\mathbb{A}_2$ . This is due to the fact that the cell  $u_{i,j}$  is merged with the cell  $u_{i,j-1}$  and thus there is no convective flux through the edge common to both cells.

The discretization of the diffusive term in equation (3.8) to second-order accuracy is somewhat more complicated as it requires an approximation of the velocity derivatives at the edges of *u*-cell and also at the fluid-body interface segments which lie in the cell. The diffusive term is decomposed into the integration over the edges of the cell and over the fluid-body interface, respectively, as

$$\frac{1}{R} \int_{\mathbb{A} \cup \mathbb{I}} \vec{n} \cdot \nabla u \, dS = \frac{1}{R} \int_{\mathbb{A}} \vec{n} \cdot \nabla u \, dS + \frac{1}{R} \int_{\mathbb{I}} \vec{n} \cdot \nabla u \, dS. \quad (3.26)$$

A finite volume approximation of the diffusive term for the edges of the cell  $u_{i,j}$  can be written as

$$\frac{1}{R} \int_{\mathbb{A}} \vec{n} \cdot \nabla u \, dS = \frac{1}{R} \int_{\mathbb{A}} n_1 \frac{\partial u}{\partial x} + n_2 \frac{\partial u}{\partial y} \, dS \approx \frac{1}{R} \sum_{k=0}^{N'} \bar{f}_{\mathbb{A}_k}^{n+1}, \quad N' = 0, \dots, 8. \quad (3.27)$$

Here,  $\bar{f}_{\mathbb{A}_k}^{n+1}$  indicates the diffusive flux through the aperture  $\mathbb{A}_k$  at time  $t = t^{n+1}$ . Again, for each edge of the cell  $u_{i,j}$  it is first checked if the standard discretization is applicable. Since the aperture  $\mathbb{A}_0$  in Figure 3.7 is composed of edges *AG* and *GF* which come from the master cell and the slave cell, respectively, the diffusive term for this edge is decomposed into two parts as

$$\frac{1}{R} \int_{\mathbb{A}_0} n_1 \frac{\partial u}{\partial x} + n_2 \frac{\partial u}{\partial y} \, dS = \frac{1}{R} \int_{AG} n_1 \frac{\partial u}{\partial x} + n_2 \frac{\partial u}{\partial y} \, dS + \frac{1}{R} \int_{GF} n_1 \frac{\partial u}{\partial x} + n_2 \frac{\partial u}{\partial y} \, dS. \quad (3.28)$$

The standard discretization through the edge  $AG$  is performed since both  $u_{i-1,j}$  and  $u_{i,j}$  cells are of **FF** type and  $p_{i-1,j}$  is not cut by the cylinder geometry, i.e.,

$$\int_{AG} n_1 \frac{\partial u}{\partial x} + n_2 \frac{\partial u}{\partial y} dS \approx -|AG|^{n+1} \frac{u_{i,j}^{n+1} - u_{i-1,j}^{n+1}}{K_i^1 - K_{i-1}^1}. \quad (3.29)$$

However, approximation such as (3.29) is not possible for the edge  $GF$ . The approach here is to express velocity derivative using the  $B$ -spline interpolation described above. The velocity derivative is approximated using the values of  $u$ -velocity at two points located at the line that passes through the center of the edge under consideration and is perpendicular to the edge. The values of  $u$ -velocity at these points are computed using the  $B$ -spline interpolation. The two points participating in this procedure are constructed differently in each of the two possible situations, as is described below. Consider the situation shown in Figure 3.9(a). Reconstruct the line parallel to the

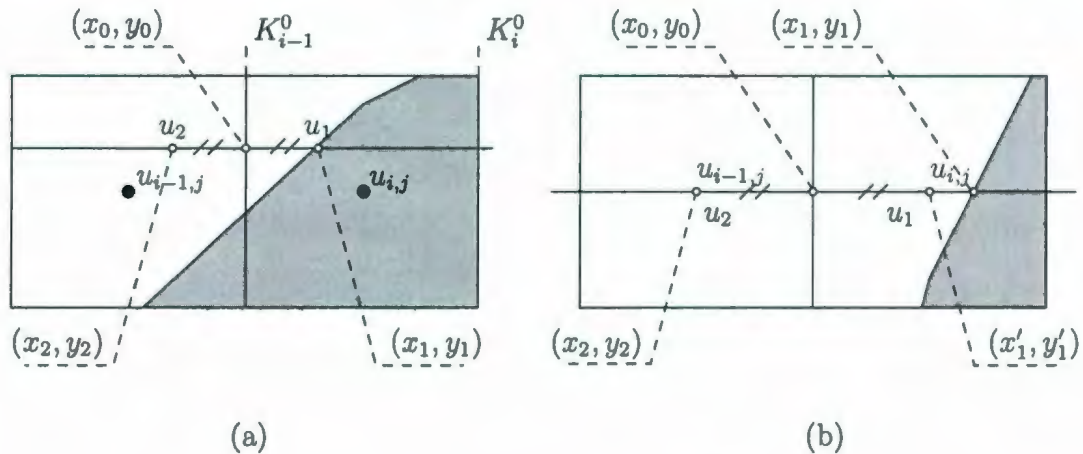


Figure 3.9: Schematic of the discretization of the  $\frac{\partial u}{\partial x}$ . The solid body is shown in gray.

$x$ -axis which passes through the point  $(x_0, y_0)$  located at the center of the aperture  $A_k$ . Let the line intersect the fluid-body interface at the point  $(x_1, y_1)$ . Then, the

distance between points  $(x_0, y_0)$  and  $(x_1, y_1)$  along the line is computed. If the distance between the points is less than half grid step, i.e.,

$$\Delta h \leq \frac{K_i^0 - K_{i-1}^0}{2}, \quad \text{where } \Delta h = x_1 - x_0, \quad (3.30)$$

then point  $(x_1, y_1)$  is reflected into point  $(x_2, y_2)$  with respect to point  $(x_0, y_0)$  as shown in Figure 3.9(a). The  $B$ -spline interpolation is used to calculate  $u$ -velocity at point  $(x_2, y_2)$ . The value of  $u$ -velocity at point  $(x_1, y_1)$  is set to the velocity of the cylinder at this point (from the no-slip condition). Finally, the derivative of  $u$ -velocity at point  $(x_0, y_0)$  is calculated by

$$\left. \frac{\partial u}{\partial x} \right|_{(x_0, y_0)} \approx \frac{u_1 - u_2}{x_1 - x_2}. \quad (3.31)$$

In the case when the line described above does not intersect the fluid-body interface or the distance between points  $(x_0, y_0)$  and  $(x_1, y_1)$  is greater than half grid step, i.e.,

$$\Delta h > \frac{K_i^0 - K_{i-1}^0}{2}, \quad (3.32)$$

the points on the left and the right sides from the point  $(x_0, y_0)$  which are located at the distance  $\Delta h$  with respect to the reference point  $(x_0, y_0)$  are used to calculate the velocity derivative. For the situation shown in Figure 3.9(b) points  $(x'_1, y'_1)$  and  $(x_2, y_2)$  are used for the derivative approximation. The  $B$ -spline interpolation is used to calculate the velocities  $u_1$  and  $u_2$  at points  $(x'_1, y'_1)$  and  $(x_2, y_2)$ , respectively, which leads to the following approximation of the velocity derivative at point  $(x_0, y_0)$

$$\left. \frac{\partial u}{\partial x} \right|_{(x_0, y_0)} \approx \frac{u_1 - u_2}{x'_1 - x_2}. \quad (3.33)$$

Using the algorithm described above, the diffusive flux through the edge  $GF$  in Figure 3.7 is evaluated as

$$\bar{f}_{GF}^{n+1} \approx -|GF|^{n+1} \frac{u_1^{n+1} - u_2^{n+1}}{x_1^{n+1} - x_2^{n+1}}, \quad (3.34)$$

where  $u_1$  is located at the center of the fluid-body interface denoted by  $EF$ . The value of  $u_1$  is computed using the no-slip condition at time  $t = t^{n+1}$ ;  $u_2$  is calculated at time  $t = t^{n+1}$  by the  $B$ -spline interpolation. For the aperture  $\mathbb{A}_1$ , a similar algorithm is used to approximate the diffusive flux.

For the horizontal apertures  $\mathbb{A}_2$  and  $\mathbb{A}_3$ , the derivative  $\frac{\partial u}{\partial y}$  should be evaluated. The standard discretization is straightforward. For example, for the aperture  $\mathbb{A}_3$  shown in Figure 3.7, the standard approximation of  $\frac{\partial u}{\partial y}$  leads to the expression

$$\left. \frac{\partial u}{\partial y} \right|_{AB} \approx \frac{u_{i,j+1}^{n+1} - u_{i,j}^{n+1}}{K_{j+1}^0 - K_j^0}. \quad (3.35)$$

Thus, the diffusive flux through the edge  $AB$  is

$$\bar{f}_{AB}^{n+1} \approx |AB|^{n+1} \frac{u_{i,j+1}^{n+1} - u_{i,j}^{n+1}}{K_{j+1}^0 - K_j^0}. \quad (3.36)$$

In the situation when the standard discretization is not applicable the same idea as for the approximation of the derivative  $\frac{\partial u}{\partial x}$  is utilized. Precisely, the point of intersection,  $(x_1, y_1)$ , of the vertical line passing through the edge center with the fluid-body interface is searched for along the  $y$ -axis (see Figure 3.10). If the distance between points  $(x_0, y_0)$  and  $(x_1, y_1)$  is less than half grid step, i.e.,

$$\Delta h \leq \frac{K_j^2 - K_{j-1}^2}{2}, \quad \text{where } \Delta h = y_0 - y_1, \quad (3.37)$$

then an intersection point  $(x_1, y_1)$  is reflected into point  $(x_2, y_2)$  with respect to point  $(x_0, y_0)$  as shown in Figure 3.9(a). The velocity  $u(x_2, y_2)$  is calculated by the  $B$ -spline interpolation. The value of  $u(x_1, y_1)$  is set to the velocity of the cylinder at the point  $(x_1, y_1)$ . This leads to the following approximation of  $\frac{\partial u}{\partial y}$  at the point  $(x_0, y_0)$

$$\left. \frac{\partial u}{\partial y} \right|_{(x_0, y_0)} \approx \frac{u_2 - u_1}{y_2 - y_1}. \quad (3.38)$$

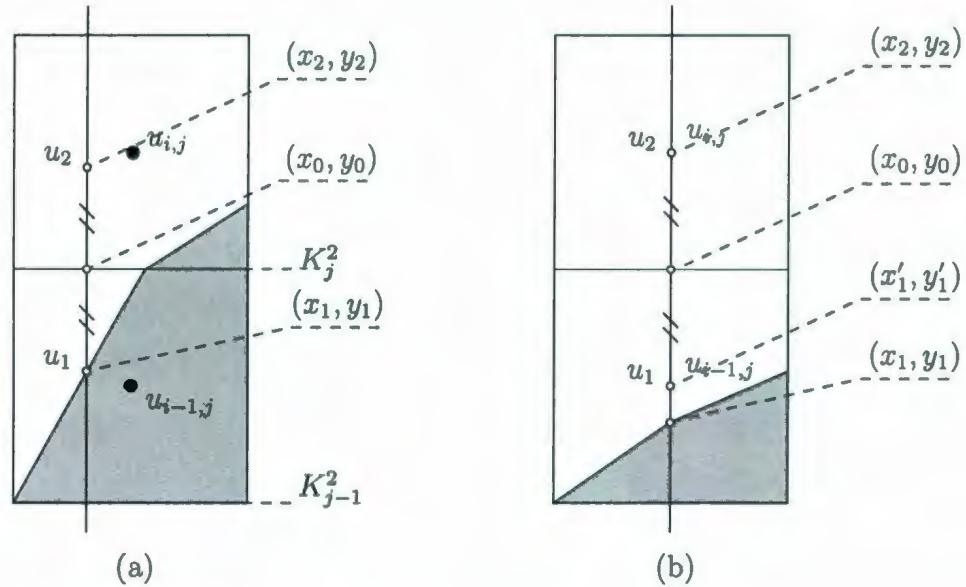


Figure 3.10: Schematic of the discretization of the  $\frac{\partial u}{\partial y}$ . The solid body is shown in gray.

Otherwise, points from the left and the right sides of the point  $(x_0, y_0)$  which are located at the distance  $\Delta h$  with respect to the reference point  $(x_0, y_0)$  are used to calculate the velocity derivative. For the situation shown in Figure 3.10(b) points  $(x'_1, y'_1)$  and  $(x_2, y_2)$  are used for the derivative approximation. The *B*-spline interpolation is used to calculate the velocities  $u_1$  and  $u_2$  in the points  $(x'_1, y'_1)$  and  $(x_2, y_2)$ , respectively, which leads to the following approximation of the velocity derivative at the point  $(x_0, y_0)$

$$\frac{\partial u}{\partial y} \Big|_{(x_0, y_0)} \approx \frac{u_2 - u_1}{y_2 - y'_1}. \quad (3.39)$$

It is noted that there is no diffusive flux through the edge *GE* shown in Figure 3.7 as this edge is common to the master and slave cells.

The approximation of the diffusive flux through the fluid-body interface segments to

second-order accuracy on the Cartesian grid requires the evaluation of the normal derivative at the center of a segment. For instance, the integral over the fluid-body interface in equation (3.26) can be written in terms of the normal derivative as

$$\frac{1}{R} \int_{\mathbb{I}} n_1 \frac{\partial u}{\partial x} + n_2 \frac{\partial u}{\partial y} dS = \frac{1}{R} \int_{\mathbb{I}} \frac{\partial u}{\partial \vec{n}} dS, \quad (3.40)$$

where  $\vec{n}$  is the inward unit normal vector to the fluid-body interface. In general, there might be maximum two fluid-body interface segments in the considered  $u_{i,j}$  cell which come from the cells  $p_{i-1,j}$  and  $p_{i,j}$ , respectively. For example, in Figure 3.7 the diffusive flux is approximated through the fluid-body interfaces  $CD$  and  $EF$ . For each segment of the fluid-body interface the algorithm of the normal derivative approximation is the following.

*Approximation of the normal derivative at the fluid-body interface.* Let point  $A(x_0, y_0)$  be located at the center of the fluid-body interface segment  $\mathbb{I}$  shown in Figure 3.11. The value of the velocity located at the point  $A$ ,  $u_A$ , is calculated from

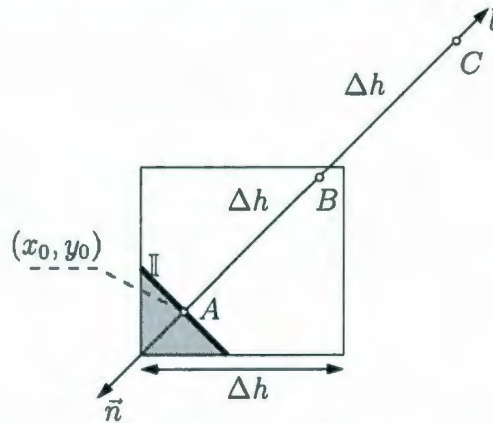


Figure 3.11: Schematic of the approximation of  $\frac{\partial u}{\partial \vec{n}}$  on the fluid-body interface segment. The solid body is shown in gray.

the no-slip condition. Points  $B$  and  $C$  are defined along the  $l$ -direction opposite to

the normal direction such that

$$B = A - \bar{n} \Delta h \quad \text{and} \quad C = A - 2\bar{n} \Delta h, \quad (3.41)$$

where  $\Delta h$  is the uniform grid step used in the vicinity of the cylinder. The velocities at the points  $B$  and  $C$ ,  $u_B$  and  $u_C$ , are calculated from the known neighbouring **FF** velocities using the  $B$ -spline interpolation. Next, the variation of velocity  $u$  along  $l$ -direction is expressed in terms of a quadratic function as

$$u(l) = al^2 + bl + c. \quad (3.42)$$

The coefficients of the quadratic function (3.42) are found from the values of  $u_A$ ,  $u_B$  and  $u_C$  by

$$a = \frac{u_A + u_C - 2u_B}{2\Delta h^2}, \quad b = \frac{u_C + 3u_A - 4u_B}{2\Delta h}, \quad c = u_A. \quad (3.43)$$

Thus, the normal derivative at a point  $(x_0, y_0)$  is evaluated by

$$\left. \frac{\partial u}{\partial \bar{n}} \right|_{(x_0, y_0)} = (2al + b)|_{l=0} = \frac{u_C + 3u_A - 4u_B}{2\Delta h}. \quad (3.44)$$

Finally, the discretization of the diffusive term at the fluid-body interface  $\mathbb{I}$  yields

$$\frac{1}{R} \int_{\mathbb{I}} \frac{\partial u}{\partial \bar{n}} dS \approx \frac{u_C^{n+1} + 3u_A^{n+1} - 4u_B^{n+1}}{2R\Delta h} \mathbb{I}^{n+1}. \quad (3.45)$$

Here, velocities  $u_A$ ,  $u_B$  and  $u_C$  are computed at time  $t = t^{n+1}$ .

The algorithm of the approximation of the convective and diffusive terms for the cell  $u_{i,j}$  can be summarized as follows:

1. Compute the number of segments which compose the edge under consideration.
2. For each segment check to see if the standard approximation is applicable.
3. Use standard approximation if applicable.
4. Otherwise, use the  $B$ -spline interpolating function to discretize the convective

and diffusive terms at this segment.

5. Approximate the diffusive flux through the fluid-body interface segments, if applicable.
6. Add each contribution to the appropriate discretized equation.

### Pressure and volumetric force.

For the approximation of the pressure and volumetric force no merging procedure is needed since **BF** cells are excluded from the consideration.

The pressure term in equation (3.8) involves the integration of the  $x$ -component of the outward unit normal vector,  $\vec{n}$ , and can be decomposed in two parts as

$$\frac{1}{\varepsilon} \int_{\text{AUI}} p n_1 \, dS = \frac{1}{\varepsilon} \int_{\text{A}} p n_1 \, dS + \frac{1}{\varepsilon} \int_{\text{I}} p n_1 \, dS. \quad (3.46)$$

Since  $n_1$  is zero at the horizontal edges of the  $u_{i,j}$  cell the discrete analog of the integral over the boundary of **FF** cell becomes

$$\frac{1}{\varepsilon} \int_{\text{AUI}} p n_1 \, dS \approx \frac{1}{\varepsilon^{n+1}} (p_{i+1,j}^{n+1} A_1^{n+1} - p_{i,j}^{n+1} A_0^{n+1}). \quad (3.47)$$

In general, there are maximum two fluid-body interfaces in the  $u_{i,j}$  cell coming from the cells  $p_{i,j}$  and  $p_{i+1,j}$ , respectively. Thus, the integral over the fluid-body interface can be evaluated as

$$\frac{1}{\varepsilon} \int_{\text{I}} p n_1 \, dS \approx \frac{1}{\varepsilon^{n+1}} (p_{i,j}^{n+1} n_{\text{I}_0} \mathbb{I}_0^{n+1} + p_{i-1,j}^{n+1} n_{\text{I}_1} \mathbb{I}_1^{n+1}), \quad (3.48)$$

where  $n_{\text{I}_0}$  and  $n_{\text{I}_1}$  indicate the  $x$ -component of the unit normal vector to the fluid-body interface segments  $\mathbb{I}_0^{n+1}$  and  $\mathbb{I}_1^{n+1}$ , respectively, calculated at time  $t = t^{n+1}$ . Consider an illustrative example in Figure 3.12. Gerrits (2001) has shown that the

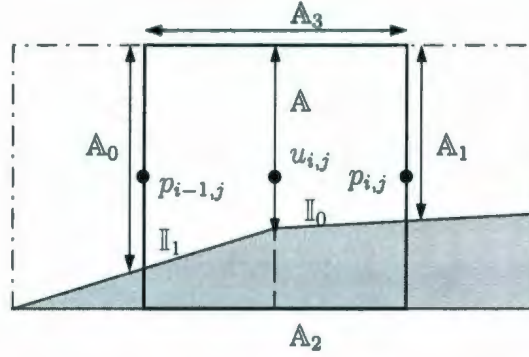


Figure 3.12: Discretization of the pressure term. The solid body is shown in gray.

$x$ -component of the unit normal vector to the fluid-body interface segment is a cosine of the angle between this segment and the corresponding vertical edge. In Figure 3.12, the cosines between the interface segments and the vertical edges are calculated as

$$n_{I_0} = \frac{A^{n+1} - A_1^{n+1}}{I_0^{n+1}} \quad \text{and} \quad n_{I_1} = \frac{A_0^{n+1} - A^{n+1}}{I_1^{n+1}}. \quad (3.49)$$

This results in the following approximation of equation (3.46)

$$\frac{1}{\varepsilon} \int_{A \cup I} p n_1 dS \approx \frac{1}{\varepsilon^{n+1}} A^{n+1} (p_{i,j}^{n+1} - p_{i-1,j}^{n+1}). \quad (3.50)$$

This approximation indicates that discretization of the pressure term is independent of the exact location of the body interface. This fact greatly simplifies the programming of the Navier-Stokes equations.

The volumetric force in the non-inertial frame of reference,  $\widehat{X}$ , is due to the gravity and the acceleration of the non-inertial frame of reference,  $\widehat{X}$ ,

$$\int_{\mathbf{v}} F_1 dV = \int_{\mathbf{v}} \left( \frac{1}{Fr^2} - a_1 \right) dV. \quad (3.51)$$

This term is approximated by using the midpoint rule as

$$\int_V \left( \frac{1}{Fr^2} - a_1 \right) dV \approx \left( \frac{1}{Fr^2} - a_1 \right) \bar{V}_{u_{i,j}}. \quad (3.52)$$

### 3.1.4 Averaging of the density

In two-phase flow models, the free surface is defined in the computational cells where a rapid change in density,  $\rho$ , and viscosity,  $\mu$ , occurs. In the present model, the ratio of the dynamic viscosity of the fluid in  $\Omega_1$ ,  $\mu_1$ , and the dynamic viscosity of the fluid in  $\Omega_2$ ,  $\mu_2$ , is set to  $\mu_1/\mu_2 = 1/100$  (i.e.,  $\nu_1/\nu_2 = 1$ ). Thus, only the density in the vicinity of the phase interface,  $\rho'$ , should be computed at time  $t = t^{n+1}$ . In this thesis,  $\rho'$  is calculated as the average of the densities  $\rho_1$  and  $\rho_2$  as

$$\rho' = \frac{F_{\Omega_1}^{n+1} \rho_1 + F_{\Omega_2}^{n+1} \rho_2}{\bar{V}^{n+1}}, \quad (3.53)$$

where  $F_{\Omega_1}^{n+1}$  and  $F_{\Omega_2}^{n+1}$  are the fractions of the fluids in the regions  $\Omega_1$  and  $\Omega_2$ , respectively, in the velocity cell ( $u_{i,j}$  or  $v_{i,j}$ ), and  $\bar{V}^{n+1}$  is the fractional volume aperture, computed at time  $t = t^{n+1}$ . It is noted that  $F_{\Omega_1}^{n+1}$  is calculated from the known fractions of the fluid in  $\Omega_2$ ,  $F_{\Omega_2}^{n+1}$ , and the body,  $F_b^{n+1}$ , in the cell by

$$F_{\Omega_1}^{n+1} = 1 - (F_{\Omega_2}^{n+1} + F_b^{n+1}). \quad (3.54)$$

The dimensionless counterpart of the averaged density,  $\rho'$ , can be written as

$$\varepsilon^{n+1} = \frac{\rho'}{\rho_2} = \frac{\gamma F_{\Omega_1}^{n+1} + F_{\Omega_2}^{n+1}}{\bar{V}^{n+1}}, \quad (3.55)$$

which is valid for all the cases. For example, when  $F_{\Omega_1}^{n+1} = 0$  (no fluid in the region  $\Omega_1$  in the cell),  $\varepsilon^{n+1} = 1$  and equation (2.69) is discretized in the region  $\Omega_2$ ; when  $F_{\Omega_2}^{n+1} = 0$  (no fluid in the region  $\Omega_2$  in the cell),  $\varepsilon^{n+1} = \gamma$  and equation (2.69) is discretized in the region  $\Omega_1$ .

## 3.2 Free surface interface capturing

An accurate modeling of the free surface flow requires algorithms for the fluid interface kinematics which must address the discrete representation of the interface and its advection through the computational domain. In the present two-phase flow model, the free surface is discretized with the VOF method [Hirt and Nichols (1981)]. To capture the free surface, the known fluid interface geometry is used to compute fluid volume fraction,  $F_{\Omega_2}$ , in each computational cell. The volume fraction,  $F_{\Omega_2}$ , is used to distinguish between the fluids in the regions  $\Omega_1$  and  $\Omega_2$ . A value of zero,  $F_{\Omega_2} = 0$ , indicates cells completely occupied by the fluid in  $\Omega_1$  or solid body and a value of one,  $F_{\Omega_2} = 1$ , indicates cells completely occupied by the fluid in  $\Omega_2$ . The value of volume fraction between zero and one,  $0 \leq F_{\Omega_2} \leq 1$ , indicates the presence of the phase interface in the cell and the value itself gives an indication of the relative proportion of the fluid in  $\Omega_2$  and the fluid in  $\Omega_1$  occupying the computational cell. At any time in the solution, the interface is reconstructed using the PLIC algorithm following the works by Gerrits (2001) and Rider and Kothe (1998). Since the free surface interface is free to move, its advection in time should be performed after the new velocity field has been calculated from the governing equations. Many different VOF advection algorithms exist [see, for example, Rider and Kothe (1998), Pilliod and Puckett (2004), Scardovelli and Zaleski (2003), Harvie and Fletcher (2000), Aulisa *et al.* (2003b)]. However, in the published VOF advection methods the advection operations may result in various inconsistencies. For example, the interface advection algorithms may produce some systematic errors, such as volume fractions,  $F_{\Omega_2}$ , that do not satisfy  $0 \leq F_{\Omega_2} \leq 1$  and thus are inconsistent with their definition. These errors

occur randomly during the computation process and they introduce the inconsistency by generating little holes (“wisp”) in the fluid region. In many cases, this results in the unphysical flow behaviour or numerical break downs. These inconsistencies are very difficult to overcome as it is not obvious where the excess or missing mass should be disposed of, or retrieved. Recently, promising results have been obtained by Aulisa *et al.* (2003b). In their work, a new advection algorithm that preserves mass exactly for two-dimensional incompressible flows on the Cartesian mesh is developed. This advection scheme can be related to the VOF unsplit advection algorithms but is in fact more general. The idea behind the advection scheme due to Aulisa *et al.* (2003b) is as follows. Consider the tessellation of a plane (the two-dimensional computational domain) in the cells (the computational cells) with area  $A$ . Then, at time  $t = t^n$  the area of the fluid in  $\Omega_2$  in each of the cells can be written as  $F_{\Omega_2, i, j}^n A_{i, j}$ . Geometrically speaking, the conservation of mass in the plane means that the total area at each time step is conserved so that

$$\sum_{i, j} F_{\Omega_2, i, j}^{n+1} A_{i, j} = \sum_{i, j} F_{\Omega_2, i, j}^n A_{i, j}. \quad (3.56)$$

Unlike the other VOF advection methods, the scheme of Aulisa *et al.* (2003b) extends the geometrical interpretation to the whole advection as a linear mapping. That is, the advection equation (1.7) is satisfied explicitly by introducing linear mappings,  $\Pi_x$  and  $\Pi_y$ , in both coordinate directions. Then, the linear mapping  $\Pi_{xy} = \Pi_x + \Pi_y$  is used to transform the fluid region at time  $t = t^n$  into the fluid region at time  $t = t^{n+1}$ . The mappings  $\Pi_x$  and  $\Pi_y$  are chosen such that (3.56) is satisfied. Thus, the resulting advection algorithm is strictly mass conserving in two dimensions. In the present numerical algorithm, the VOF advection method due to Aulisa *et al.* (2003b) is used to advect the free surface in time.

### Free surface interface reconstruction

The reconstruction of the free surface interface is not a unique process and depends on the assumed reconstruction algorithm. In this thesis, the PLIC algorithm due to Gerrits (2001) is utilized. In the PLIC methods, the phase interface is approximated in each computational cell with a linear interface defined as

$$\vec{n} \cdot \vec{x} + \bar{d} = 0. \quad (3.57)$$

As was mentioned earlier,  $\bar{d}$  is the line distance from the origin. It is noted that any cell having volume fractions,  $F_{\Omega_2}$ , between zero and one will possess the interface defined by equation (3.57). In this thesis, the unit normal vector,  $\vec{n}$ , is chosen to point outward the fluid, hence (3.57) is positive for any point  $\vec{x}$  lying within the fluid, zero for any point  $\vec{x}$  lying on the line, and negative for any point  $\vec{x}$  lying outside of the fluid. In what follows, the algorithms for computation of the unit normal vector,  $\vec{n}$ , and the line distance from the origin,  $\bar{d}$ , are explained.

**Computation of the normal vector.** In general, the determination of the normal vector is not a unique process and the accuracy of the PLIC method depends on the precise choice of the normal vector. The exact location of the fluid interface is not known and is reconstructed from the local  $F_{\Omega_2}$  data at any time in the solution. In the VOF methods, the normal vector to the free surface can be determined by the volume fraction gradient

$$\vec{n} = \nabla F_{\Omega_2}. \quad (3.58)$$

Comprehensive reviews of other methods can be found in Rider and Kothe (1998), Pilliod and Puckett (2004) and Scardovelli and Zaleski (2003). Following the work by Gerrits (2001), the free surface interface normal vector is approximated in each cell  $p_{i,j}$  having  $0 < F_{\Omega_2,i,j} < 1$  after the discretization of equation (3.58) with respect to eight neighbours surrounding the cell,

$$\begin{pmatrix} K_{i+1}^0 - K_i^0 & 0 \\ K_{i+1}^0 - K_i^0 & K_{j+1}^0 - K_j^0 \\ 0 & K_{j+1}^0 - K_j^0 \\ K_{i-1}^0 - K_i^0 & K_{j+1}^0 - K_j^0 \\ K_{i-1}^0 - K_i^0 & 0 \\ K_{i-1}^0 - K_i^0 & K_{j-1}^0 - K_j^0 \\ 0 & K_{j-1}^0 - K_j^0 \\ K_{i+1}^0 - K_i^0 & K_{j-1}^0 - K_j^0 \end{pmatrix} \cdot \begin{pmatrix} n_1 \\ n_2 \end{pmatrix} = \begin{pmatrix} F_{\Omega_2,i+1,j} - F_{\Omega_2,i,j} \\ F_{\Omega_2,i+1,j+1} - F_{\Omega_2,i,j} \\ F_{\Omega_2,i,j+1} - F_{\Omega_2,i,j} \\ F_{\Omega_2,i-1,j+1} - F_{\Omega_2,i,j} \\ F_{\Omega_2,i-1,j} - F_{\Omega_2,i,j} \\ F_{\Omega_2,i-1,j-1} - F_{\Omega_2,i,j} \\ F_{\Omega_2,i,j-1} - F_{\Omega_2,i,j} \\ F_{\Omega_2,i+1,j-1} - F_{\Omega_2,i,j} \end{pmatrix} \quad (3.59)$$

as illustrated in Figure 3.13. The linear system of equations (E.1) is then multiplied from both sides of equation with transpose matrix taken for the left matrix in equation (E.1). The resulting system of linear equations is solved by Cramer's rule. Finally, the calculated normal vector is normalized by

$$\vec{n} = \frac{\nabla F_{\Omega_2}}{|\nabla F_{\Omega_2}|}. \quad (3.60)$$

**Computation of the line distance.** The computation of the line distance,  $\bar{d}$ , is the most difficult reconstruction task because the value of  $\bar{d}$  is constrained by mass conservation. In other words, the value of  $\bar{d}$  is constrained such that the resulting

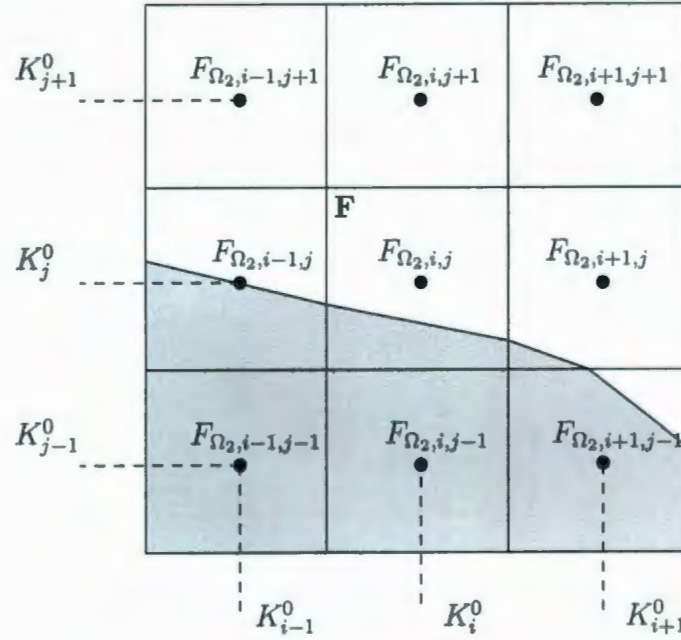


Figure 3.13: An approximation of the free surface normal vector. The solid body is shown in gray.

line passes through the computational cell with a truncation volume,  $\mathbb{V}(\bar{d})$ , equal to the cell volume aperture,  $\mathbb{V}$ , so that

$$\mathbb{V}(\bar{d}) - \mathbb{V} = f(\bar{d}), \quad (3.61)$$

where  $f(\bar{d})$  is a non-linear function. In order to determine the line distance,  $\bar{d}$ , one has to invert (3.61). The inverse problem consists of finding  $\bar{d}$  given the cell volume aperture,  $\mathbb{V}$ . It is noted that in (3.61)  $\mathbb{V}$  can vary linearly, quadratically, or cubically with  $\bar{d}$ , depending upon the coordinate system and the shape of the polygon formed by the interface segment truncating the computational cell. Following the work by Rider and Kothe (1998), (3.61) is inverted iteratively in each cell  $p_{i,j}$  having  $0 < F_{\Omega_2, i, j} < 1$ . The line distance,  $\bar{d}$ , is declared “found” when the function  $f(\bar{d})$  becomes zero (to within some tolerance). A number of algorithms can be used to find the root of

the  $f(\bar{d})$  function. These include the bisection method, the secant method, Newton's method, Newton-Raphson method, Brent's method, etc [see, for example, Forsythe *et al.* (1977)]. In this thesis, Brent's algorithm [Brent (1973)] is used to find an optimal guess for  $\bar{d}$ . In Brent's method, a combination of the bisection, the secant and the inverse quadratic interpolation methods is utilized. At every iteration, Brent's method decides which method out of these three is likely to perform best, and proceeds by doing a step according to that method. This yields a robust and fast algorithm for the root finding. The algorithm of the computation of the line distance due to Rider and Kothe (1998) can be summarized as follows. First, the truncation volume,  $\mathbb{V}(\bar{d})$ , is found. Second,  $\mathbb{V}(\bar{d})$  is compared to the cell volume aperture,  $\mathbb{V}$ , to see if  $\mathbb{V}(\bar{d})$  differs from  $\mathbb{V}$  by some prescribed tolerance. Otherwise, Brent's algorithm is used to find the new guess for the line distance,  $\bar{d}$ , in equation (3.61).

### Free surface interface advection

Once the free surface is reconstructed, its motion must be modeled with a suitable advection algorithm. In this thesis, the free surface interface is advected in time using the geometrical area preserving VOF advection method of Aulisa *et al.* (2003b). The volume of the fluid contained in the cell  $p_{i,j}$  at time  $t = t^n$  is advected onto the volume of the fluid at time  $t = t^{n+1}$  with the linear mapping  $\Pi_{xy} = \Pi_x + \Pi_y$ . The linear mapping in  $x$ -direction,  $\Pi_x : x' \rightarrow x$ , defined by

$$x = a_1 x' + b_1, \quad (3.62)$$

where

$$a_1 = \frac{K_{i+1}^1 - K_i^1}{K_{i+1}^1 - K_i^1 + |u_{i,j} \Delta t| + |u_{i+1,j} \Delta t|}, \quad (3.63)$$

$$b_1 = \frac{K_i^1 |u_{i+1,j} \Delta t| + K_{i+1}^1 |u_{i,j} \Delta t|}{K_{i+1}^1 - K_i^1 + |u_{i,j} \Delta t| + |u_{i+1,j} \Delta t|} \quad (3.64)$$

maps the horizontal edges of pressure cells. Similarly, the linear mapping in  $y$ -direction,  $\Pi_y : y' \rightarrow y$ , is defined by

$$y = a_2 y' + b_2, \quad (3.65)$$

where

$$a_2 = 1 + \frac{|v_{i,j} \Delta t| + |v_{i,j+1} \Delta t|}{K_{j+1}^2 - K_j^2}, \quad (3.66)$$

$$b_2 = -\frac{K_{j+1}^2 |v_{i,j} \Delta t| + K_j^2 |v_{i,j+1} \Delta t|}{K_{j+1}^2 - K_j^2}. \quad (3.67)$$

The algorithm of the fluid mapping is illustrated in Figure 3.14, where the fluid is compressed in the  $x$ -direction and expands in the  $y$ -direction. Mapping  $\Pi_x$  maps

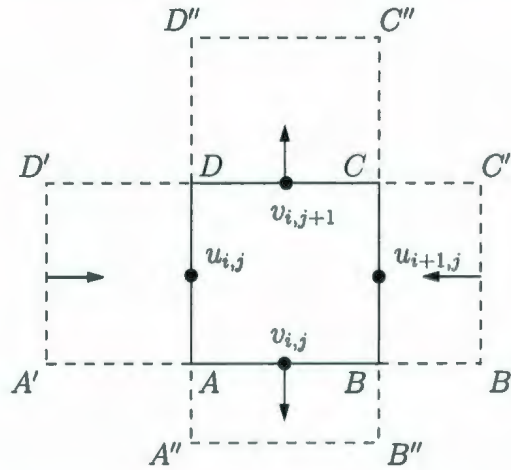


Figure 3.14: Fluid mapping algorithm.

the horizontal edges of the pre-image of the pressure cell  $p_{i,j}$  onto  $p_{i,j}$  cell. In other

words, the rectangle  $A'B'C'D'$  is mapped (compressed) onto the rectangle  $ABCD$  in  $x$ -direction. Similarly, mapping  $\Pi_y$  maps (expands) rectangle  $ABCD$  onto the rectangle  $A''B''C''D''$  in  $y$ -direction. Since  $u_{i,j} > 0$  and  $u_{i+1,j} < 0$ , over time  $t = \Delta t$  the fluid is transferred into the cell  $p_{i,j}$  from its left and right neighbour cells as illustrated in Figure 3.15(a). The contributions are defined as intersection of pre-

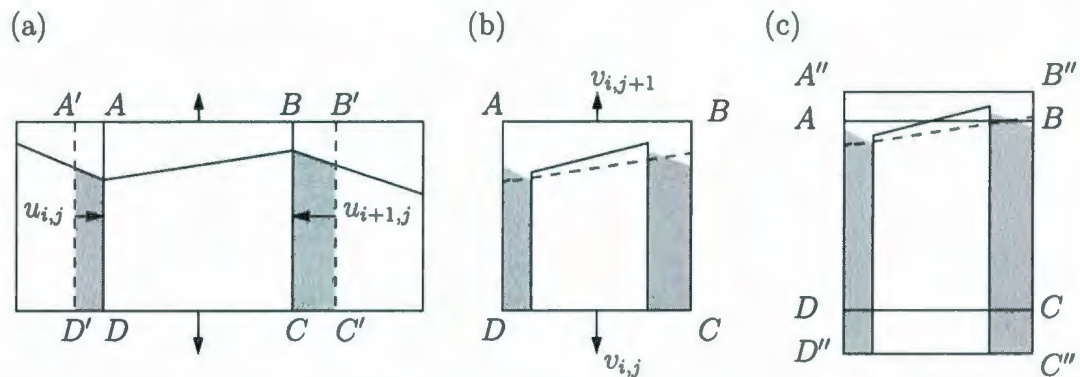


Figure 3.15: Fluid advection algorithm: (a) advection of the convective fluxes along the  $x$ -coordinate, (b) mapping onto the image cell, (c) advection of the convective fluxes along the  $y$ -coordinate.

image edge with region occupied by the fluid in the corresponding neighbour cell. However,  $v_{i,j} < 0$  and  $v_{i+1,j} > 0$ . Consequently, the fluid is transferred from the cell  $p_{i,j}$  into its top and bottom neighbour cells as shown in Figure 3.15(b). Therefore, the total volume of the fluid in each of the neighbour cells is calculated at time  $t = t^{n+1}$  as the sum of all the fluid contributions into this cell. Finally, Figure 3.15(c) shows the advected volume of fluid corresponding to the cell  $p_{i,j}$  at time  $t = t^{n+1}$ . This volume of fluid results in contributions to the central cell  $p_{i,j}$  as well as to its top and bottom neighbours.

### 3.3 Discretization of the computational domain boundary conditions

The computational domain is truncated by the inflow boundary from the left side, by the outflow boundary from the right side and by the free slip boundaries from the top and the bottom sides as shown in Figure 3.16. The computational domain boundary conditions (2.71)-(2.74) are solved in the appropriate  $\mathbf{D}$  cells and are used to calculate the values of  $u$  and  $v$  velocities which are located on the border of the computational domain, but involved into the discretization of the governing equations. In what follows, the discretization of the computational domain boundary conditions is discussed.

The computational domain size plays a key role for the accurate numerical simulation of unsteady flow when free surface effects are included. The numerical experiments indicate that the restricted computational domain may lead to an artificial alteration in the height of the free surface. One of the reasons is that when the free surface wave reaches inflow boundary, it should naturally propagate through this boundary. On the other hand, the inflow boundary conditions (2.45) prohibit the propagation of the free surface wave through the inflow boundary. This results in an artificial elevation of the height of the fluid in the region  $\Omega_2$  at the inflow boundary and then, over a sufficient time interval, in the whole computational domain. The artificial changes in the height of the free surface affect the value of the lift force acting on the surface of the cylinder since the calculation of the lift force involves subtracting the buoyancy force. In Section 4, a number of computational domain sizes are tested to guarantee

that the computational domain boundary conditions are correct and the free surface flow quantities are accurately predicted.

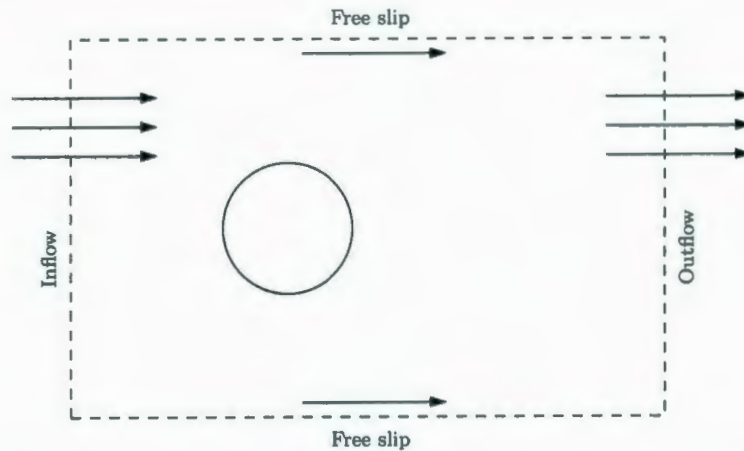


Figure 3.16: Computational domain boundary conditions.

### Inflow

The inflow boundary conditions state that the fluid enters the computational domain with the uniform stream velocity, i.e,  $u = 1$ ,  $v = 0$ . In the the non-inertial frame of reference,  $\hat{X}$ , the inflow boundary conditions can be written as

$$u = 1 - v_1, \quad v = -v_2. \quad (3.68)$$

The discrete analog of equations (3.68) takes the form

$$u_{1,j}^{n+1} + v_1^{n+1} - 1 = 0, \quad v_{0,j}^{n+1} + v_2^{n+1} = 0, \quad \text{where } j = 1, \dots, M - 1, \quad (3.69)$$

after making use of the finite difference approximation.

### Outflow

The outflow boundary conditions are applied at the right boundary of the compu-

tational domain through which the flow leaves the domain. The outflow boundary conditions are invariant in the non-inertial frame of reference,  $\widehat{X}$ , i.e.,

$$\frac{1}{R} \frac{\partial u}{\partial x} + \frac{\bar{h}}{Fr^2} = p, \quad \frac{\partial v}{\partial x} = 0. \quad (3.70)$$

Equations (3.70) are discretized using the finite difference approximation as

$$\frac{1}{R} \frac{u_{N-1,j}^{n+1} - u_{N-2,j}^{n+1}}{K_{N-1}^1 - K_{N-2}^1} - p_{N-2,j}^{n+1} + \frac{\bar{h}^{n+1}}{Fr^2} = 0, \quad \text{where } j = 1, \dots, M-2 \quad (3.71)$$

and

$$v_{N-1,j}^{n+1} - v_{N-2,j}^{n+1} = 0, \quad \text{where } j = 1, \dots, M-2, \quad (3.72)$$

respectively. It is noted that at time  $t = t^{n+1}$  the height of the fluid in the region  $\Omega_2$  at the outflow boundary,  $\bar{h}^{n+1}$ , is computed from the actual height of the fluid in  $\Omega_2$  at the outflow.

### Free slip

The free slip boundary conditions are used at the top and bottom boundaries of the computational domain. That is, it is assumed that the tangential velocity,  $u$ , does not change, i.e.,  $\frac{\partial u}{\partial x} = 0$ , and the normal velocity,  $v$ , is prescribed by  $v = 0$ . In the non-inertial frame of reference,  $\widehat{X}$ , the free slip boundary conditions can be written as

$$\frac{\partial u}{\partial x} = 0, \quad v = -v_2. \quad (3.73)$$

The finite difference approximation is used to discretize equations (3.73). At the top boundary of the computational domain, the discrete free slip boundary conditions can be written as

$$u_{i,M-1}^{n+1} - u_{i,M-2}^{n+1} = 0, \quad v_{i,M-1}^{n+1} + v_2^{n+1} = 0, \quad \text{where } i = 1, \dots, N-2. \quad (3.74)$$

Similarly, at the bottom boundary of the computational domain, the discrete free slip boundary conditions can be written as

$$u_{i,1}^{n+1} - u_{i,0}^{n+1} = 0, \quad v_{i,1}^{n+1} + v_{i,0}^{n+1} = 0, \quad \text{where } i = 1, \dots, N - 2. \quad (3.75)$$

### 3.4 Calculation of the lift and drag forces, and the mechanical energy transfer

Unsteady flow past the circular cylinder excites a periodic flow induced resultant force,  $\vec{F}_s^* = (D, L, 0)$ , acting on the surface of the cylinder, given by

$$\vec{F}_s^* = \frac{d}{2} \int_0^{2\pi} \bar{\sigma} \cdot \vec{n} \, d\theta, \quad (3.76)$$

where  $\vec{n} = (\cos \theta, \sin \theta, 0)$  is the outward unit normal vector to the cylinder surface;  $L$  and  $D$  are the dimensional lift and drag forces, respectively. The presence of the acceleration due to gravity in the Navier-Stokes equations (2.69) implies that there is a buoyancy force acting on the cylinder. In other words, pressure varies around cylinder as a consequence of the hydrostatic pressure, i.e., the resultant force acting on the surface of the cylinder includes a buoyancy term. This component is subtracted to calculate the flow induced resultant force acting on the surface of the cylinder [see Reichl (2001) for details]. Thus, a periodic flow induced resultant force acting on the surface of the cylinder in the presence of the free surface can be calculated using

$$\vec{F}_s^* = \frac{d}{2} \int_0^{2\pi} \bar{\sigma} \cdot \vec{n} \, d\theta - \frac{d}{2} \int_0^{2\pi} p_h^* \vec{n} \, d\theta, \quad (3.77)$$

where the dimensionless counterpart of  $\vec{F}_s^*$  is given by

$$\vec{F}_s = \frac{2\vec{F}_s^*}{\rho U^2 d}. \quad (3.78)$$

The  $y$ -component of  $\vec{F}_s$ , known as the lift coefficient,  $C_L$ , yields

$$C_L = C_{L,p} + C_{L,f} - \frac{\pi}{2} \frac{1}{Fr^2}, \quad (3.79)$$

where

$$C_{L,p} = \int_0^{2\pi} p \sin \theta \, d\theta, \quad C_{L,f} = \frac{1}{R} \int_0^{2\pi} \vec{n} \cdot \nabla v \, d\theta \quad (3.80)$$

are the pressure and the viscous (friction) contributions to the lift coefficient, respectively. The  $x$ -component of  $\vec{F}_s$  results in the drag coefficient,  $C_D$ ,

$$C_D = C_{D,p} + C_{D,f}, \quad (3.81)$$

where the pressure and the viscous contributions to the drag coefficient are

$$C_{D,p} = \int_0^{2\pi} p \cos \theta \, d\theta, \quad C_{D,f} = \frac{1}{R} \int_0^{2\pi} \vec{n} \cdot \nabla u \, d\theta, \quad (3.82)$$

respectively. The interpolations of the discrete pressure and vorticity fields to the cylinder surface required for the implementation of equations (3.79) and (3.81) are performed using second-order  $B$ -splines. The mean lift and drag coefficients are calculated as

$$\widehat{C}_L = \frac{1}{kT} \int_t^{t+kT} C_L \, dt, \quad \widehat{C}_D = \frac{1}{kT} \int_t^{t+kT} C_D \, dt, \quad (3.83)$$

respectively, where  $k$  indicates a number of periods of oscillation.

When the cylinder moves relative to the fluid there is an exchange of mechanical energy between the fluid and the cylinder. For the cylinder subject to in-line oscillations in uniform flow the total energy transfer over one period of oscillation,  $T^*$ , can be

defined as

$$E^* = \int_0^{T^*} D \dot{x}^*(t^*) dt^*, \quad (3.84)$$

where the overdot indicates the differentiation by time [see, for example, Blackburn and Henderson (1999)]. The dimensionless counterpart of  $E^*$  can be written as

$$E = \frac{2E^*}{\rho U^2 d^2}. \quad (3.85)$$

It is noted that mechanical energy transfer,  $E$ , is positive when the energy is transferred from the fluid to the cylinder and negative, otherwise.

### 3.5 Initial conditions

In this thesis, the uniform flow is used as the initial condition, where the flow velocities at time  $t = 0$  are defined by

$$u_{i,j} = 1 - v_1, \quad \text{where } i = 0, \dots, N, \quad j = 0, \dots, M - 1. \quad (3.86)$$

$$v_{i,j} = -v_2, \quad \text{where } i = 0, \dots, N - 1, \quad j = 0, \dots, M. \quad (3.87)$$

It is assumed that at time  $t = 0$ , the free surface is undisturbed. It is noted that there is no initial condition for the pressure field. This is due to the fact that pressure is not involved into the discretization of the governing equations and the boundary conditions at explicit time level.

### 3.6 Numerical simulation flowchart

The numerical algorithm, described in this chapter, is implemented in the C++ language. Figure 3.17 illustrates the numerical simulation flowchart. The main steps of

the program are (i) the *initialization* of  $u_{i,j}^0$ ,  $v_{i,j}^0$ ,  $F_{\Omega_2,i,j}^0$ ,  $V_{i,j}^0$  and  $A_{i,j}^0$ ; and (ii) the *time iteration*, where the new values of variables  $p_{i,j}^{n+1}$ ,  $u_{i,j}^{n+1}$ ,  $v_{i,j}^{n+1}$ ,  $F_{\Omega_2,i,j}^{n+1}$ ,  $V_{i,j}^{n+1}$  and  $A_{i,j}^{n+1}$  at the new time  $t = t^{n+1}$  are calculated.

At the *initialization* step, the velocities  $u_{i,j}^0$  and  $v_{i,j}^0$  are initialized, accordingly, using the uniform flow initial conditions (3.86) and (3.87). The initial values of  $F_{\Omega_2,i,j}^0$  are calculated from the assumption that the free surface is undisturbed at the initial time. The initial values of  $V_{i,j}^0$  and  $A_{i,j}^0$  are calculated from the geometry of the body.

The *time iteration* involves the following steps. First, the free surface is advected with the local velocity field  $\bar{u}^n = (u_{i,j}^n, v_{i,j}^n, 0)$  and the new values of  $F_{\Omega_2,i,j}^{n+1}$  are calculated. The fluid-body interface is advected based on the prescribed motion of the body. Second, the fluid and fluid-body interfaces are reconstructed from the values of  $F_{\Omega_2,i,j}^{n+1}$ . The values of  $F_{\Omega_2,i,j}^{n+1}$  are used to label pressure cells and velocity knots. The geometry labeling is used to build a system of linear equations of the form  $Ax = b$ , where  $A = (a_{i,j})$  is the matrix of this linear system,  $b$  is the vector of free terms and  $x$  is the vector of unknowns. Finally, the new values of  $u_{i,j}^{n+1}$ ,  $v_{i,j}^{n+1}$  and  $p_{i,j}^{n+1}$  are calculated by iterative solution of the system of linear equations. This is done by making use of the Trilinos numerical solver library [Sala *et al.* (2004)]. At each time iteration, a preconditioned linear system  $PAx = Pb$  is solved using the generalized minimal residual method, where  $P$  is an incomplete  $LU$  preconditioner with a threshold. The threshold parameter is chosen so as to minimize the amount of memory needed to store the preconditioner and at the same time to maximize the rate of convergence of the iterative solver. The convergence criteria is  $\|PAx - Pb\| \leq 10^{-6}$ .

Figure 3.18 shows the structure of the matrix of the linear system,  $A$ . The matrix

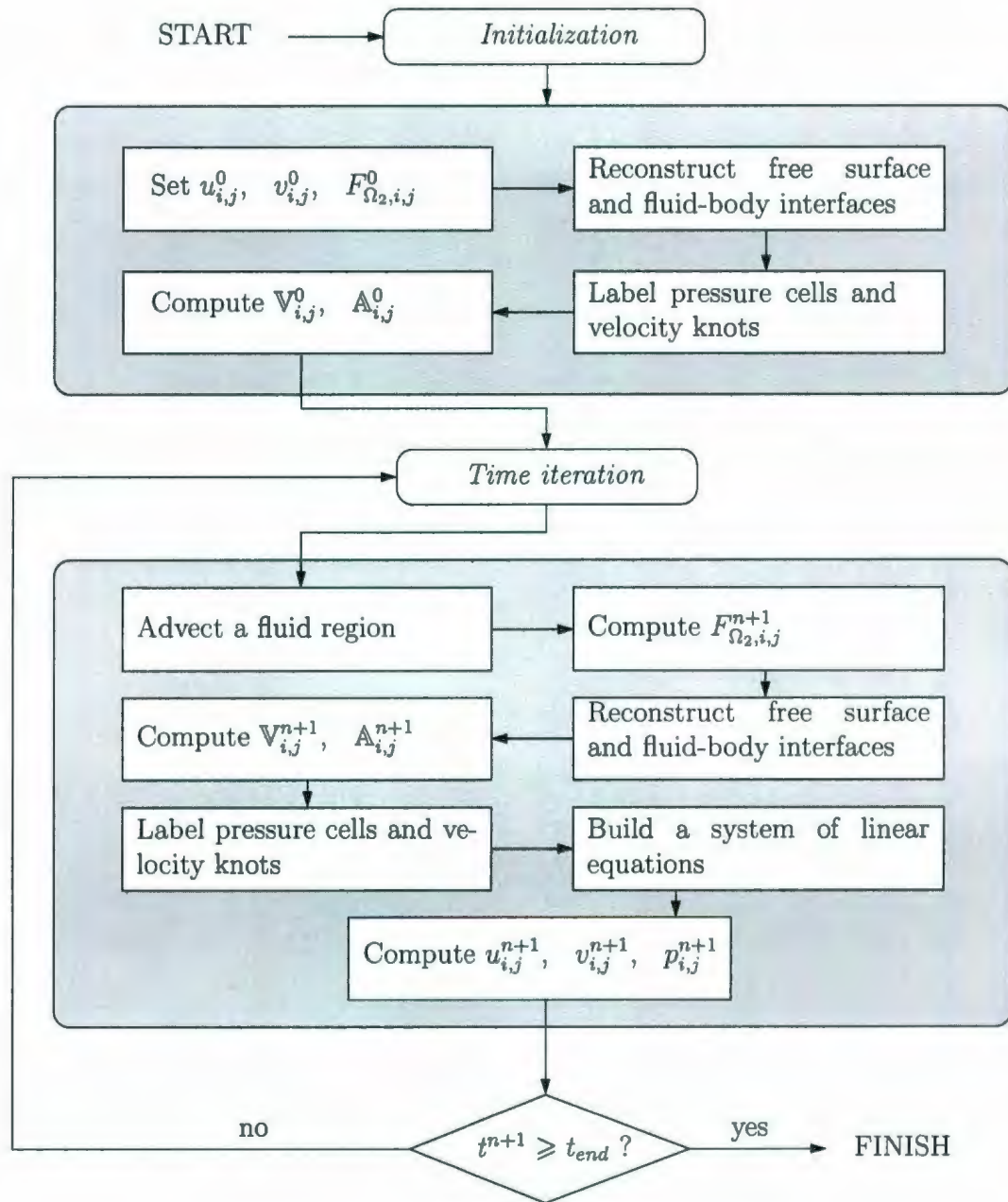


Figure 3.17: Numerical simulation flowchart.

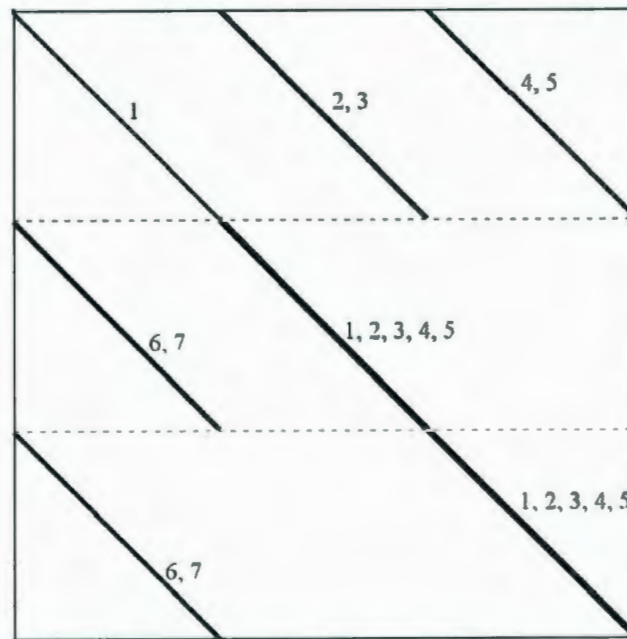


Figure 3.18: The structure of the matrix of the linear system,  $A$ .

$A$  is a sparse matrix with a size  $3 \times N \times M$ , where  $N$  and  $M$  denote the number of grid knots in the  $x$ - and  $y$ -directions, respectively. The structure of the matrix  $A$  can be divided into three horizontal blocks as shown by the dashed lines in Figure 3.18. The upper block is built of the discrete continuity equations added for the pressure knots,  $p_{i,j}$ . It is noted that the pressure is not involved in the continuity equation and thus the part of the diagonal of matrix  $A$  lying in the upper block (line "1") has zero elements. On the other hand, the nonzero elements on the line "1" correspond to the pressure knots which are located either in the cylinder or at the computational domain boundary. The four lines from the right hand side of the line "1" in the upper block correspond to the  $u_{i,j}$  (line "2"),  $u_{i+1,j}$  (line "3"),  $v_{i,j}$  (line "4") and  $v_{i,j+1}$  (line "5") velocities which are involved in the discrete continuity equations. The middle and lower blocks of the matrix  $A$  correspond to  $u_{i,j}$  and  $v_{i,j}$  velocities, respectively. These

blocks are built of the discrete momentum equations added for  $u_{i,j}$  and  $v_{i,j}$  knots, respectively. In the middle block, the  $u_{i,j}$  knots constitute the part of the diagonal of matrix  $A$  which belongs to this block (line "1"). The four lines from the left and right hand sides of the diagonal correspond to the four neighbour velocities,  $u_{i-1,j}$  (line "2"),  $u_{i+1,j}$  (line "3"),  $u_{i,j-1}$  (line "4") and  $u_{i,j+1}$  (line "5"), which are involved in the discrete momentum equations for the knots  $u_{i,j}$ . Two more lines from the left hand side of the diagonal correspond to the pressure knots,  $p_{i-1,j}$  (line "6") and  $p_{i,j}$  (line "7"), which are involved in the discrete momentum equations for the knots  $u_{i,j}$ . Similarly, in the lower block of the matrix  $A$ , the diagonal elements are  $v_{i,j}$  (line "1"). The four lines from the left and right hand sides of the diagonal correspond to the four neighbour velocities,  $v_{i-1,j}$  (line "2"),  $v_{i+1,j}$  (line "3"),  $v_{i,j-1}$  (line "4") and  $v_{i,j+1}$  (line "5"), which are involved in the discrete momentum equations for the knots  $v_{i,j}$ . Two more lines from the left hand side of the diagonal correspond to the pressure knots,  $p_{i,j-1}$  (line "6") and  $p_{i,j}$  (line "7"), which are involved in the discrete momentum equations for the knots  $v_{i,j}$ .

## 4. Numerical algorithm validation

In this chapter, the ability of the present numerical model to approximate free surface flows with moving bluff bodies and other relevant viscous flows is discussed. Specifically, the test problems are restricted to the two-dimensional, unsteady, laminar flow of a viscous incompressible fluid around circular cylinders. The numerical algorithm is first tested to determine the accuracy of the spatial and temporal discretizations. The numerical accuracy of the solution procedure also depends on the computational parameters such as the time step,  $\Delta t$ , and grid geometry parameters, i.e., the proximity of the computational domain boundaries and the near wake grid resolution. A series of numerical experiments is conducted to determine the optimal values of the computational and grid geometry parameters. The set of computational and grid geometry parameters are chosen so that the difference between present and previous computed results varies within about 3.0%.

In the subsections below, the validation of numerical algorithm is presented for uniform flow past (i) a stationary cylinder; (ii) a cylinder undergoing forced recti-linear oscillations (oscillations at an angle  $\eta = 60^\circ$  with respect to the free stream, transverse, in-line oscillations); (iii) a cylinder undergoing forced combined transverse and rotational, and combined in-line and rotational oscillations; (iv) a steadily rotating cylinder in the absence of a free surface. The validation of the present numerical model is also presented for uniform flow past (i) a stationary cylinder and (ii) a cylinder undergoing forced translational oscillations in the in-line direction in the presence of a free surface.

The present numerical simulations are performed on a cluster of four dual-core AMD Opteron 265 and twenty five dual-core AMD Opteron 2218 (IBM) computers located at the Department of Mathematics and Statistics, Memorial University of Newfoundland. Depending on the time step values and the time at which the calculations are terminated, it requires 120 to 240 hours to run the numerical code using the grid system  $370 \times 240$  for the flow parameter ranges  $100 \leq R \leq 10^3$ ,  $0.13 \leq A \leq 0.5$ ,  $0.5 \leq f/f_0 \leq 4.0$ . Hence, to calculate the behaviour of the flow for large values of the time up to  $t = 120$  (when the time step  $\Delta t = 0.01$ , grid system  $370 \times 240$ ) requires about 240 hours.

## 4.1 Spatial and temporal accuracy tests

Spatial and temporal accuracies of numerical method are typically checked by comparing the numerical solution to analytical one. Since exact analytical solutions to

| Parameter         | Grid cells per cylinder diameter |          |          | $\Delta t$ |          |          |
|-------------------|----------------------------------|----------|----------|------------|----------|----------|
|                   | 40                               | 60       | 90       | 0.004      | 0.002    | 0.001    |
| $\ \bar{p} - p\ $ | 0.002677                         | 0.001188 | 0.000538 | 0.000491   | 0.000243 | 0.000122 |
| $\ \bar{u} - u\ $ | 0.021027                         | 0.011165 | 0.005635 | 0.000575   | 0.000291 | 0.000147 |
| $\ \bar{v} - v\ $ | 0.017875                         | 0.008519 | 0.003980 | 0.000597   | 0.000295 | 0.000147 |

Table 4.1:  $L^2$  norm of the relative errors of the pressure,  $p$ , and velocity components,  $u$ ,  $v$ , as the time step and the number of grid cells per cylinder diameter vary for the stationary cylinder case in the absence of a free surface at  $R = 10^3$  when  $t = 0.1$ .

the continuity and Navier-Stokes equations of unsteady flow past a circular cylinder are not available, the fully converged results obtained by the finest grid possible are used as the “exact” solutions [see, for example, Anderson and Reider (1996)].

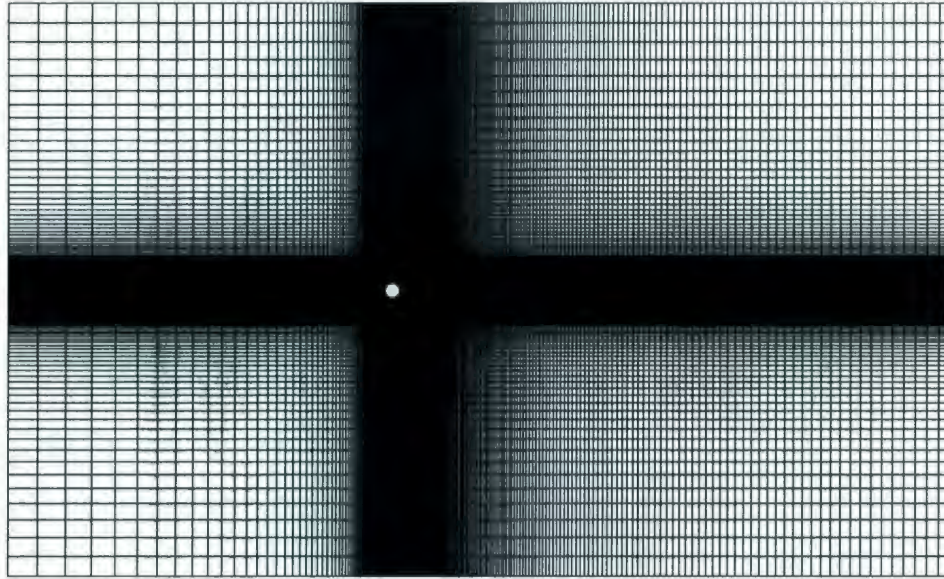


Figure 4.1: An example of the computational grid (pressure cells) with  $278 \times 178$  elements.

In this thesis, the spatial and temporal accuracies of the method are evaluated by solving the test problem of an initial flow past a stationary cylinder in the absence of a free surface. The Reynolds number of  $R = 10^3$  is chosen for the accuracy tests. This Reynolds number is high enough to present the flow structure in detail, yet still low enough to allow for full resolution on fine grids. The relative errors in the predicted quantities are computed at  $t = 0.1$  using the discrete  $L^2$  norm defined as

$$\|\bar{\xi} - \xi\| = \Delta h \left( \sum_{i,j} (\bar{\xi}_{i,j} - \xi_{i,j})^2 \right)^{1/2}, \quad (4.1)$$

where  $\bar{\xi}$  is the analytical solution,  $\xi$  is the computed quantity and  $\Delta h$  is the uniform

spatial grid step. Since exact analytical solution to this problem is not available, the present numerical predictions obtained with the grid system of 120 cells per cylinder diameter are used for full resolution. Three uniform grid systems  $90 \times 90$ ,  $60 \times 60$  and  $40 \times 40$  are used for the spatial and temporal accuracy tests. The uniform spatial grid step values are  $\Delta h = 1/90, 1/60, 1/40$ , respectively.

Table 4.1 shows the calculated spatial and temporal relative errors of the pressure,  $p$ , and velocity components,  $u$ ,  $v$ , at  $t = 0.1$  as the near wake grid resolution and the time step vary. The results indicate that the present numerical algorithm has an accuracy of second-order in space and of first-order in time, as expected.

## 4.2 Choice of the computational parameters

The numerical calculations are carried out using an exponential staggered Cartesian grid as described in Gubanov (2006). The grid system  $20 \times 30 \times 30$  with  $278 \times 178$  elements is illustrated in Figure 4.1. In this figure, only pressure computational cells are shown. In the work by Gubanov (2006), the exponential distribution of grid knots is defined as follows. Let  $N$  denote the number of knots. The exponential distribution of  $N$  knots,  $\{x_i\}_{i=1}^N$ , in the interval  $[x_a, x_b]$  can then be defined as

$$x_i = x_a + (x_b - x_a) \frac{e^{a\varsigma_i} - 1}{e^a - 1}, \quad \varsigma_i = \frac{i - 1}{N - 1}, \quad i = 1, \dots, N, \quad (4.2)$$

where  $\varsigma_i$  is the uniform distribution of  $N$  knots in the interval  $[0, 1]$ . The exponential grid parameter,  $a$ , is computed numerically by finding the root of the function

$$f(a) = \Delta h - (x_b - x_a) \frac{e^{a/(N-1)} - 1}{e^a - 1}. \quad (4.3)$$

This is done by making use of Brent's root finding algorithm [Brent (1973)]. It is noted that  $a$  is chosen so that the first grid step of the exponential grid in the grids overlap region equals to the uniform grid step,  $\Delta h$ .

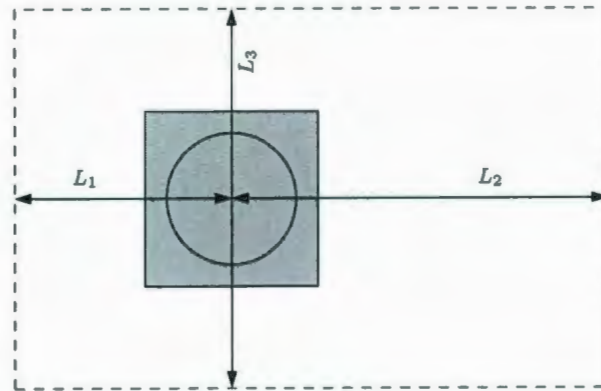


Figure 4.2: Grid geometry parameters. The shaded region is the uniform grid region.

The computational domain geometry is defined with respect to the *mean* position of the cylinder. In the vicinity of the mean cylinder position, the grid has fine resolution and is uniform. Outside of the uniform grid region, the grid expands exponentially towards the four boundaries of the computational domain. The grid geometry parameters are illustrated in Figure 4.2, where  $L_1$ ,  $L_2$ ,  $L_3$  define the locations of the computational domain boundaries with respect to the mean position of the cylinder. In this figure, the shaded region is the uniform grid region.

**Computational domain size.** A number of computational domain sizes are tested to estimate the values of  $L_1$ ,  $L_2$ ,  $L_3$  sufficient for the full development of the flow field. The domain size tests are carried out for uniform flow past a stationary cylinder in the (i) absence of a free surface at  $R = 100$  and (ii) presence of a free surface at  $R = 200$ :  $Fr = 0.3$ ,  $h = 0.55$ .

| Parameter       | $L_1$ |       |       | $L_2$ |       |       | $L_3$ |       |       |
|-----------------|-------|-------|-------|-------|-------|-------|-------|-------|-------|
|                 | 10    | 15    | 20    | 20    | 30    | 40    | 20    | 30    | 40    |
| $f_0$           | 0.165 | 0.165 | 0.164 | 0.164 | 0.165 | 0.165 | 0.168 | 0.166 | 0.165 |
| $C_{L,max}$     | 0.330 | 0.323 | 0.320 | 0.260 | 0.328 | 0.330 | 0.333 | 0.330 | 0.328 |
| $C_{D,max}$     | 1.351 | 1.334 | 1.327 | 1.331 | 1.350 | 1.351 | 1.361 | 1.352 | 1.350 |
| $\widehat{C}_D$ | 1.341 | 1.324 | 1.317 | 1.322 | 1.339 | 1.341 | 1.351 | 1.343 | 1.339 |

Table 4.2: The effect of the computational domain size on the maximum drag and lift coefficients,  $C_{D,max}$  and  $C_{L,max}$ ; the mean drag coefficient,  $\widehat{C}_D$ ; the natural vortex shedding frequency,  $f_0$ , for the case of uniform flow past a stationary cylinder in the absence of a free surface at  $R = 100$ .

Table 4.2 shows the comparisons of the predicted maximum drag and lift coefficients,  $C_{D,max}$  and  $C_{L,max}$ ; the mean drag coefficient,  $\widehat{C}_D$ ; the natural vortex shedding frequency,  $f_0$ , for the case of uniform flow past a stationary cylinder in the absence of a free surface at the Reynolds number of  $R = 100$ . This table indicates that the numerical grid with  $L_1 = 10$ ,  $L_2 = 30$ ,  $L_3 = 30$  predicts the computed quantities with the maximum error of order less than 1.8% when compared to the reference grid with the computational domain size  $20 \times 40 \times 40$ . This level of accuracy is considered to be acceptable for the present investigations of uniform flow past the cylinder in the absence of a free surface.

The computational domain size plays a key role for the accurate numerical simulation of unsteady flow when free surface effects are included. The numerical experiments indicate that the restricted computational domain may lead to an artificial alteration in the height of the free surface. This observation agrees with the one reported in

| Parameter    | $L_1$ |       |       | $L_2$ |       |       | $L_3$ |       |       |
|--------------|-------|-------|-------|-------|-------|-------|-------|-------|-------|
|              | 15    | 20    | 30    | 20    | 30    | 40    | 30    | 40    | 60    |
| $f _{f_s}$   | 0.198 | 0.200 | 0.203 | 0.196 | 0.200 | 0.200 | 0.205 | 0.200 | 0.200 |
| $C_{L,rms}$  | 0.695 | 0.716 | 0.721 | 0.697 | 0.710 | 0.716 | 0.724 | 0.714 | 0.710 |
| $C_{D,rms}$  | 1.576 | 1.594 | 1.630 | 1.562 | 1.595 | 1.594 | 1.632 | 1.608 | 1.595 |
| $h _{L,max}$ | 1.048 | 1.047 | 1.043 | 1.047 | 1.041 | 1.036 | 1.041 | 1.043 | 1.060 |
| $h _{L,min}$ | 0.948 | 0.897 | 0.874 | 0.897 | 0.879 | 0.879 | 0.875 | 0.884 | 0.947 |

Table 4.3: The effect of the computational domain size on the maximum and minimum local heights of the free surface,  $h|_{L,max}$  and  $h|_{L,min}$ ; the RMS value of the lift coefficient,  $C_{L,rms}$ ; the RMS value of the drag coefficient,  $C_{D,rms}$ ; the natural vortex shedding frequency,  $f|_{f_s}$ , for the case of uniform flow past a stationary cylinder in the presence of a free surface at  $R = 200$ :  $Fr = 0.3$ ,  $h = 0.55$ .

the work by Reichl (2001). One of the reasons is that when the free surface wave reaches inflow boundary, it should naturally propagate through this boundary. On the other hand, the inflow boundary conditions (2.45) prohibit the propagation of the free surface wave through the inflow boundary. This results in an artificial elevation of the height of the fluid in  $\Omega_2$  at the inflow boundary and then, over a sufficient time interval, in the whole computational domain. The artificial changes in the height of the free surface affect the value of the lift force acting on the surface of the cylinder since the calculation of the lift force involves subtracting the buoyancy force. In order to ensure that the chosen values of  $L_1$ ,  $L_2$ ,  $L_3$  are sufficient to predict free surface flow quantities accurately, further tests are conducted for uniform flow past a stationary cylinder in the presence of a free surface at  $R = 200$ :  $Fr = 0.3$ ,  $h = 0.55$ .

The flow is simulated up to  $t = 120$  and is quasi-periodic over this interval of time. Therefore, the root mean square (RMS) lift coefficient,  $C_{L,rms}$ , and the RMS drag coefficient,  $C_{D,rms}$ , are used to measure the magnitude of variations in the lift and the drag coefficients. Table 4.3 shows the effect of the computational domain size on the maximum and minimum local heights of the free surface,  $h|_{L,max}$  and  $h|_{L,min}$ ; the RMS value of the lift coefficient,  $C_{L,rms}$ ; the RMS value of the drag coefficient,  $C_{D,rms}$ ; the natural vortex shedding frequency,  $f|_{fs}$ , for the case of uniform flow past a stationary cylinder in the presence of a free surface at  $R = 200$ :  $Fr = 0.3$ ,  $h = 0.55$ . The maximum and minimum local heights of the free surface are measured at the time when the lift coefficient reaches its maximum. Table 4.3 indicates that the grid with  $L_1 = 20$ ,  $L_2 = 30$ ,  $L_3 = 40$  yields results which are accurate to maximum 3% when compared to the reference grid with the computational domain size  $30 \times 40 \times 60$ . This level of accuracy is assumed to be sufficient for the present study of uniform flow past a cylinder in the presence of a free surface.

**Grid resolution.** The accuracy of calculation of the surface lift and drag forces is governed by the number of cells per cylinder diameter, i.e., by the near wake grid resolution. To examine the effect of the near wake grid resolution, three different grids with 90, 60, 40 cells per cylinder diameter, having the same computational domain size, are used. The time step value,  $\Delta t = 0.005$ , is chosen for the grid resolution tests. The grid resolution tests are carried out for uniform flow past a stationary cylinder in the (i) absence of a free surface at  $R = 100$  and (ii) presence of a free surface at  $R = 200$ :  $Fr = 0.3$ ,  $h = 0.7$ .

| Parameter       | Grid cells per diameter |       |       | $\Delta t$ |        |       |
|-----------------|-------------------------|-------|-------|------------|--------|-------|
|                 | 40                      | 60    | 90    | 0.01       | 0.0075 | 0.005 |
| Value           | 40                      | 60    | 90    | 0.01       | 0.0075 | 0.005 |
| $f_0$           | 0.168                   | 0.168 | 0.168 | 0.166      | 0.167  | 0.168 |
| $C_{L,max}$     | 0.336                   | 0.335 | 0.335 | 0.301      | 0.333  | 0.335 |
| $C_{D,max}$     | 1.376                   | 1.363 | 1.362 | 1.352      | 1.360  | 1.363 |
| $\widehat{C}_D$ | 1.367                   | 1.354 | 1.353 | 1.343      | 1.351  | 1.354 |

Table 4.4: The effects of the near wake grid resolution and the time step,  $\Delta t$ , on the maximum drag and lift coefficients,  $C_{D,max}$  and  $C_{L,max}$ ; the mean drag coefficient,  $\widehat{C}_D$ ; the natural vortex shedding frequency,  $f_0$ , for the case of uniform flow past a stationary cylinder in the absence of a free surface at  $R = 100$ .

Table 4.4 shows the comparison between the three grids with different spatial resolutions for the case of uniform flow past a stationary cylinder in the absence of a free surface at  $R = 100$ . This table indicates that increasing the number of cells per cylinder diameter from 60 to 90 has a negligible effect on the computed quantities. The grid resolution of 40 cells per diameter gives the maximum error of order 1% in the computed quantities when compared to those with the grid resolution of 90 cells per diameter. The grid resolution of 60 cells per diameter is chosen for the current investigation of uniform flow past the cylinder in the absence of a free surface to capture the physical development of the flow in the boundary layer region accurately at large values of the Reynolds numbers.

The comparisons of the predicted RMS values of the lift and drag coefficients,  $C_{L,rms}$  and  $C_{D,rms}$ ; the natural vortex shedding frequency,  $f|_{fs}$ , for the case of uniform flow past a stationary cylinder in the presence of a free surface at  $R = 200$ :  $Fr = 0.3$ ,

| Parameter   | Grid cells per diameter |       |       | $\Delta t$ |        |       |
|-------------|-------------------------|-------|-------|------------|--------|-------|
|             | 40                      | 60    | 90    | 0.01       | 0.0075 | 0.005 |
| $f _{f_s}$  | 0.210                   | 0.210 | 0.211 | 0.206      | 0.208  | 0.210 |
| $C_{L,rms}$ | 0.693                   | 0.707 | 0.723 | 0.711      | 0.711  | 0.707 |
| $C_{D,rms}$ | 1.538                   | 1.564 | 1.580 | 0.564      | 0.564  | 1.564 |

Table 4.5: The effects of the near wake grid resolution and the time step,  $\Delta t$ , on the RMS value of the lift coefficient,  $C_{L,rms}$ ; the RMS value of the drag coefficient,  $C_{D,rms}$ ; the natural vortex shedding frequency,  $f|_{f_s}$ , for the case of uniform flow past a stationary cylinder in the presence of a free surface at  $R = 200$ :  $Fr = 0.3$ ,  $h = 0.7$ .

$h = 0.7$  as number of grid cells per cylinder diameter varies are shown in Table 4.5. This table indicates that the grids with grid resolutions of 40 and 60 cells per diameter give the maximum errors of order 4.2% and 2.2%, respectively, in the computed quantities when compared to those with the grid resolution of 90 cells per diameter. Thus, the grid resolution of 60 cells per diameter is chosen for the current investigation of uniform flow past the cylinder in the presence of a free surface.

**Time step.** The sensitivity of the accuracy of computations to the value of the time step is tested using the same grid for three different values of the time steps,  $\Delta t = 0.005, 0.0075, 0.01$ . The grid resolution tests (the grid resolution is 60 cells per cylinder diameter) are carried out for uniform flow past a stationary cylinder in the (i) absence of a free surface at  $R = 100$  and (ii) presence of a free surface at  $R = 200$ :  $Fr = 0.3$ ,  $h = 0.7$ .

Table 4.4 shows the comparisons between the results obtained with three different

time steps for the case of uniform flow past a stationary cylinder in the absence of a free surface at  $R = 100$ . It is seen that as the time step increases from  $\Delta t = 0.0075$  to  $\Delta t = 0.01$ , the order of maximum error in the computed quantities increases from 0.6% to 1.6%, respectively, when compared to the results obtained with the time step  $\Delta t = 0.005$ .

The effect of the time step on the  $C_{L,rms}$ ,  $C_{D,rms}$  and  $f|_{fs}$ , for the case of uniform flow past a stationary cylinder in the presence of a free surface at  $R = 200$ :  $Fr = 0.3$ ,  $h = 0.7$  is shown in Table 4.5. This table indicates that increasing the time step from  $\Delta t = 0.0075$  to  $\Delta t = 0.01$  has a negligible effect (the maximum error is 0.6%) on the computed quantities when compared to the results obtained with the time step  $\Delta t = 0.005$ . Thus, the time step  $\Delta t = 0.01$  seems to be a good compromise between the accuracy of the calculations and the computational time required to perform the calculations. This time step value is used in the present thesis.

### 4.3 Uniform flow past a stationary cylinder in the absence of a free surface

The accuracy of the numerical algorithm is first checked by carrying out computations for the initial development of uniform flow past a stationary cylinder case at the Reynolds numbers of  $R = 500$  and  $10^3$ . The Reynolds number values chosen allow comparison with the numerical results of Li *et al.* (2004), Ploumhans and Winckelmans (2000) and Anderson and Reider (1996). The development of the drag coeffi-

cient,  $C_D$ , at  $R = 500$  is compared with the numerical results of Li *et al.* (2004) and Ploumhans and Winckelmans (2000) in Figure 4.3. A kinetic-theory-based lattice-Boltzmann method is utilized in the work of Li *et al.* (2004) while Ploumhans and Winckelmans (2000) used a vortex method based on the particle strength exchange scheme for diffusion. The predicted drag coefficient shown in Figure 4.3 is in excellent agreement with the numerical results of Ploumhans and Winckelmans (2000) and in good agreement with the numerical results of Li *et al.* (2004).

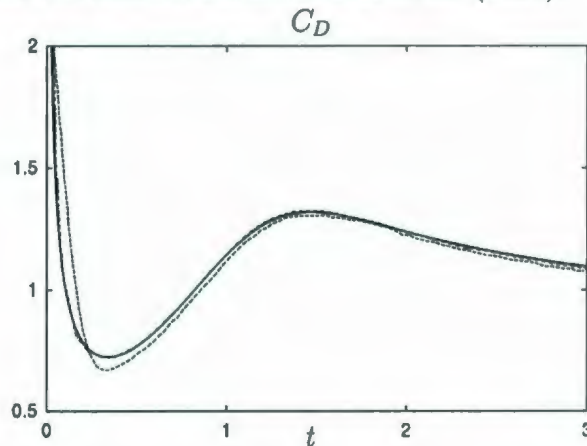


Figure 4.3: The time evolution of the drag coefficient,  $C_D$ , for the stationary cylinder case in the absence of a free surface at  $R = 500$ : numerical results of Li *et al.* (2004) (dashed) and Ploumhans and Winckelmans (2000) (dash-dot); present results (solid).

In Figures 4.4-4.6, the computed results of several initial properties such as the drag coefficient,  $C_D$ ; the evolution of the maximum vorticity,  $\zeta_{max}$ ; the surface pressure distribution,  $p_0$ ; the surface vorticity distribution,  $\zeta_0$ , and the equivorticity lines and the streamlines from the present numerical scheme are compared with the numerical results of Anderson and Reider (1996). In the work of Anderson and Reider (1996), the numerical model is based on the stream function/vorticity formulation of the

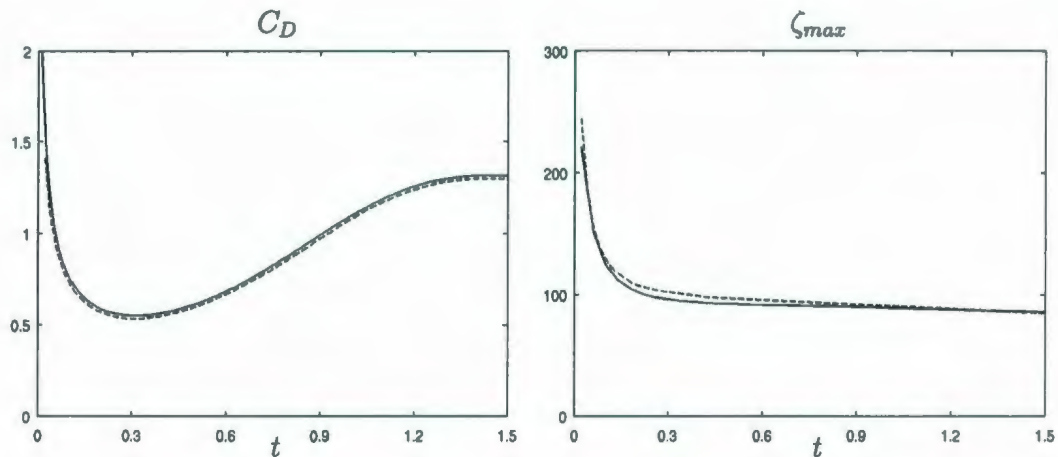


Figure 4.4: The time evolution of the drag coefficient,  $C_D$ , (left) and the maximum vorticity,  $\zeta_{max}$ , (right) for the stationary cylinder case in the absence of a free surface at  $R = 10^3$ : numerical results of Anderson and Reider (1996) (dashed); present results (solid).

continuity and Navier-Stokes equations which are computed based on an explicit finite difference method of second-order (or fourth-order) accuracy in space and of fourth-order accuracy in time. Their numerical approach differs from other finite difference implementations (when using the vorticity formulation of the continuity and Navier-Stokes equations) in their use of infinity boundary conditions for the stream function and their particular method for satisfying vorticity conditions. There are two main advantages in this approach. First, it allows one to easily obtain high accuracy in both the interior and boundary values of vorticity. Second, it allows one to implement time dependent conditions without any loss of time accuracy. In the present thesis, the primitive variables formulation of the governing equations is employed. The present computations have shown that the MatLab function `curl(x,y,u,v)` for computing the vorticity from the velocity field results in the same order of accuracy. In what follows,

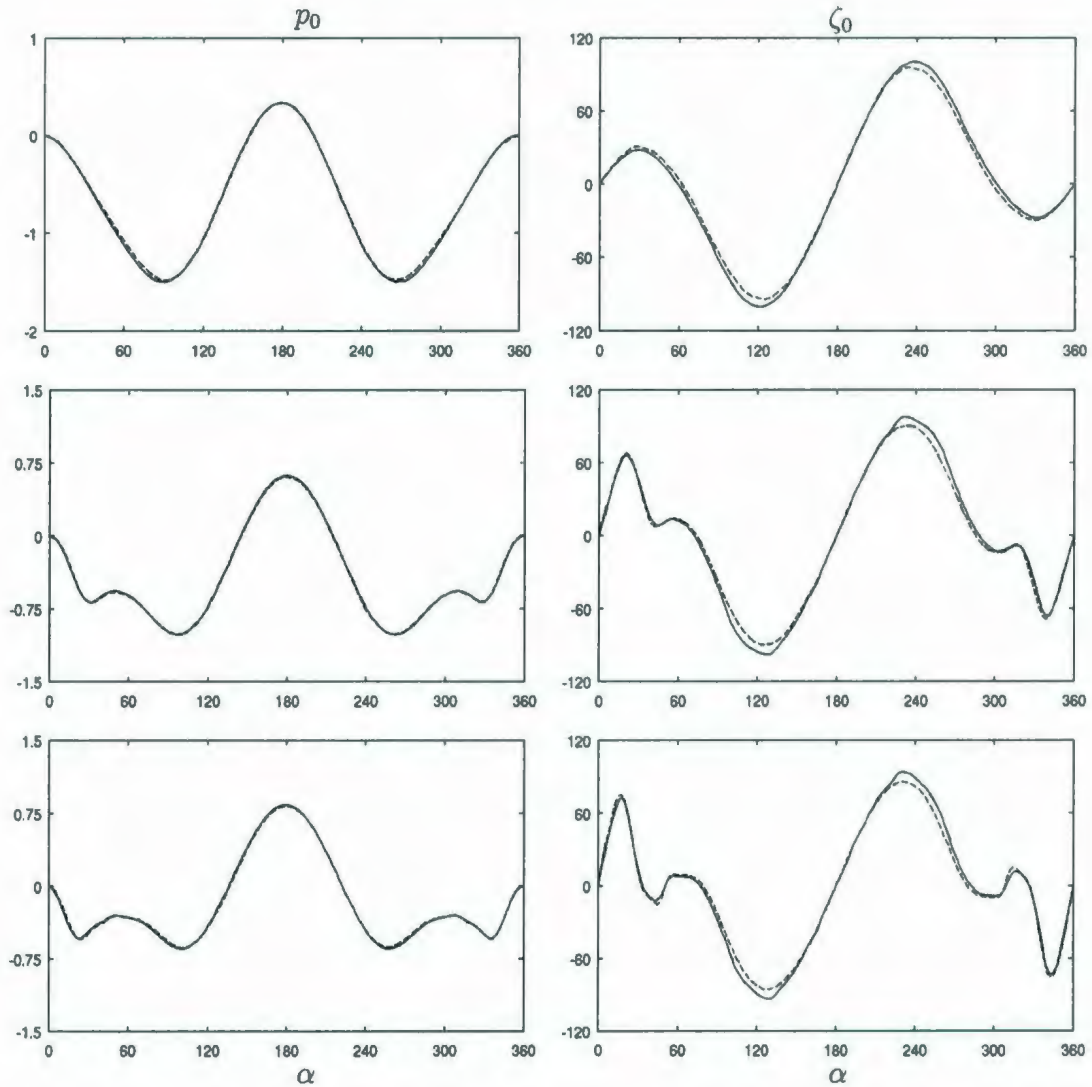


Figure 4.5: The surface pressure distribution,  $p_0$ , (left) and the surface vorticity distribution,  $\zeta_0$ , (right) for the stationary cylinder case in the absence of a free surface at  $R = 10^3$  (from top to bottom:  $t = 0.5, 1.0, 1.5$ ): numerical results of Anderson and Reider (1996) (dashed); present results (solid).

the vorticity,  $\zeta$ , is calculated by interpolating velocity components,  $u, v$ , into pressure knots and then taking the curl of the resulting vector field,  $\text{curl}(\mathbf{x}, y, u, v)$ , in MatLab.

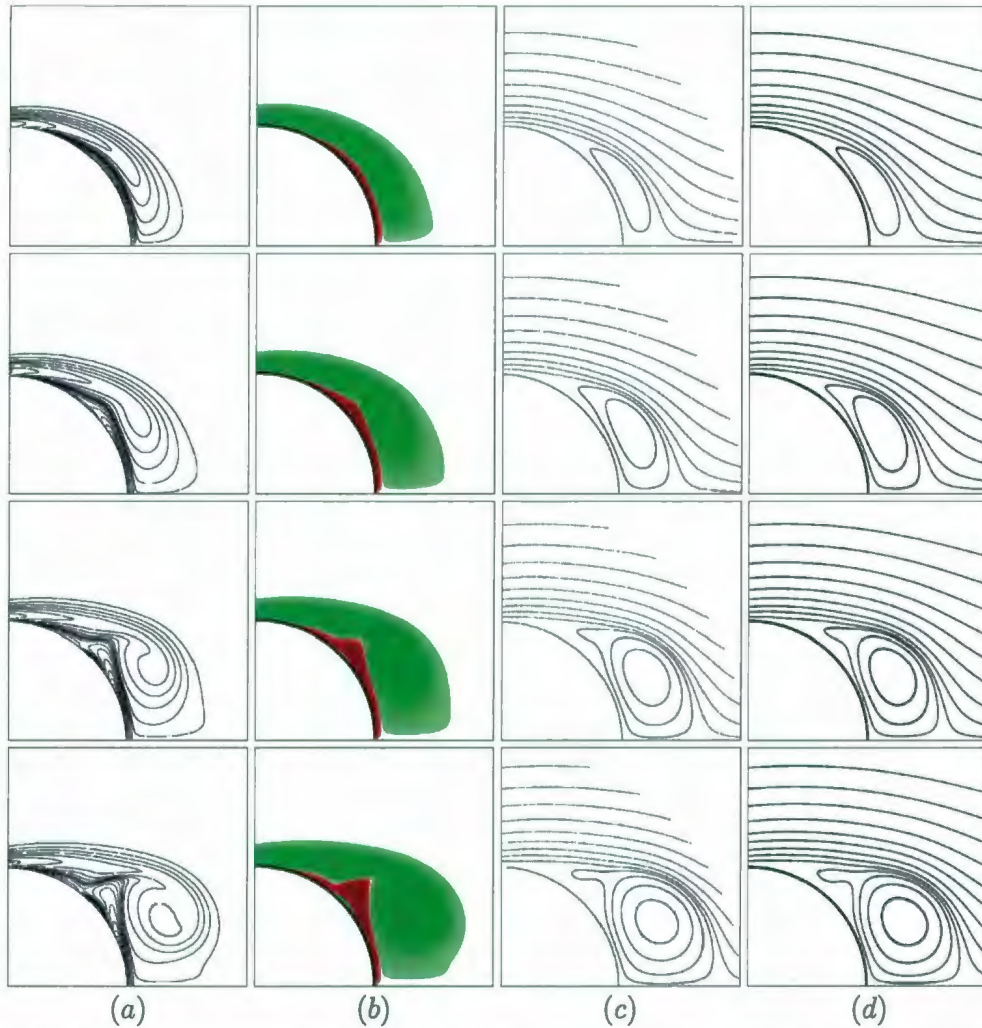


Figure 4.6: The equivorticity lines ((a), (b)) and the streamlines ((c), (d)) for the stationary cylinder case in the absence of a free surface at  $R = 10^3$  (from top to bottom:  $t = 0.75, 1.0, 1.25, 1.5$ ): ((a), (c)) numerical results of Anderson and Reider (1996); ((b), (d)) present results. Red colours correspond to positive vorticity (counterclockwise rotation) and green colours indicate negative vorticity (clockwise rotation). From top to bottom the values of the streamlines are: 0.683, 0.586, 0.471, 0.380, 0.280, 0.217, 0.144, 0.078, 0.008, -0.008; 0.748, 0.644, 0.538, 0.428, 0.320, 0.220, 0.112, 0.007, -0.007, -0.006; 0.633, 0.518, 0.374, 0.181, 0.109, 0.042, 0.007, 0.002, -0.080, -0.042, -0.007; 0.659, 0.556, 0.415, 0.315, 0.215, 0.148, 0.045, 0.007, -0.114, -0.074, -0.045, -0.005.

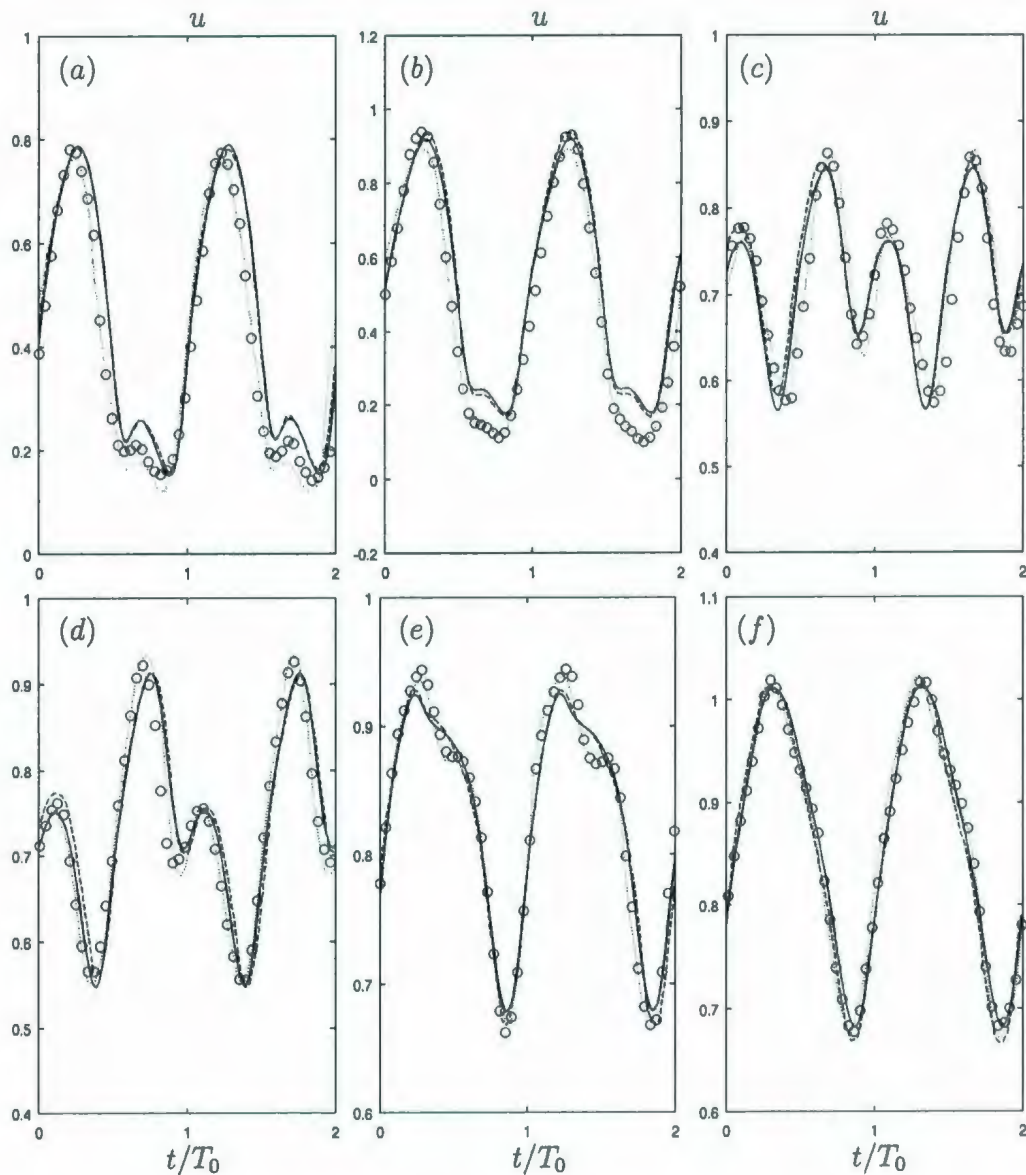


Figure 4.7: The time evolution of the  $u$ -velocity of the fluid over two periods of vortex shedding,  $t/T_0 = 2$ , for the stationary cylinder case in the absence of a free surface at  $R = 106$ : experimental results of Anagnostopoulos (1997) (circles); numerical results of Anagnostopoulos (1997) (dotted) and Al-Mdallal (2004) (dashed); present results (solid) at the locations: (a)  $(x, y) = (2.7, 0.32)$ , (b)  $(x, y) = (2.7, 0.43)$ , (c)  $(x, y) = (4.9, 0.17)$ , (d)  $(x, y) = (4.9, 0.33)$ , (e)  $(x, y) = (7.5, 0.5)$ , (f)  $(x, y) = (7.5, 0.75)$ .

Here,  $x$  and  $y$  are the spatial coordinates of the pressure knots in which vorticity is being computed. In Cartesian coordinates, the stream function,  $\psi$ , is defined by

$$u = \frac{\partial\psi}{\partial y}, \quad v = -\frac{\partial\psi}{\partial x}. \quad (4.4)$$

The stream function,  $\psi$ , is computed by integrating (4.4) in the computational domain. Nevertheless, Figures 4.4-4.6 show excellent agreement between the results.

The time evolution of the  $u$ -velocity of the fluid and the pressure distribution for uniform flow past a stationary cylinder at  $R = 106$  are compared with the numerical results of Al-Mdallal (2004) and the numerical and experimental results of Anagnostopoulos (1997). It is well known, if unaltered, any numerical method [see, for example, Braza *et al.* (1986)] produces symmetric vortices behind the cylinder for all the times, for the mathematical models used to describe these cases although the physical flows are asymmetric. This behaviour results from the fact that, at any instant, the total speed of the upper and lower parts of the cylinder (and thus the behaviour of the fluid in these regions) are exactly the same as a result of the symmetric boundary conditions imposed on the flow. However, physically realistic flows of this type are not symmetric and thus a velocity gradient must exist for the fluid on the cylinder surface. Taking this into account, an artificial perturbation in which a clockwise rotation of the circular cylinder is followed after a short period of time by a counterclockwise rotation can be imposed to break this perfect numerical symmetry [Al-Mdallal (2004), Justesen (1991), Braza *et al.* (1986)]. Following the work of Braza *et al.* (1986), the perturbation is implemented with the angular displacement given

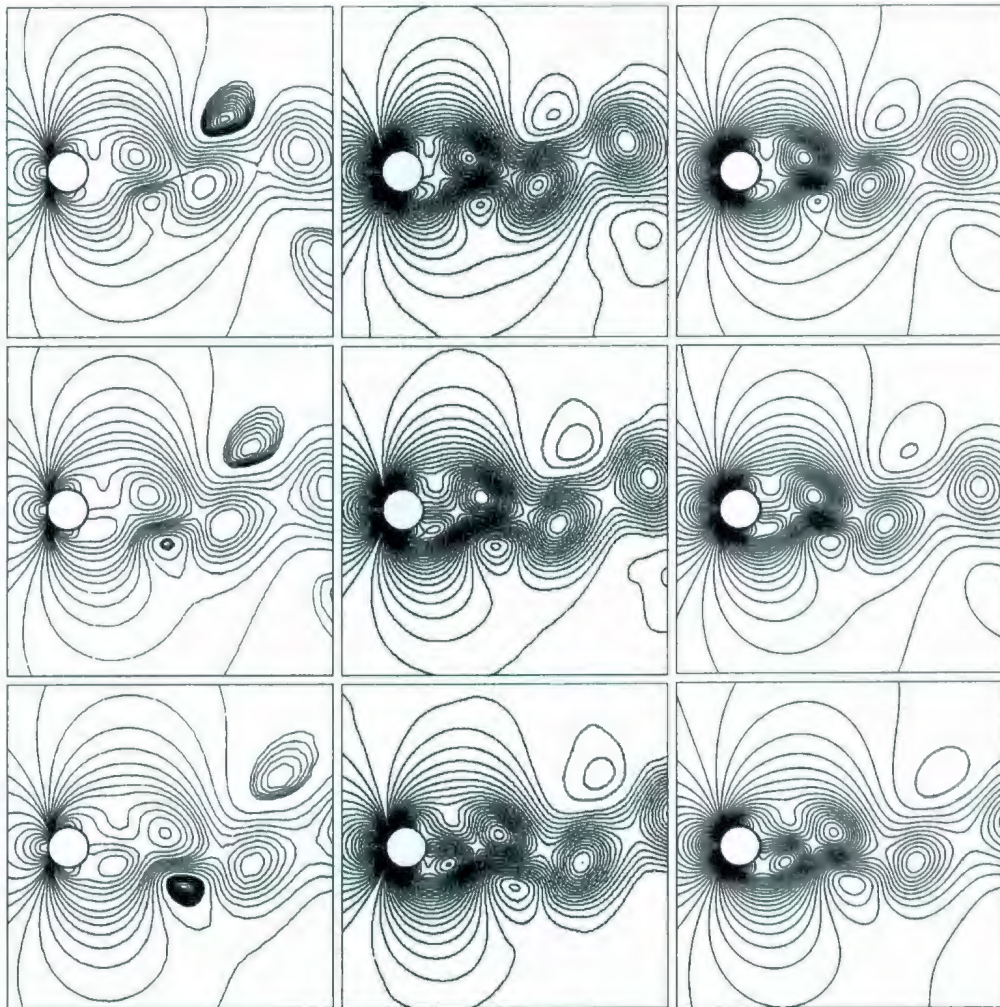


Figure 4.8: The pressure distribution in the near wake region for the stationary cylinder case in the absence of a free surface at  $R = 106$  (from top to bottom:  $t/T_0 = 0, 1/8, 1/12$  ( $T_0 = 5.9$ )): numerical results of Anagnostopoulos (1997) (left) and Al-Mdallal (2004) (middle); present results (right).

by

$$\alpha(t) = \begin{cases} 0.3, & 1.45 \leq t \leq 2.1, \\ -0.2, & 2.15 \leq t \leq 3.0, \\ 0, & \text{otherwise.} \end{cases} \quad (4.5)$$

In the works of Al-Mdallal (2004) and Anagnostopoulos (1997), the stream function/vorticity formulation of the continuity and Navier-Stokes equations is utilized. The Poisson equation is solved to calculate the pressure field. In the work by Al-Mdallal (2004), the method of solution is based on spectral finite difference approximations while Anagnostopoulos (1997) used the Galerkin finite volume method in his calculations. Figure 4.7 shows the comparison of the time evolution of  $u$ -velocity over the two periods of vortex shedding,  $t/T_0 = 2$ , where the predicted period of vortex shedding is  $T_0 = 5.9$ . The time,  $t/T_0 = 0$ , corresponds to the time when the zero lift coefficient appears in the time history of  $C_L$  over a shedding period. The time history of  $u$ -velocity of the fluid is depicted at six different locations in the near wake of the cylinder:  $(x, y) = (2.7, 0.32)$ ,  $(2.7, 0.43)$ ,  $(4.9, 0.17)$ ,  $(4.9, 0.33)$ ,  $(7.5, 0.5)$ ,  $(7.5, 0.75)$ . It is noted that in the experimental work by Anagnostopoulos (1997), the time history of  $u$ -velocity of the fluid is captured for slightly higher Reynolds number,  $R = 115$ , than  $R = 106$  which is used in his computations. This is due to the fact that in the numerical simulation the proximity of the domain boundaries induces the numerical diffusion. As a result, the effective Reynolds number becomes slightly higher than the theoretical one. The discrepancy between the present results and the results of Anagnostopoulos (1997) that appeared in the wake is smaller than that close to the cylinder. It is noted that the frequency of the velocity traces curves is exactly the same as the natural vortex shedding frequency,  $f_0$ .

| $R$             | Reference                       | $f_0$       | $\widehat{C}_D$ | $C_{L,max}$ |
|-----------------|---------------------------------|-------------|-----------------|-------------|
| 100             | Present                         | 0.168       | 0.335           | 1.354       |
|                 | Liu <i>et al.</i> (1998)        | 0.164       | 0.339           | 1.35        |
|                 | Ku (1995)                       | 0.1675      | 0.228           | 1.358       |
|                 | Wen and Lin (2001) <sup>†</sup> | 0.165-0.167 | -               | -           |
|                 | Henderson (1995) <sup>†</sup>   | -           | -               | -           |
| 200             | Present                         | 0.1981      | 1.3399          | 0.70        |
|                 | Poncet (2004)                   | 0.199       | 1.3389          | 0.70        |
|                 | Henderson (1997)                | 0.1972      | 1.3412          | -           |
|                 | De Palma <i>et al.</i> (2006)   | 0.19        | 1.34            | 0.68        |
|                 | Wen and Lin (2001) <sup>†</sup> | -           | 1.30            | -           |
| 300             | Present                         | 0.2100      | 1.3725          | 0.94        |
|                 | Poncet (2004)                   | 0.211       | 1.3820          | 0.96        |
|                 | Henderson (1997)                | 0.2113      | 1.3769          | -           |
|                 | Ye <i>et al.</i> (1999)         | 0.21        | 1.38            | -           |
| 400             | Present                         | 0.2195      | 1.4110          | 1.08        |
|                 | Poncet (2004)                   | 0.2228      | 1.4080          | 1.08        |
|                 | Henderson (1997)                | 0.2198      | 1.4142          | -           |
|                 | He <i>et al.</i> (2000)         | 0.221       | 1.423           | -           |
| 500             | Present                         | 0.2258      | 1.4400          | 1.20        |
|                 | Poncet (2004)                   | 0.230       | 1.4433          | 1.23        |
|                 | Henderson (1997)                | 0.2254      | 1.4449          | -           |
| 10 <sup>3</sup> | Present                         | 0.242       | 1.40            | 1.462       |
|                 | Poncet (2004)                   | 0.241       | 1.45            | 1.5264      |
|                 | Henderson (1997)                | 0.2372      | -               | -           |

Table 4.6: The comparison of the predicted natural vortex shedding frequency,  $f_0$ ; the maximum lift coefficient,  $C_{L,max}$ ; the mean drag coefficients,  $\widehat{C}_D$ , with the previous numerical and experimental(<sup>†</sup>) results.

The pressure distribution in the near wake of the stationary cylinder in the absence of a free surface at  $R = 106$  is shown in Figure 4.8. The snapshots are taken at the instants  $t/T_0 = 0, 1/8, 1/12$ . The predicted profiles of the  $u$ -velocity of the fluid and the pressure distribution in the near wake region shown in Figures 4.7 and

4.8, respectively, are in good agreement with the results of Al-Mdallal (2004) and Anagnostopoulos (1997).

The periodic properties of uniform flow past a cylinder can be clearly observed in time evolution of the surface hydrodynamic forces. A series of numerical experiments is conducted to ensure the accurate calculation of the lift and drag coefficients. The Kármán frequency,  $f_0$ , is calculated using the Fourier analysis of the lift coefficient,  $C_L$ . For the case of uniform flow past a stationary cylinder, the Fourier analysis yields the frequency spectra in which the dominant frequency is  $f_0$ . In Table 4.6, the predicted values of the maximum lift coefficient,  $C_{L,max}$ , the mean drag coefficient,  $\widehat{C}_D$ , and the predicted natural shedding frequency,  $f_0$ , are displayed at  $R = 100, 200, 300, 400, 500, 10^3$ . The predicted present results are in good agreement with previous numerical and experimental studies for the Reynolds number range  $100 \leq R \leq 10^3$ .

#### **4.4 Uniform flow past an oscillating cylinder in the absence of a free surface**

The initial flow simulations are conducted at  $R = 855$  for uniform flow past an oscillating circular cylinder in the absence of a free surface. Two types of forced oscillatory motion: (i) combined rotational and transverse oscillations, and (ii) combined rotational and in-line oscillations are considered. The imposed translational and rotational oscillatory motions of the cylinder are described as

$$x(t) = y(t) = -A \cos(2\pi ft), \quad \alpha(t) = -A_\alpha \cos(2\pi f_\alpha t), \quad (4.6)$$

respectively. The amplitude of the translational and rotational displacements,  $A$ , and  $A_\alpha$ , are set to 0.13 and  $30^\circ$ , respectively. The frequency of the translational oscilla-

tion is the same as for the rotational oscillation, i.e.,  $f = f_\alpha$ . In Figures 4.9-4.12, the computed results of several initial properties such as the surface pressure distribution,  $p_0$ ; the surface vorticity distribution,  $\zeta_0$ ; the drag and lift coefficients,  $C_D$  and  $C_L$ , are shown in which the present results are compared with the analytical and numerical results of Al-Mdallal (2004) for the frequency ratio  $f/f_0 = 1$  ( $f_0 = 0.194$ ). In Al-Mdallal's work, the near wake structure and fluid forces are generated by a circular cylinder under combined recti-linear and rotational oscillation placed in a steady uniform flow. The governing equations in stream function/vorticity formulation are solved using a finite difference scheme which utilizes global conditions of an integral character. A non-inertial coordinate transformation is used to conformally map the unbounded domain outside the cylinder to a rectangular domain which is discretized by a set of uniformly spaced grid points. Figures 4.9 and 4.10 show the initial time development of the surface vorticity and pressure distributions,  $\zeta_0$ , and  $p_0$ , respectively, for the case  $R = 855$ :  $A = 0.13$ ,  $A_\alpha = 30^\circ$ ,  $f/f_0 = 1$  when  $t = 0.05, 0.25, 0.5$ . The numerical and experimental results are in good agreement and excellent agreement between the numerical results is obtained at  $t = 0.5$ . The minor differences between the numerical results at  $t = 0.05$  and  $0.25$  might be due to the fact that uniform flow solution is used as the initial condition in the present study unlike in the work by Al-Mdallal (2004). The boundary-fitted grid is implemented and a spectral finite difference algorithm is used in Al-Mdallal's work. On the other hand, in this thesis a non-boundary-fitted grid system is implemented in the numerical solution scheme and then SINTEF multilevel  $B$ -spline approximation library is used to interpolate the values of vorticity and pressure to the points on the cylinder surface.

The initial time evolution of force coefficients is shown in Figures 4.11 and 4.12 for

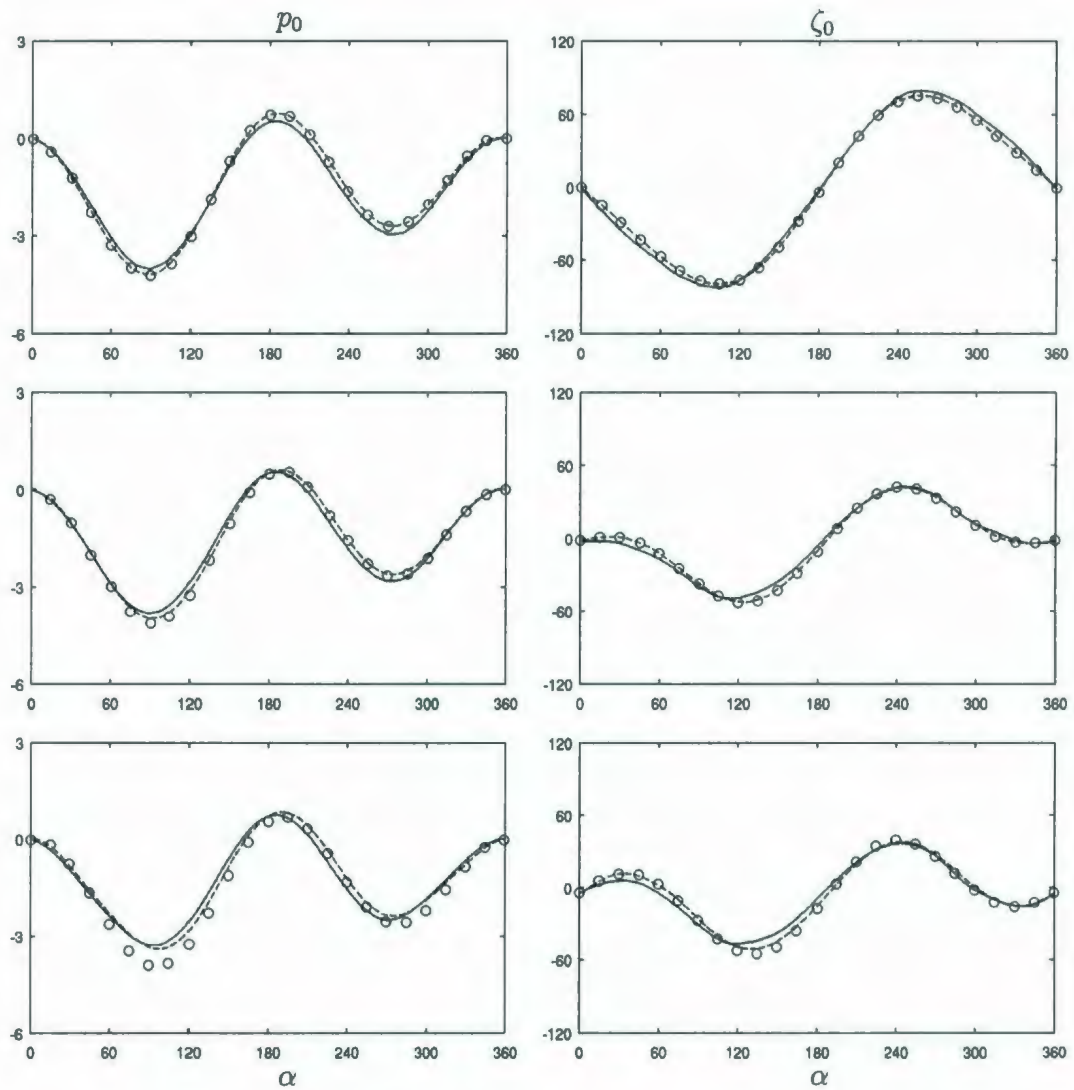


Figure 4.9: The surface pressure distribution,  $p_0$ , (left) and the surface vorticity distribution,  $\zeta_0$ , (right) for the combined rotational and transverse oscillation case in the absence of a free surface at  $R = 855$ :  $A = 0.13$ ,  $A_\alpha = 30^\circ$ ,  $f/f_0 = 1$  (from top to bottom:  $t = 0.05, 0.25, 0.5$ ): analytical results of Al-Mdallal (2004) (circles); numerical results of Al-Mdallal (2004) (dashed); present results (solid).

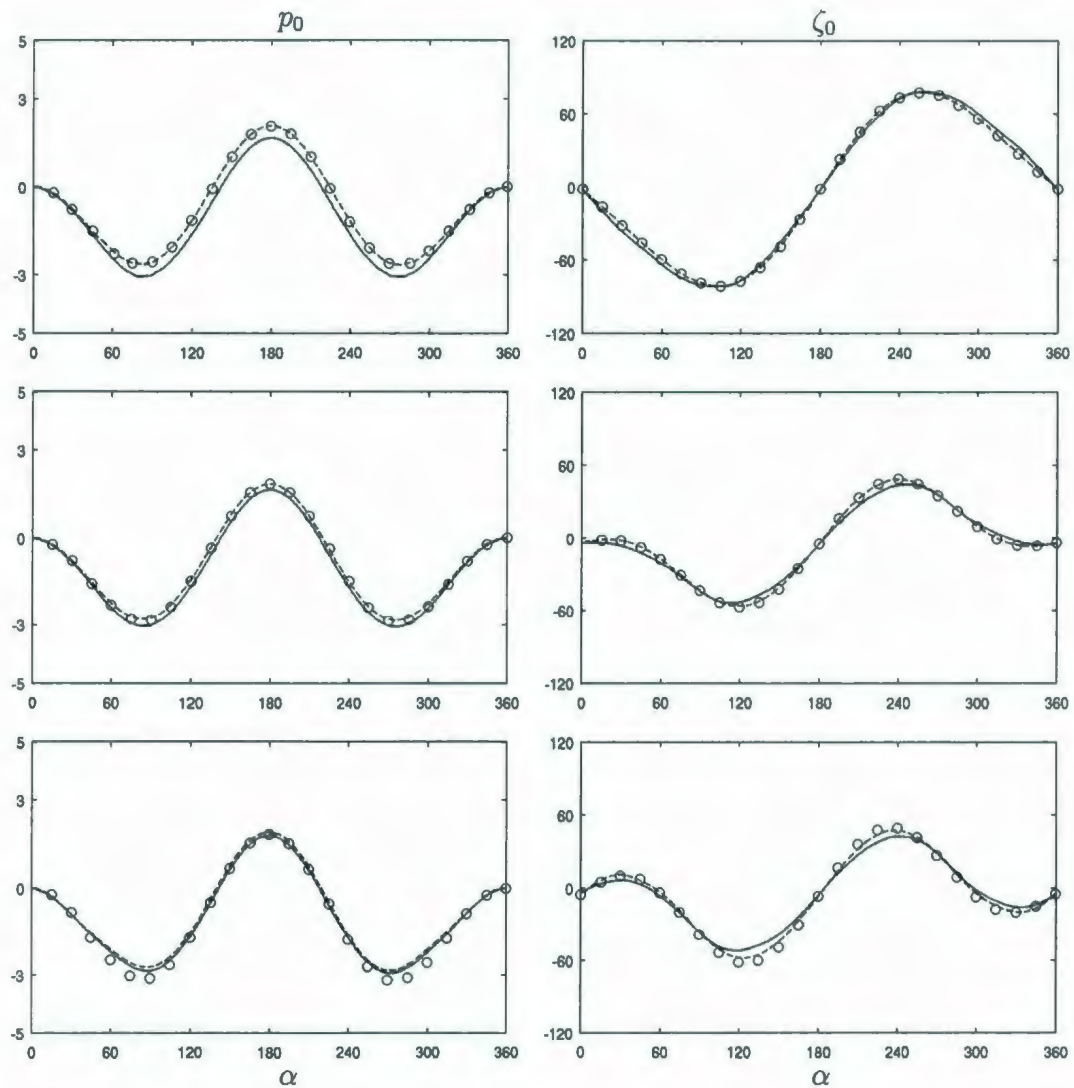


Figure 4.10: The surface pressure distribution,  $p_0$ , (left) and the surface vorticity distribution,  $\zeta_0$ , (right) for the combined rotational and in-line oscillation case in the absence of a free surface at  $R = 855$ :  $A = 0.13$ ,  $A_\alpha = 30^\circ$ ,  $f/f_0 = 1$  (from top to bottom:  $t = 0.05, 0.25, 0.5$ ): analytical results of Al-Mdallal (2004) (circles); numerical results of Al-Mdallal (2004) (dashed); present results (solid).

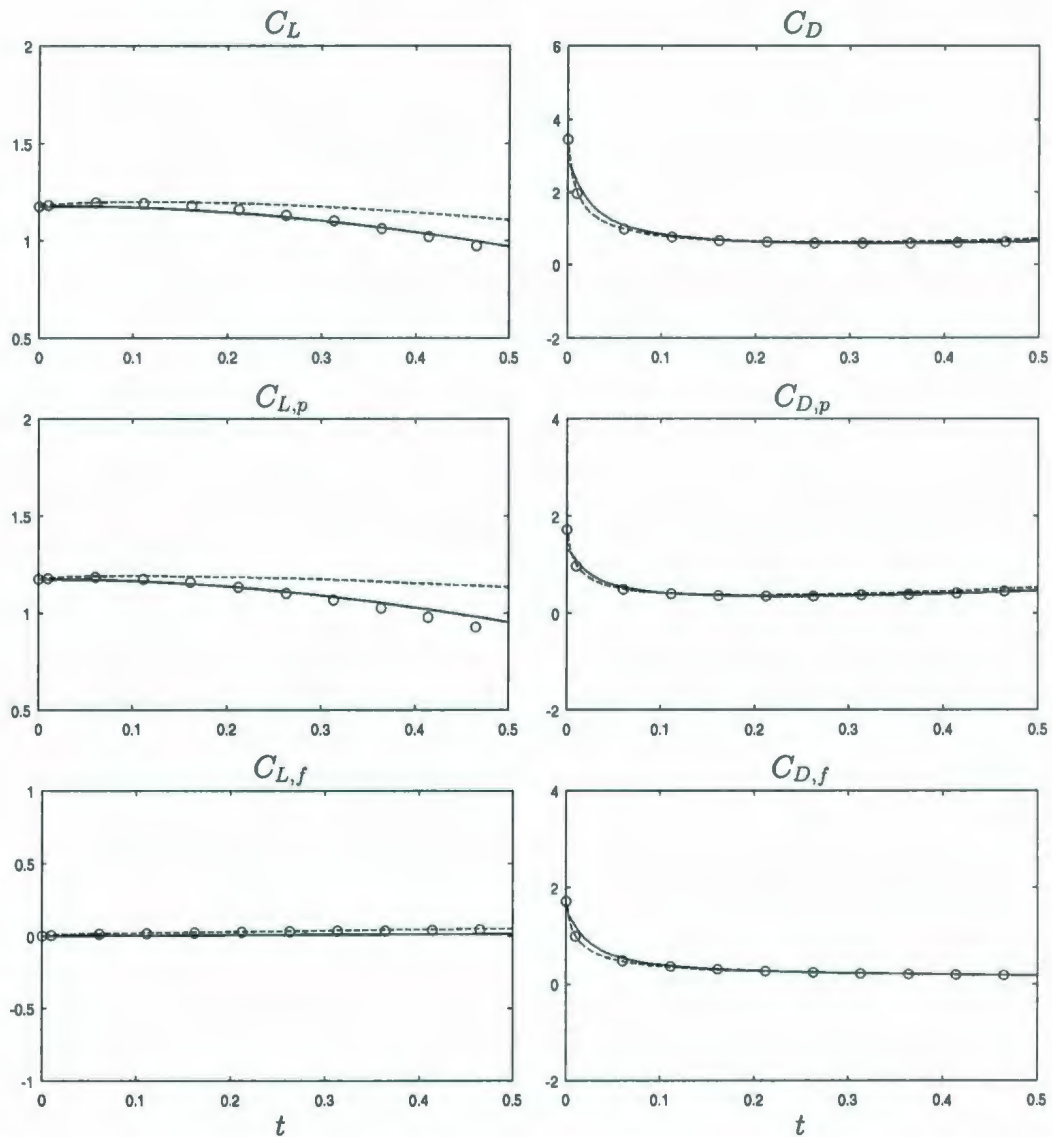


Figure 4.11: The lift coefficients,  $C_L$ ,  $C_{L,f}$  and  $C_{L,p}$ , (left) and the drag coefficients,  $C_D$ ,  $C_{D,f}$  and  $C_{D,p}$ , (right) for the combined rotational and transverse oscillation case in the absence of a free surface at  $R = 855$ :  $A = 0.13$ ,  $A_\alpha = 30^\circ$ ,  $f/f_0 = 1$  (from top to bottom:  $t = 0.05, 0.25, 0.5$ ): analytical results of Al-Mdallal (2004) (circles); numerical results of Al-Mdallal (2004) (dashed); present results (solid).

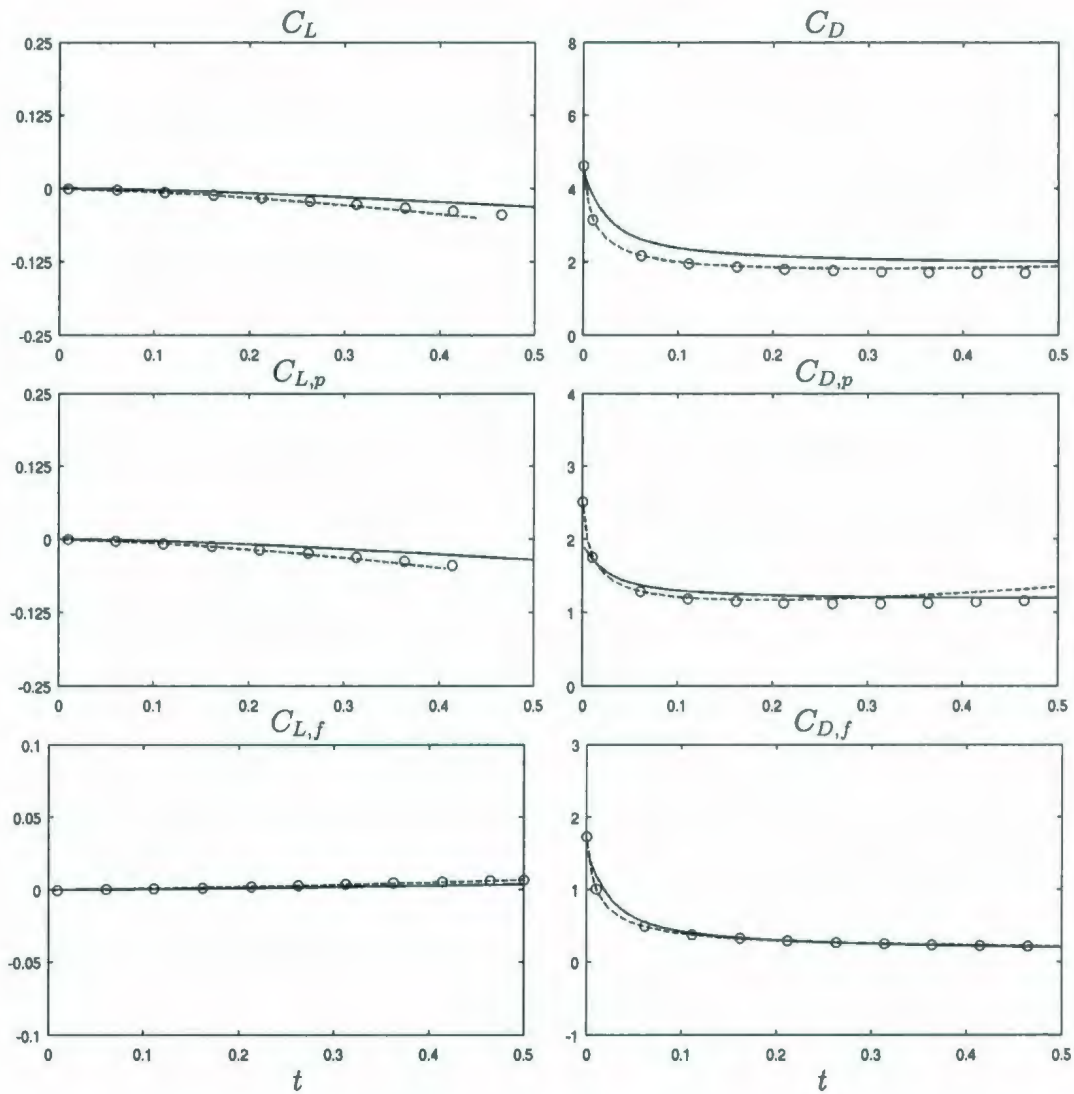


Figure 4.12: The lift coefficients,  $C_L$ ,  $C_{L,f}$  and  $C_{L,p}$ , (left) and the drag coefficients,  $C_D$ ,  $C_{D,f}$  and  $C_{D,p}$ , (right) for the combined rotational and in-line oscillation case in the absence of a free surface at  $R = 855$ :  $A = 0.13$ ,  $A_\alpha = 30^\circ$ ,  $f/f_0 = 1$  (from top to bottom:  $t = 0.05, 0.25, 0.5$ ): analytical results of Al-Mdallal (2004) (circles); numerical results of Al-Mdallal (2004) (dashed); present results (solid).

the case  $R = 855$ :  $A = 0.13$ ,  $A_\alpha = 30^\circ$ ,  $f/f_0 = 1$  at  $t = 0.05, 0.25, 0.5$ , where  $C_{D,f}$  and  $C_{L,f}$  are coefficients due to the friction and  $C_{D,p}$  and  $C_{L,p}$  are coefficients due to the pressure. These figures show good agreement between the results.

| Reference       | Present | Su <i>et al.</i> (2007) |
|-----------------|---------|-------------------------|
| $C_{L,max}$     | 0.92    | 0.97                    |
| $\widehat{C}_D$ | 1.70    | 1.70                    |

Table 4.7: The comparison of the maximum lift coefficient,  $C_{L,max}$  and the mean drag coefficient,  $\widehat{C}_D$ , for the case of uniform flow past a cylinder subject to in-line oscillations in the absence of a free surface at  $R = 100$ :  $A = 0.14$ ,  $f/f_0 = 2.0$  with the numerical results of Su *et al.* (2007).

To compare with the numerical findings of Su *et al.* (2007), numerical simulations are performed at  $R = 100$  for uniform flow past a circular cylinder subject to in-line oscillations in the absence of a free surface. The imposed translational in-line motion of the cylinder is described as

$$x(t) = -A \cos(2\pi ft). \quad (4.7)$$

This flow is examined numerically by Su *et al.* (2007) at the in-line displacement amplitude of  $A = 0.14$  and the frequency ratio,  $f/f_0 = 2$  ( $f_0 = 0.168$ ). In this study, the immersed boundary approach is utilized and a finite difference scheme is used to discretize the governing equations. The maximum lift coefficient,  $C_{L,max}$ , and the mean drag coefficient,  $\widehat{C}_D$ , for the in-line oscillation case at  $R = 100$ :  $A = 0.14$ ,  $f/f_0 = 2$  are compared with the results of Su *et al.* (2007) in Table 4.7. The results show good agreement.

The development of the vorticity over the one period of the vortex shedding,  $T_0 = 2T$ ,

is compared with the results of Su *et al.* (2007) in Figure 4.13 at  $R = 100$ . The numerical results are in good agreement in the near wake.

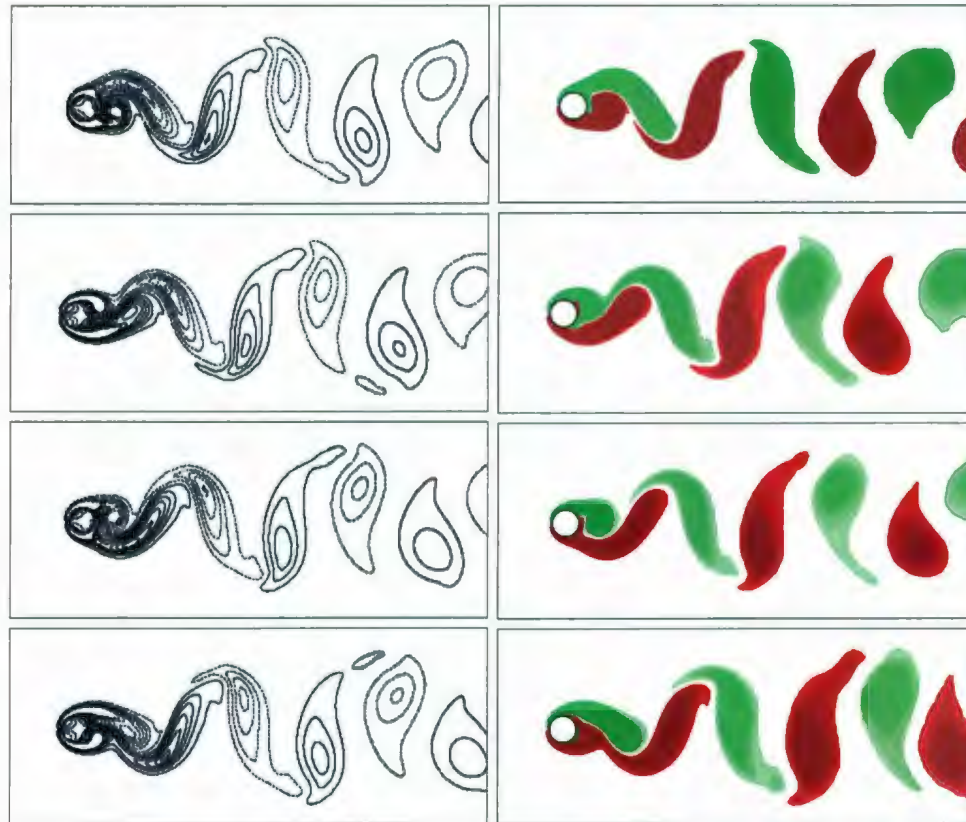


Figure 4.13: The equivorticity lines for the case of uniform flow past a cylinder subject to in-line oscillations in the absence of a free surface at  $R = 100$ :  $A = 0.14$ ,  $f/f_0 = 2$  (from top to bottom:  $t/T_0 = 1/4, 1/2, 3/4, 1.0$  ( $T_0 = 5.91$ )): numerical results of Su *et al.* (2007) (left); present results (right). Red colours correspond to positive vorticity (counterclockwise rotation) and green colours indicate negative vorticity (clockwise rotation).

The final set of the lift and drag forces verifications is made for the case of uniform flow past a cylinder subject to transverse oscillations in the absence of a free surface

at (i)  $R = 100$ :  $A = 0.2$ ,  $f/f_0 = 1$  and (ii)  $R = 185$ :  $A = 0.2$ ,  $f/f_0 = 1.1$ . The

| Reference                    | $C_{L,max}$ | $C_{D,max}$ | $\widehat{C}_D$ |
|------------------------------|-------------|-------------|-----------------|
| Present                      | 0.270       | 1.620       | 1.526           |
| Karanth <i>et al.</i> (1995) | 0.274       | 1.625       | 1.500           |

Table 4.8: The comparison of the maximum lift coefficient,  $C_{L,max}$ ; the maximum drag coefficient,  $C_{D,max}$ ; the mean drag coefficient,  $\widehat{C}_D$ , for the case of uniform flow past a cylinder subject to transverse oscillations in the absence of a free surface at  $R = 100$ :  $A = 0.2$ ,  $f/f_0 = 1$  with the numerical results of Karanth *et al.* (1995).

imposed translational transverse motion of the cylinder is described by

$$y(t) = -A \cos(2\pi ft). \tag{4.8}$$

The predicted present results are compared with the numerical results of Karanth *et al.* (1995) and Guilmineau and Queutey (2002). In each of the studies, a finite dif-

| Reference                     | $C_{L,rms}$ | $C_{D,rms}$ | $\widehat{C}_D$ |
|-------------------------------|-------------|-------------|-----------------|
| Present                       | 0.895       | 1.431       | 1.422           |
| Guilmineau and Queutey (2002) | 0.897       | 1.440       | 1.420           |

Table 4.9: The comparison of the RMS lift coefficient,  $C_{L,rms}$ ; the RMS drag coefficient,  $C_{D,rms}$ ; the mean drag coefficient,  $\widehat{C}_D$ , for the case of uniform flow past a cylinder subject to transverse oscillations in the absence of a free surface at  $R = 185$ :  $A = 0.2$ ,  $f/f_0 = 1.1$  with the numerical results of Guilmineau and Queutey (2002).

ference scheme is used to discretize the governing equations. In the work of Karanth *et al.* (1995), the governing equations in their stream function/vorticity formulation are solved on the boundary-fitted grid while Guilmineau and Queutey (2002) used a coordinate transformation technique. Table 4.8 shows the comparisons of the max-

imum lift coefficient,  $C_{L,max}$ ; the maximum drag coefficient,  $C_{D,max}$ ; the mean drag coefficient,  $\widehat{C}_D$ , for the transverse oscillation case at  $R = 100$ :  $A = 0.2$ ,  $f/f_0 = 1$  with the numerical results of Karanth *et al.* (1995). The present results and the numerical results of Karanth *et al.* (1995) are in good agreement.

The comparisons of the RMS lift coefficient,  $C_{L,rms}$ ; the RMS drag coefficient,  $C_{D,rms}$ ; the mean drag coefficient,  $\widehat{C}_D$ , for the transverse oscillation case at  $R = 185$ :  $A = 0.2$ ,  $f/f_0 = 1.1$  ( $f_0 = 0.214$ ) with the numerical results of Guilmineau and Queutey (2002) are shown in Table 4.9. The results shown in Table 4.9 are in good agreement. It is noted that in the work by Guilmineau and Queutey (2002), the reported value of  $C_{D,rms} = 0.144$  is inconsistent with the corresponding time history of the drag coefficient,  $C_D$  [see Guilmineau and Queutey (2002), Figure 10(d), p. 786]. The RMS of the data extracted from Figure 10(d), [Guilmineau and Queutey (2002), p. 786] results in  $C_{D,rms} = 1.440$ .

The next verifications are for the cases of uniform flow past a cylinder undergoing (i) recti-linear oscillations at an angle  $\eta = 60^\circ$  and (ii) in-line oscillations at  $R = 855$ . The motion of the cylinder is defined as

$$x(t) = -A \cos(2\pi ft), \quad y(t) = -A \cos(2\pi ft) \tan(\eta). \quad (4.9)$$

In Figures 4.14 and 4.15, the present predictions of the development of the flow in terms of the equivorticity lines at  $A = 0.13$  for the frequency ratios  $f/f_0 = 0.5, 1.0, 2.0, 3.0, 4.0$  ( $f_0 = 0.194$ ) are compared with those obtained from the experimental study of Ongoren and Rockwell (1988) and the numerical results by Al-Mdallal (2004). The snapshots are taken at the instant corresponding to the maximum negative displacement of the cylinder. Following the work by Al-Mdallal (2004), the present

computations are carried out over (i)  $5T$  for  $f/f_0 = 0.5$ ; (ii)  $9T$  for  $f/f_0 = 1.0$ ; (iii)  $20T$  for  $f/f_0 = 2.0$  and (iv)  $30T$  for  $f/f_0 = 3.0, 4.0$ . Figures 4.14 and 4.15 show relatively good qualitative agreement between the present equivorticity lines and those obtained in the works by Ongoren and Rockwell (1988) and Al-Mdallal (2004). The differences between the results might be due to the following reasons. In Al-Mdallal's work, the governing equations are solved in their stream function/vorticity formulation using the boundary-fitted grid system  $8 \times 8 \times 16$  (when the time step is  $\Delta t = 0.01$ , the uniform grid step is  $\Delta h = 0.025$ ) while in the present thesis vorticity is computed from the velocity field. In order to accurately capture the development of the shear layer for the high Reynolds number  $R = 855$ , the present numerical calculations are performed using the grid system  $15 \times 25 \times 20$  when the time step is  $\Delta t = 0.005$  and the uniform grid step in the vicinity of the cylinder is  $\Delta h = 0.0125$ . It is also noted that the number of oscillation cycles for the experimental runs by Ongoren and Rockwell (1988) is considerably higher than that of the present case.

## **4.5 Uniform flow past a steady rotating cylinder in the absence of a free surface**

As the final set of verifications in the absence of a free surface, the simulations for the case of uniform flow past a steadily rotating cylinder about its axis are carried out at  $R = 200, 500$  by setting the translational and rotational cylinder displacements in (4.6) to  $x(t) = y(t) = 0$  and  $\alpha(t) = 1.0, 2.0$ , respectively. The early development of the flow ( $t \leq 6$ ) is compared with the numerical results of Takada and Tsutahara (1998) and Badr and Dennis (1985) at  $R = 500$  and  $\alpha(t) = 1.0$  in Figure 4.16.

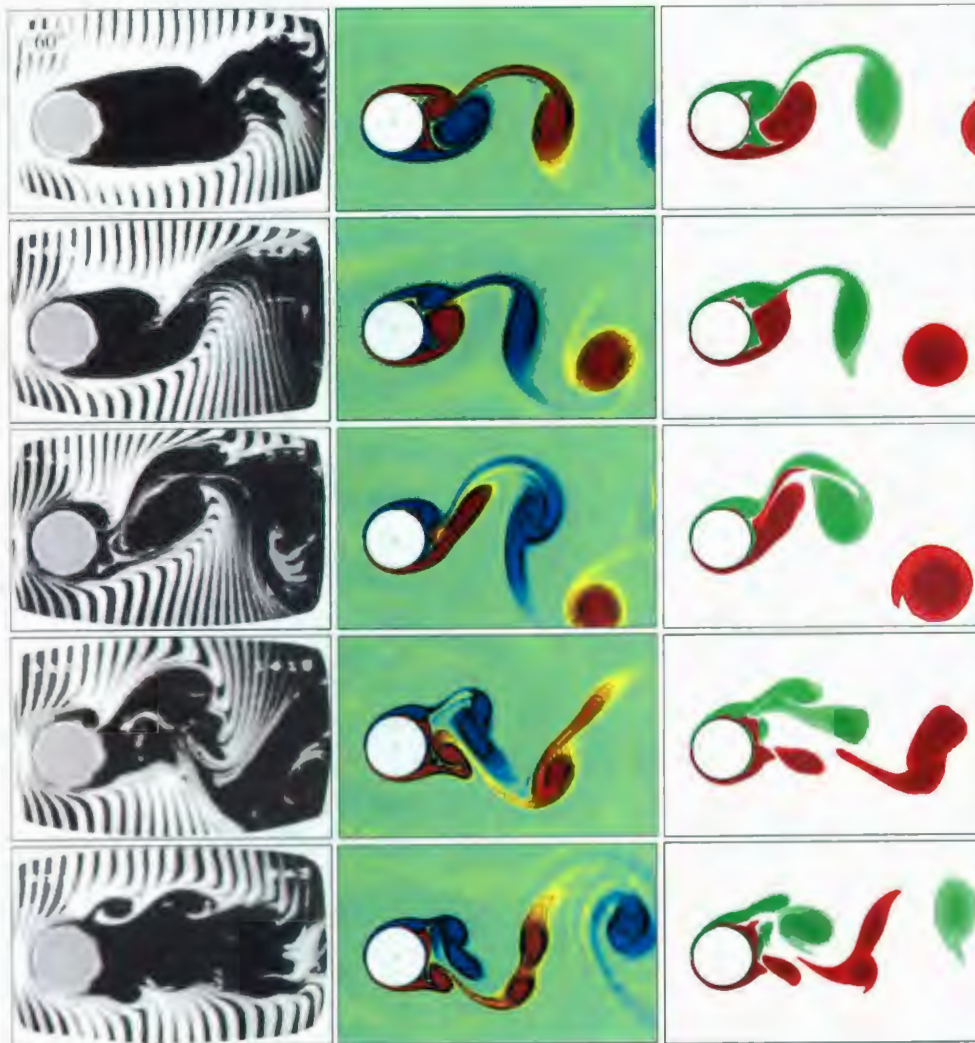


Figure 4.14: The equivorticity lines for the case of uniform flow past an oscillating cylinder at the angle  $\eta = 60^\circ$  in the absence of a free surface at  $R = 855$ :  $A = 0.13$  (from top to bottom:  $f/f_0 = 0.5, 1.0, 2.0, 3.0, 4.0$ ): experimental results of Ongoren and Rockwell (1988) (left); numerical results of Al-Mdallal (2004) (middle); present results (right). Red colours correspond to positive vorticity (counterclockwise rotation) and green colours indicate negative vorticity (clockwise rotation). The snapshots are taken at the instant corresponding to the maximum negative displacement of the cylinder.

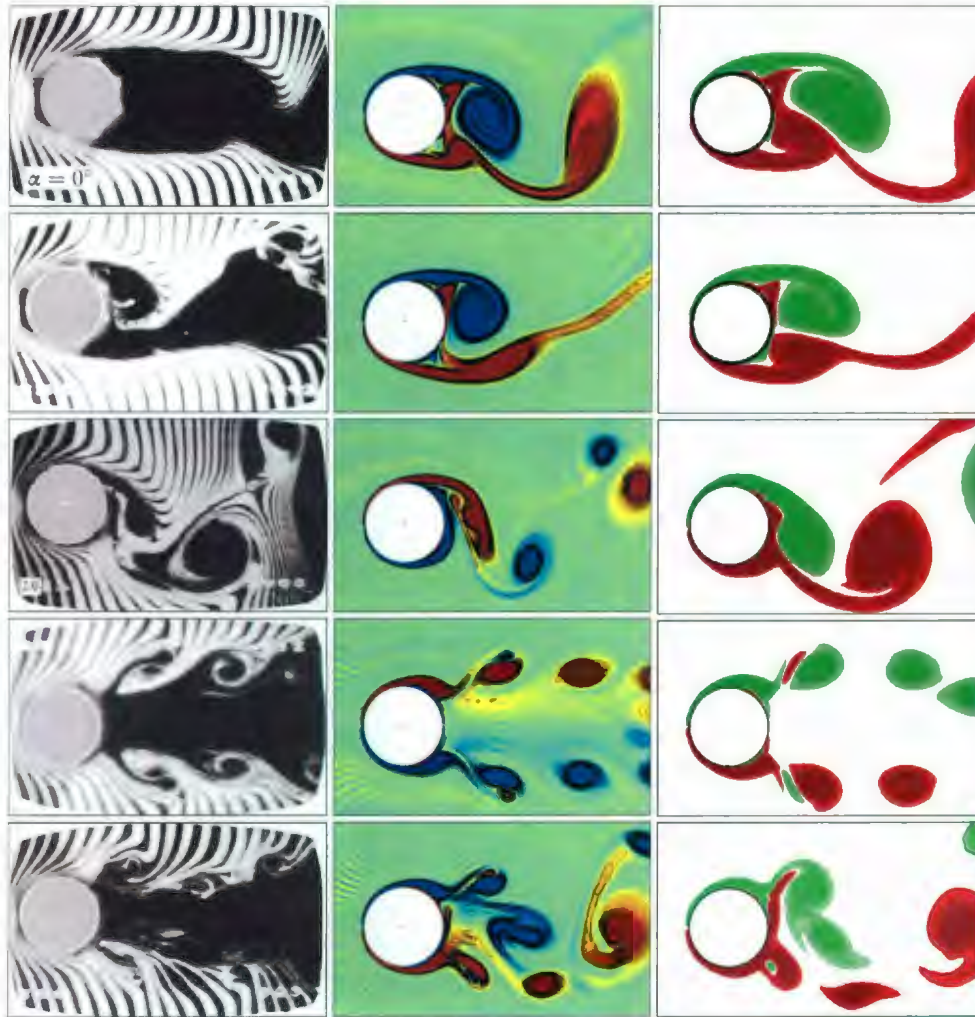


Figure 4.15: The equivorticity lines for the case of uniform flow past a cylinder subject to in-line oscillations in the absence of a free surface at  $R = 855$ :  $A = 0.13$  (from top to bottom:  $f/f_0 = 0.5, 1.0, 2.0, 3.0, 4.0$ ): experimental results of Ongoren and Rockwell (1988) (left); numerical results of Al-Mdallal (2004) (middle); present results (right). Red colours correspond to positive vorticity (counterclockwise rotation) and green colours indicate negative vorticity (clockwise rotation). The snapshots are taken at the instant corresponding to the maximum negative displacement of the cylinder.

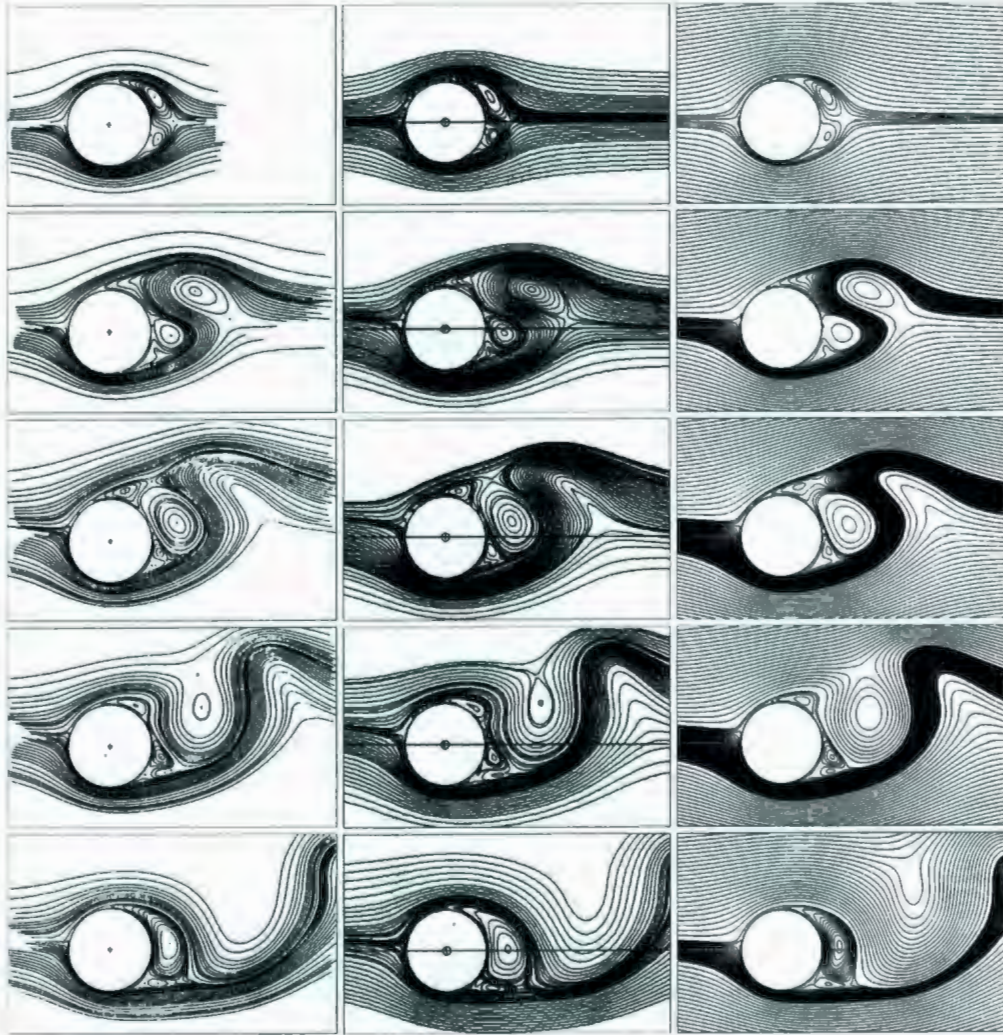


Figure 4.16: The streamline patterns in the near wake region for impulsively started steadily rotating cylinder in the absence of a free surface at  $R = 500$ :  $\alpha(t) = 1.0$  (from top to bottom:  $t = 1.0, 1.5, 4.0, 5.0, 6.0$ ): numerical results of Badr and Dennis (1985) (left); Takada and Tsutahara (1998) (middle); present results (right).

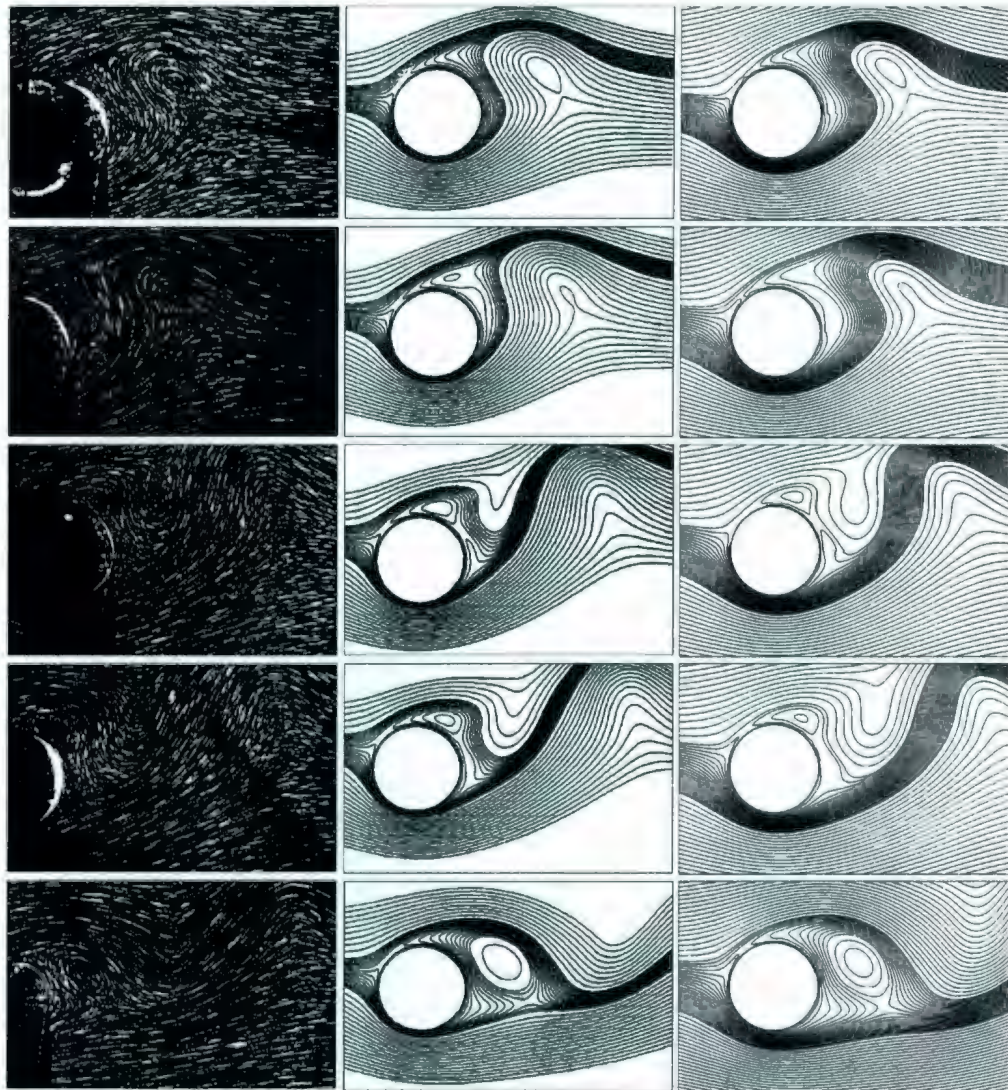


Figure 4.17: The streamline patterns in the near wake region for impulsively started steadily rotating cylinder in the absence of a free surface at  $R = 200$ :  $\alpha(t) = 2.0$  (from top to bottom:  $t = 2.0, 3.0, 4.0, 4.5, 6.5$ ): experimental results of Coutanceau and Menard (1985) (left); numerical results of Nair *et al.* (1998) (middle); present results (right).

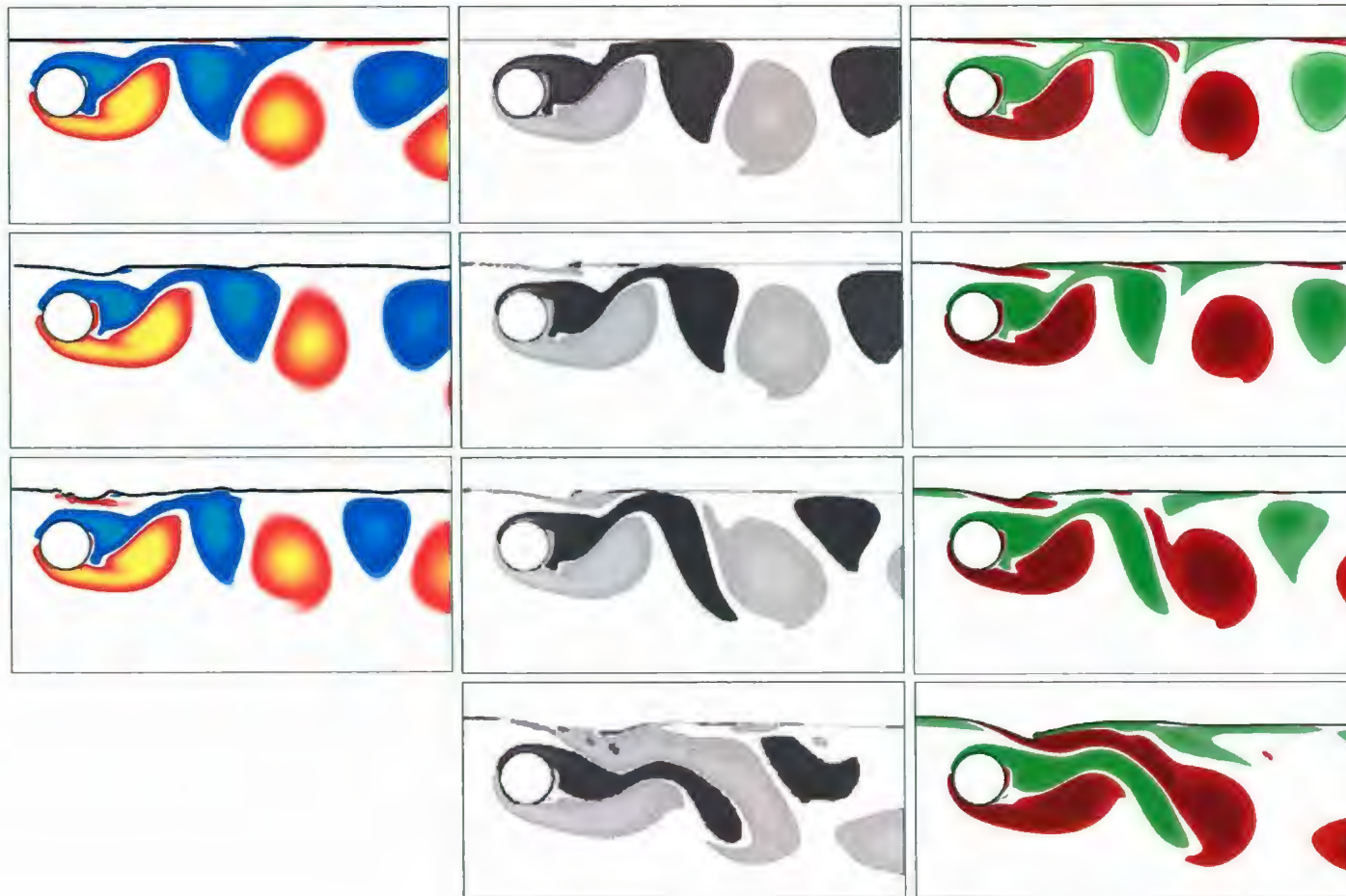


Figure 4.18: The equivorticity lines and the free surface deformations for the case of uniform flow past a stationary cylinder in the presence of a free surface at  $R = 180$ ,  $h = 0.55$  (from top to bottom:  $Fr \approx 0.0$  ( $t = 19.9$ ),  $Fr = 0.3$  ( $t = 19$ ),  $0.4$  ( $t = 33.2$ ),  $0.6$  ( $t = 20.2$ )): numerical results of Gubanov (2006) (left); Reichl *et al.* (2005) (middle); present results (right).

Takada and Tsutahara (1998) implements the lattice-Boltzmann method to solve the problem of impulsively started flow past a circular cylinder whereas a spectral finite difference scheme is utilized in the work by Badr and Dennis to calculate the flow for both small and moderate values of the time.

In Figure 4.17, the predicted streamline patterns are compared with the experimental results of Coutanceau and Menard (1985) and the numerical results of Nair *et al.* (1998) at relatively small values of time ( $2.0 \leq t \leq 6.5$ ) at  $R = 200$  and  $\alpha(t) = 2.0$ . Nair *et al.* (1998) solved the governing equations in their stream function/vorticity formulation by using a third-order upwind scheme and an *O*-type grid. For both Figures 4.16 and 4.17, the compared results are in excellent agreement.

## 4.6 Uniform flow past a cylinder in the presence of a free surface

In this section, the accuracy of the present numerical scheme is verified for the cases of the two-dimensional uniform flow past (i) a stationary cylinder and (ii) a cylinder subject to in-line oscillations in the presence of a free surface. For the stationary cylinder case the flow patterns are compared to the numerical results of Reichl *et al.* (2005) for the ranges of Froude numbers,  $0.0 \leq Fr \leq 0.6$ , and the cylinder submergence depths,  $0.1 \leq h \leq 1.0$ , at  $R = 180$ . The numerical simulations for the case of uniform flow past the cylinder subject to in-line oscillations are conducted at  $R = 917$ :  $f/f_0 = 1$ ,  $A = 0.96$ ,  $h = 11.23$ ,  $Fr = 0.07$ . The resulting flow patterns are compared with the experimental results of Cetiner and Rockwell (2001).

In Tables 4.10 and 4.11, the effect of the submergence depth,  $h$ , on predicted values of the local Froude number,  $Fr|_L$ ; the frequency ratio,  $f|_{fs}/f_0$  ( $f_0 = 0.191$ ); the  $u$ -velocity at  $R = 180$ :  $Fr = 0.3$ ,  $0.1 \leq h \leq 1.0$ , and  $Fr = 0.4$ ,  $0.16 \leq h \leq 1.0$ , respectively, are compared with the numerical results of Reichl *et al.* (2005). The

| Ref. | Reichl <i>et al.</i> (2005) |               |           | Present |               |           |
|------|-----------------------------|---------------|-----------|---------|---------------|-----------|
|      | $Fr _L$                     | $f _{fs}/f_0$ | $\hat{u}$ | $Fr _L$ | $f _{fs}/f_0$ | $\hat{u}$ |
| 0.10 | 1.09                        | -             | 0.70      | 1.09    | -             | 0.71      |
| 0.16 | 0.92                        | -             | 1.03      | 0.92    | -             | 1.04      |
| 0.22 | 0.82                        | 0.73          | 1.10      | 0.82    | 0.73          | 1.09      |
| 0.40 | 0.73                        | 1.01          | 1.35      | 0.73    | 1.00          | 1.34      |
| 0.55 | 0.66                        | 1.07          | 1.41      | 0.66    | 1.07          | 1.41      |
| 0.70 | 0.57                        | 1.10          | 1.39      | 0.57    | 1.09          | 1.40      |
| 1.00 | 0.47                        | 1.09          | 1.33      | 0.46    | 1.08          | 1.33      |

Table 4.10: The effect of the submergence depth,  $h$ , on the local Froude number,  $Fr|_L$ ; the frequency ratio,  $f|_{fs}/f_0$ ; the average  $u$ -velocity in the region directly above the cylinder,  $\hat{u}$ , for uniform flow past a stationary cylinder in the presence of a free surface at  $R = 180$ :  $Fr = 0.3$ ,  $0.1 \leq h \leq 1.0$ . Comparison with the numerical results of Reichl *et al.* (2005).

$u$ -velocity is averaged based on the local free surface height,  $h|_L$ , in the region directly above the cylinder. This is undertaken for each Froude number,  $Fr$ , and the submergence depth,  $h$ , case considered in Tables 4.10 and 4.11 at the time when maximum lift occurs. For the cases when no vortex periodic shedding is observed, the average  $u$ -velocity is computed close to the point where maximum lift occurs.

| Ref. | Reichl <i>et al.</i> (2005) |                |           | Present |                |           |
|------|-----------------------------|----------------|-----------|---------|----------------|-----------|
|      | $Fr _L$                     | $f _{f_s}/f_0$ | $\hat{u}$ | $Fr _L$ | $f _{f_s}/f_0$ | $\hat{u}$ |
| 0.16 | 1.20                        | -              | -         | 1.19    | -              | -         |
| 0.22 | 1.08                        | -              | 0.97      | 1.08    | -              | 0.97      |
| 0.40 | 0.90                        | 0.94           | 1.22      | 0.90    | 0.96           | 1.22      |
| 0.55 | 0.82                        | 1.06           | 1.30      | 0.82    | 1.07           | 1.30      |
| 0.70 | 0.76                        | 1.10           | 1.34      | 0.75    | 1.10           | 1.34      |
| 1.00 | 0.64                        | 1.11           | 1.36      | 0.63    | 1.10           | 1.36      |

Table 4.11: The effect of the submergence depth,  $h$ , on the local Froude number,  $Fr|_L$ ; the frequency ratio,  $f|_{f_s}/f_0$ ; the average  $u$ -velocity in the region directly above the cylinder,  $\hat{u}$ , for uniform flow past a stationary cylinder in the presence of a free surface at  $R = 180$ :  $Fr = 0.4, 0.16 \leq h \leq 1.0$ . Comparison with the numerical results of Reichl *et al.* (2005).

The local Froude number,  $Fr|_L$ , is calculated based on the maximum dimensional  $u$ -velocity in the region directly above the cylinder,  $\bar{u}^*$ , at the time when the lift coefficient reaches its maximum and the dimensional local free surface height,  $h^*|_L$ , by using  $Fr|_L = \bar{u}^*/\sqrt{(g^*h^*|_L)}$ . The predicted results are in excellent agreement with the numerical results of Reichl *et al.* (2005).

Figure 4.18 shows the comparison of the near wake structures as well as free surface deformations between the present computational method and the numerical results of Reichl *et al.* (2005) and Gubanov (2006) at  $R = 180, 0.0 \leq Fr \leq 0.6, h = 0.55$ . It is seen that for small and moderate values of the Froude numbers,  $0.0 \leq Fr \leq 0.3$ , the results are in excellent agreement. For higher Froude numbers,  $Fr > 0.3$ , the surface

distortion becomes considerably larger than the cases for smaller values of the Froude number,  $Fr$ , due to the induced surface curvature. For this type of flow the wake has much more asymmetric pattern than the Froude number cases  $0.0 \leq Fr \leq 0.3$  and the numerical simulation becomes very sensitive to the specific algorithm used for tracking the free surface. This can be clearly seen from the equivorticity plots displayed in Figure 4.18 at  $Fr = 0.4$ . As was stated earlier, the two-phase flow model is used in both the present study and the work by Reichl *et al.* (2005) unlike the investigation by Gubanov (2006). The present results and the numerical results of Reichl *et al.* (2005) are in excellent agreement.

In Gubanov's work, the motion of the fluid in  $\Omega_1$  is neglected and the free surface boundary conditions (1.4) and (1.5) are satisfied explicitly to track the free surface. This leads to the discrepancy between Gubanov's results and the other numerical results displayed in Figure 4.18. This figure shows relatively good agreement between the near wake structures of the present study and the numerical work by Reichl *et al.* (2005) at  $Fr = 0.6$ . It is noted that Reichl *et al.* (2005) exploits a segregated solver on an unstructured boundary-fitted grid with a prescribed pressure at the outflow

$$\frac{\partial p}{\partial x} = 0, \quad \frac{\partial p}{\partial y} = \frac{1}{Fr^2} \quad (4.10)$$

as implemented in FLUENT 5, while in this study a coupled solver on a structured, non-boundary-fitted grid with the open boundary conditions (2.55) and (2.57) is utilized.

The further comparison of the near wake structures as well as free surface deformations between the present computational method and the numerical results of Reichl *et al.* (2005) at  $R = 180$ ,  $0 \leq Fr \leq 0.6$ ,  $h = 0.16$  is shown in Figure 4.19. For small cylinder submergence depths, there is a strong interaction between vorticity from the cylinder

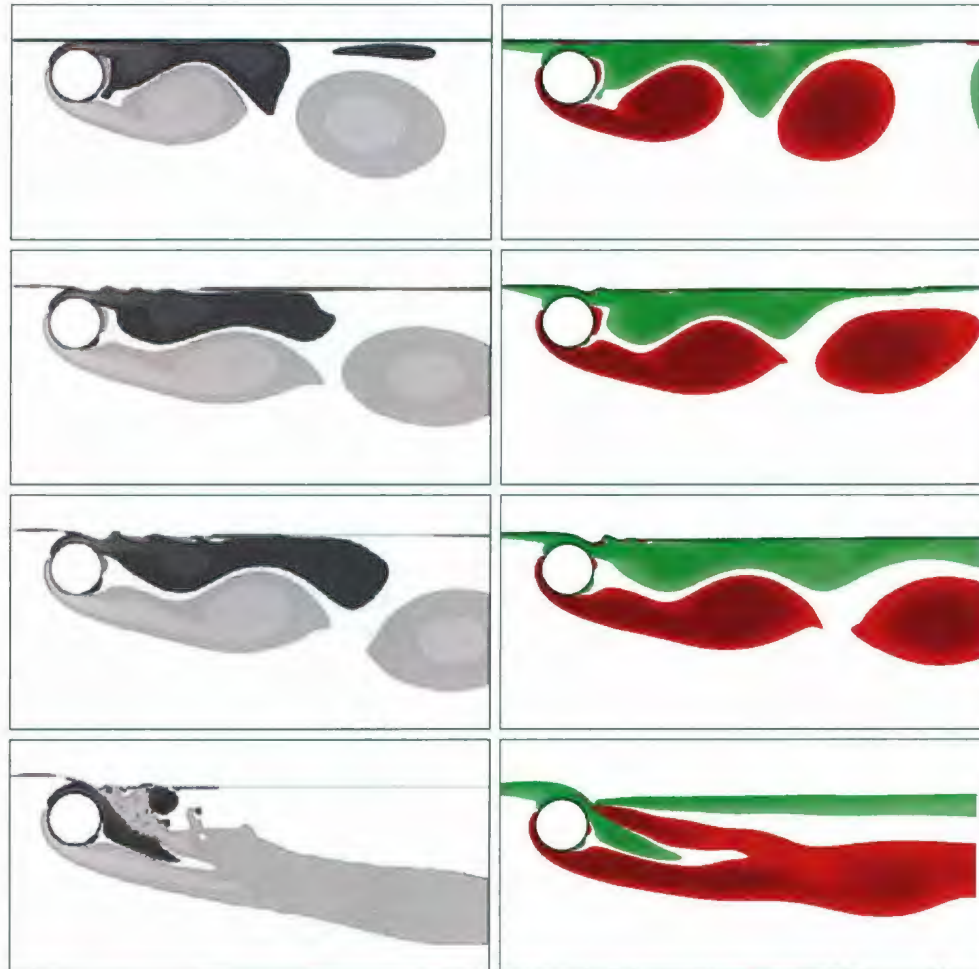


Figure 4.19: The equivorticity lines and the free surface deformations for the case of uniform flow past a stationary cylinder in the presence of a free surface at  $R = 180$ ,  $h = 0.16$  (from top to bottom:  $Fr \approx 0.0$  ( $t = 61.3$ ),  $Fr = 0.3$  ( $t = 16$ ),  $0.4$  ( $t = 50.4$ ),  $0.6$  ( $t = 40$ )): numerical results of Reichl *et al.* (2005) (left); present results (right).

and vorticity from the free surface. For Froude numbers  $Fr \geq 0.3$  the closeness of the free surface induces large time-dependent surface curvature and thus a substantial vorticity near the free surface is expected. The substantial positive vorticity from the

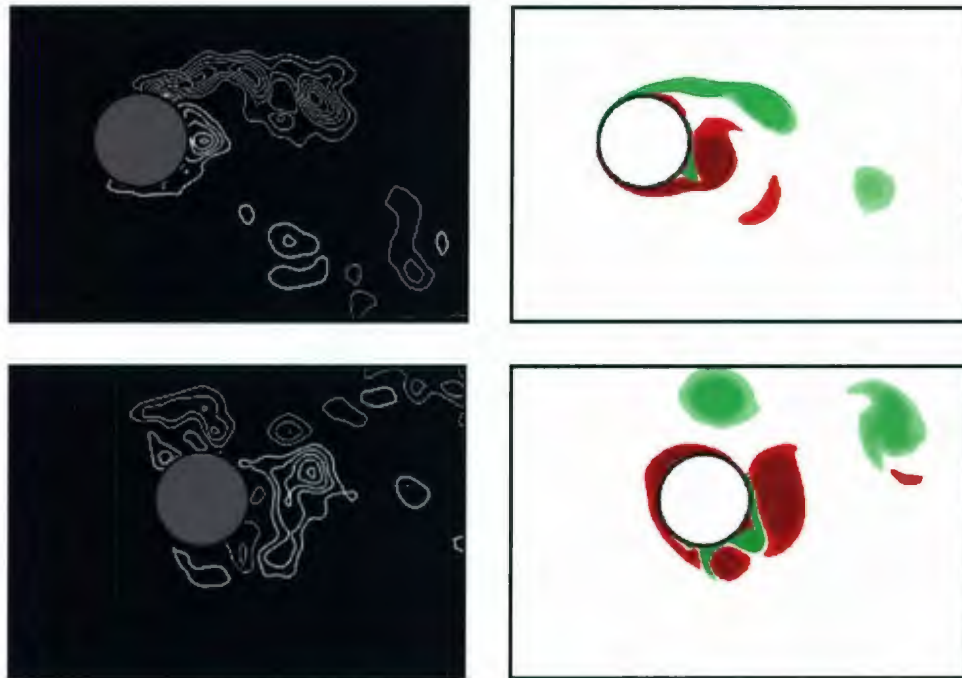


Figure 4.20: The equivorticity lines for the case of uniform flow past the cylinder subject to in-line oscillations in the presence of a free surface at  $R = 917$ :  $f/f_0 = 1$ ,  $A = 0.96$ ,  $h = 11.23$ ,  $Fr = 0.07$ : experimental results of Cetiner and Rockwell (2001) (left); present results (right).

free surface is clearly shown by the results obtained in this study unlike the results of Reichl *et al.* (2005). On the other hand, the present results reveal an unphysical phenomena of the advection of the vorticity from the cylinder against the uniform stream. This is due to the limitation of present numerical algorithm at submergence depths  $h < 0.5$ .

Finally, the near wake structures obtained in this study for the case of the cylinder subject to in-line oscillations in the presence of a free surface at  $R = 917$ :  $f/f_0 = 1$ ,  $A = 0.96$ ,  $h = 11.23$ ,  $Fr = 0.07$  are compared with the experimental results of

Cetiner and Rockwell (2001). The comparison is shown in Figure 4.20. The imposed translational in-line motion of the cylinder is defined by (4.7). In Figure 4.20, the snapshots at the top are taken at the time when the lift coefficient,  $C_L$ , reaches its minimum; the snapshots at the bottom are taken at the time when  $C_L$  is zero. Bearing in mind that the number of cylinder oscillation cycles for the experimental runs by Cetiner and Rockwell (2001) is considerably larger than that of the present case, it may be noted that the results are in relatively good agreement.

## 5. Forced in-line oscillations of a circular cylinder beneath a free surface: Locked-on modes and fluid forces

In this chapter, the results for two-dimensional flow past a circular cylinder subject to forced in-line oscillations beneath a free surface are presented. The unsteady near wake structures and lock-on phenomena as well as fluid forces are investigated at the Reynolds number of  $R = 200$  when  $f/f_0 = 1.0, 2.0, 3.0, 4.0$  ( $f_0 = 0.198$ ) and a fixed displacement amplitude,  $A = 0.13$ . The flow characteristics for Froude numbers,  $Fr \approx 0.0$  ( $= 0.03$ ) and  $Fr = 0.2, 0.4$ , and cylinder submergence depths,  $h = 0.25, 0.5, 0.75$ , are examined. The numerical simulations are also conducted for the case when the free surface is absent (symbolically represented by  $h = \infty$ ) under the same oscillation conditions. The results are analyzed using numerical flow visualization (equivorticity patterns, streamlines, pressure contours) as well as the fluid forces acting on the cylinder surface. The observed features are compared with the reference case  $h = \infty$  to better understand the effect from the inclusion of the free surface.

The classical definition of the lock-on phenomena is based on the existence of a strong spectral peak in the power spectral density (PSD) of the lift coefficient. However, the determination of locked-on regimes of vortex shedding is not confined in PSD spectrum. The other techniques used to determine lock-on modes include the repetition of the velocity traces [Anagnostopoulos (2000)], the repetition of vortex shedding in

---

the near wake region over an integer number of cylinder oscillation periods [Ongoren and Rockwell (1988)] and the repetition of the Lissajous patterns of the lift coefficient [Cetiner and Rockwell (2001)]. In this thesis, the near wake vorticity contours and Lissajous patterns of the lift coefficient are used to define the lock-on modes following partly the methodology of Ongoren and Rockwell (1988) and Cetiner and Rockwell (2001). The connection between vortex shedding modes and fluctuating fluid forces is also investigated using PSD of the lift and drag coefficients through Fourier analysis. The vortex shedding modes are classified following the terminology of Williamson and Roshko (1988). The Lissajous representations of the lift and drag coefficients are also used to demonstrate the mechanism of mechanical energy transfer between the fluid and the cylinder, degree of phase-locking or a loss of lock-on and associated phase shift. The effect of the free surface on the mechanical energy transfer is also explained by using the energy transfer equation (3.84). For selected cases, proper orthogonal decomposition of the vorticity field is used to interpret unsteady near wake structures in terms of POD eigen-modes.

The present numerical simulations are performed on a cluster of four dual-core AMD Opteron 265 and twenty five dual-core AMD Opteron 2218 (IBM) computers located at the Department of Mathematics and Statistics, Memorial University of Newfoundland. The unsteady flow calculations are conducted for the time up to  $t = 150$  when  $h = \infty$  and up to  $t = 100$  when  $h = 0.25, 0.5, 0.75$ , using the grid system  $20 \times 30 \times 40$  with  $252 \times 196$  elements. This requires about 504 hours of computational time.

## 5.1 Vortex shedding modes and fluid forces in the absence of the free surface ( $h = \infty$ )

The present numerical simulations in the absence of the free surface are conducted at  $R = 200$ :  $A = 0.13$ ,  $f/f_0 = 1.0, 2.0, 3.0, 4.0$  ( $1.0 \leq f/f_0 \leq 4.0$ ). Locked-on asymmetric mode of vortex formation is observed when  $f/f_0 = 2.0$  unlike the other frequency ratio cases  $f/f_0 = 1.0, 3.0, 4.0$ .

The time history of the fluctuating lift coefficient,  $C_L$ , plotted with the cylinder displacement,  $x(t)$ , the PSD of  $C_L$  and the corresponding Lissajous patterns of  $C_L$  at  $R = 200$ :  $A = 0.13$ ,  $1.0 \leq f/f_0 \leq 4.0$ ,  $h = \infty$  are shown in Figure 5.1. It is evident that when  $f/f_0 = 1.0, 3.0, 4.0$ , the  $C_L$  traces exhibit non-repeatable signatures. This observation is also suggested by the corresponding Lissajous patterns. It is clearly seen that the trajectories of  $C_L(x)$  are non-congruent from cycle to cycle of cylinder oscillation. This indicates large phase variations between the fluctuating lift coefficient,  $C_L$ , and the cylinder motion. On the other hand, at  $f/f_0 = 2.0$ , the  $C_L$  trace exhibits repeatable persistent signatures every two cycles of cylinder oscillation,  $2T$ . The repeatability of the  $C_L$  patterns for  $f/f_0 = 2.0$  indicates the lock-on between the cylinder motion and the fluctuating  $C_L$ . The Lissajous traces of  $C_L$  at  $f/f_0 = 2.0$  have remarkably congruent shape. These observations suggest that when  $f/f_0 = 2.0$  the vortex shedding in the near wake region is locked-on over two periods of the cylinder motion,  $2T$ . It is noted that for each frequency ratio,  $f/f_0$ , symmetrical shapes of  $C_L(x)$  are attained in the upper and lower half planes. The PSD corresponding to the signatures of  $C_L$  suggest at least two well defined peaks:

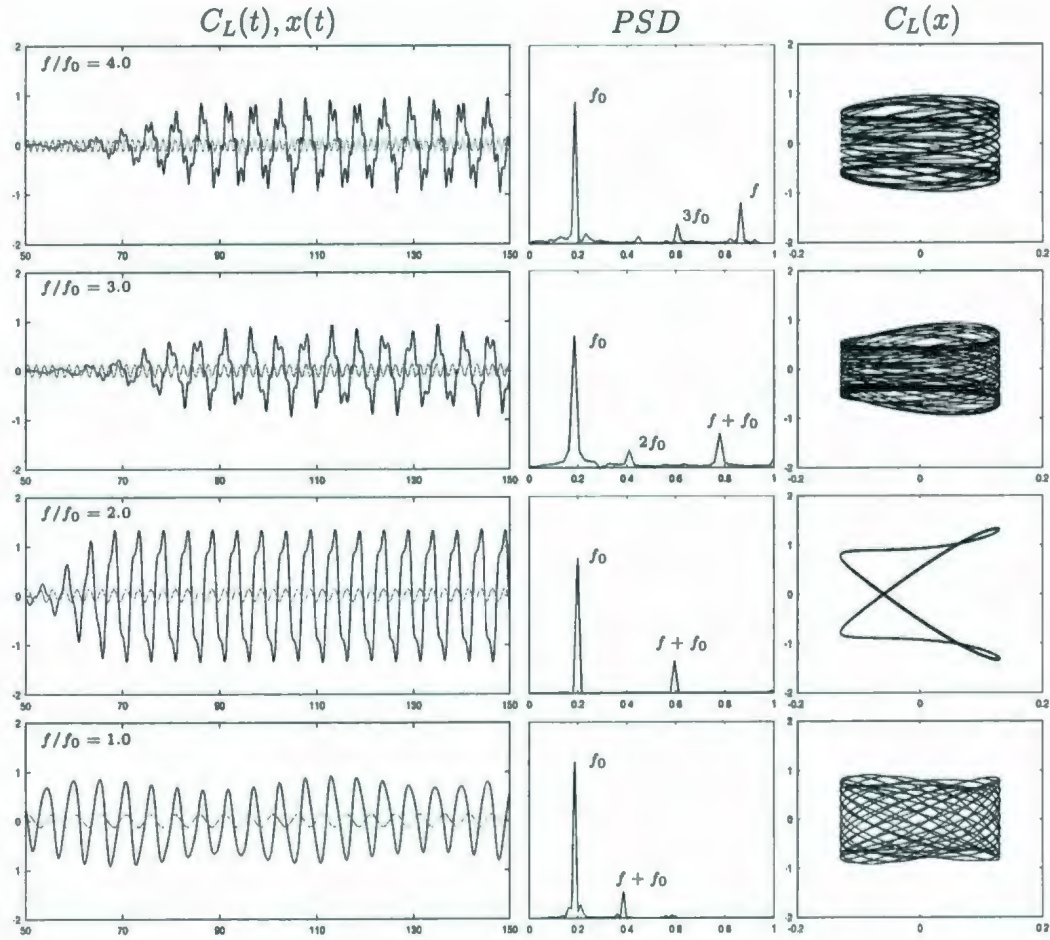


Figure 5.1: The time variation of the lift coefficient,  $C_L$ , (black) and the in-line displacement,  $x(t)$ , (gray); PSD of  $C_L$ ; Lissajous patterns of  $C_L$  at  $R = 200$ :  $A = 0.13$ ,  $1.0 \leq f/f_0 \leq 4.0$ ,  $h = \infty$ .

$f_0$ ,  $f + f_0$  when  $f/f_0 = 1.0, 2.0, 3.0$  and  $f_0, f$  when  $f/f_0 = 4.0$ . It is also seen that one dominant peak develops in the PSD as  $f/f_0$  increases.

The time history of the fluctuating drag coefficient,  $C_D$ , plotted with the cylinder displacement,  $x(t)$ , the PSD of  $C_D$  and the corresponding Lissajous patterns of  $C_D$  for  $1.0 \leq f/f_0 \leq 4.0$  are shown in Figure 5.2. It is seen that when  $f/f_0 = 2.0, 3.0, 4.0$ ,

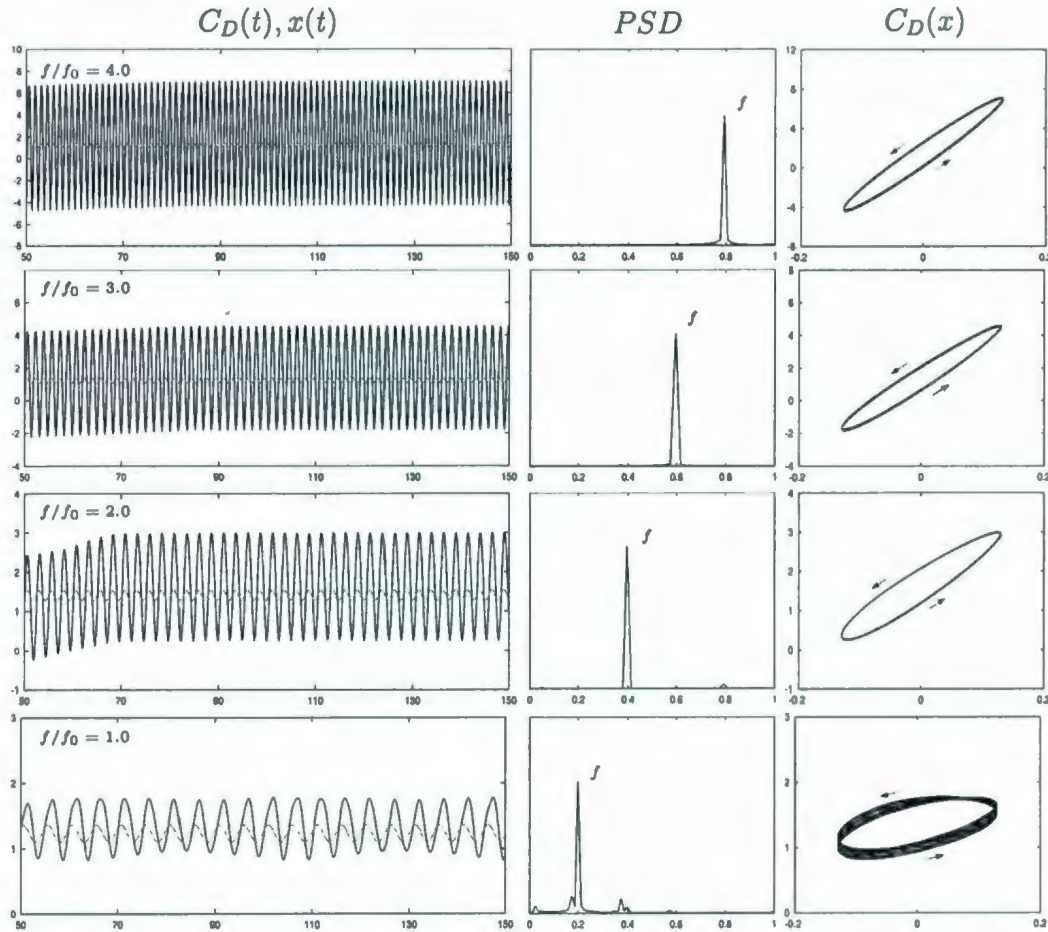


Figure 5.2: The time variation of the drag coefficient,  $C_D$ , (black) and the in-line displacement,  $x(t)$ , (gray); PSD of  $C_D$ ; Lissajous patterns of  $C_D$  at  $R = 200$ :  $A = 0.13$ ,  $1.0 \leq f/f_0 \leq 4.0$ ,  $h = \infty$ .

the traces of  $C_D$  exhibit persistent repeatable signatures over one cycle of cylinder oscillation,  $T$ . The corresponding  $C_D(x)$  traces show congruent shapes indicating the phase-locking between the fluctuating drag coefficient,  $C_D$ , and the cylinder motion. At  $f/f_0 = 1.0$ , the trace of  $C_D$  exhibits almost repeatable but non-persistent signature over one cycle of cylinder oscillation,  $T$ . The corresponding Lissajous trajectories are less congruent from cycle to cycle, which indicates that phase variations between the

fluctuating drag coefficient,  $C_D$ , and the cylinder motion increase. Figure 5.2 shows that at each of the frequency ratios,  $f/f_0$ , the hysteresis loops of substantial extent occur in the upper half plane. Moreover, these loops shift towards the lower half plane as the ratio  $f/f_0$  increases. It is noted that for the cylinder subject to in-line oscillations, the Lissajous trajectories of  $C_D$  versus in-line cylinder displacement,  $x(t)$ , can be related to the mechanical energy transfer between the fluid and the cylinder as follows. As it was mentioned earlier, the total energy transfer over one period of cylinder oscillation,  $T$ , can be defined as

$$E = \int_0^T C_D \dot{x}(t) dt, \quad (5.1)$$

where the overdot indicates the differentiation by time. The geometrical interpretation of (5.1) is the signed area enclosed by hysteresis loops of  $C_D(x)$  where the sign is defined by a direction of the Lissajous trajectories [see, for example, Cetiner and Rockwell (2001)]. In all figures that follow, the directions of Lissajous trajectories,  $C_D(x)$ , are indicated by arrows. In Figure 5.2, the directions of all  $C_D(x)$  traces are counterclockwise ( $E$  is negative) and thereby, the energy transfer is from the cylinder to the fluid. The PSD of  $C_D$  indicates the existence of one peak that occurs at the forcing frequency,  $f$ , for each of the frequency ratios,  $1.0 \leq f/f_0 \leq 4.0$ . This indicates that the drag coefficient,  $C_D$ , oscillates with  $f$  in all cases.

Figure 5.3 displays the equivorticity and streamline patterns, and the pressure distribution in the near wake over two periods of cylinder oscillation,  $2T$ , when  $f/f_0 = 2.0$ . All the snapshots that follow, at  $t = 0T$  correspond to the instant when the cylinder reaches its maximum displacement,  $x(t) = A$ . In all the equivorticity plots that follow, red colours correspond to positive vorticity (counterclockwise rotation) and blue

colours indicate negative vorticity (clockwise rotation). All the streamline patterns that follow are plotted in the frame of reference (symbolically denoted by  $\tilde{X}$ ) which moves with the uniform flow. The velocities in  $X$  and  $\tilde{X}$  frames of reference are related as

$$\tilde{u} = u - 1, \quad \tilde{v} = v, \quad (5.2)$$

where  $\tilde{\vec{u}} = (\tilde{u}, \tilde{v}, 0)$  and  $\vec{u} = (u, v, 0)$  are the dimensionless fluid velocities in  $\tilde{X}$  and  $X$  frames of reference, respectively. In Figure 5.3, the snapshots at  $t = 0T$  and  $t = 2T$  are almost identical. Therefore, the lock-on occurs over  $2T$ . The vortex shedding mode at this frequency is the asymmetric **2S** mode, per  $2T$ , in which two vortices alternately shed from the upper and lower sides of the cylinder over one period of cylinder oscillation,  $T$ . The pressure distribution presented in the last column of Figure 5.3 indicates that the high (positive) pressure region is associated with the stagnation region (region where the uniform flow contacts the cylinder). This figure suggests that at  $t = 0T$  the low (negative) pressure region develops at the lower side of the cylinder following the development of the positive vortex in the lower vortex shedding layer. As the positive vortex develops, the high pressure region in stagnation seems to move in the counterclockwise direction up to time instant  $t = T$ . At the same time,  $0T \leq t \leq T$ , the low pressure region completely shifts to the upper side of the cylinder. Furthermore, the development of the negative vortex in the upper vortex shedding layer over  $T \leq t \leq 2T$  leads to the movement of the low pressure region from the upper side of the cylinder to the lower side of the cylinder. In addition, the high pressure region in stagnation moves in the clockwise direction over  $T \leq t \leq 2T$ . Taking an overview of Figure 5.3, it can also be seen that the pressure decreases towards vortex centers, indicating the rotation of the fluid inside

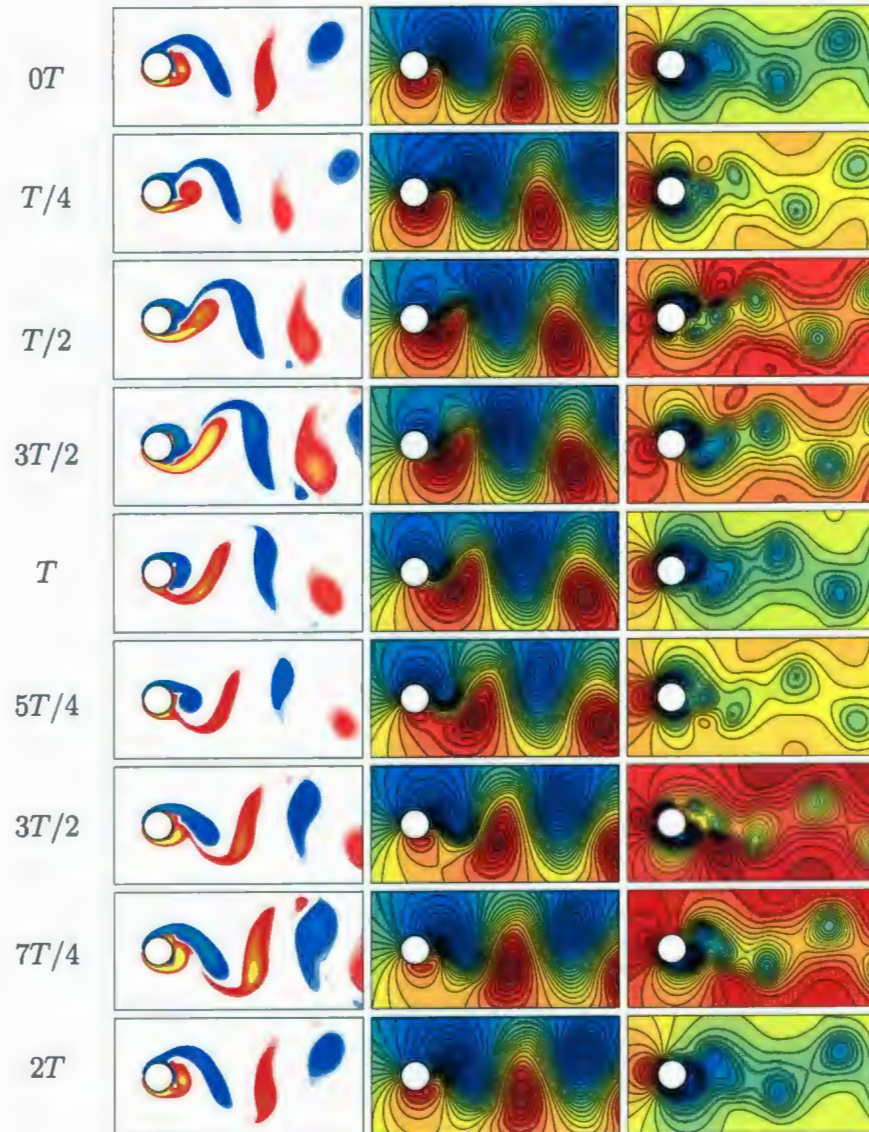


Figure 5.3: The equivorticity patterns (left), the streamline patterns (middle) and the pressure distribution in the near wake (right) over two periods of cylinder oscillation,  $2T$ , at  $R = 200$ :  $A = 0.13$ ,  $f/f_0 = 2.0$ ,  $h = \infty$  ( $T \approx 2.525$ ,  $101 \leq t \leq 106$ ). The locked-on **2S** mode, per  $2T$ , is observed.

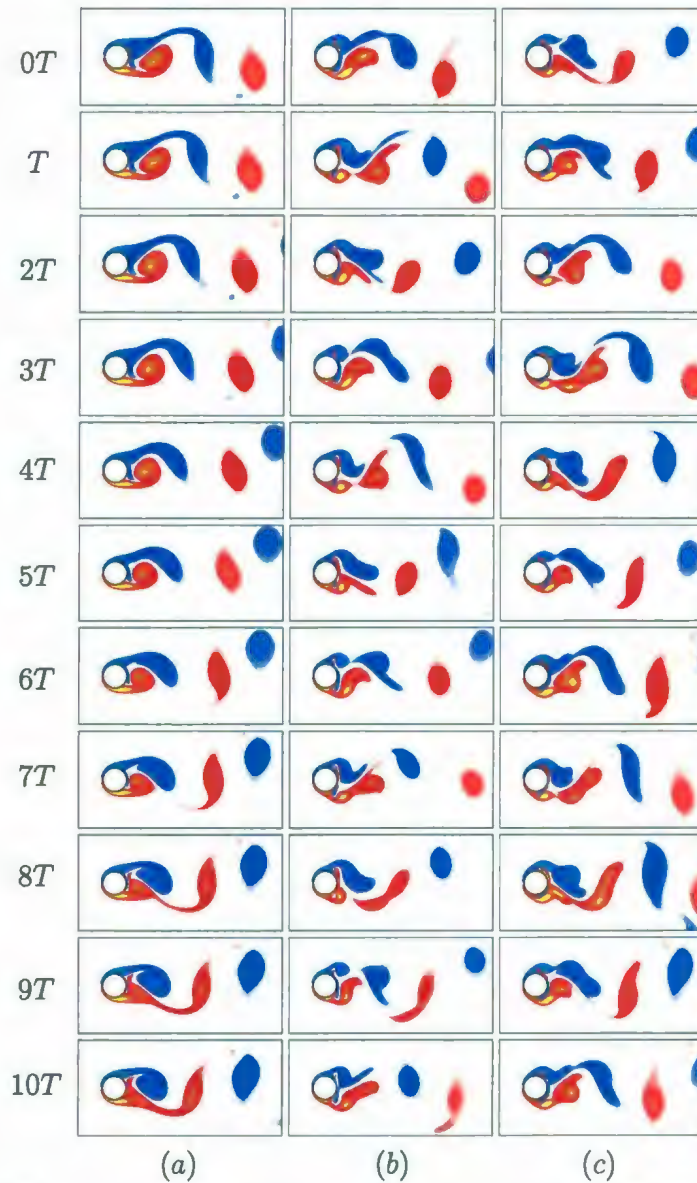


Figure 5.4: The equivorticity patterns over ten periods of cylinder oscillation,  $10T$ , at  $R = 200$ :  $A = 0.13$ ,  $h = \infty$  and (a)  $f/f_0 = 1.0$  ( $T \approx 5.051$ ,  $80.8 \leq t \leq 131.3$ ), (b)  $f/f_0 = 3.0$  ( $T \approx 1.684$ ,  $101 \leq t \leq 118$ ), (c)  $f/f_0 = 4.0$  ( $T \approx 1.263$ ,  $127.5 \leq t \leq 138.9$ ) (non-periodic state).

each vortex. Moreover, the absolute value of the pressure in the vortex center seems to decrease as the vortex propagates into the near wake of the cylinder.

To support the claim that at  $f/f_0 = 1.0, 3.0, 4.0$  the vortex shedding is not locked-on to the cylinder motion, a series of instantaneous equivorticity plots over ten periods of cylinder oscillation,  $10T$ , is plotted in Figure 5.4. This figure clearly shows that the frequency of the vortex shedding is not locked-on to the frequency of cylinder oscillation.

In the range of the frequency ratios  $f/f_0 \geq 3.0$ , the vortex shedding seems to be more complicated due to the strong interaction between the cylinder and the shed vortices. For these frequency ratios, the immediate coalescence or merging of co-rotating vortices is observed in the near wake region. A similar phenomenon for the combined transverse and in-line motion of the pivoting cylinder at  $R \approx 700$  is reported in the experimental work by Flemming and Williamson (2005). In their work, a close up study of the vortex formation involving the vortex coalescence phenomenon is performed as follows: (i) the vortices being developed in the shear layers over the vortex shedding cycle,  $T_0$ , are subsequently marked as "1", "2", "3", etc.; (ii) the vortices which result from the coalescence of the smaller vortices are symbolically represented as the sum of the markers of the vortices which coalesce. For example, the vortex is designated as "1+2" if it results from the coalescence of the vortices marked as "1" and "2". In what follows, the methodology of Flemming and Williamson (2005) is adopted to describe the vortex coalescence phenomenon.

Figure 5.5 displays the vortex coalescence phenomenon for  $f/f_0 = 4.0$  over two periods of cylinder oscillation,  $2T$ . In this figure, two negative vortices, "1" and "2", and two

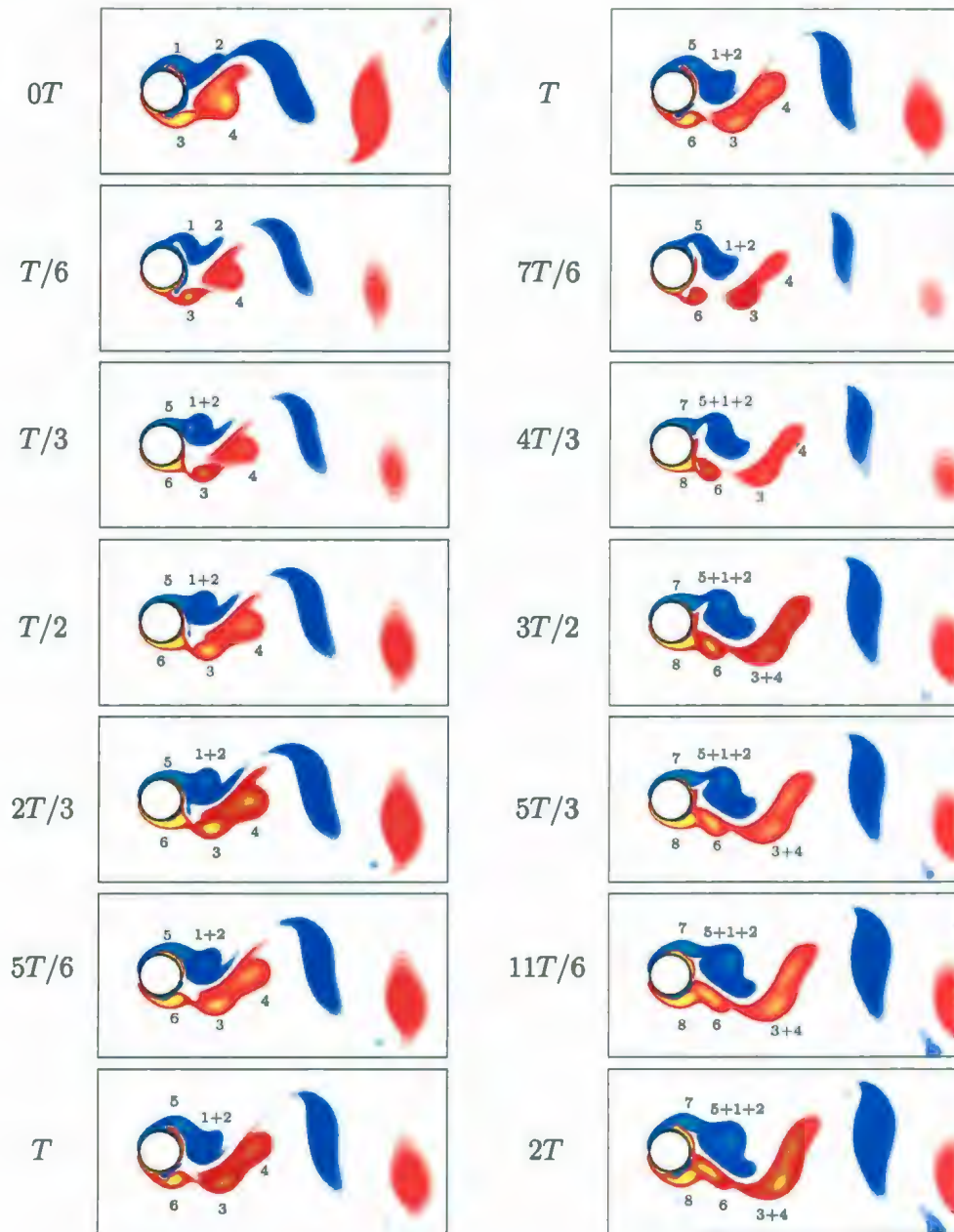


Figure 5.5: The vortex coalescence phenomenon in the near wake of the cylinder over two periods of cylinder oscillation,  $2T$ , at  $R = 200$ :  $A = 0.13$ ,  $f/f_0 = 4.0$  ( $T \approx 1.263$ ,  $133.8 \leq t \leq 136.3$ ),  $h = \infty$  (non-periodic state).

positive vortices, "3" and "4", develop from the upper and lower sides of the cylinder, respectively ( $0T \leq t \leq T/6$ ). The two co-rotating vortices, "1" and "2", coalesce to form a single negative vortex, "1 + 2" ( $t = T/3$ ), while the negative vortex "5" develops in the upper shear layer of the cylinder ( $T/3 \leq t \leq 7T/6$ ). At  $t = 4T/3$ , the vortex "5" coalesces with the vortex "1+2" to form a single negative vortex "5+1+2". On the other hand, the negative vortex "7" develops in the upper share layer of the cylinder. Similarly, the two vortices, "3" and "4", coalesce to form a single positive vortex, "3 + 4", in the lower vortex shedding layer ( $t = 3T/2$ ). Moreover, the positive vortices "6" and "8" develop over the time  $T/3 \leq t \leq 2T$  and  $4T/3 \leq t \leq 2T$ , respectively. It is noted that over the time  $0T \leq t \leq 2T$  both "1 + 2" and "3 + 4" vortices remain detached. Thus, single negative vortices "5 + 1 + 2" and "7", and single positive vortices, "3 + 4", "6" and "8", are being formed, respectively, in the upper and lower vortex shedding layers over this period of time. It is noted that the vortex coalescence phenomenon occurs when (i) one of the two co-rotating vortices is convected with a higher velocity than the other and thereby, these vortices approach one another and (ii) one of the two co-rotating vortices is larger than the other [see Braza *et al.* (1986) for details].

## 5.2 Vortex shedding modes and fluid forces in the presence of the free surface at $h = 0.25, 0.5, 0.75$

The flow characteristics are examined for Froude numbers  $Fr \approx 0.0$  and  $Fr = 0.2, 0.4$ . It is well known that limiting cases of  $Fr \rightarrow 0.0, g \rightarrow \infty$  and  $Fr \rightarrow \infty, g \rightarrow 0.0$

correspond to supergravity and microgravity flows, respectively. Thus, the limiting case of the Froude number  $Fr \approx 0.0$  can be obtained by assuming that  $g \rightarrow \infty$ . Consequently, at  $Fr \approx 0.0$ , the free surface is expected to act similar to a non-deformable surface. The numerical experiments have shown that the pressure signal exhibits pronounced spikes for the case  $Fr \approx 0.0$ . Thus, the flow characteristics cannot be identified, clearly, using the fluctuating fluid forces information.

### 5.2.1 Froude number $Fr \approx 0.0$

The case for  $R = 200$ ,  $A = 0.13$  and  $h = 0.25$  is considered first while the frequency ratio,  $f/f_0$ , varies from 1.0 to 4.0 by increments of 1.0. The observed flow behaviour is (i) non-periodic for  $f/f_0 \leq 3.0$  and (ii) quasi-periodic, per  $5T$ , for  $f/f_0 = 4.0$ .

The typical equivorticity and streamline patterns over five periods of cylinder oscillation,  $5T$ , when  $f/f_0 = 4.0$  are displayed in Figure 5.6. It is noted that in the presence of the free surface streamline patterns in the fluid region  $\Omega_1$  correspond to the steady uniform stream case. In what follows, the streamline patterns in fluid region  $\Omega_2$  are only presented (the streamline patterns in the region  $\Omega_1$  are eliminated). In this figure, the negative vortex developed in the previous vortex shedding cycle becomes detached at  $t \approx T$ . On the other hand, three weak co-rotating vortices develop from the lower side of the cylinder, over  $0T \leq t \leq T$ , and then coalesce to form a single large vortex at the instant  $t \approx T$ . After this period of time, three weak co-rotating vortices are formed from the upper side of the cylinder which causes the shedding of a single positive vortex from the lower side of the cylinder at instant  $t \approx 7T/2$ .

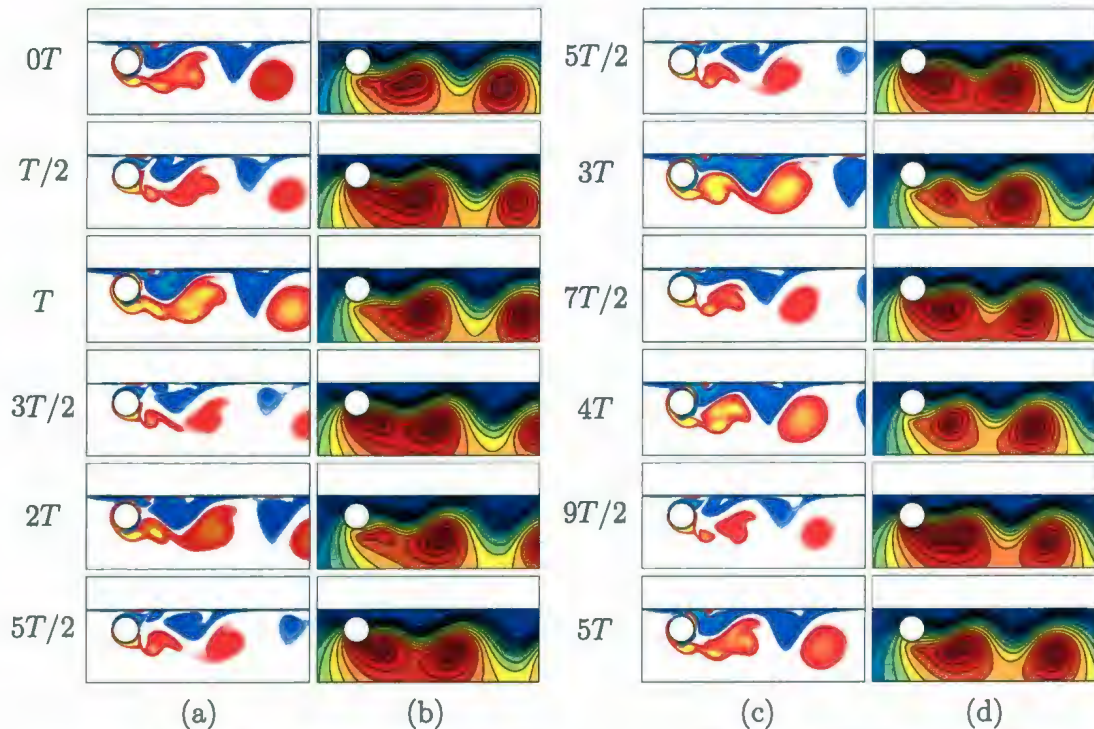


Figure 5.6: The equivorticity patterns ((a), (c)) and the streamline patterns ((b), (d)) over five periods of cylinder oscillation,  $5T$ , at  $R = 200$ :  $A = 0.13$ ,  $f/f_0 = 4.0$ ,  $h = 0.25$ ,  $Fr \approx 0.0$  ( $T \approx 1.263$ ,  $30.25 \leq t \leq 36.55$ ). The quasi-locked-on **C(2S)** mode, per  $5T$ , is observed.

Similarly, three weak co-rotating vortices coalesce in the upper vortex shedding layer to form a single large vortex ( $0T \leq t \leq 3T$ ) which is then shed at  $t \approx T$  in the next vortex shedding cycle. In other words, the cylinder alternately sheds a single vortex from each side over  $5T$ . It is noted that the development of each vortex is a result of coalescence of three weak vortices in the vortex shedding layer. Thus, this vortex shedding mode is designated as the quasi-locked-on **C(2S)** mode, per  $5T$ , using the terminology of Williamson and Roshko (1988). It is seen that the presence of the free surface significantly weakens the negative vortex formed from the upper side of the

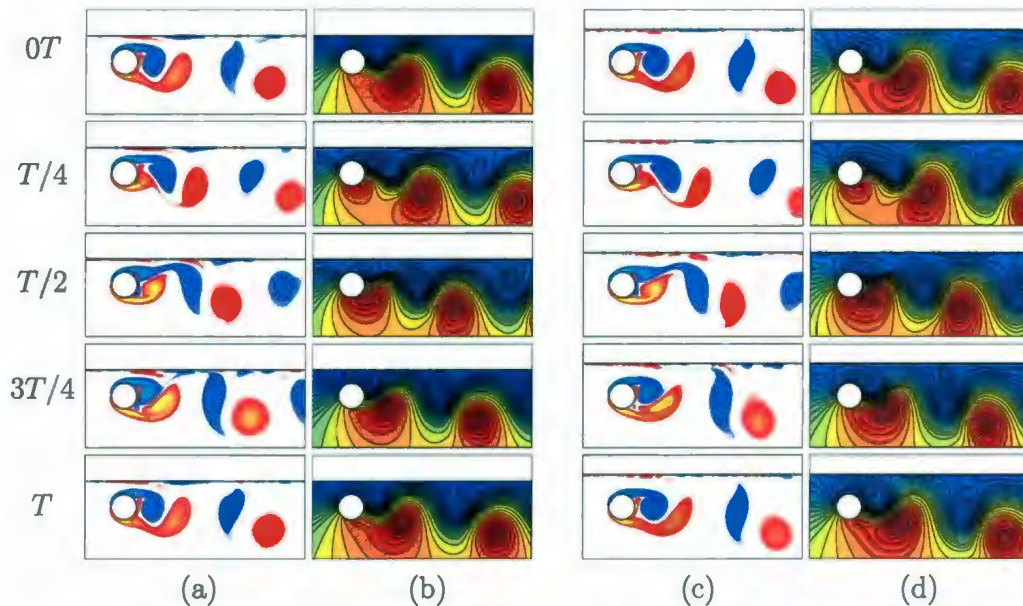


Figure 5.7: The equivorticity patterns ((a), (c)) and the streamline patterns ((b), (d)) over one period of cylinder oscillation,  $T$ , at  $R = 200$ :  $A = 0.13$ ,  $f/f_0 = 1.0$ ,  $Fr \approx 0.0$ , ((a),(b))  $h = 0.5$  ( $T \approx 5.051$ ,  $90.85 \leq t \leq 95.95$ ); ((c),(d))  $h = 0.75$  ( $T \approx 5.051$ ,  $65.65 \leq t \leq 70.65$ ). The locked-on  $2S$  mode, per  $T$ , is observed.

cylinder. It is also noted that negligible free surface deformations are observed which lead to the development of a little amount of oppositely signed vorticity near the free surface. Comparing the results shown in Figures 5.4 and 5.6, it can be seen that the effect of the limiting Froude number,  $Fr \approx 0.0$ , and the free surface presence at  $h = 0.25$  is to stabilize the vortex shedding at  $f/f_0 = 4.0$  to produce quasi-locked-on  $C(2S)$  mode, per  $5T$ . On the other hand, the effect of  $Fr \approx 0.0$  and  $h = 0.25$  seems to destabilize lock-on state at  $f/f_0 = 2.0$  when compared to the reference case  $h = \infty$ .

For larger cylinder submergence depths,  $h = 0.5, 0.75$ , different vortex shedding modes and flow regimes resulting in significant changes in the near wake structure have been observed. It is noted that a similar phenomenon has been also reported in

the numerical work by Reichl *et al.* (2005) and the experimental work of Sheridan *et al.* (1995, 1997) for the case of uniform flow past a stationary cylinder in the presence of the free surface. In fact, the works of Reichl *et al.* (2005) ( $R = 180, 0 \leq Fr \leq 0.7$  and  $0.1 \leq h \leq 0.5$ ) and Sheridan *et al.* (1995, 1997) ( $0 < h \leq 0.75, 5990 \leq R \leq 9120$  and  $0.47 \leq Fr \leq 0.72$ ) have shown that at certain  $Fr$ - $h$  combinations, the presence of the free surface causes a switching between the near wake states. These studies found that the near wake spontaneously changes from one state to another in a pseudo-periodic manner. The present numerical simulations indicate that the vortex shedding becomes locked-on to the cylinder motion when  $f/f_0 \leq 2.0$ . The observed locked-on asymmetric vortex shedding modes are **2S**, per  $T$ , when  $f/f_0 = 1.0, h = 0.5, 0.75$ ; **C(2S)**, per  $2T$ , and **P+S**, per  $2T$ , when  $f/f_0 = 2.0, h = 0.5, 0.75$ , respectively. As the frequency ratio increases,  $f/f_0 \geq 3.0$ , the flow behaviour becomes more complicated. In fact, the present numerical simulations confirm the existence of two distinctly different flow regimes for  $f/f_0 = 3.0, 4.0, h = 0.5$  and  $f/f_0 = 3.0, h = 0.75$ . It has been observed that the flow is quasi-periodic within a short period of time after the vortex shedding begins and then the transition of the flow into the non-periodic state occurs. It is noted that a similar phenomenon is also reported in the experimental study by Cetiner and Rockwell (2001) for the case of cylinder subject to in-line oscillations in uniform flow in the presence of the free surface ( $R = 917, 2075, Fr = 0.07, 0.158, A = 0.96, f/f_0 = 0.44, 1.0$  and  $h = 0.06, 0.19, 11.23$ ). Their work has shown that for certain  $Fr$ - $h$  combinations the vortex shedding exhibits locked-on (or quasi-locked-on) states at least over several cycles of cylinder oscillation and then the transition to the non-locked-on state occurs. In all cases that follow, when the transition of the flow from the quasi-periodic state into the non-periodic state is ob-

served, the regime in which the flow is quasi-periodic is designated as “quasi-periodic”; the non-periodic flow state is designated as “non-periodic”. Thus, in quasi-periodic state, the quasi-locked-on vortex shedding modes are designated as **C(2S)**, per  $3T$ , when  $f/f_0 = 3.0$ ,  $h = 0.5$ ; **2P**, per  $4T$ , when  $f/f_0 = 4.0$ ,  $h = 0.5$  and **C(P+S)**, per  $3T$ , when  $f/f_0 = 3.0$ ,  $h = 0.75$ . At the highest frequency ratio,  $f/f_0 = 4.0$ , the locked-on **C(P+S)**, per  $4T$ , mode is observed when  $h = 0.75$ .

Figure 5.7 shows the equivorticity and streamline patterns over one period of cylinder oscillation,  $T$ , when  $f/f_0 = 1.0$ ,  $h = 0.5, 0.75$ . The vortex formations at this frequency ratio occur in the locked-on asymmetric **2S** mode, per  $T$ , in which two vortices are alternately shed from both sides of the cylinder over one period of cylinder oscillation. It is clearly seen that the near wake structures at  $h = 0.5$  and  $0.75$  show almost the same behaviour. However, the decrease in the vortex formation length ( $\approx 14.3\%$ ) is evident as the cylinder submergence depth is reduced from  $h = 0.75$  to  $0.5$ . It is noted that the vortex formation length is defined as the length of the positive vortex developing in the lower vortex shedding layer and can be measured as the distance between the cylinder surface and the end of the re-circulation zone along the near wake centerline. Furthermore, as  $h$  is reduced to  $0.5$ , the proximity of the free surface tends to bring the vortices closer together as shown in Figure 5.7(a). The appearance of the opposite signed vorticity near the free surface suggests that for the limiting case  $Fr \approx 0.0$ , the free surface acts similar to a non-deformable surface. However, unlike the case of the non-deformable surface, the free surface allows a local surface acceleration which yields a diffusion of the vorticity across the free surface interface.

The typical equivorticity and streamline patterns over two periods of cylinder oscillation,  $2T$ , when  $f/f_0 = 2.0$  and  $h = 0.5, 0.75$  are displayed in Figure 5.8. The vortex shedding modes are the locked-on asymmetric **C(2S)** mode, per  $2T$ , when  $h = 0.5$  and the locked-on asymmetric **P+S** mode, per  $2T$ , when  $h = 0.75$ . In Figure 5.8(a,b), two co-rotating vortices coalesce to form a single large positive vortex which is then shed in the downstream of the cylinder ( $0T \leq t < 4T/5$ ). On the other hand, a single negative vortex develops over  $0T \leq t \leq 6T/5$  and then sheds at  $t = 7T/5$ . At  $h = 0.75$ , a pair of positive vortices developed in the previous vortex shedding cycle is shed into the near wake of the cylinder at  $t = 4T/5$ . Furthermore, the negative vortex develops in the upper vortex shedding layer over  $0T \leq t \leq 8T/5$  and is then shed into the near wake of the cylinder ( $t = 9T/5$ ). Taking an overview of Figure 5.8, it is evident that the development of the negative vortex in the upper shedding layer is similar for both  $h = 0.5$  and  $0.75$ . However, the proximity of the free surface seems to affect the development of the positive vorticity from the lower side of the cylinder by inducing the coalescence of the small vortices. Moreover, the decrease of the cylinder submergence depth,  $h$ , is seen to speed up the vortex shedding process and the negative vortices propagate more rapidly into the downstream. Figure 5.8 indicates that at both cylinder submergence depths,  $h = 0.5$  and  $0.75$ , the vortex formation length is approximately the same.

In the case when  $f/f_0 = 3.0$ , two distinctly different near wake states are observed when  $h = 0.5, 0.75$ . At the smaller cylinder submergence depth,  $h = 0.5$ , the vortex shedding produces quasi-locked-on **C(2S)** mode, per  $3T$ , within twelve periods of cylinder oscillation,  $12T$  (quasi-periodic state). At  $t = 12T$ , a switchover in the flow behaviour is observed and the flow becomes non-periodic. Similarly, at  $h = 0.75$ ,

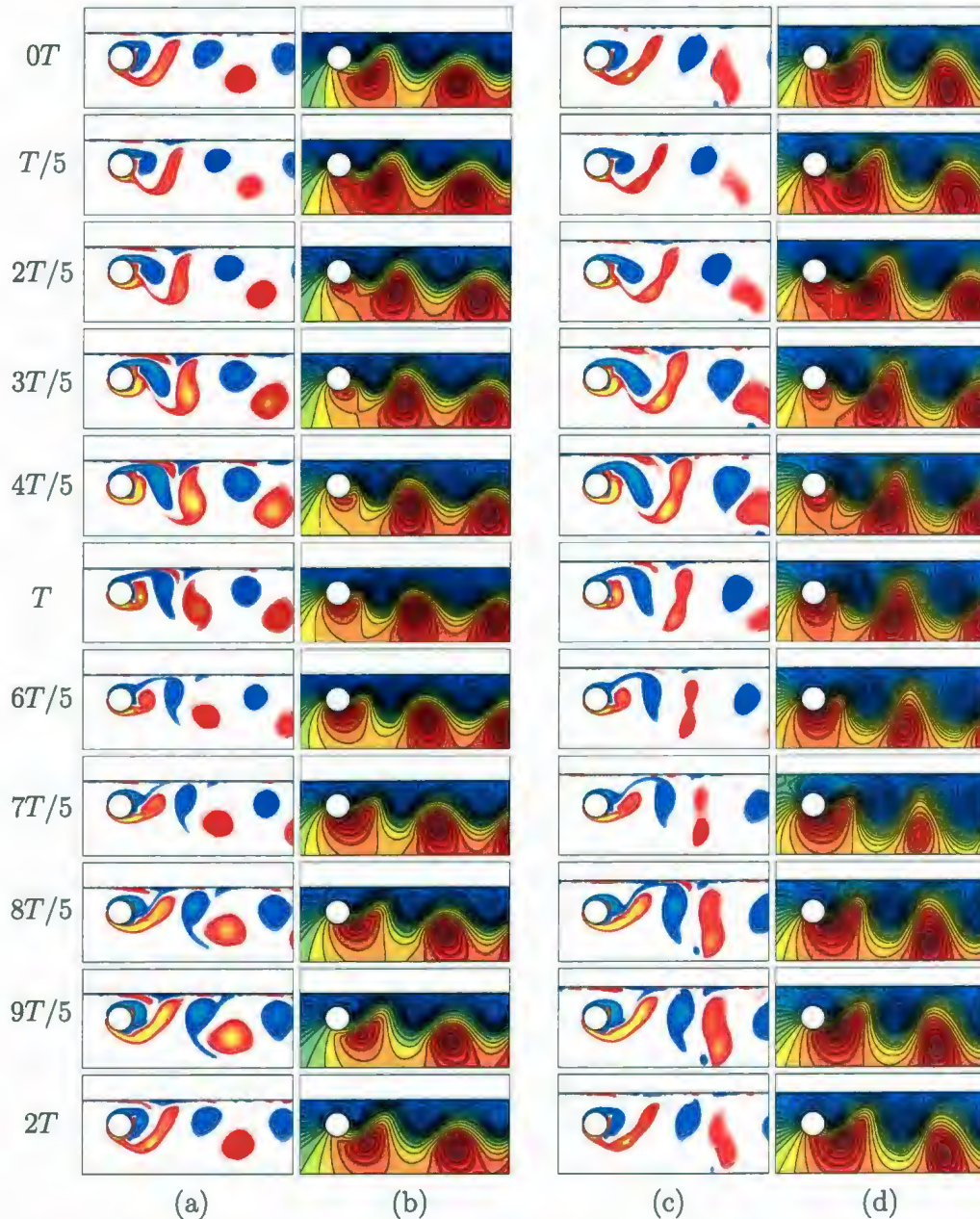


Figure 5.8: The equivorticity patterns ((a), (c)) and the streamline patterns ((b), (d)) over two periods of cylinder oscillation,  $2T$ , at  $R = 200$ :  $A = 0.13$ ,  $f/f_0 = 2.0$ ,  $Fr \approx 0.0$ , ((a),(b))  $h = 0.5$ ; ((c),(d))  $h = 0.75$  ( $T \approx 2.525$ ,  $95.95 \leq t \leq 100.95$ ). The locked-on C(2S) and P+S modes, per  $2T$ , are observed when  $h = 0.5, 0.75$ , respectively.

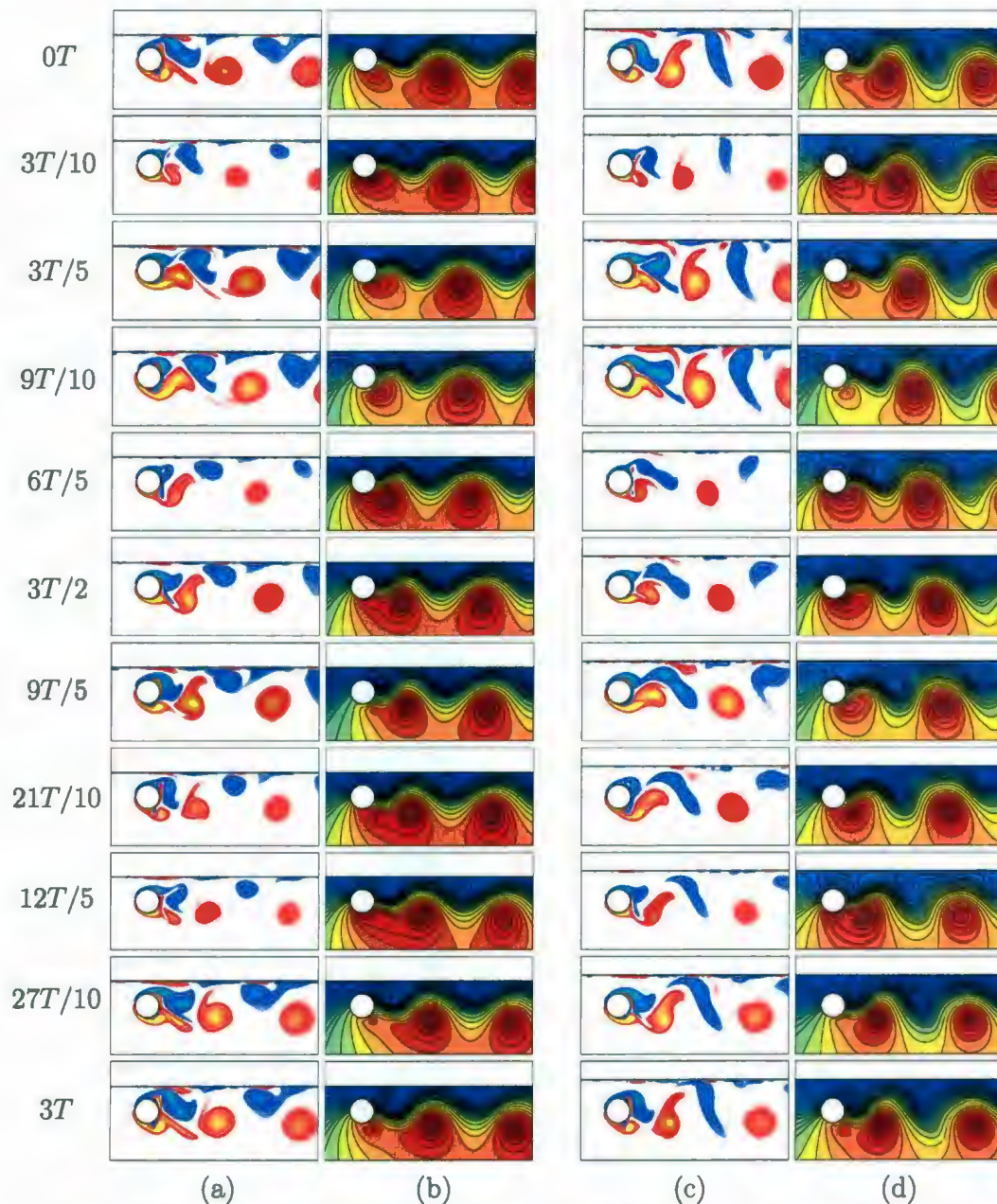


Figure 5.9: The equivorticity patterns ((a), (c)) and the streamline patterns ((b), (d)) over three periods of cylinder oscillation,  $3T$ , at  $R = 200$ :  $A = 0.13$ ,  $f/f_0 = 3.0$ ,  $Fr \approx 0.0$ , ((a),(b))  $h = 0.5$  ( $T \approx 1.684$ ,  $21.85 \leq t \leq 26.85$ ); ((c),(d))  $h = 0.75$  ( $T \approx 1.684$ ,  $57.15 \leq t \leq 62.25$ ). The quasi-locked-on C(2S) and C(P+S) modes, per  $3T$ , are observed within  $12T$  and  $24T$  when  $h = 0.5, 0.75$ , respectively.

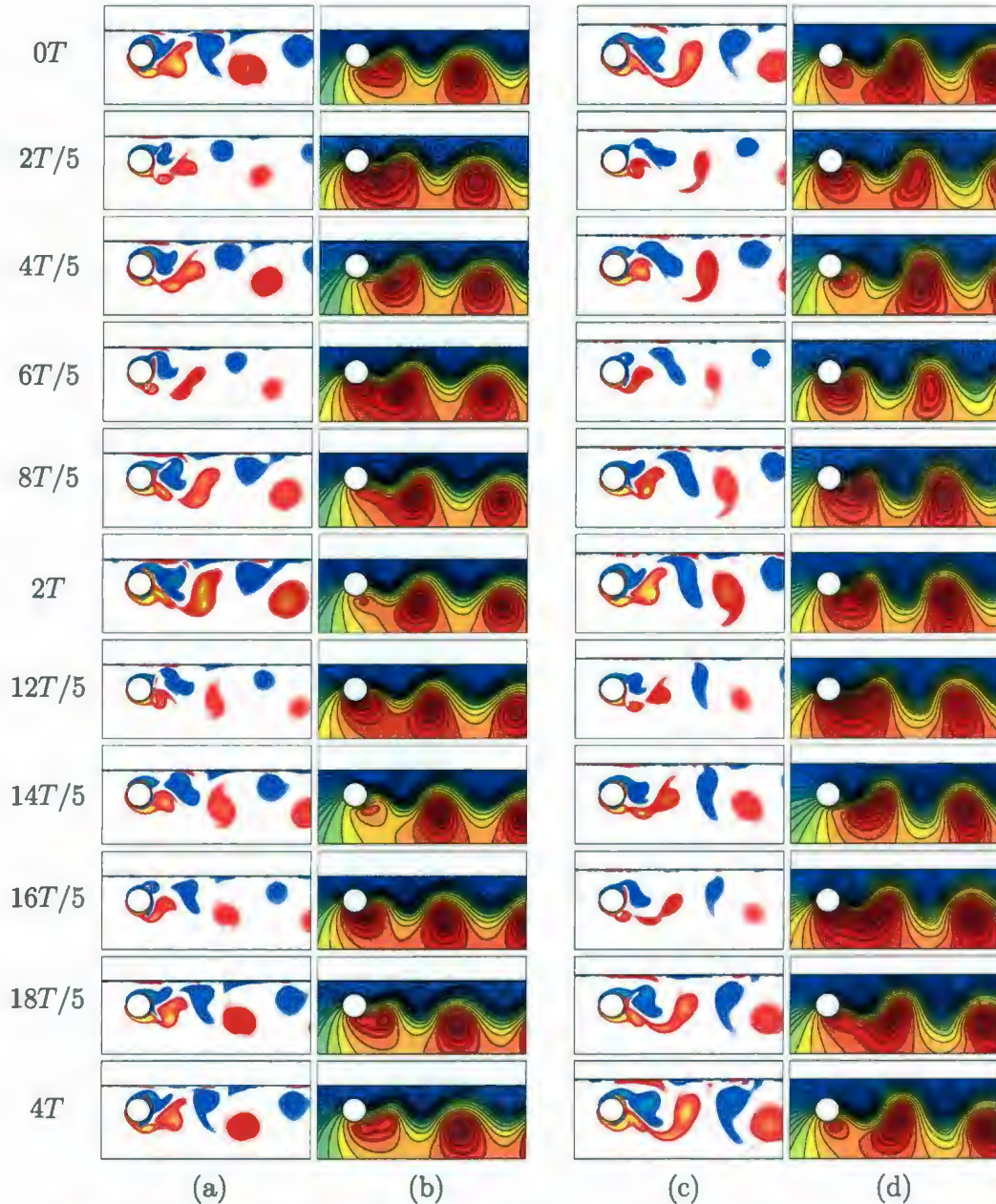


Figure 5.10: The equivorticity patterns ((a), (c)) and the streamline patterns ((b), (d)) over four periods of cylinder oscillation,  $4T$ , at  $R = 200$ :  $A = 0.13$ ,  $f/f_0 = 4.0$ ,  $Fr \approx 0.0$ , ((a),(b))  $h = 0.5$  ( $T \approx 1.263$ ,  $40.35 \leq t \leq 45.45$ ); ((c),(d))  $h = 0.75$  ( $T \approx 1.263$ ,  $78.25 \leq t \leq 83.25$ ). The quasi-locked-on  $2P$  mode, per  $4T$ , is observed within  $20T$  when  $h = 0.5$ . The locked-on  $C(P+S)$  mode, per  $4T$ , is observed when  $h = 0.75$ .

the vortex shedding is quasi-locked-on to the motion of the cylinder in **C(P+S)** mode, per  $3T$ , within  $24T$  (quasi-periodic state) and then the transition of the flow into the non-periodic state is observed. Figure 5.9 displays the equivorticity and streamline patterns when  $f/f_0 = 3.0$ ,  $h = 0.5, 0.75$ . At  $h = 0.5$ , a pair of small co-rotating vortices develops in the upper vortex shedding layer over  $0T \leq t \leq 3T/5$ . These vortices coalesce at  $t = 3T/5$  to produce a large negative vortex which is shed immediately ( $t \approx 9T/10$ ). Similarly, a pair of small co-rotating vortices coalesce to produce a single large positive vortex being shed into the downstream of the cylinder ( $3T/5 \leq t \leq 9T/5$ ). On the other hand, in the quasi-locked-on **C(P+S)** mode, per  $3T$ , shown in Figure 5.9(c,d), a pair of negative vortices sheds at  $3T/2$  and two small vortices develop in the lower vortex shedding layer over  $3T/2 \leq t \leq 12T/5$ . The two co-rotating vortices coalesce to form a single large positive vortex which becomes detached at  $t \approx 3T$ . As is seen from Figure 5.9, the near wake shows further signs of the influence of the free surface with the negative vortices propagating towards the free surface. At the larger cylinder submergence depth,  $h = 0.75$ , the shed vortices appear to be elongated in the transverse direction. As the cylinder submergence depth,  $h$ , is reduced to 0.5, the vortices become more oval shaped when propagating into the downstream of the cylinder. The proximity of the free surface at  $h = 0.5$  seems to speed up the vortex shedding process when compared to the case of  $h = 0.75$ . It is interesting to note that at these depths of the cylinder submergence depth,  $h = 0.5, 0.75$ , a large portion of the opposite signed vorticity diffuses into both the free surface and the near wake.

The last frequency ratio considered in this section is  $f/f_0 = 4.0$ . For this frequency ratio, when  $h = 0.5$  the vortex shedding produces quasi-locked-on **2P** mode,

per  $4T$ , within  $20T$  (quasi-periodic state) and the flow becomes non-periodic at  $20T < t < 80T$  whereas the locked-on **C(P+S)** mode, per  $4T$ , is observed when  $h = 0.75$ . The typical equivorticity and streamline patterns for  $f/f_0 = 4.0$  when  $h = 0.5, 0.75$  are displayed in Figure 5.10. This figure shows that at  $h = 0.5$ , a pair of positive and a pair of negative vortices are shed in the near wake over  $0T < t \leq 6T/5$  and  $6T/5 < t \leq 12T/5$ , respectively. When  $h = 0.75$ , a pair of negative vortices and the positive vortex (developed in the previous vortex shedding cycle) are shed over  $0T < t \leq 2T/5$ . Furthermore, a pair of small positive vortices develops in the lower vortex shedding layer ( $2T/5 < t \leq 8T/5$ ). These positive vortices coalesce to form a single vortex which becomes detached at  $t = 2T/5$  in the next vortex shedding cycle. As is seen from Figure 5.10, the affect of the decrease in the cylinder submergence depth,  $h$ , is to shorten ( $\approx 45.6\%$ ) the vortex formation length. It is also interesting to note that the negative vortices tend to propagate upward the cylinder in both of the cases shown in Figure 5.10. The shed negative vortices become more oval shaped close to the free surface when  $h = 0.5$ . In contrast, at  $h = 0.75$ , the shed negative vortices appear to be elongated in the transverse direction. It is also seen that at  $h = 0.5$ , the shed vortices tend to be close to each other unlike the case when  $h = 0.75$ .

The effect of the free surface inclusion at  $Fr \approx 0.0$ ,  $h = 0.25, 0.5, 0.75$  and the frequency ratio,  $f/f_0$ , on flow regimes, vortex shedding modes and their periods,  $T_0$ , is summarized in Table 5.1. This table indicates that the presence of the free surface at  $Fr \approx 0.0$ ,  $h = 0.25$  seems to break up the periodicity for  $f/f_0 = 2.0$  when compared to the corresponding case in the absence of the free surface. Furthermore, at the high frequency ratio  $f/f_0 = 4.0$ , the effect of the free surface ( $Fr \approx 0.0$ ) at  $h = 0.25$  seems to stabilize the vortex shedding so that the quasi-locked-on **C(2S)** mode, per  $5T$ , is

|         | $h = 0.25$    |       | $h = 0.5$  |       | $h = 0.75$  |       | $h = \infty$ |       |
|---------|---------------|-------|--|-------|---|-------|--------------|-------|
| $f/f_0$ | Mode          | $T_0$ | Mode   | $T_0$ | Mode  | $T_0$ | Mode         | $T_0$ |
| 1.0     | non-locked    | -     | <b>2S</b>  | $T$   | <b>2S</b>   | $T$   | non-locked   | -     |
| 2.0     | non-locked    | -     | <b>C(2S)</b>   | $2T$  | <b>P+S</b>  | $2T$  | <b>2S</b>    | $2T$  |
| 3.0     | non-locked    | -     | <b>C(2S)*</b> (within $12T$ );<br>non-locked ( $12T < t < 60T$ ) | $3T$  | <b>C(P+S)*</b> (within $24T$ );<br>non-locked ( $24T < t < 60T$ ) | $3T$  | non-locked   | -     |
| 4.0     | <b>C(2S)*</b> | $5T$  | <b>2P*</b> (within $20T$ );<br>non-locked ( $20T < t < 80T$ )    | $4T$  | <b>C(P+S)</b>   | $4T$  | non-locked   | -     |

Table 5.1: The effect of the free surface inclusion at  $Fr \approx 0.0$ ,  $h = 0.25, 0.5, 0.75$  and the frequency ratio,  $f/f_0$ , on flow regimes, vortex shedding modes and their periods,  $T_0$ , at  $R = 200$ ,  $A = 0.13$ ,  $1.0 \leq f/f_0 \leq 4.0$ . The superscript “\*” denotes quasi-locked-on modes.

attained unlike in the case  $h = \infty$ . As the cylinder submergence depth,  $h$ , is increased, the presence of the free surface ( $Fr \approx 0.0$ ) seems to stabilize the vortex shedding and the locked-on and quasi-locked-on states of vortex formations can be attained for the flows which are non-periodic in the absence of the free surface. As  $f/f_0$  becomes greater than one, at  $h = 0.5$ , the near wake vorticity breaks up to produce distinctly different modes of vortex shedding when compared to those produced at  $h = 0.75$ . The common observed modes of vortex shedding are the asymmetric **2S** mode when  $h = 0.5$  ( $f/f_0 \leq 3.0$ ) and the asymmetric **P+S** mode when  $h = 0.75$  ( $f/f_0 \geq 2.0$ ). It is also noted that the coalescence between the vortices in the vortex shedding layers appears at the high frequency ratios,  $f/f_0 = 2.0, 3.0$  when  $h = 0.5$  and  $f/f_0 = 3.0, 4.0$  when  $h = 0.75$ .

Figure 5.11 summarizes the effect of the cylinder submergence depth,  $h$  ( $= 0.25, 0.5, 0.75$ ), and the frequency ratio,  $f/f_0$  ( $= 1.0, 2.0, 3.0, 4.0$ ), on the equivorticity patterns for the case  $R = 200$ ,  $A = 0.13$  when  $Fr \approx 0.0$ . The reference case  $h = \infty$  is also

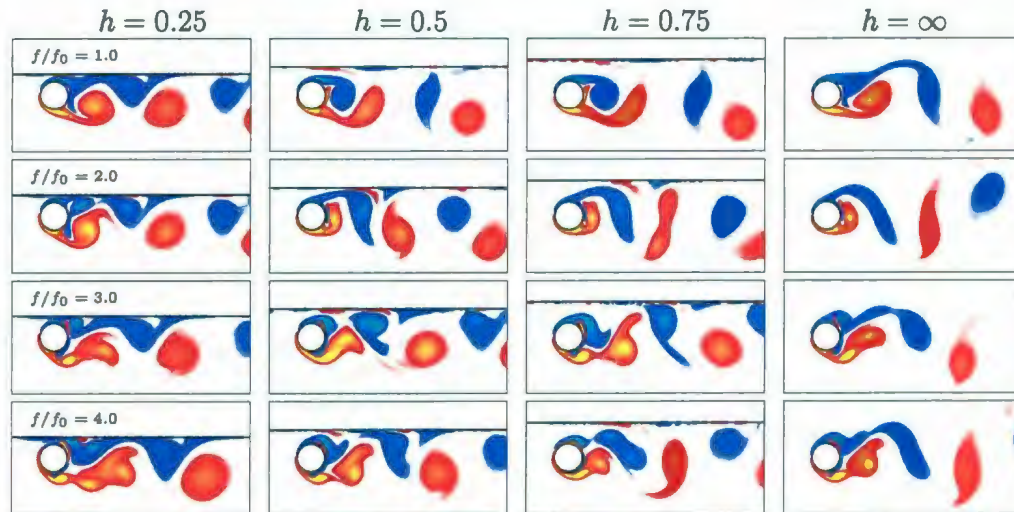


Figure 5.11: The effect of the cylinder submergence depth,  $h$ , and the frequency ratio,  $f/f_0$ , on the equivorticity patterns at  $R = 200$ :  $A = 0.13$ ,  $Fr \approx 0.0$ . All snapshots are taken at the instant  $x(t) = A$ .

shown in this figure. The snapshots are taken at the instant  $x(t) = A$ . It is noted that for the periodic/quasi-periodic cases the snapshots are taken over the time interval in which the flow reaches to a periodic/quasi-periodic state. For non-periodic cases, the commonly appearing equivorticity plots at  $x(t) = A$  (within the time interval  $0 < t \leq 100$ ) are shown in Figure 5.11. Taking an overview of Figure 5.11, it is seen that in all the cases ( $h = 0.25, 0.5, 0.75$ ), the free surface deformations are negligible which suggests that surface interface acts as a non-deformable surface irrespective of the values of  $h$  and  $f/f_0$ . It can be noted from this figure that there is some diffusion of the opposite signed vorticity across the interface and the near wake seems to be more skew symmetric (centerline of the near wake is directed downwards slightly) as  $h$  decreases from  $\infty$  to 0.5. A remarkable difference in the near wake structure is observed when the cylinder is located very close to the free surface ( $h = 0.25$ ). At the

cylinder submergence depth,  $h = 0.25$ , the rapid diffusion of the negative vorticity across the interface is observed (due to a local surface acceleration) and thereby, the upper vortex shedding layer is largely dissipated into the downstream of the cylinder. Thus, the near wake becomes more controlled by positive vortex structures as the cylinder submergence depth,  $h$ , decreases from  $\infty$  to 0.25. Figure 5.11 suggests that as the cylinder submergence depth,  $h$ , is reduced from  $\infty$  to 0.25, the shape and the strength of the vortices become altered such that the vortices traveling downstream of the cylinder become more oval shaped with their major axis lying almost parallel to the free surface. It is also noted from this figure that as  $h$  decreases from 0.75 to 0.25, the vortex formation length seems to increase, in general, (maximum by  $\approx 66.7\%$ ) when  $f/f_0 \geq 2.0$  and to decrease when  $f/f_0 = 1.0$ . Figure 5.11 also shows that for all cylinder submergence depths,  $h = 0.25, 0.5, 0.75$ , the flow behaviour becomes more complicated as  $f/f_0$  increases. For  $f/f_0 = 1.0$  the near wake behaviour is not too dissimilar to that from the reference case  $h = \infty$  while a marked difference in the near wake behaviour is observed for larger frequency ratios,  $f/f_0 \geq 2.0$ , when compared to the case  $h = \infty$ . When  $h = 0.25, 0.5, 0.75$ , and  $f/f_0 \geq 2.0$ , the vortex formation length seems to increase, in general, (maximum by  $\approx 66.7\%$ ) when compared to the reference case  $h = \infty$ . Moreover, as  $f/f_0$  increases from 1.0 to 4.0, the length of the upper vortex layer becomes enlarged so that this layer seems to be largely dissipated into the downstream of the cylinder. This is due to the fact that for the cases  $h = 0.25, 0.5, 0.75$ , the increase in  $f/f_0$  seems to speed up the diffusion of the negative vorticity across the free surface and the near wake becomes dominated by the positive vorticity. This emphasizes the inhibiting influence of the frequency ratio,  $f/f_0$ , on the near wake behaviour when the free surface is present.

### 5.2.2 Froude number $Fr = 0.2$

In this section, the case for  $R = 200$ ,  $A = 0.13$  and  $h = 0.25, 0.5, 0.75$  is considered while the frequency ratio,  $f/f_0$ , varies from 1.0 to 4.0 by increments of 1.0. The

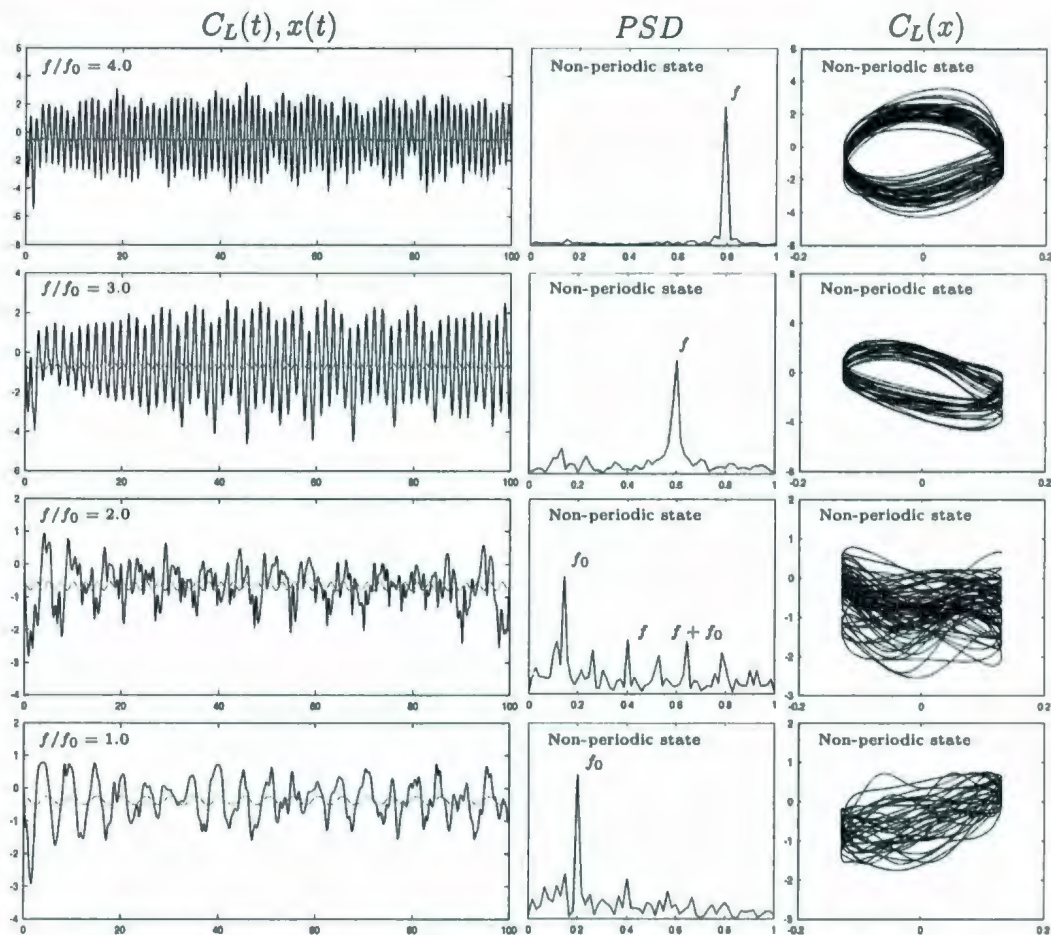


Figure 5.12: The time variation of the lift coefficient,  $C_L$ , (black) and the in-line displacement,  $x(t)$ , (gray); PSD of  $C_L$ ; Lissajous patterns of  $C_L$  at  $R = 200$ :  $A = 0.13$ ,  $1.0 \leq f/f_0 \leq 4.0$ ,  $Fr = 0.2$ ,  $h = 0.25$ .

observed flow behaviour is (i) non-periodic for  $1.0 \leq f/f_0 \leq 4.0$  at  $h = 0.25$  and for  $f/f_0 \geq 3.0$  at  $h = 0.5, 0.75$  and (ii) quasi-periodic, per  $T$ , for  $f/f_0 = 1.0$ , and per

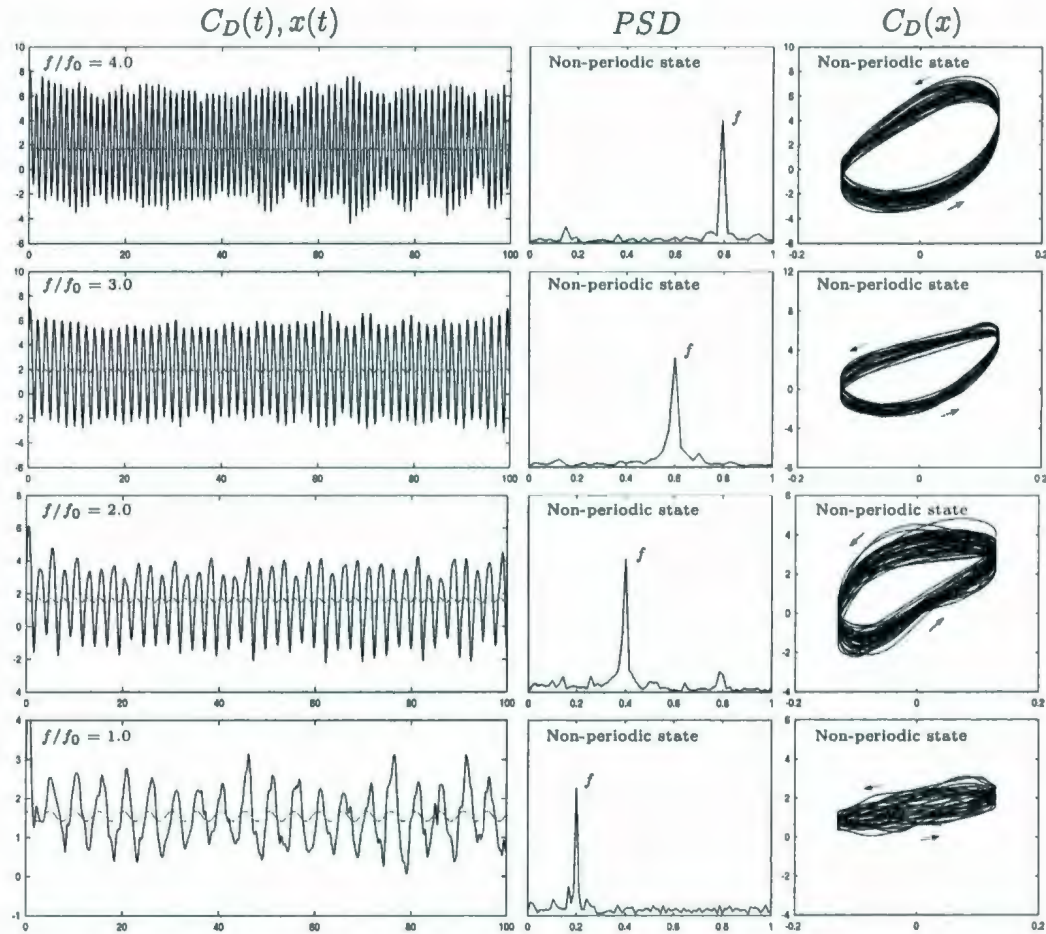


Figure 5.13: The time variation of the drag coefficient,  $C_D$ , (black) and the in-line displacement,  $x(t)$ , (gray); PSD of  $C_D$ ; Lissajous patterns of  $C_D$  at  $R = 200$ :  $A = 0.13$ ,  $1.0 \leq f/f_0 \leq 4.0$ ,  $Fr = 0.2$ ,  $h = 0.25$ .

$2T$ , for  $f/f_0 = 2.0$  at  $h = 0.5, 0.75$ .

The time history of the lift coefficient,  $C_L$ , the PSD of  $C_L$  and the Lissajous patterns of  $C_L$  for the case when  $Fr = 0.2$ ,  $h = 0.25$  are displayed in Figure 5.12. It is evident that neither of the  $C_L$  curves shows a repetitive pattern which indicates locked-on states. The non-locked-on states of the near wake for this range of param-

eters are also confirmed by the corresponding traces of  $C_L(x)$ . At large frequency ratios,  $f/f_0 \geq 3.0$ , the Lissajous patterns exhibit more congruent shapes than that of  $f/f_0 \leq 2.0$ . In all cases shown in Figure 5.12, the traces of  $C_L(x)$  show a definite decrease in repeatability due to the loss of phase-locking. At  $f/f_0 \leq 2.0$ , the free surface is seen to produce hysteresis loops lying largely in the lower half plane. On the other hand, when  $f/f_0 \geq 3.0$ , the hysteresis loops shift towards the upper half plane. Considering the PSD plots in Figure 5.12, it is seen that the effect of the free surface is to destabilize the persistence of  $C_L$  patterns when compared to the case when the free surface is absent (see Figure 5.1). The PSD of  $C_L$  indicates that for  $f/f_0 \leq 2.0$  the dominant peak occurs at  $f_0$  whereas for the larger frequency ratios,  $f/f_0 \geq 3.0$ , the dominant peak is observed at  $f$ . It is noted that at  $f/f_0 = 2.0$ , the interaction between the vortex shedding and the cylinder oscillations result in a fluctuating lift coefficient,  $C_L$ , with a complex behaviour such that it creates a difficulty in calculating the PSD of  $C_L$  as is shown in Figure 5.12.

The time history of the drag coefficient,  $C_D$ , the PSD of  $C_D$  and the Lissajous patterns of  $C_D$  for the case  $Fr = 0.2$ ,  $h = 0.25$  are shown in Figure 5.13. This figure suggests that for each frequency ratio,  $1.0 \leq f/f_0 \leq 4.0$ , the traces of  $C_D$  are generally destabilized relative to the case when the free surface is absent (see Figure 5.2). In all cases, the patterns of  $C_D$  are non-repetitive. Spectra corresponding to the  $C_D$  signatures show one dominant peak that occurs at  $f$  when  $1.0 \leq f/f_0 \leq 4.0$ . Thus, it is evident that in all cases,  $C_D$  oscillates with the forcing frequency,  $f$ . The plots of  $C_D(x)$  again show non-congruent trajectories which indicate the loss of phase-locking between the cylinder motion and the fluctuating drag coefficient,  $C_D$ . It is also seen that the hysteresis loops of  $C_L(x)$  essentially confine in the upper half plane. The

effect of  $f/f_0$  seems to shift hysteresis loops further into both the upper and lower half planes. At all the considered frequency ratios,  $f/f_0$ , the directions of the hysteresis loops of  $C_D(x)$  are counterclockwise. This indicates that for each frequency ratio,  $f/f_0$ , the energy transfer is from the cylinder to the fluid. It is also noted that as  $f/f_0$  increases, the area enclosed by  $C_D(x)$  traces becomes larger and thus the amount of the energy transferred from the cylinder to the fluid increases.

At larger cylinder submergence depths,  $h = 0.5, 0.75$ , the near wake vorticity breaks up to produce quasi-locked-on modes of the vortex formation at small frequency ratios  $f/f_0 \leq 2.0$ . The lock-on has not been observed at any other value of the frequency ratio,  $f/f_0 \geq 3.0$  for the cases  $Fr = 0.2, h = 0.5, 0.75$ . Figures 5.14 and 5.15 show the time histories of the lift coefficient,  $C_L$ , the PSD of  $C_L$  and the Lissajous patterns of  $C_L$  for  $h = 0.5, 0.75$ , respectively. At cylinder submergence depths  $h = 0.5, 0.75$  the traces of  $C_L$  exhibit almost repeatable patterns, per  $T$ , when  $f/f_0 = 1.0$  and per  $2T$ , when  $f/f_0 = 2.0$ . However, it is noted that the traces of  $C_L$  are less persistent from cycle to cycle of cylinder oscillation and thereby, the increase in phase variations between  $C_L$  and the cylinder motion is evident. The corresponding spectra and Lissajous trajectories indicate that the lift coefficient,  $C_L$ , oscillates at the natural vortex shedding frequency,  $f_0$ , (dominant peak in the PSD) when  $f/f_0 \leq 2.0$ . For  $f/f_0 \geq 3.0$ , neither of the  $C_L$  trajectories shows the repeatable patterns. Moreover, the corresponding traces of  $C_L(x)$  exhibit highly non-congruent shapes. Thus, it is concluded that when  $f/f_0 \geq 3.0$ , the vortex shedding frequency is not synchronized with the frequency of cylinder oscillation,  $f$ . At both cylinder submergence depths,  $h = 0.5, 0.75$ , the PSD analysis of  $C_L$  for  $f/f_0 \geq 3.0$  shows two well defined peaks, at approximately  $f_0, f$  when  $f/f_0 = 3.0$  and  $f_0, 3f_0$  when  $f/f_0 = 4.0$ . Moreover, at

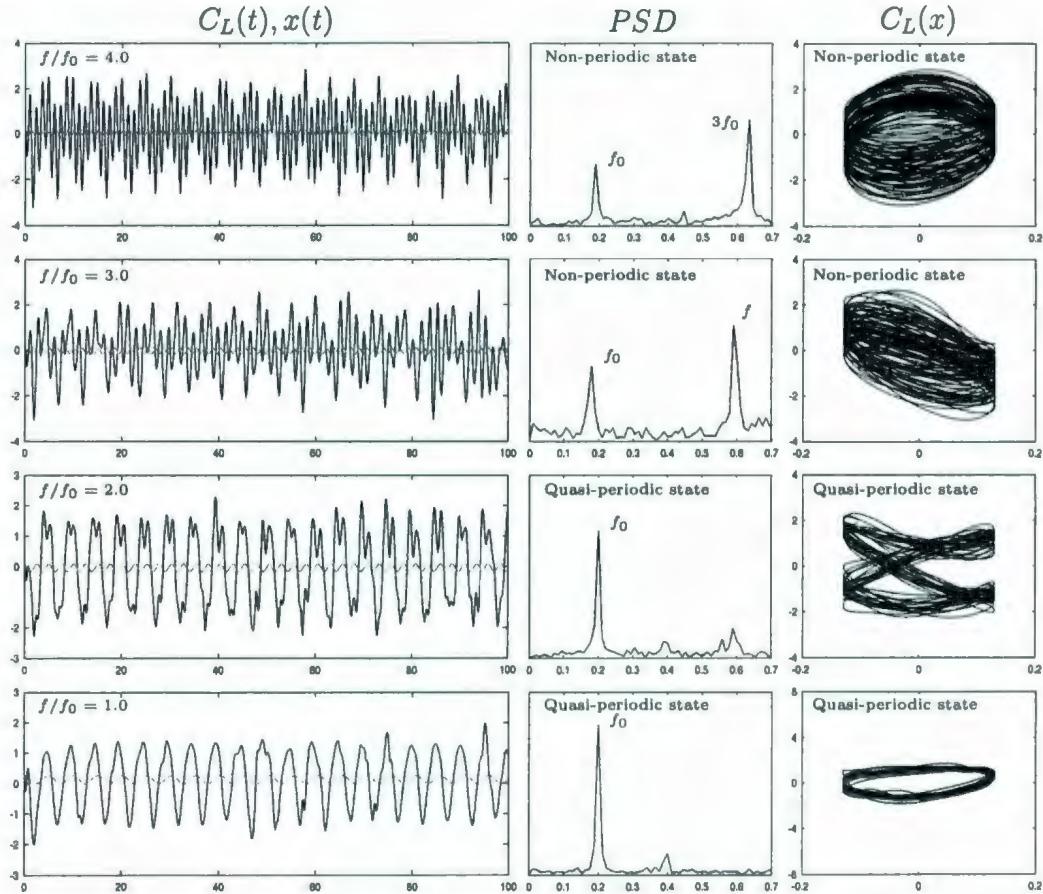


Figure 5.14: The time variation of the lift coefficient,  $C_L$ , (black) and the in-line displacement,  $x(t)$ , (gray); PSD of  $C_L$ ; Lissajous patterns of  $C_L$  at  $R = 200$ :  $A = 0.13$ ,  $1.0 \leq f/f_0 \leq 4.0$ ,  $Fr = 0.2$ ,  $h = 0.5$ .

$h = 0.75$ , two dominant peaks,  $f_0$  and  $f$ , develop when  $f/f_0 = 3.0$ . It is also seen that the effect of  $f_0$  weakens as  $f/f_0$  increases from 1.0 to 4.0. Considering the last columns in Figures 5.14 and 5.15, it is seen that the hysteresis loops of  $C_L(x)$  are confined in both upper and lower half planes.

The plots of Figures 5.16 and 5.17 show that the signatures of  $C_D$ , for the cases

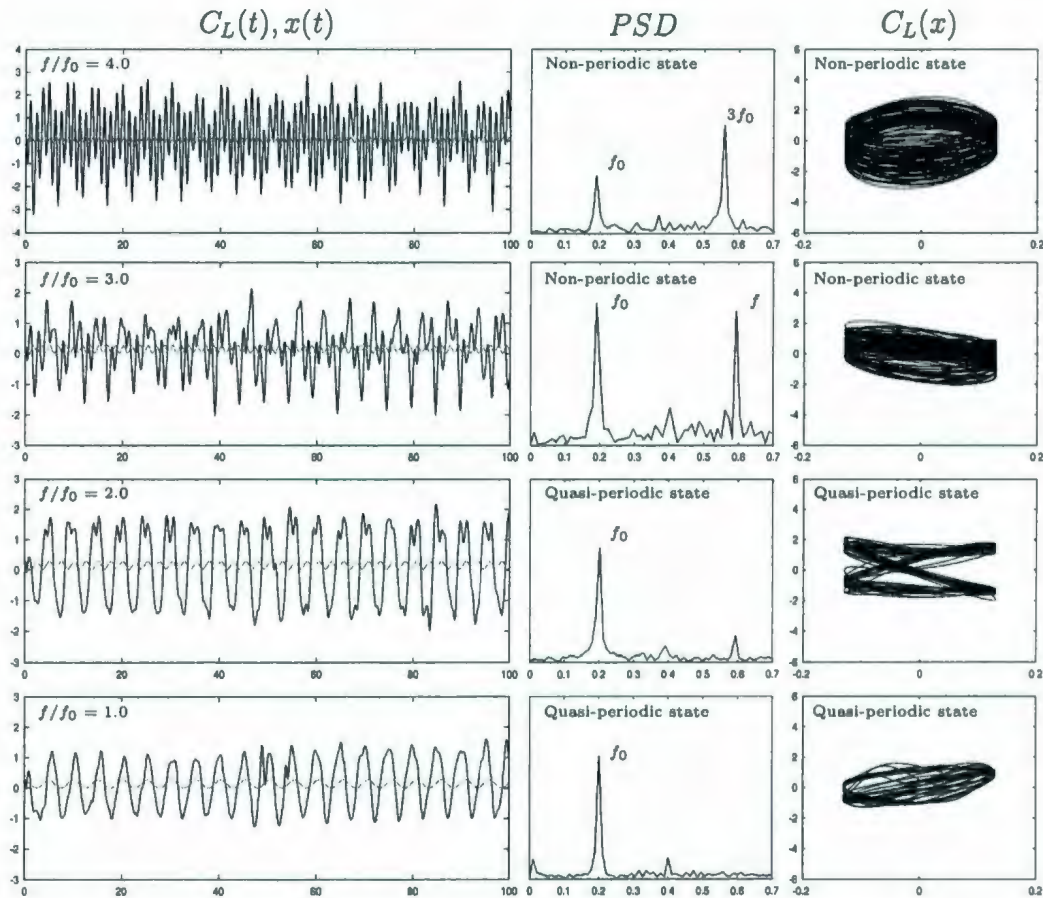


Figure 5.15: The time variation of the lift coefficient,  $C_L$ , (black) and the in-line displacement,  $x(t)$ , (gray); PSD of  $C_L$ ; Lissajous patterns of  $C_L$  at  $R = 200$ :  $A = 0.13$ ,  $1.0 \leq f/f_0 \leq 4.0$ ,  $Fr = 0.2$ ,  $h = 0.75$ .

when  $h = 0.5, 0.75$ , are almost repeatable over one period of cylinder oscillation,  $T$ , and two periods of cylinder oscillation,  $2T$ , for  $f/f_0 = 1.0$  and  $2.0$ , respectively. However, the shapes of  $C_D$  traces are less persistent from cycle to cycle of cylinder oscillation. These observations are also confirmed by the corresponding Lissajous trajectories of  $C_D$ . The loops of  $C_D(x)$  exhibit less congruent shapes from cycle to cycle of cylinder oscillation and thereby, the fluctuating drag coefficient,  $C_D$ , is

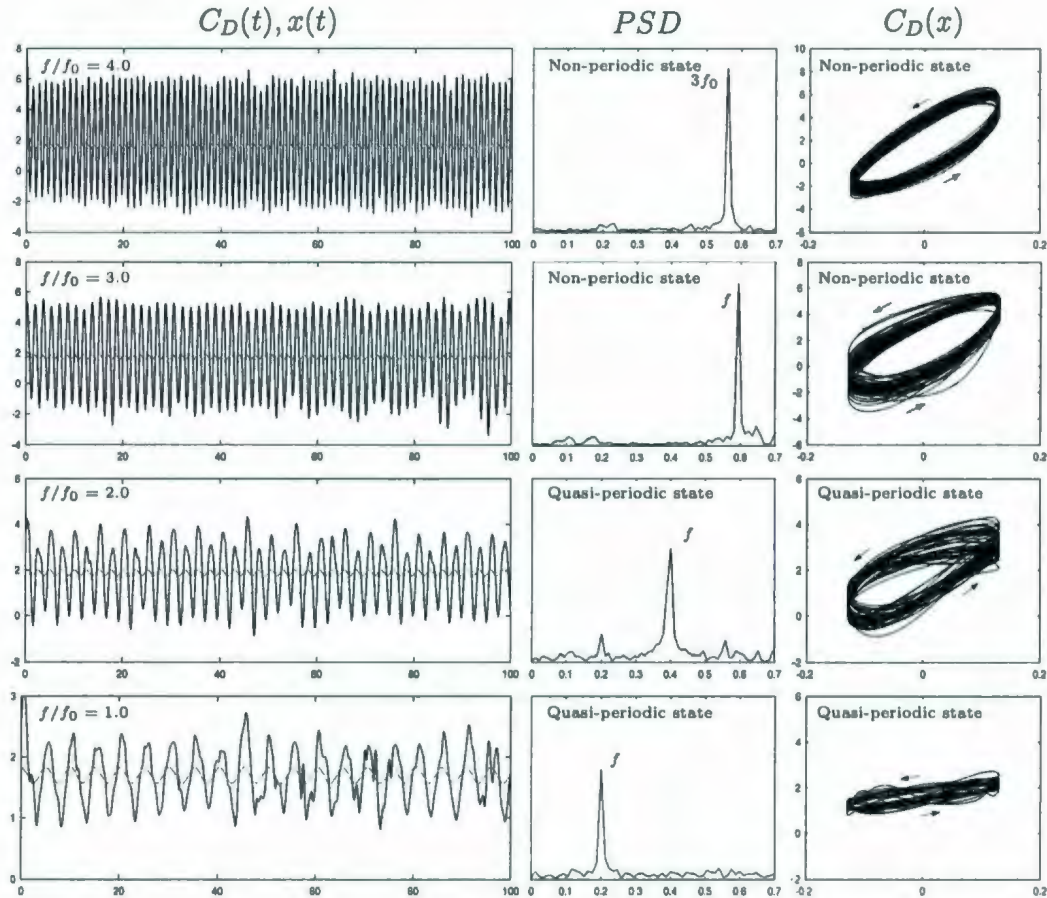


Figure 5.16: The time variation of the drag coefficient,  $C_D$ , (black) and the in-line displacement,  $x(t)$ , (gray); PSD of  $C_D$ ; Lissajous patterns of  $C_D$  at  $R = 200$ :  $A = 0.13$ ,  $1.0 \leq f/f_0 \leq 4.0$ ,  $Fr = 0.2$ ,  $h = 0.5$ .

quasi-phased-locked to the cylinder motion when  $f/f_0 \leq 2.0$ . On the other hand, at  $f/f_0 \geq 3.0$ , the trajectories of  $C_D$  seem to be more persistent than those at smaller frequency ratios. The corresponding Lissajous trajectories,  $C_D(x)$ , indicate the increase in phase-locking between  $C_D$  and the cylinder motion. Thus, for the case  $Fr = 0.2$ ,  $h = 0.5, 0.75$ , the effect of  $f/f_0$  is seen to stabilize the fluctuating drag force,  $C_D$ . The signatures of  $C_D$  are almost repetitive over one period of cylinder

oscillation,  $T$ , when  $f/f_0 \geq 3.0$ ,  $h = 0.5, 0.75$ . These observations indicate that for the frequency ratios,  $f/f_0 = 3.0, 4.0$ , and cylinder submergence depths,  $h = 0.5, 0.75$ , the fluctuating drag coefficient,  $C_D$ , is quasi-phase-locked, per  $T$ , to the cylinder motion. Considering the PSD of  $C_D$  shown in Figures 5.16 and 5.17, it is evident that one dominant peak develops when  $f/f_0 = 1.0, 2.0, 3.0, 4.0$ . This peak occurs at  $f$  when  $f/f_0 = 1.0, 2.0, 3.0$  while at  $3f_0$  when  $f/f_0 = 4.0$ . The hysteresis loops

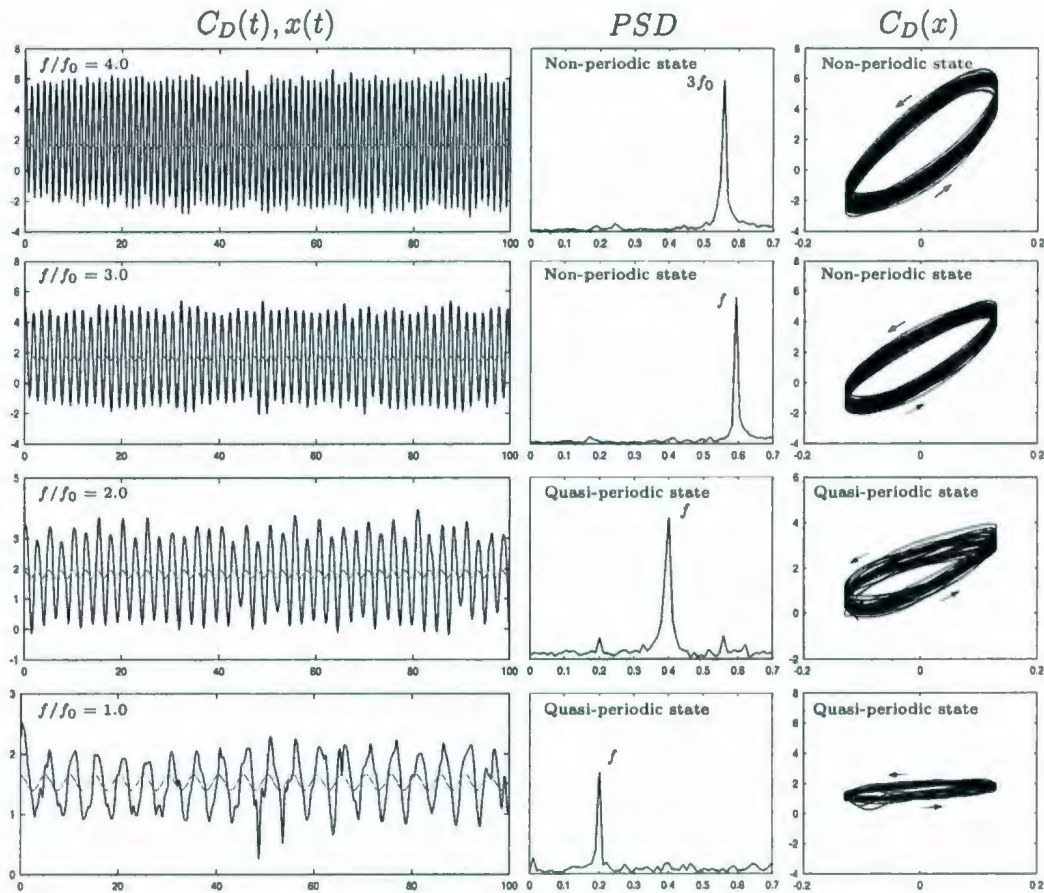


Figure 5.17: The time variation of the drag coefficient,  $C_D$ , (black) and the in-line displacement,  $x(t)$ , (gray); PSD of  $C_D$ ; Lissajous patterns of  $C_D$  at  $R = 200$ :  $A = 0.13$ ,  $1.0 \leq f/f_0 \leq 4.0$ ,  $Fr = 0.2$ ,  $h = 0.75$ .

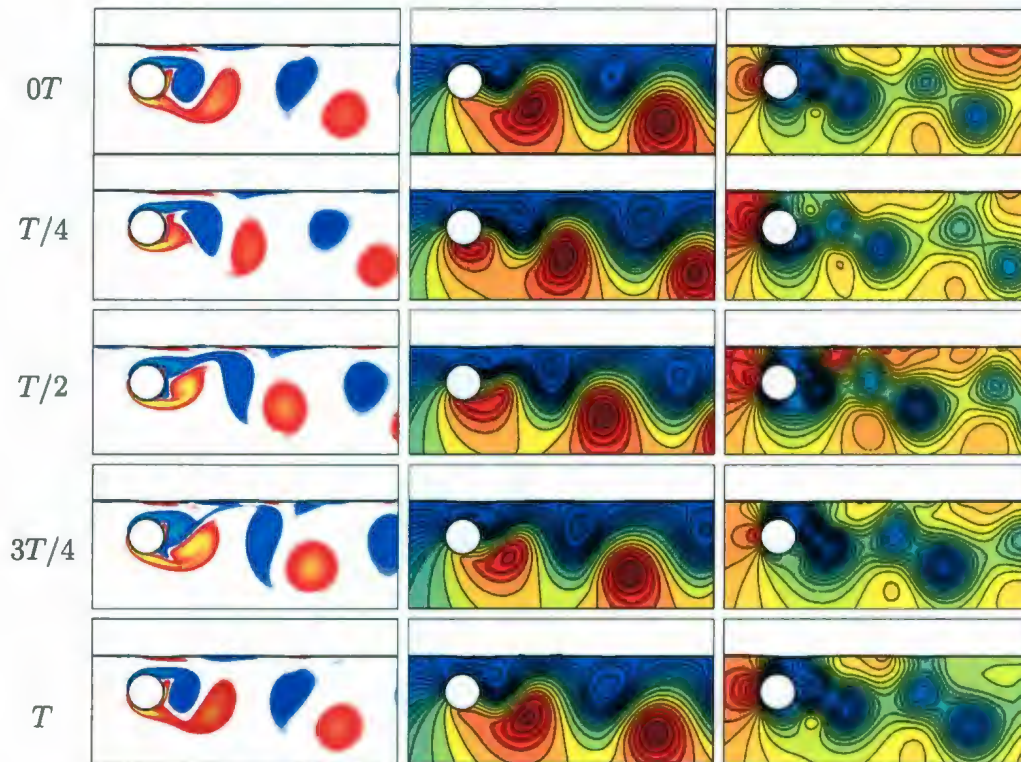


Figure 5.18: The equivorticity patterns (left), the streamline patterns (middle) and the pressure distribution in the near wake (right) over one period of cylinder oscillation,  $T$ , at  $R = 200$ :  $A = 0.13$ ,  $f/f_0 = 1.0$ ,  $h = 0.5$ ,  $Fr = 0.2$  ( $T \approx 5.051$ ,  $80.7 \leq t \leq 85.7$ ). The quasi-locked-on **2S** mode, per  $T$ , is observed.

of  $C_D(x)$  are essentially confined in the upper half plane and they shift towards the lower half plane as  $f/f_0$  increases. Considering the area enclosed by the Lissajous trajectories, it is evident that the energy transfer between the cylinder and the fluid increases as  $f/f_0$  increases.

Figures 5.18 and 5.19 display the equivorticity patterns, the streamline patterns and the pressure distribution in the near wake of the cylinder over one period of cylinder

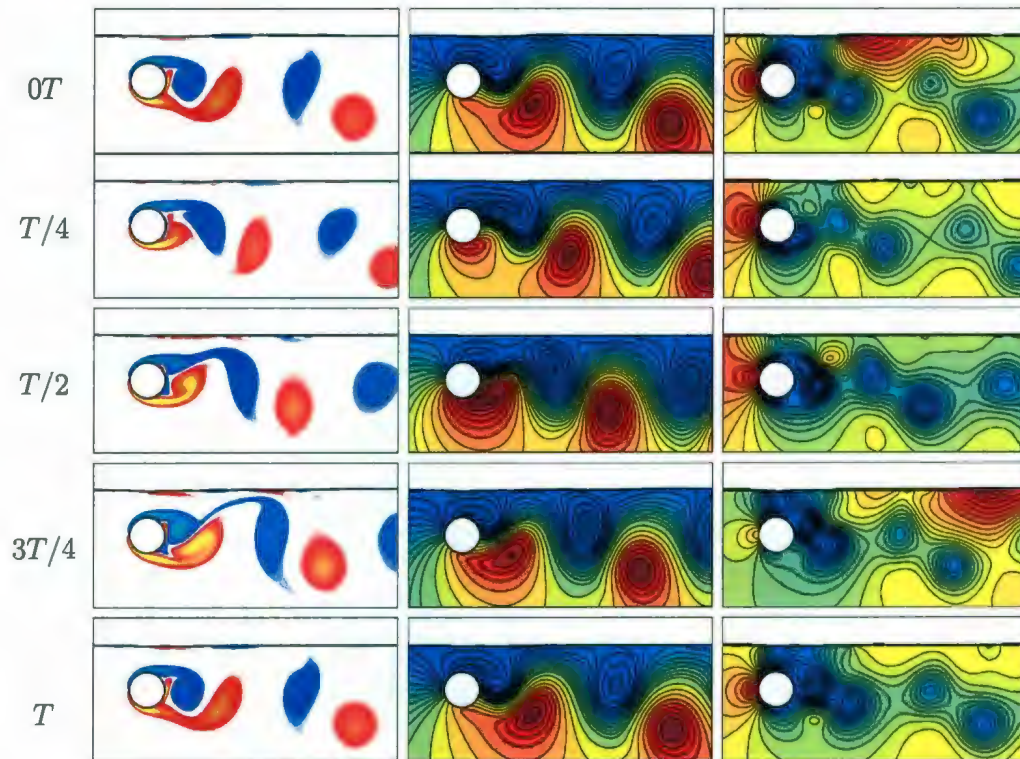


Figure 5.19: The equivorticity patterns (left), the streamline patterns (middle) and the pressure distribution in the near wake (right) over one period of cylinder oscillation,  $T$ , at  $R = 200$ :  $A = 0.13$ ,  $f/f_0 = 1.0$ ,  $h = 0.75$ ,  $Fr = 0.2$  ( $T \approx 5.051$ ,  $80.7 \leq t \leq 85.7$ ). The quasi-locked-on **2S** mode, per  $T$ , is observed.

oscillation,  $T$ , for the case  $Fr = 0.2$ ,  $h = 0.5, 0.75$ , respectively, when  $f/f_0 = 1.0$ . At both cylinder submergence depths,  $h = 0.5, 0.75$ , the vortex shedding mode is the quasi-locked-on asymmetric **2S** mode, per  $T$ . The pressure plots shown in Figures 5.18 and 5.19 indicate that the low pressure region is generated at the upper side of the cylinder as the negative vortex develops ( $0T \leq t \leq T/2$ ). Moreover, the low pressure region seems to shift to the upper side of the cylinder completely at  $t \approx 3T/4$  and thus the negative vortex sheds. The high pressure in the stagnation area seems to move

in the counterclockwise direction up to  $t \approx T/2$  when the negative vortex develops whereas it starts to move in the clockwise direction following the development of the positive vortex over  $T/2 \leq t \leq T$ . It is interesting to note that at  $h = 0.5, 0.75$  there is a sufficiently high pressure near the free surface interface. For the smaller cylinder submergence depth,  $h = 0.5$ , sufficiently high pressure region near the interface is observed approximately  $6d$  downstream of the cylinder at the time when the fully developed positive vortex from the lower side of the cylinder approaches the interface and thus the free surface becomes sufficiently disturbed ( $t = 0T, T$ ). On the other hand, at  $h = 0.75$ , sufficiently high pressure region near the free surface is largely dissipated by approximately  $6d$  downstream of the cylinder at the instants  $t = 0T$  and  $t = T$ ; sufficiently high pressure region is also observed approximately  $6d$  downstream of the cylinder at the instants  $t = T/4, 3T/4$  when  $h = 0.75$ . Figures 5.18 and 5.19 also suggest that the development of the positive vorticity near the interface in the region above the cylinder seems to induce a significantly low pressure in this region. Taking an overview of Figures 5.18 and 5.19, it can be seen that near wake structure at  $h = 0.5$  is similar to that obtained at  $h = 0.75$ . However, there is a slight decrease in vortex formation length ( $\approx 5\%$ ) as  $h$  decreases to 0.5. As the cylinder submergence depth,  $h$ , is reduced, the near wake is more influenced by the proximity of the free surface and thereby, the shed vortices become more oval shaped. It is noted that at  $Fr = 0.2$ , the ability of the vortices to diffuse is more evident as the free surface curvature becomes more pronounced than that in the limiting case  $Fr \approx 0.0$ . Thus, as the cylinder approaches the free surface, the vorticity diffuses stronger across the interface and a larger amount of opposite signed vorticity is expected near the free surface.

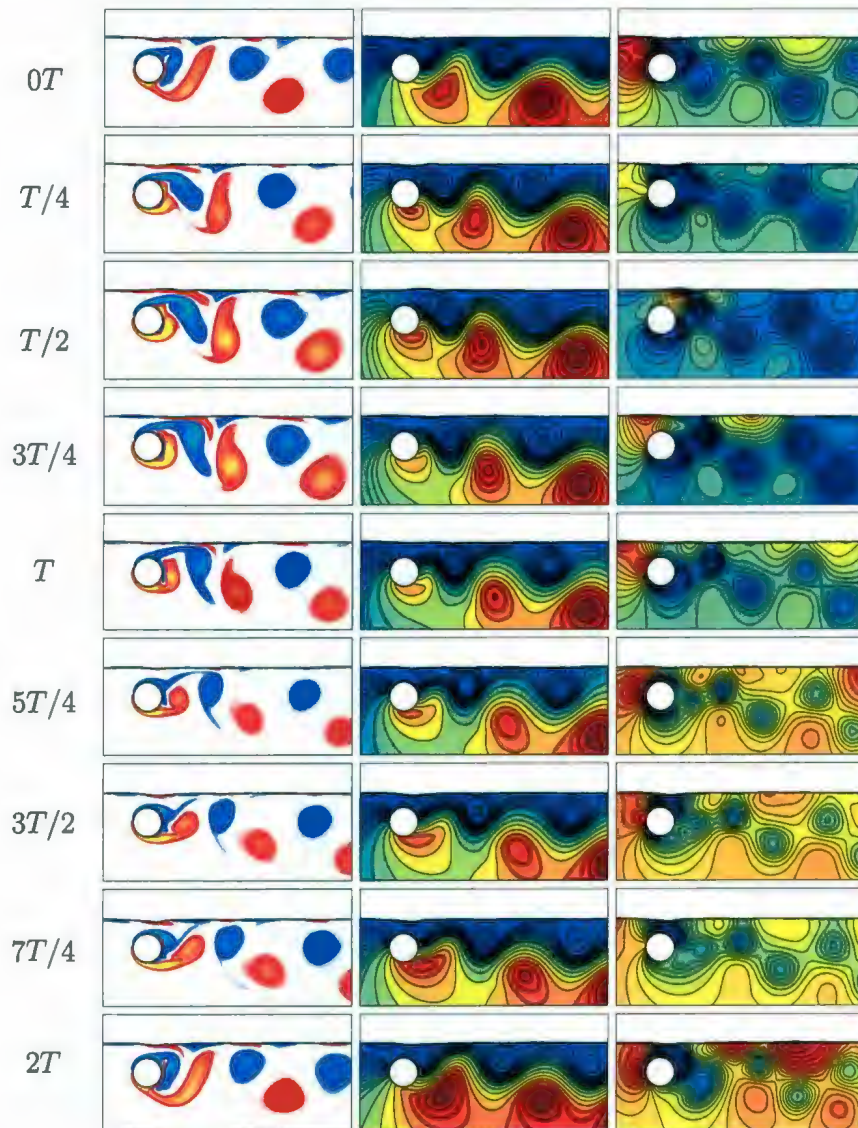


Figure 5.20: The equivorticity patterns (left), the streamline patterns (middle) and the pressure distribution in the near wake (right) over two periods of cylinder oscillation,  $2T$ , at  $R = 200$ :  $A = 0.13$ ,  $f/f_0 = 2.0$ ,  $Fr = 0.2$ ,  $h = 0.5$  ( $T \approx 2.525$ ,  $80.7 \leq t \leq 85.7$ ). The quasi-locked-on **2S** mode, per  $2T$ , is observed.

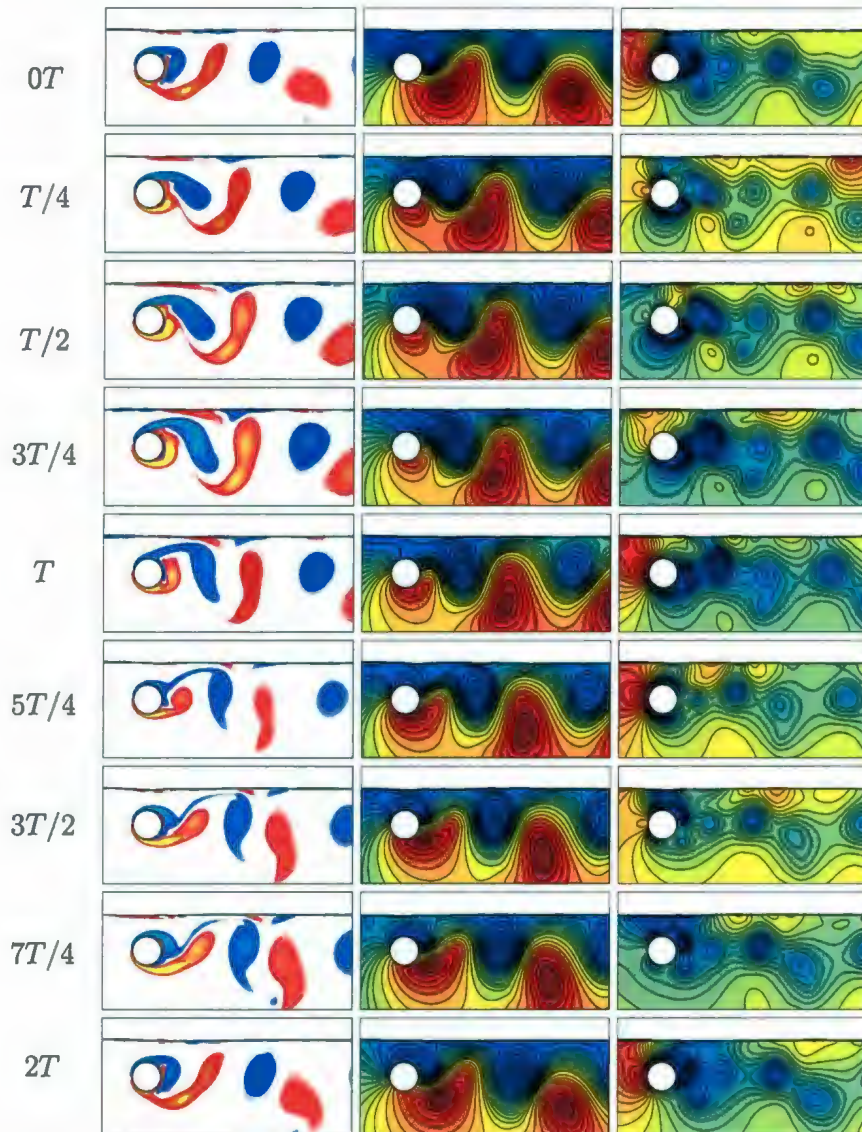


Figure 5.21: The equivorticity patterns (left), the streamline patterns (middle) and the pressure distribution in the near wake (right) over two periods of cylinder oscillation,  $2T$ , at  $R = 200$ :  $A = 0.13$ ,  $f/f_0 = 2.0$ ,  $Fr = 0.2$ ,  $h = 0.75$  ( $T \approx 2.525$ ,  $70.7 \leq t \leq 75.7$ ). The quasi-locked-on P+S mode, per  $2T$ , is observed.

For the frequency ratio  $f/f_0 = 2.0$ , the equivorticity and streamline patterns, and the pressure distribution in the near wake of the cylinder over two periods of cylinder oscillation,  $2T$ , are plotted in Figures 5.20 and 5.21 when  $h = 0.5, 0.75$ , respectively. The vortex shedding modes at this frequency are the quasi-locked-on asymmetric **2S** mode, per  $2T$ , when  $h = 0.5$  and the quasi-locked-on asymmetric **P+S** mode, per  $2T$ , when  $h = 0.75$ . It can be seen from Figure 5.20 that the formation and shedding of the negative vortex is associated with the shift of the low pressure region from the upper to the lower side of the cylinder ( $t \approx 5T/4$ ). The reverse process leads to the development and shedding of the positive vortex ( $t \approx T/4$ ). Moreover, the development of the positive vorticity near the free surface interface in the region above the cylinder seems to induce the local raise in the interface, resulting in the movement of the high pressure into the curved surface region. This situation is best illustrated by the pressure plots taken within the time interval  $3T/4 \leq t \leq 3T/2$ . As the level of interface curvature decreases, the high pressure seems to shift to the stagnation region. Figure 5.20 also indicates the existence of the significantly high pressure near the free surface as surface waves propagate into the downstream of the cylinder. At the larger cylinder submergence depth,  $h = 0.75$ , Figure 5.21 shows that a pair of positive vortices is shed into the downstream of the cylinder over  $0T \leq t \leq 3T/4$  due to the shift of the low pressure region to the lower side of the cylinder. A large vortex develops in the upper vortex shedding layer ( $0T \leq t \leq 5T/4$ ) and becomes detached at  $t \approx 3T/2$ , following the shift of the low pressure region. Taking an overview of Figures 5.20 and 5.21, it is evident that both the distance between the vortices and the vortex formation length are decreased with the decrease in  $h$ . The observed decrease in the vortex formation length is approximately 12.5%. The size of shed vortices

is larger at  $h = 0.75$  when compared to those at  $h = 0.5$ . Moreover, at the smaller cylinder submergence depth,  $h = 0.5$ , the form of the propagating vortices is oval while at  $h = 0.75$  these vortices appear to be elongated in the transverse direction. It is clearly seen from these figures that the negative vortices are restricted in their upward movement by the free surface and thereby, the reorientation of the shed vortices is observed. For example, at  $h = 0.5$ , the major axis of the shed vortices has a horizontal position with respect to the free surface while at the larger cylinder submergence depth,  $h = 0.75$ , the form of the vortices is very similar to the reference case of  $h = \infty$  shown in Figure 5.3 with the major axis of the vortices lying perpendicular to the interface. It is also noted that the large amount of opposite signed vorticity near the interface is observed at  $h = 0.5$  while this amount is significantly reduced as  $h$  increases. Comparison of the pressure plots shown in Figures 5.20 and 5.21 indicates that the secondary vorticity from the free surface leads to the existence of the regions of the sufficiently high pressure near the interface at the smaller cylinder submergence depth,  $h = 0.5$ . Moreover, at  $h = 0.5$ , the high pressure region seems to switch over between the stagnation and curved surface region whereas at  $h = 0.75$ , the high pressure is always associated with the stagnation.

Figure 5.22 summarizes the effect of the cylinder submergence depth,  $h$  ( $= 0.25, 0.5, 0.75$ ), and the frequency ratio,  $f/f_0$  ( $= 1.0, 2.0, 3.0, 4.0$ ), on the equivorticity patterns for the case  $R = 200$ ,  $A = 0.13$  when  $Fr = 0.2$ . The reference case  $h = \infty$  is also shown in this figure. The snapshots are taken at the instant  $x(t) = A$ . It is noted that for the periodic/quasi-periodic cases the snapshots are taken over the time interval in which the flow reaches to a periodic/quasi-periodic state. For non-periodic cases, the commonly appearing equivorticity plots at  $x(t) = A$  (within the time interval

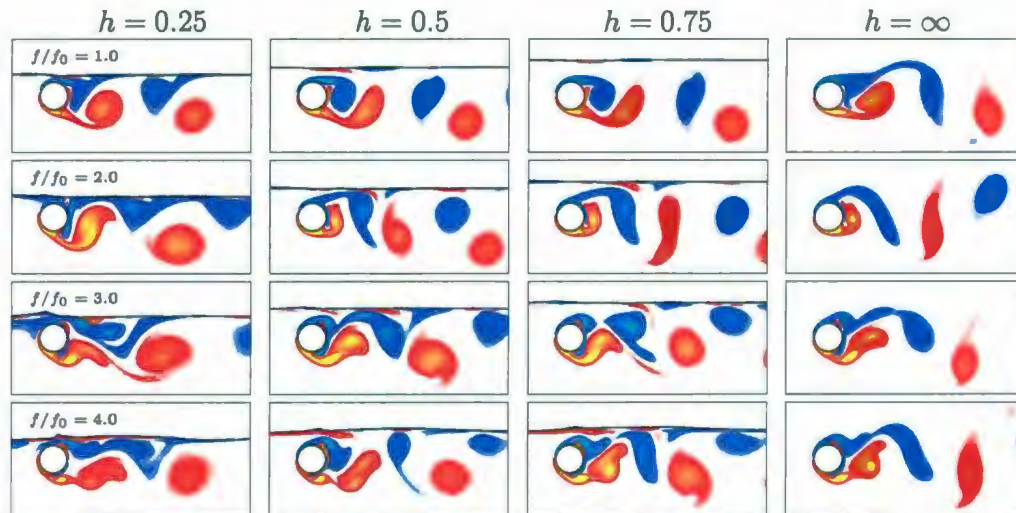


Figure 5.22: The effect of the cylinder submergence depth,  $h$ , and the frequency ratio,  $f/f_0$ , on the equivorticity patterns at  $R = 200$ :  $A = 0.13$ ,  $Fr = 0.2$ . All snapshots are taken at the instant  $x(t) = A$ .

$0 < t \leq 100$ ) are shown in Figure 5.22. It is clearly seen that minimal free surface deformations occur for  $h = 0.25, 0.5, 0.75$  and all  $f/f_0$  shown in Figure 5.22. The surface curvature becomes more pronounced as  $h$  decreases to 0.25 for each frequency ratio,  $f/f_0 = 1.0, 2.0, 3.0, 4.0$ . As a result, the amount of secondary vorticity increases due to the increase in the radius of curvature as  $h$  decreases from 0.75 to 0.5. For the case when  $h = 0.5, 0.75$ , the near wake shows a similar behaviour when compared to that at  $h = \infty$  for each frequency ratio,  $f/f_0$ . Moreover, as the cylinder submergence depth decreases to 0.5, there is some diffusion of the opposite signed vorticity across the interface and the near wake seems to be more skew symmetric. It is also seen that the vortex formation length remains almost the same for each frequency ratio,  $f/f_0$ , shown in Figure 5.22 as  $h$  decreases from  $\infty$  to 0.5. At the smallest cylinder submergence depth,  $h = 0.25$ , the near wake is very dissimilar to

the cases at larger cylinder submergence depths ( $h = 0.5, 0.75$ ). The first column in Figure 5.22 corresponding to the case when  $h = 0.25$  clearly shows that for all cases, the negative vorticity on the upper side of the cylinder annihilates and diffuses due to a strong interaction with the free surface interface and the near wake becomes dominated by positive vortex structures. Figure 5.22 also shows that at  $h = 0.25, 0.5, 0.75$  the positive vortices traveling downstream of the cylinder become more oval shaped while for the reference case  $h = \infty$  the shed positive vortices are elongated in the transverse direction. Taking an overview of Figure 5.22, it can be seen that as  $f/f_0$  increases from 2.0 to 4.0, the formation length seems to increase (maximum by  $\approx 33.3\%$ ) for all cylinder submergence depths,  $h = 0.25, 0.5, 0.75, \infty$ . Moreover, it is evident that both the interface curvature and the amount of opposite signed vorticity near the free surface increase with the variations in the frequency ratio,  $f/f_0$ . An examination of the vorticity plots in Figure 5.11 indicates that for the highest frequency ratio,  $f/f_0 = 4.0$ , and the smallest cylinder submergence depth,  $h = 0.25$ , the free surface curvature becomes considerably pronounced and the induced interface curvature leads to a viscous transport of the opposite signed vorticity into the free surface. As a result, the local interface sharpening is observed. Furthermore, at  $h = 0.25$ , as  $f/f_0$  increases from 1.0 to 4.0, the length of the upper vortex layer becomes enlarged so that this layer largely dissipates into the downstream of the cylinder (being removed from the fluid by diffusion and cross-annihilation). Thus, it is clearly seen that, in general, the amount of negative vorticity decreases while the amount of positive vorticity increases as  $f/f_0$  increases. This phenomenon is observed for the cases when  $h = 0.25$ . At larger cylinder submergence depths,  $h = 0.5, 0.75$ , the negative vortex traveling into the near wake seems to be lifted upward toward

to the free surface by the propagating large positive vortex as  $f/f_0$  increases. This results in the reorientation of the negative vortices as they reach the free surface, i.e., they become elongated in the horizontal direction and weaken due to the interaction with the interface.

The effect of the free surface inclusion at  $Fr = 0.2$ ,  $h = 0.25, 0.5, 0.75$  and the frequency ratio,  $f/f_0$ , on vortex shedding modes and their periods,  $T_0$ , the fluctuating fluid forces as well as the mechanical energy transfer is summarized in Tables 5.2-5.5. Table 5.2 shows that for the case  $Fr = 0.2$ , the presence of the free surface seems

|         | $h = 0.25$ |       | $h = 0.5$  |       | $h = 0.75$    |       | $h = \infty$ |       |
|---------|------------|-------|------------|-------|---------------|-------|--------------|-------|
| $f/f_0$ | Mode       | $T_0$ | Mode       | $T_0$ | Mode          | $T_0$ | Mode         | $T_0$ |
| 1.0     | non-locked | -     | <b>2S*</b> | $T$   | <b>2S*</b>    | $T$   | non-locked   | -     |
| 2.0     | non-locked | -     | <b>2S*</b> | $2T$  | <b>(P+S)*</b> | $2T$  | <b>2S</b>    | $2T$  |
| 3.0     | non-locked | -     | non-locked | -     | non-locked    | -     | non-locked   | -     |
| 4.0     | non-locked | -     | non-locked | -     | non-locked    | -     | non-locked   | -     |

Table 5.2: The effect of the free surface inclusion at  $Fr = 0.2$ ,  $h = 0.25, 0.5, 0.75$  and the frequency ratio,  $f/f_0$ , on vortex shedding modes and their periods,  $T_0$ , at  $R = 200$ :  $A = 0.13$ ,  $1.0 \leq f/f_0 \leq 4.0$ . The superscript “\*” denotes quasi-locked-on modes.

to break up the periodicity of the vortex shedding when  $h = 0.25$  and  $f/f_0 = 2.0$ . On the other hand, at larger cylinder submergence depths,  $h = 0.5, 0.75$ , the free surface is seen to stabilize the flow behaviour for  $f/f_0 = 1.0$  when compared to the reference case  $h = \infty$ . The vortex shedding frequency becomes quasi-locked-on to the forcing frequency of cylinder oscillation at this  $f/f_0$ . Taking an overview of the

results obtained for  $f/f_0 = 2.0$ , it can be clearly seen that for this frequency ratio the near wake is destabilized at  $Fr = 0.2$ ,  $h = 0.75$  and the frequency of the vortex shedding becomes quasi-locked-on to the cylinder motion. The periods of the vortex shedding are  $T$  for  $f/f_0 = 1.0$  and  $2T$  for  $f/f_0 = 2.0$  irrespective of the values of  $h$ . For  $f/f_0 = 2.0$ , a switchover in the vortex shedding modes is observed as  $h$  decreases from  $\infty$  to 0.5. The **2S** mode persists at  $h = 0.5, \infty$  while at  $h = 0.75$  the effect of the free surface is to produce **P+S** mode.

Tables 5.3 and 5.4 display the values of the mean and RMS values of the lift and drag coefficients,  $\hat{C}_L$ ,  $\hat{C}_D$ ,  $C_{L,rms}$  and  $C_{D,rms}$ . The corresponding values of  $\hat{C}_L$ ,  $\hat{C}_D$ ,  $C_{L,rms}$  and  $C_{D,rms}$  coefficients for the reference case of  $h = \infty$  are also presented in these tables. Comparison of the results shown in Table 5.3 indicates that for  $h = 0.25$ ,

| $f/f_0 / h$ | $\hat{C}_L$ |         |        |          | $\hat{C}_D$ |        |        |          |
|-------------|-------------|---------|--------|----------|-------------|--------|--------|----------|
|             | 0.25        | 0.5     | 0.75   | $\infty$ | 0.25        | 0.5    | 0.75   | $\infty$ |
| 1.0         | -0.3501     | 0.1613  | 0.1686 | -0.0028  | 1.4952      | 1.6843 | 1.5139 | 1.3442   |
| 2.0         | -0.5895     | -0.0283 | 0.1855 | -0.0012  | 1.5507      | 1.8527 | 1.8230 | 1.6464   |
| 3.0         | -0.7086     | 0.0037  | 0.1520 | -0.0011  | 1.8846      | 1.7295 | 1.6229 | 1.3916   |
| 4.0         | -0.5359     | 0.0297  | 0.1409 | -0.0028  | 1.6115      | 1.5816 | 1.5697 | 1.4064   |

Table 5.3: The effect of the free surface inclusion at  $Fr = 0.2$ ,  $h = 0.25, 0.5, 0.75$  and the frequency ratio,  $f/f_0$ , on the mean lift and drag coefficients,  $\hat{C}_L$  and  $\hat{C}_D$ , at  $R = 200$ :  $A = 0.13$ ,  $1.0 \leq f/f_0 \leq 4.0$ .

0.5, 0.75 and all values of  $f/f_0$ , the absolute values of the mean lift coefficient,  $\hat{C}_L$ , are increased significantly when compared to that at  $h = \infty$ , except for the case

| $f/f_0 / h$ | $C_{L,rms}$ |        |        |          | $C_{D,rms}$ |        |        |          |
|-------------|-------------|--------|--------|----------|-------------|--------|--------|----------|
|             | 0.25        | 0.5    | 0.75   | $\infty$ | 0.25        | 0.5    | 0.75   | $\infty$ |
| 1.0         | 0.6654      | 0.9370 | 0.8011 | 0.5380   | 1.6387      | 1.7369 | 1.5670 | 1.3776   |
| 2.0         | 0.7918      | 1.2119 | 1.2022 | 0.9284   | 2.3615      | 2.2469 | 2.1325 | 1.9074   |
| 3.0         | 1.8715      | 1.1292 | 0.8259 | 0.4668   | 3.3958      | 3.0026 | 2.7560 | 2.6421   |
| 4.0         | 1.9139      | 1.2689 | 0.9668 | 0.5015   | 3.5504      | 3.3247 | 3.4879 | 4.2629   |

Table 5.4: The effect of the free surface inclusion at  $Fr = 0.2$ ,  $h = 0.25, 0.5, 0.75$  and the frequency ratio,  $f/f_0$ , on the RMS lift and drag coefficients,  $C_{L,rms}$  and  $C_{D,rms}$ , at  $R = 200$ :  $A = 0.13$ ,  $1.0 \leq f/f_0 \leq 4.0$ .

$f/f_0 = 3.0$ ,  $h = 0.5$ . The mean lift coefficient,  $\widehat{C}_L$ , varies in the interval between  $-0.7086$  and  $0.1855$  when the free surface is present whereas the values of  $\widehat{C}_L$  are nearly zero at  $h = \infty$ , as expected. The maximum increase in the absolute values of  $\widehat{C}_L$  is observed for the smallest cylinder depth,  $h = 0.25$ , when  $f/f_0 = 3.0$ . It is also seen that there is a switchover in the sign of the  $\widehat{C}_L$  as  $h$  decreases from  $\infty$  to  $0.25$ . At  $h = \infty, 0.25$ , the values of  $\widehat{C}_L$  are negative. On the other hand, at  $h = 0.5, 0.75$ ,  $\widehat{C}_L$  takes positive values, except for the case  $f/f_0 = 2.0$ ,  $h = 0.5$ . Furthermore, the effect of decreasing  $h$  from  $0.75$  to  $0.25$  is to decrease the values of  $\widehat{C}_L$  such that the values of  $\widehat{C}_L$  shift into the negative half plane. As  $f/f_0$  increases from  $1.0$  to  $4.0$ ,  $\widehat{C}_L$  seems to decrease, except for the cases  $f/f_0 = 4.0$ ,  $h = 0.25$ ;  $f/f_0 = 3.0, 4.0$ ,  $h = 0.5$ ;  $f/f_0 = 2.0$ ,  $h = 0.75$ . Taking an overview of Table 5.3, it is evident that the presence of the free surface has a slight effect on the values of the mean drag coefficient,  $\widehat{C}_D$ , for all the values of the cylinder submergence depth,  $h$ , and the frequency ratio,  $f/f_0$ . As  $h$  decreases from  $\infty$  to  $0.25$ , the values of  $\widehat{C}_D$  increase (by a maximum factor of

1.35), except for the cases  $f/f_0 = 1.0, 2.0$  when  $h = 0.25$ . On the other hand, as  $f/f_0$  increases, the values of  $\widehat{C}_D$  seem to increase for the cases  $h = \infty, 0.25$  (by a maximum factor of 1.26), except for  $f/f_0 = 3.0, h = \infty$  and  $f/f_0 = 4.0, h = 0.25$ ; whereas the decrease in  $\widehat{C}_D$  is observed at  $h = 0.5, 0.75$  (by a maximum factor of 1.17), except for the case  $f/f_0 = 2.0$ .

Table 5.4 indicates that decreasing the value of the cylinder submergence depth,  $h$ , from  $\infty$  to 0.25 seems to increase the values of the RMS lift coefficient,  $C_{L,rms}$ , significantly, except for the cases  $f/f_0 = 1.0, 2.0$  when  $h = 0.25$ . The maximum increase observed for  $C_{L,rms}$  values is by a factor of 3.82. On the other hand, for  $f/f_0 \leq 3.0$  the RMS drag coefficient,  $C_{D,rms}$ , increases slightly as  $h$  decreases from  $\infty$  to 0.25, except for the case  $f/f_0 = 1.0, h = 0.25$ . In fact, the maximum increase observed in  $C_{D,rms}$  values is by a factor of 1.3. It is interesting to note that for the highest frequency ratio,  $f/f_0 = 4.0$ ,  $C_{D,rms}$  decreases as  $h$  is reduced from  $\infty$  to 0.5 and increases as  $h$  decreases from 0.5 to 0.25. Further, the increase in the frequency ratio,  $f/f_0$ , leads to the increase in the values of the RMS lift coefficient,  $C_{L,rms}$ , at  $h = 0.25, 0.5, 0.75, \infty$  (by a maximum factor of 2.85), except for the cases  $f/f_0 = 3.0, h = 0.5, 0.75, \infty$ . It is also seen that  $C_{D,rms}$  increases as  $f/f_0$  increases for all values of  $h$  shown in Table 5.4. The maximum increase observed for  $C_{D,rms}$  values is by a factor of 3.1.

Table 5.5 shows the effect of the cylinder submergence depth,  $h$  ( $= 0.25, 0.5, 0.75$ ), and the frequency ratio,  $f/f_0$  ( $= 1.0, 2.0, 3.0, 4.0$ ), on the total mechanical energy transfer,  $E$ , for the case  $R = 200, A = 0.13$  when  $Fr = 0.2$ . The reference case  $h = \infty$  is also shown in this table. It can be seen that the total energy transfer,  $E$ , is negative

| $f/f_0$ | $h = 0.25$ | $h = 0.5$ | $h = 0.75$ | $h = \infty$ |
|---------|------------|-----------|------------|--------------|
| 1.0     | -0.4687    | -0.2099   | -0.3192    | -0.2759      |
| 2.0     | -1.5237    | -0.7640   | -0.7021    | -0.3718      |
| 3.0     | -2.5882    | -1.6468   | -1.3258    | -0.6167      |
| 4.0     | -2.9833    | -1.7942   | -1.3448    | -0.1008      |

Table 5.5: The effect of the free surface inclusion at  $Fr = 0.2$ ,  $h = 0.25, 0.5, 0.75$  and the frequency ratio,  $f/f_0$ , on the total mechanical energy transfer,  $E$ , at  $R = 200$ :  $A = 0.13$ ,  $1.0 \leq f/f_0 \leq 4.0$ .

irrespective of the values of  $h$  and  $f/f_0$ . This indicates that for all cases shown in Table 5.5, the negative energy is delivered from the cylinder to the fluid. The physical meaning of the negative energy transfer is that the fluid produces a resistance against the forced motion of the cylinder, indicating that these forced oscillations could not occur due to flow-induced forces [see, for example, Carberry (2002)]. Taking an overview of Table 5.5, it is seen that, in general, decreasing the cylinder submergence depth,  $h$ , from  $\infty$  to 0.25 and increasing the frequency ratio,  $f/f_0$ , from 1.0 to 4.0 seem to increase the absolute values of the energy transfer,  $E$ . In other words, the fluid resistance against the forced motion of the cylinder increases as  $h$  decreases and  $f/f_0$  increases.

### 5.2.3 Froude number $Fr = 0.4$

This section deals with the near wake behaviour for the Froude number of 0.4. Reichl *et al.* (2005) have shown that at Froude numbers in excess of  $0.3 \sim 0.4$ , the free surface

deformations become substantial and the localized interface sharpening and wave breaking occur. This yields to introduction of a substantial quantity of opposite signed vorticity from the free surface which interacts with the the upper vorticity shedding layer through diffusion and thereby, substantially changes the wake evolution. In order to examine the inhibiting influence of the free surface on the flow regimes, the near wake states, the fluctuating fluid forces as well as the total energy transfer,  $E$ , when  $Fr = 0.4$ , a series of the numerical simulations at  $h = 0.25, 0.5, 0.75$  is considered. The present investigation confirms that for the considered range of parameters ( $R = 200, A = 0.13, 1.0 \leq f/f_0 \leq 4.0$ ), the free surface presence seems to produce different flow regimes. That is, the flow field is stabilized within a short period of time after the vortex shedding begins and then the near wake transition to the non-locked-on state is observed. It is noted that a similar phenomenon has been observed for the case of the non-deformable surface ( $Fr \approx 0.0$ ). The present investigation also shows that for the Froude number of 0.4, it is possible to generate distinctly different patterns of the vortex formation then that of classical vortex shedding modes observed for a cylinder subject to transverse oscillations in uniform flow [Williamson and Roshko (1988)], provided that the cylinder is located sufficiently close to the free surface. Moreover, it is shown that the presence of the free surface provides the possibility for quasi-locked-on vortex formation not only from the cylinder but also from the free surface. In what follows, these new vortex formation modes are addressed and the mechanism that govern the flow is proposed.

The case when the free surface is located at  $h = 0.25$  is described first. The time evolution of the fluctuating lift coefficient,  $C_L$ , the PSD of  $C_L$  and the traces of  $C_L(x)$

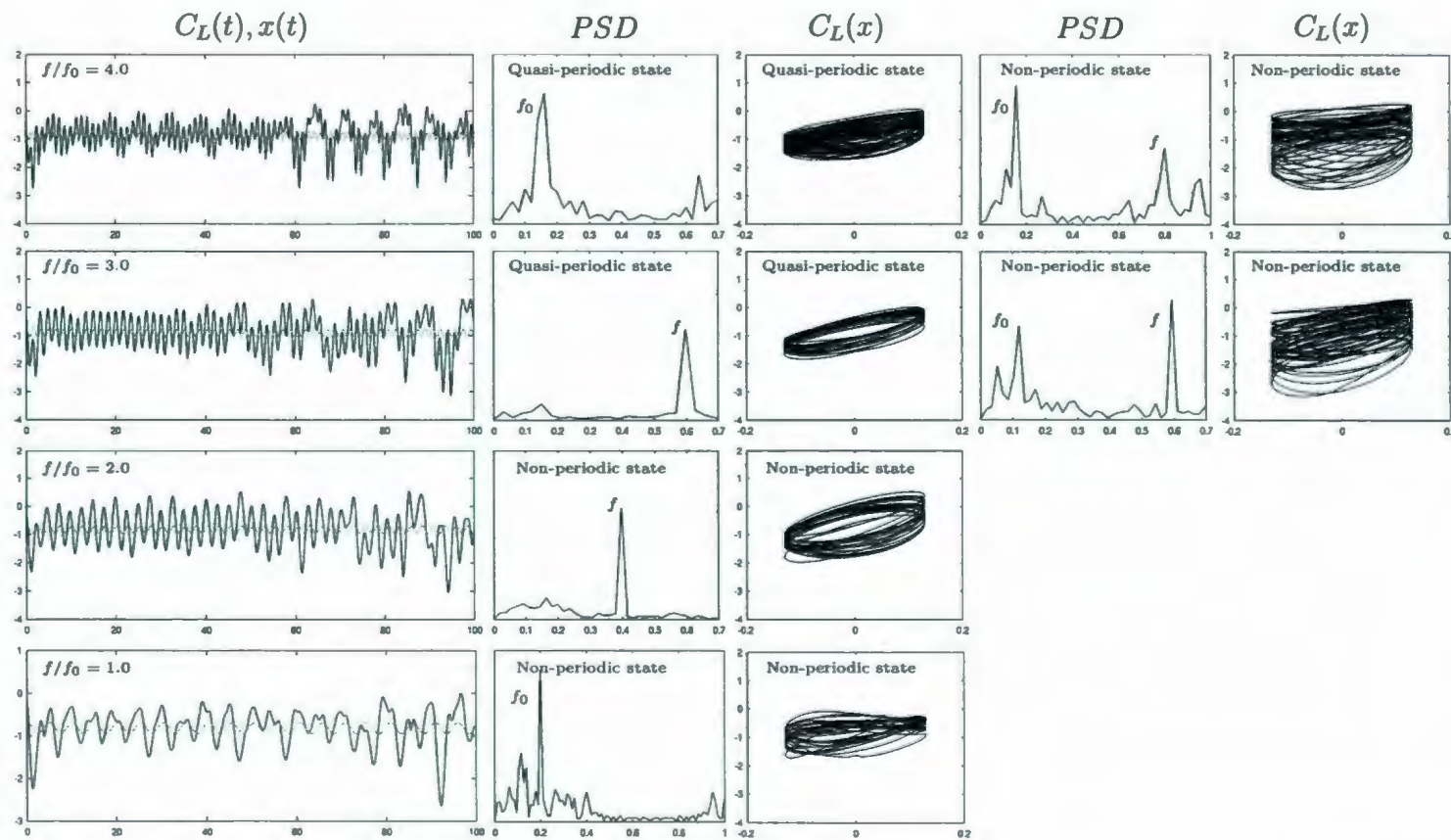


Figure 5.23: The time variation of the lift coefficient,  $C_L$ , (black) and the in-line displacement,  $x(t)$ , (gray); PSD of  $C_L$ ; Lissajous patterns of  $C_L$  at  $R = 200$ :  $A = 0.13$ ,  $1.0 \leq f/f_0 \leq 4.0$ ,  $Fr = 0.4$ ,  $h = 0.25$ .

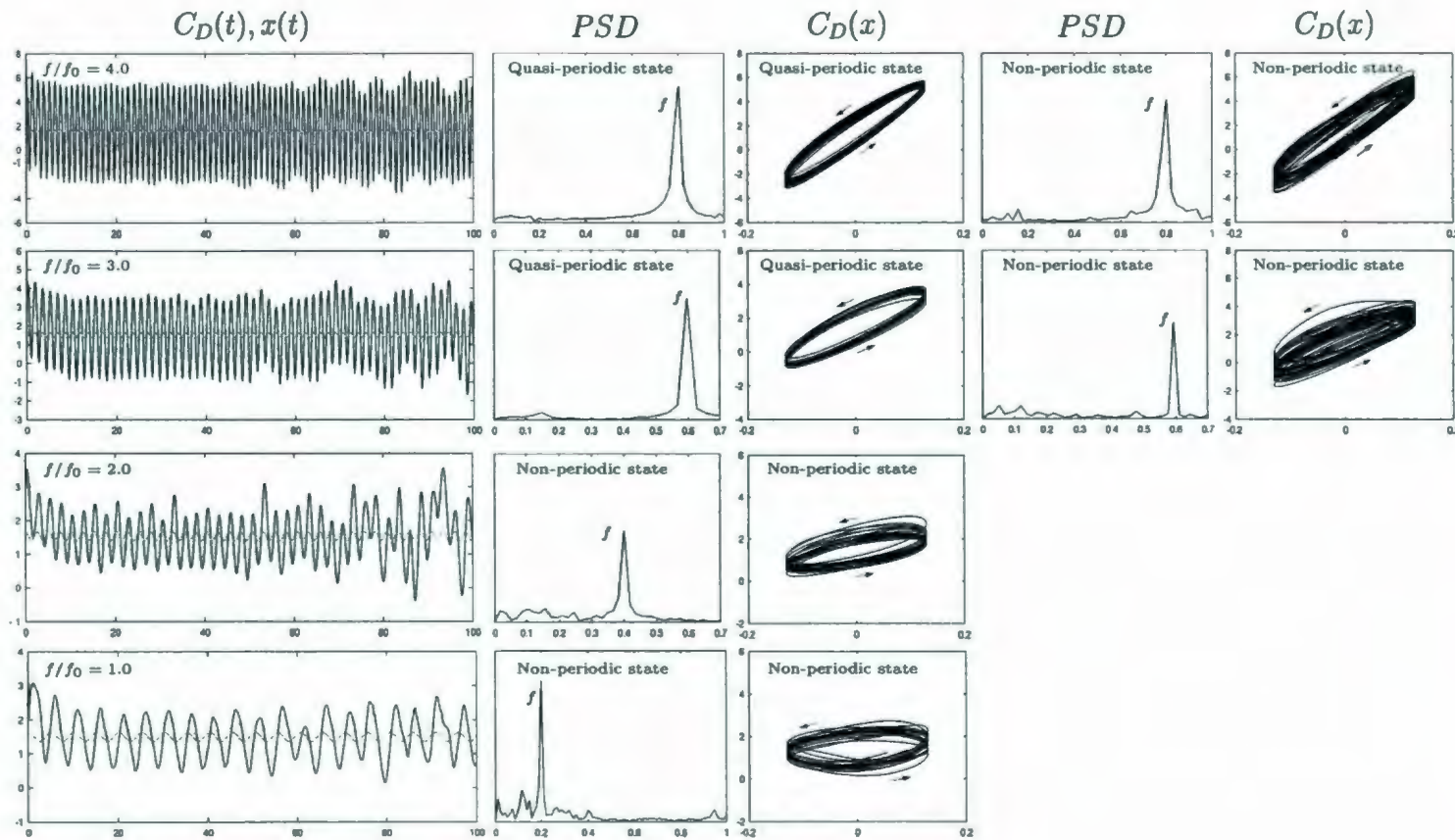


Figure 5.24: The time variation of the drag coefficient,  $C_D$ , (black) and the in-line displacement,  $x(t)$ , (gray); PSD of  $C_D$ ; Lissajous patterns of  $C_D$  at  $R = 200$ :  $A = 0.13$ ,  $1.0 \leq f/f_0 \leq 4.0$ ,  $Fr = 0.4$ ,  $h = 0.25$ .

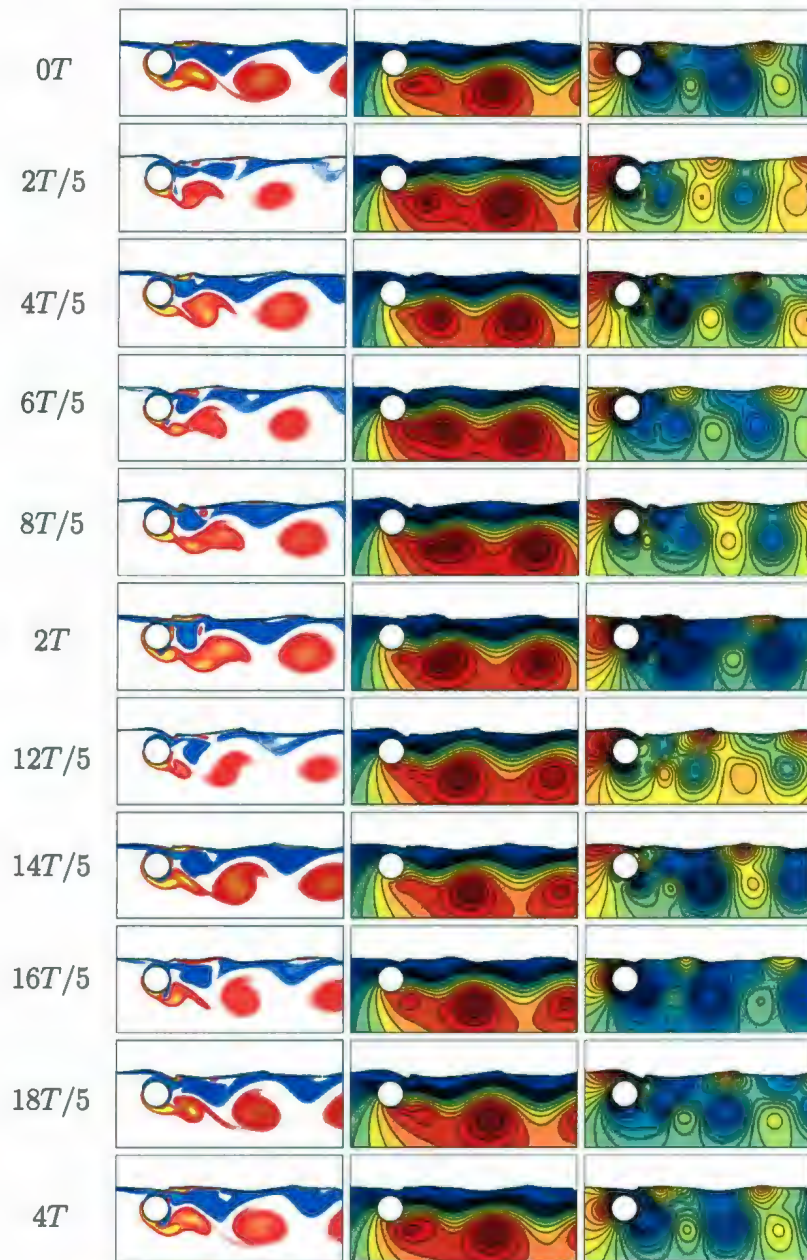


Figure 5.25: The equivorticity patterns (left), the streamline patterns (middle) and the pressure distribution in the near wake (right) over four periods of cylinder oscillation,  $4T$ , at  $R = 200$ :  $A = 0.13$ ,  $f/f_0 = 3.0$ ,  $Fr = 0.4$ ,  $h = 0.25$  ( $T \approx 1.684$ ,  $38.6 \leq t \leq 45.4$ ). The quasi-locked-on  $C(2S)$  mode, per  $4T$ , is observed within  $20T$ .

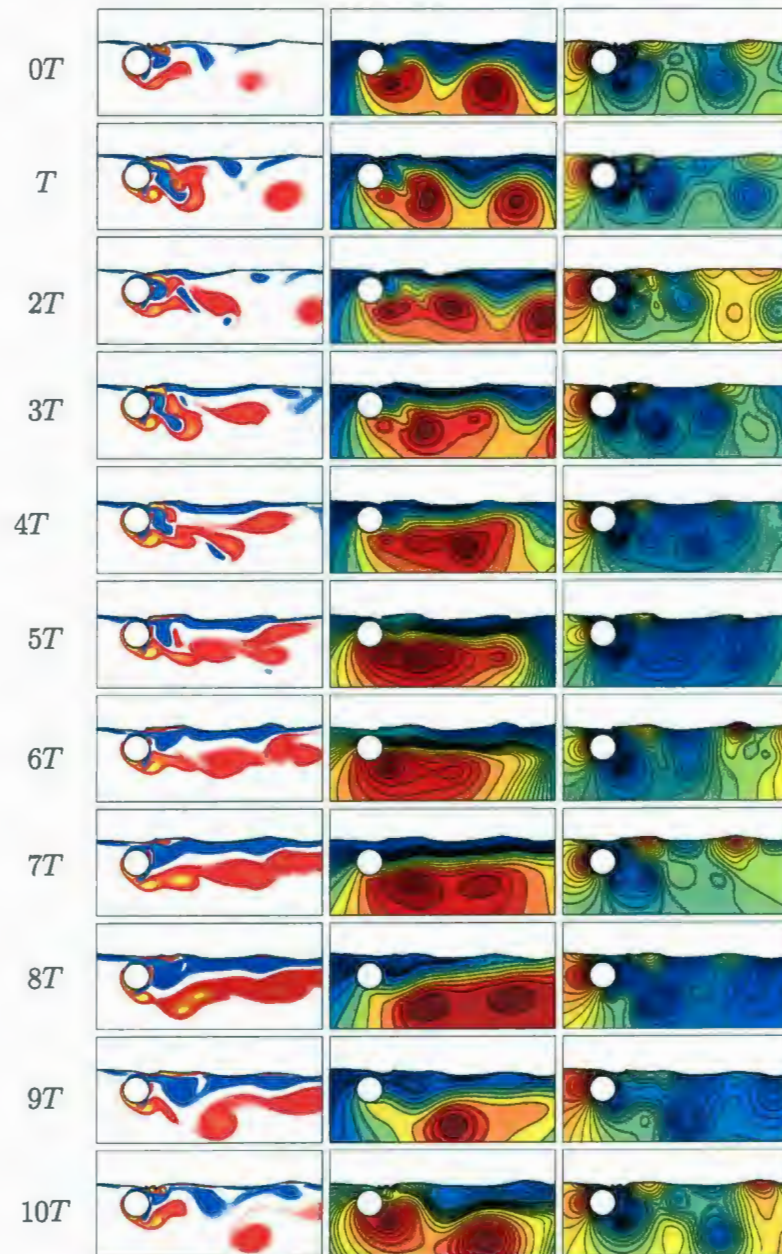


Figure 5.26: The equivorticity patterns (left), the streamline patterns (middle) and the pressure distribution in the near wake (right) over ten periods of cylinder oscillation,  $10T$ , at  $R = 200$ :  $A = 0.13$ ,  $f/f_0 = 3.0$ ,  $Fr = 0.4$ ,  $h = 0.25$  ( $T \approx 1.684$ ,  $69 \leq t \leq 85.8$ ) (non-periodic state).

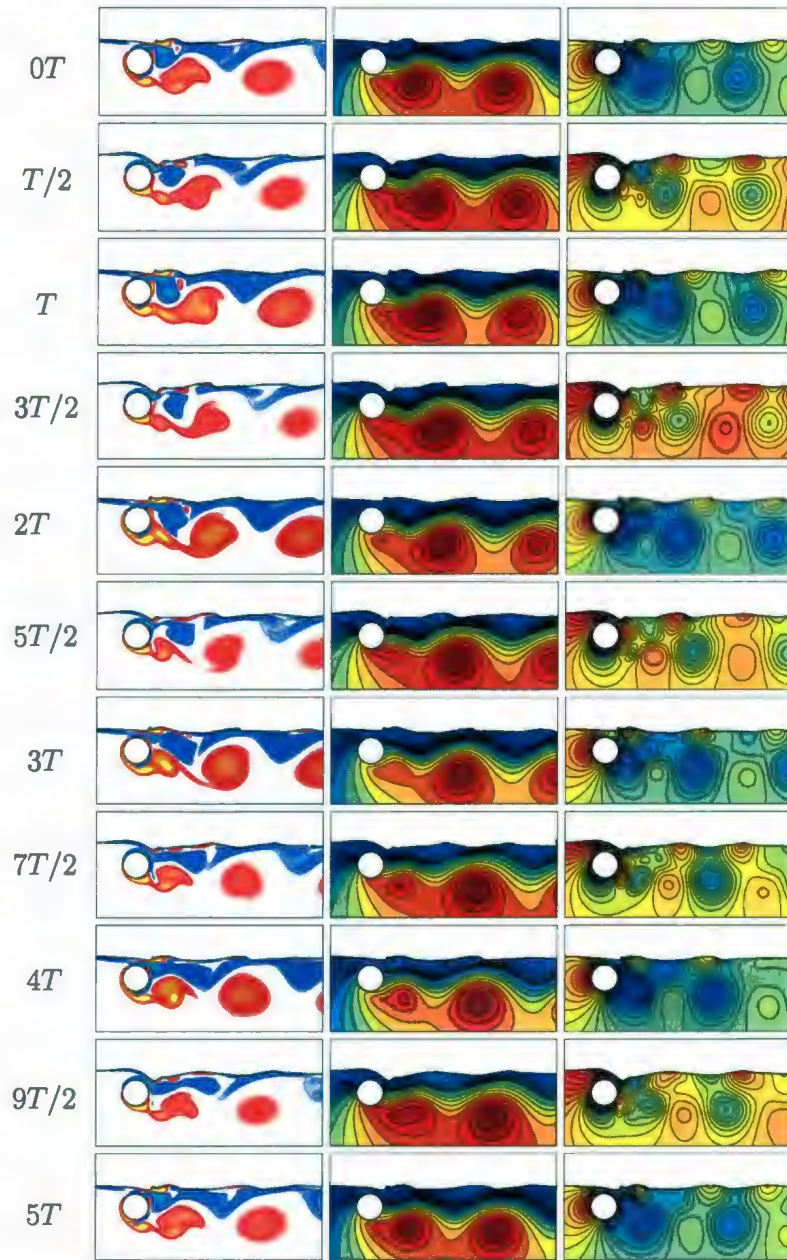


Figure 5.27: The equivorticity patterns (left), the streamline patterns (middle) and the pressure distribution in the near wake (right) over five periods of cylinder oscillation,  $5T$ , at  $R = 200$ :  $A = 0.13$ ,  $f/f_0 = 4.0$ ,  $Fr = 0.4$ ,  $h = 0.25$  ( $T \approx 1.263$ ,  $25.2 \leq t \leq 31.5$ ). The quasi-locked-on C(2S) mode, per  $5T$ , is observed within  $20T$ .

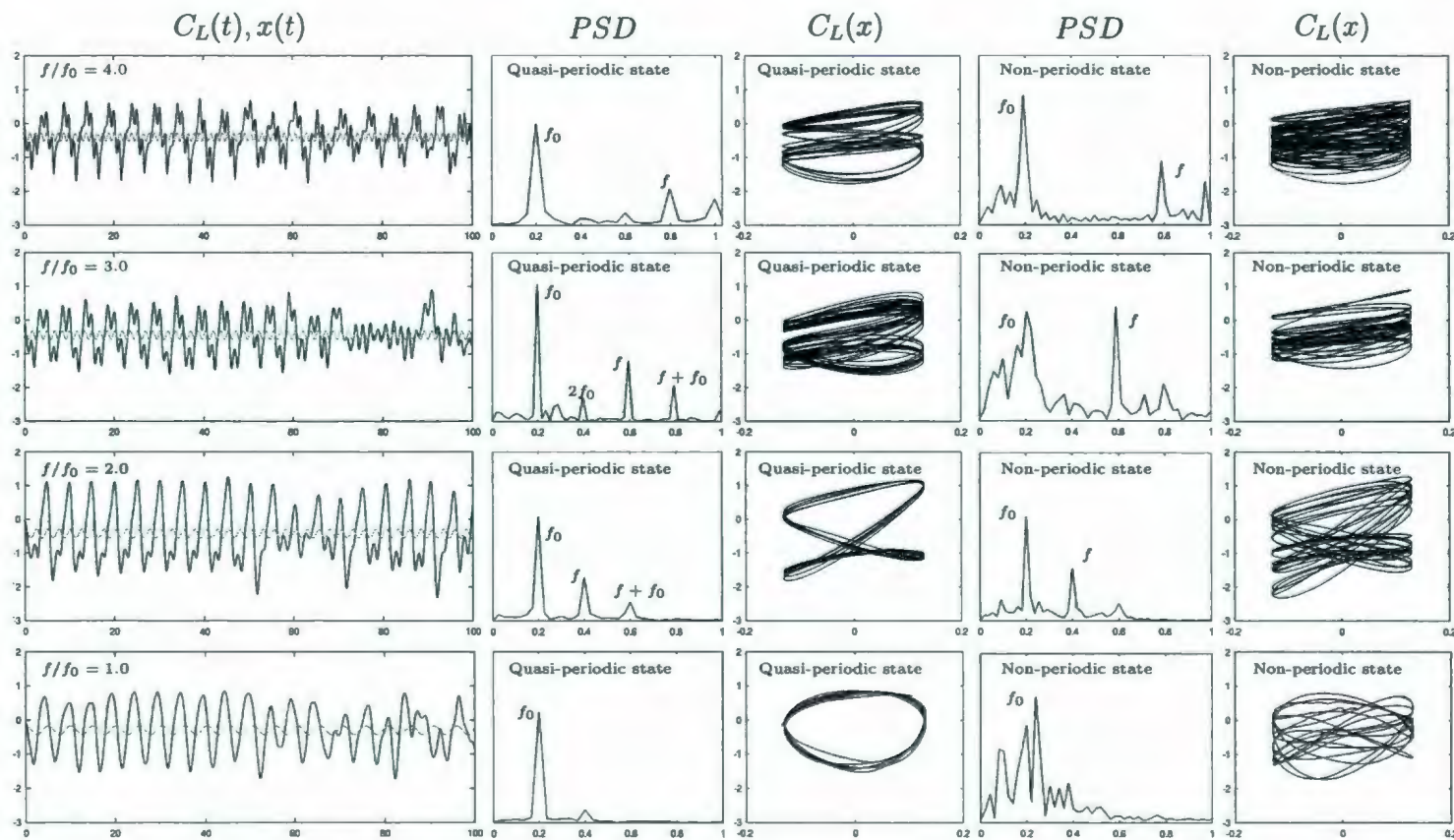


Figure 5.28: The time variation of the lift coefficient,  $C_L$ , (black) and the in-line displacement,  $x(t)$ , (gray); PSD of  $C_L$ ; Lissajous patterns of  $C_L$  at  $R = 200$ :  $A = 0.13$ ,  $1.0 \leq f/f_0 \leq 4.0$ ,  $Fr = 0.4$ ,  $h = 0.5$ .

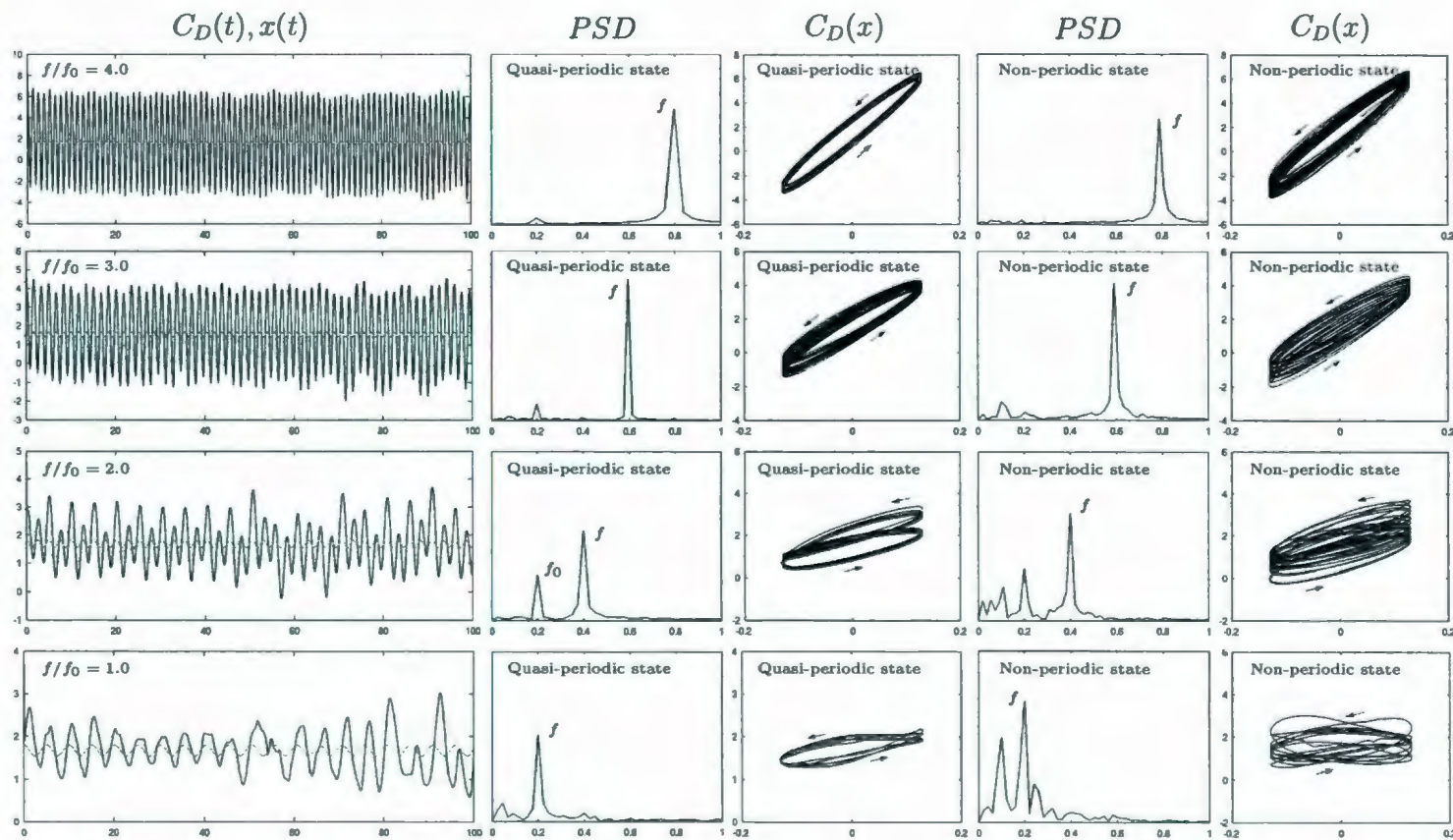


Figure 5.29: The time variation of the drag coefficient,  $C_D$ , (black) and the in-line displacement,  $x(t)$ , (gray); PSD of  $C_D$ ; Lissajous patterns of  $C_D$  at  $R = 200$ :  $A = 0.13$ ,  $1.0 \leq f/f_0 \leq 4.0$ ,  $Fr = 0.4$ ,  $h = 0.5$ .

for the case  $h = 0.25$  are displayed in Figure 5.23. This figure clearly shows that when  $f/f_0 \leq 2.0$ , neither of the  $C_L$  traces has a repetitive path which indicates lock-on states. Thus, it is concluded that the flow is non-periodic at these frequency ratios. Spectra of  $C_L$  corresponding to  $f/f_0 \leq 2.0$  indicate that the dominant peak occurs at the forcing frequency,  $f$ , at both of these frequencies ( $f = f_0$  for  $f/f_0 = 1.0$ ). The Lissajous trajectories exhibit highly non-congruent shapes and thus the loss of phase-locking between  $C_L$  and the cylinder motion for  $f/f_0 \leq 2.0$  becomes evident. For the higher frequency ratios,  $f/f_0 \geq 3.0$ , the signatures of the lift coefficient,  $C_L$ , clearly indicate the transition of the flow from the quasi-periodic state to the non-periodic state. The switchover is observed at approximately  $t = 42$  and  $t = 60$  for the frequency ratios of  $f/f_0 = 3.0, 4.0$ , respectively. The traces of lift coefficient,  $C_L$ , are almost repeatable over  $4T$  and  $5T$  for  $f/f_0 = 3.0, 4.0$ , respectively (quasi-periodic state). It is noted that at  $f/f_0 = 4.0$ , the  $C_L$  signatures are less repetitive than those obtained for  $f/f_0 = 3.0$ . This indicates that when  $h = 0.25$  the lift coefficient,  $C_L$ , is destabilized as  $f/f_0$  increases from 3.0 to 4.0. As the switching time is reached, at both of these frequencies,  $f/f_0 = 3.0, 4.0$ , the traces of  $C_L$  become highly non-persistent and thereby, indicate the transition to the non-periodic state of the near wake. The PSD of  $C_L$  (quasi-periodic state) shows the existence of one dominant peak for both  $f/f_0 = 3.0, 4.0$ . It is interesting to note that at higher frequency ratio,  $f/f_0 = 4.0$ , the dominant peak occurs at the natural vortex shedding frequency,  $f_0$ , while at  $f/f_0 = 3.0$  the dominant peak develops at  $f$ . This indicates that for the case  $h = 0.25$  when  $f/f_0 = 4.0$  the effect of the forcing frequency,  $f$ , becomes very weak with respect to  $f_0$ . In non-periodic state, the corresponding spectra show at least two well defined peaks,  $f_0$  and  $f$ , for both  $f/f_0 = 3.0, 4.0$ . Thus, in this flow regime,

the oscillations of the lift coefficient,  $C_L$ , are governed by the two frequencies, the natural vortex shedding frequency,  $f_0$ , and the vortex shedding frequency,  $f$ . Taking an overview of the hysteresis loops of  $C_L(x)$  when  $f/f_0 \geq 3.0$ , it can be seen that in quasi-periodic state, the hysteresis loops of  $C_L(x)$  are less congruent from cycle to cycle of the cylinder oscillation, indicating the increase in phase variations between the cylinder motion and the fluctuating lift coefficient. The traces of  $C_L(x)$  shown in the last column of Figure 5.23 (non-periodic state) indicate the complete loss of the phase-locking for  $f/f_0 = 3.0, 4.0$ . Comparing the Lissajous plots in Figure 5.23, it is evident that for each of the frequency ratios,  $f/f_0 = 1.0, 2.0, 3.0, 4.0$ , a large fraction of the hysteresis loops confine in the lower half plane. This again indicates that the flow field is significantly affected by the presence of the free surface. More precisely, the free surface effect seems to break up the symmetry of the  $C_L(x)$  signatures obtained for the reference case of  $h = \infty$  by shifting the hysteresis loops into the lower half plane. Finally, when the cylinder is close to the free surface,  $h = 0.25$ , the signatures of  $C_L$  are largely confined in the negative half plane.

Time dependent variations of the drag coefficient,  $C_D$ , the PSD of  $C_D$  and the Lissajous patterns of  $C_D$  for the case  $Fr = 0.4, h = 0.25$  are presented in Figure 5.24. At small frequency ratios,  $f/f_0 \leq 2.0$ , the traces of  $C_D$  exhibit non-repeatable signatures. On the other hand, when  $f/f_0 \geq 3.0$ , the form of the  $C_D$  traces is almost periodic over  $4T$  and  $5T$ , respectively, for  $f/f_0 = 3.0$  and  $4.0$ . Thus, variations in the frequency ratio,  $f/f_0$ , seem to stabilize the patterns of the drag coefficient,  $C_D$ . It is also seen that the effect of  $f/f_0$  is to increase the positive peaks of  $C_D$ . Spectra of  $C_D$  suggest that at each frequency ratio the fluctuations of  $C_D$  occur at the dominant frequency equal to the forcing frequency,  $f$ . The signatures of  $C_D(x)$  are almost

congruent at  $f/f_0 \geq 3.0$  (quasi-periodic state) and thereby, indicate that  $C_D$  is quasi-phase-locked to the cylinder motion at these frequencies. On the other hand, when  $f/f_0 \leq 2.0$  and also when a switchover is observed in the flow regime ( $f/f_0 \geq 3.0$ , non-periodic state), the shapes of Lissajous patterns are less congruent from cycle to cycle of cylinder oscillation, indicating increased phase variations. It is seen that the hysteresis loops are largely confined in the upper half plane and their direction is counterclockwise. Thus, there is a mechanical energy transfer from the cylinder to the fluid. It is also interesting to note that these loops have a generally similar form irrespective of the frequency ratio,  $f/f_0$ , and the observed flow regimes.

Figure 5.25 displays the equivorticity and streamline patterns, and the pressure distribution in the near wake over four periods of cylinder oscillation,  $4T$ , for the case  $Fr = 0.4$ ,  $h = 0.25$  when  $f/f_0 = 3.0$  (quasi-periodic state). The vortex shedding mode is the modified quasi-locked-on **C(2S)** mode, per  $4T$ , within  $20T$ . The flow becomes non-periodic at  $20T < t < 60T$ . It is seen from Figure 5.25 that the positive vortex developed in the previous vortex shedding cycle sheds into the downstream of the cylinder at  $t \approx 2T/5$ . On the other hand, two co-rotating weak vortices develop from the lower side of the cylinder over  $0T \leq t \leq 4T/5$  and then coalesce at  $t = 4T/5$ . The new weak vortex is being developed over  $6T/5 \leq t \leq 8T/5$  which then coalesces with the previously formed positive vortex to produce a single large vortex. In other words, three weak co-rotating vortices coalesce over  $0T \leq t \leq 8T/5$  to form a single positive vortex which becomes detached in the next vortex shedding cycle at  $t \approx 2T/5$ , following the shift of the low pressure region to the lower side of the cylinder. An interesting aspect which should be addressed here is that the negative vortex sheds but, in fact, remains attached to negative vortex shedding

layer. Figure 5.25 shows that the negative vortex becomes detached at  $t = 12T/5$  by both the positive vortex being developed in the lower vortex shedding layer and by the positive vorticity being developed near the free surface. The corresponding pressure distribution shows that the shedding of the negative vortex is associated with the large size low pressure region concentrated at the front of the cylinder. It is also interesting to note that at  $t = 12T/5$  the positive vortex at the lower side of the cylinder shows the region of the lowest pressure whereas the positive vorticity being developed near the free surface represents the high pressure region. The shed negative vortex immediately coalesces with the negative vortex shedding layer and then it propagates (being “pushed” by the propagating large positive vortex) into the near wake. Moreover, the “pushed” vortex becomes attached both to the negative vortex shedding layer and to the free surface. Finally, this vortex detaches and diffuses across the interface at the distance far away from the cylinder (approximately 10 diameters of the cylinder,  $10d$ ). The equivorticity plots shown in Figure 5.25 suggest that at  $h = 0.25$ , the free surface curvature is significantly pronounced, giving rise to so called “surface scars” which represent regions where the interface curvature changes sign. It is seen that the surface scar becomes sharper approximately at the point of maximum lift,  $t = 4T/5$ . Reichl *et al.* (2005) suggest that the sharpening of the interface is presumably due to the local Froude number in the region directly above the cylinder,  $Fr|_L$ . It is recalled that the local Froude number,  $Fr|_L$ , can be calculated based on the maximum dimensional  $u$ -velocity in the region directly above the cylinder,  $\bar{u}^*$ , at the time when the lift coefficient reaches its maximum and the dimensional local free surface height,  $h^*|_L$ , by using  $Fr|_L = \bar{u}^* / \sqrt{(g^* h^*|_L)}$ . The local Froude number,  $Fr|_L$ , generally becomes considerably higher than the global Froude

number,  $Fr$ , for the small cylinder submergence depth,  $h$ , and thereby, a sharpened scar occurs in the region where  $Fr|_L \rightarrow 1$ . When this happens, the accelerated fluid in the scar region interacts with the slower fluid from above the positive vortices and thereby, a shift from the surface scar to the localized wave breaking phenomenon occurs. The wave breaking is observed at  $t = 8T/5$  as shown in Figure 5.25. Reichl *et al.*'s work has shown that for small cylinder submergence depths,  $h$ , the negative vortices seem to decay rapidly into the downstream due to the viscous transport of the negative vorticity across the interface. Hence, the negative vorticity is being removed from the fluid by diffusion and cross-annihilation. This results in the near wake being dominated by the positive vortex structures. An examination of the vorticity plots in Figure 5.25 suggests that a similar phenomenon is also observed in the present numerical simulations for the case  $Fr = 0.4$ ,  $h = 0.25$  when  $f/f_0 = 3.0$ . In Figure 5.25, the pressure plots clearly show that the positive vortices represent the regions of the lowest pressure and thereby, have the greatest impact in the near wake. It is also seen that the positive vortices move faster than the negative ones. This is due to the fact that the convective velocity of the negative vortices decreases as surface curvature increases. The shed positive vortex seems to be lifted upward slightly by the downward movement of the fluid from the upper side of the cylinder. This results in the transport of the slow fluid from the region just about the shed vortex close to the free surface, resulting in the interface rising at positions downstream of the cylinder (regions of high pressure) as shown by Figure 5.25. To better understand the effect of both the Froude number,  $Fr = 0.4$  and the small cylinder submergence depth,  $h = 0.25$ , on the near wake evolution, a series of instantaneous snapshots over  $10T$  is plotted for non-periodic state, in Figure 5.26, for the case  $Fr = 0.4$ ,  $h = 0.25$  when

$f/f_0 = 3.0$ . Figure 5.26 shows that the flow is completely chaotic in the considered time interval. The main features of the flow are the stretching of the positive shear layer and the vortex roll-up delay.

For  $f/f_0 = 4.0$ , the equivorticity patterns, the streamline patterns and the pressure distribution in the near wake over five periods of cylinder oscillation,  $5T$ , for the case  $Fr = 0.4$ ,  $h = 0.25$  are shown in Figure 5.27 (quasi-periodic state). This figure indicates that the flow behaviour is very similar to the aforementioned case when  $f/f_0 = 3.0$  and  $Fr = 0.4$ ,  $h = 0.25$ . The observed mode of the vortex shedding formation is classified as the modified quasi-locked-on **C(2S)** mode, per  $5T$ , within  $20T$ . It can be seen from this figure that the negative vortex developed in the previous vortex shedding cycle becomes detached at  $t \approx T/2$ . Further, three co-rotating weak vortices develop and then coalesce in the lower vortex shedding layer over  $0T \leq t \leq 2T$ . The coalescence of these vortices results in a single large positive vortex that sheds at  $t \approx 7T/2$ . The negative vortex develops over  $T/2 \leq t \leq 5T$  and becomes detached by both the positive vortex being developed in the lower vortex shedding layer and by the positive vorticity being developed near the free surface in the next vortex shedding cycle ( $t \approx T/2$ ). It is interesting to note that the shed negative vortex dissipates near the free surface and tends to coalesce with the vortex being developed in the upper vortex shedding layer. An examination of the pressure plots indicates that again the positive vortices represent the regions of the lowest pressure and thus the near wake is controlled by the positive vortex structures. Moreover, the pronounced variations in the free surface level enhance the high and low pressure regions near the curved free surface interface. Furthermore, the highest pressure region associated with the stagnation seems to switch over between the rear of the cylinder and the

region directly above the cylinder when the free surface rises sufficiently this region.

Figure 5.28 displays the time histories of the lift coefficient,  $C_L$ , the PSD of  $C_L$  and the Lissajous trajectories,  $C_L(x)$ , for the case  $Fr = 0.4$ ,  $h = 0.5$ . It is evident that at each frequency ratio, the flow exhibits two regimes. The switching times are  $t \approx 52$  for  $f/f_0 = 1.0, 2.0, 4.0$  and  $t \approx 62$  for  $f/f_0 = 3.0$ . The corresponding spectra and the Lissajous trajectories are plotted for each of the flow regimes in Figure 5.28. In quasi-periodic state, all of  $C_L$  traces exhibit segments of almost repeatable signatures and thereby, indicate the quasi-locked-on wake states. The  $C_L$  trace is quasi-locked-on to the cylinder motion over  $T$  when  $f/f_0 = 1.0$ ; over  $2T$  when  $f/f_0 = 2.0$ ; over  $3T$  when  $f/f_0 = 3.0$  and over  $4T$  when  $f/f_0 = 4.0$ . Corresponding spectra of  $C_L$  suggest one well defined peak for  $f/f_0 = 1.0$  at  $f_0$ ; three well defined peaks for  $f/f_0 = 2.0$  at  $f_0, f$  and  $f + f_0$ ; four well defined peaks for  $f/f_0 = 3.0$  at  $f_0, 2f_0, f$  and  $f + f_0$ ; two well defined peaks for  $f/f_0 = 4.0$  at  $f_0$  and  $f$ . Taking an overview of the PSD of  $C_L$ , it is evident that the presence of the free surface seems to enhance the effect of the forcing frequency,  $f$ , relative to the case of  $h = \infty$  when  $f/f_0 = 2.0, 3.0$ . For each of the frequency ratios,  $1.0 \leq f/f_0 \leq 4.0$ , the dominant peak occurs at  $f_0$  when  $h = 0.5, \infty$ . Further representations of the lift coefficient,  $C_L$ , are given by the Lissajous trajectories,  $C_L(x)$ , which exhibit congruent shapes for small frequency ratios,  $f/f_0 \leq 2.0$ ; the less congruent hysteresis loops are observed for higher frequencies,  $f/f_0 \geq 3.0$ . Thus, the effect of varying the frequency ratio,  $f/f_0$ , is to destabilize the flow by enhancing the phase shifts between the fluctuations of the lift coefficient,  $C_L$ , and the cylinder motion. The pronounced phase variations are seen in non-periodic state for all  $f/f_0$ , indicating the complete loss of the phase-locking between  $C_L$  and the cylinder motion. In all of the flow regimes for each

$f/f_0 = 1.0, 2.0, 3.0, 4.0$ , the hysteresis loops of  $C_L(x)$  are largely shifted in the lower half plane comparing to those at  $h = \infty$ .

The corresponding time histories of the drag coefficient,  $C_D$ , the PSD of  $C_D$  and the Lissajous trajectories,  $C_D(x)$ , for the case  $Fr = 0.4, h = 0.5$  are shown in Figure 5.29. At  $f/f_0 = 1.0$ , less persistent patterns of  $C_D$  are observed. As  $f/f_0$  increases, the traces of the drag coefficient,  $C_D$ , exhibit more persistent shapes. Thus, in quasi-periodic state,  $C_D$  is quasi-locked on to the cylinder motion over  $T$  when  $f/f_0 = 1.0$ , over  $2T$  when  $f/f_0 = 2.0$ , over  $3T$  when  $f/f_0 = 3.0$  and over  $4T$  when  $f/f_0 = 4.0$ . The PSD of  $C_D$  suggest one peak,  $f$ , for  $f/f_0 = 1.0, 3.0, 4.0$  and two well defined peaks,  $f_0$  and  $f$ , for  $f/f_0 = 2.0$ . In all cases, the dominant peak occurs at the forcing frequency of cylinder oscillation,  $f$ , and the effect of  $f_0$  is seen to weaken rapidly relative to  $f$  as  $f/f_0$  increases. In the non-periodic state,  $C_D$  is dominated by the forcing frequency of cylinder oscillation,  $f$ . The traces of  $C_D(x)$  show less congruent shapes when  $f/f_0 = 1.0, 3.0$ . Thus, the flow is more destabilized at these frequency ratios,  $f/f_0$ , relative to the cases  $f/f_0 = 2.0, 4.0$ . Large phase variations and thereby, loss of the phase-locking are indicated by the last column in Figure 5.29. The directions of the hysteresis loops of  $C_D(x)$  suggest that the mechanical energy transfer is from the cylinder to the fluid irrespective of the presence of the free surface and the frequency ratio values,  $f/f_0 = 1.0, 2.0, 3.0, 4.0$ . The plots of  $C_D(x)$  also show that the hysteresis loops of large extent are essentially confined in the upper half plane.

For the case of  $f/f_0 = 1.0$ , the equivorticity patterns, the streamline patterns and the pressure distribution in the near wake over one period of cylinder oscillation,  $T$ , for

the case  $Fr = 0.4$ ,  $h = 0.5$  are displayed in Figure 5.30 (quasi-periodic state). The vortex shedding mode is designated as modified quasi-locked-on asymmetric **C(2S)** mode, per  $T$ , within  $5T$ . It is clearly seen from Figure 5.30 that the large amount of positive vorticity (region of the low pressure) develops in the region above the cylinder close to the curved free surface. This vorticity grows over  $0T \leq t < T/4$  and then coalesces with the positive vortex being developed in the lower vortex shedding layer ( $t < T/4$ ). As a result, the vortex street becomes significantly altered such that the coalesced positive vortices from both the free surface and the lower side of cylinder envelop the negative vortex being developed in the upper vortex shedding layer. On the other hand, the growing negative vortex eventually cuts through the coalesced vortices ( $t \approx T/4$ ) and thereby, a large positive vortex sheds into the near wake, following the shift of the low pressure region. It is interesting to note that the propagating positive vortex remains coalesced with the positive vorticity from the free surface. It is also noted that the negative vortex developing from the upper side of the cylinder becomes severely stretched over  $T/4 \leq t \leq 3T/4$  such that it tends to decay shortly after shedding (after traveling roughly  $3 \sim 4d$  downstream). Moreover, the previously shed negative vortices seem to be lifted upward and thereby, rapidly defuse across the interface. The pressure plots indicate that the near wake is dominated by the positive vortices as the very low pressure is associated with the centers of the positive vortex structures. It is also noted that at  $t = T/2$ , sufficiently high pressure is induced in the region where the fully developed negative vortex interacts with the secondary vorticity from the free surface.

Figure 5.31 shows the equivorticity patterns, the streamline patterns and the pressure distribution in the near wake over two periods of cylinder oscillation,  $2T$ , for the

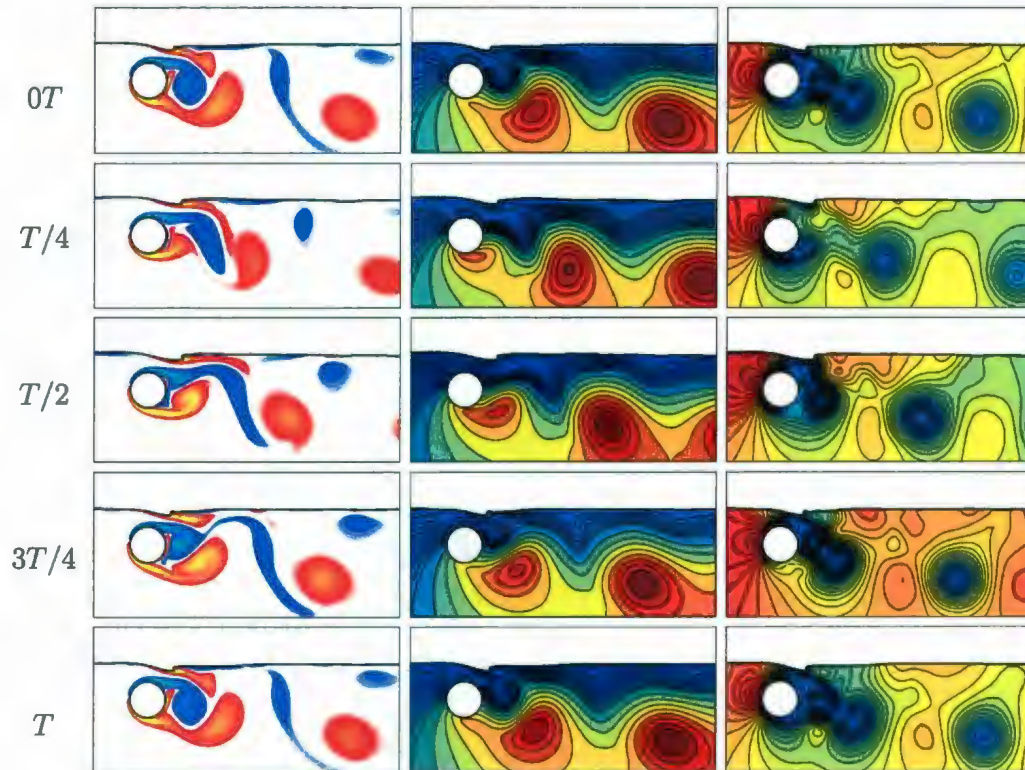


Figure 5.30: The equivorticity patterns (left), the streamline patterns (middle) and the pressure distribution in the near wake (right) over one period of cylinder oscillation,  $T$ , at  $R = 200$ :  $A = 0.13$ ,  $f/f_0 = 1.0$ ,  $Fr = 0.4$ ,  $h = 0.5$  ( $T \approx 5.051$ ,  $35.3 \leq t \leq 40.4$ ). The quasi-locked-on C(2S) mode, per  $T$ , is observed within  $5T$ .

case  $Fr = 0.4$ ,  $h = 0.5$  when  $f/f_0 = 2.0$  (quasi-periodic state). At this frequency ratio, the vortex formation becomes quasi-locked-on to the cylinder motion and the observed vortex shedding mode is designated as modified quasi-locked-on asymmetric C(2S) mode, per  $2T$ , within  $14T$ . The equivorticity plots indicate that a positive vortex from the lower side of the cylinder coalesces with the positive vortex from the free surface over  $T/2 < t < 3T/4$  and thereby, envelops the negative vortex which develops from the upper side of the cylinder. The corresponding pressure plots show

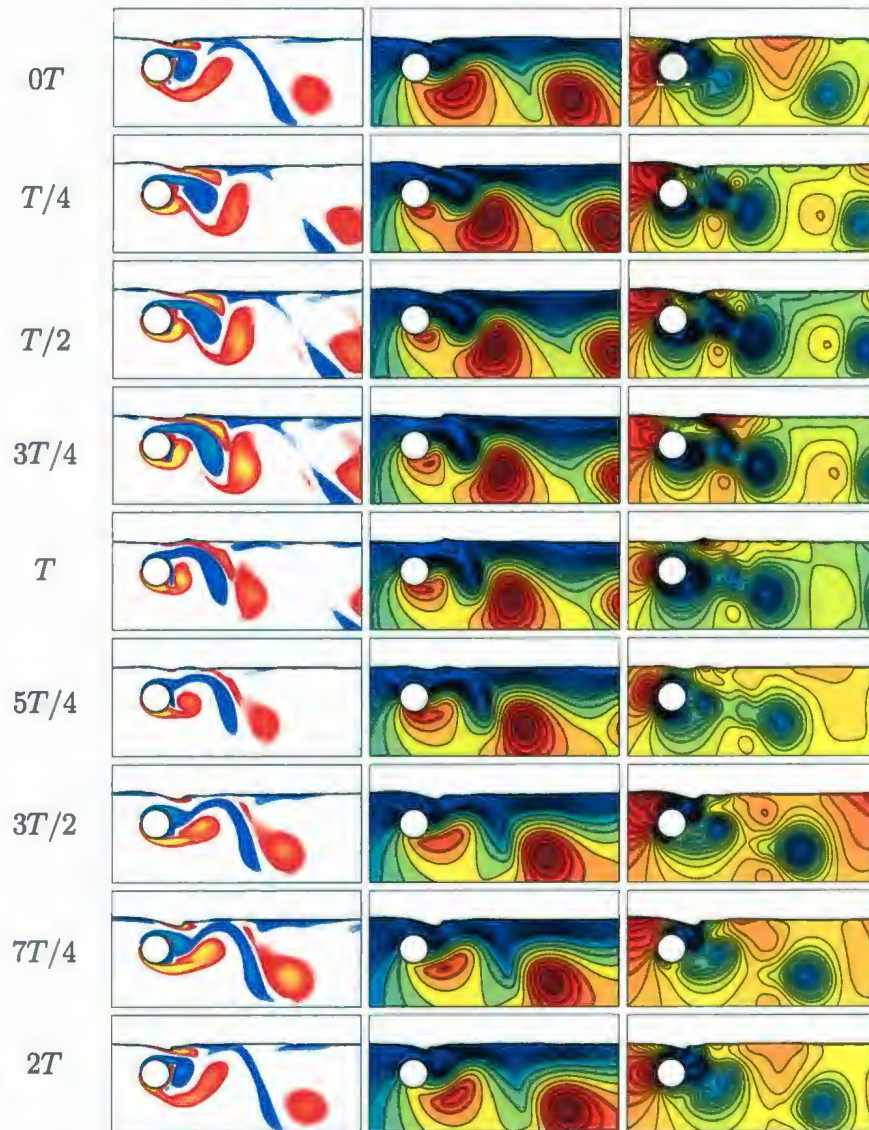


Figure 5.31: The equivorticity patterns (left), the streamline patterns (middle) and the pressure distribution in the near wake (right) over two periods of cylinder oscillation,  $2T$ , at  $R = 200$ :  $A = 0.13$ ,  $f/f_0 = 2.0$ ,  $Fr = 0.4$ ,  $h = 0.5$  ( $T \approx 2.525$ ,  $30.3 \leq t \leq 35.3$ ). The quasi-locked-on  $C(2S)$  mode, per  $2T$ , is observed within  $14T$ .

| Serial number | Eigenvalues ( $\times 10^3$ ) |        |        |
|---------------|-------------------------------|--------|--------|
|               | (a)                           | (b)    | (c)    |
| 1             | 1.2532                        | 1.1541 | 0.7939 |
| 2             | 0.5201                        | 0.5593 | 0.4724 |
| 3             | 0.3526                        | 0.2494 | 0.2697 |
| 4             | 0.2600                        | 0.1869 | 0.1732 |
| 5             | 0.0539                        | 0.0586 | 0.1249 |
| 6             | 0.0430                        | 0.0429 | 0.0883 |
| 7             | 0.0245                        | 0.0299 | 0.0690 |
| 8             | 0.0203                        | 0.0273 | 0.0539 |
| 9             | 0.0188                        | 0.0257 | 0.0496 |
| 10            | 0.0051                        | 0.0214 | 0.0444 |

Table 5.6: Leading eigenvalues for (a):  $h = \infty$ ,  $f/f_0 = 2.0$ ,  $t = 100$  to  $150$ ; (b):  $Fr = 0.4$ ,  $h = 0.5$ ,  $f/f_0 = 2.0$ ,  $t = 20$  to  $50$  (quasi-periodic state); (c):  $Fr = 0.4$ ,  $h = 0.5$ ,  $f/f_0 = 2.0$ ,  $t = 60$  to  $100$  (non-periodic state) at  $R = 200$ :  $A = 0.13$ .

that the development of the positive vortex from the free surface in the region above the cylinder induces the low pressure in this region and the absolute value of the pressure associated with this vortex rapidly decreases as the vortex coalesces with the positive vortex from the lower side of the cylinder. Furthermore, it is clearly seen from Figure 5.31 that the pronouncedly stretched negative vortex sheds at  $t \approx 2T$ , following the shift of the lower pressure region, and is immediately broken up into two

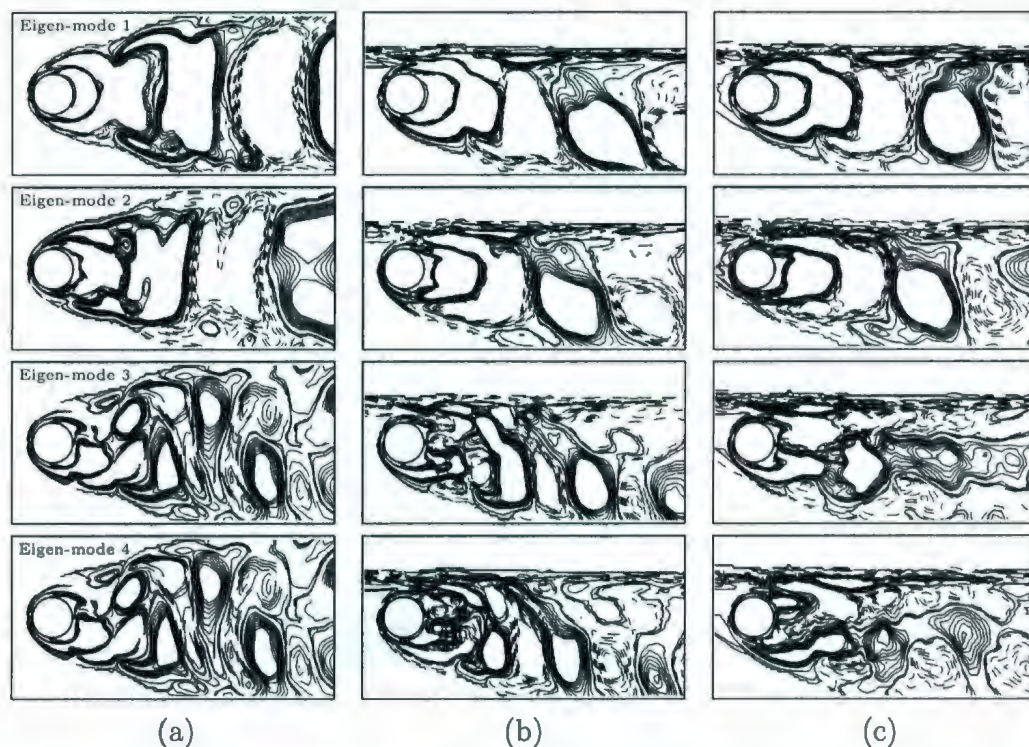


Figure 5.32: POD eigen-modes for (a):  $h = \infty$ ,  $f/f_0 = 2.0$ ,  $t = 100$  to  $150$ ; (b):  $Fr = 0.4$ ,  $h = 0.5$ ,  $f/f_0 = 2.0$ ,  $t = 20$  to  $50$  (quasi-periodic state); (c):  $Fr = 0.4$ ,  $h = 0.5$ ,  $f/f_0 = 2.0$ ,  $t = 60$  to  $100$  (non-periodic state) at  $R = 200$ :  $A = 0.13$ .

vortex structures, “small” and “large” negative vortices, in the next vortex shedding cycle by the growing layer of positive vorticity from the lower side of the cylinder. The developing positive vortex seems to lift the “small” negative vortex very close to the free interface, where this negative vorticity rapidly diffuses across the interface, and then the positive vortex sheds at  $t \approx 3T/2$ . It is also interesting to note that the “large” negative vortex follows the previously shed positive vortex in the downward direction far away from the free surface unlike the case of  $f/f_0 = 1.0$ . Moreover, the negative vortex tends to catch the positive vortex such that the distance between the two is very short. In addition, the negative vortex remains stretched and is very small

in size relative to the size of the positive vortex while the positive vortex tends to be oval shaped. Taking an overview of the pressure plots shown in Figure 5.31, it can be seen that the highest pressure region associated with the stagnation seems to switch over between the rear of the cylinder and the region directly above the cylinder when the free surface is sufficiently curved (raised) in this region. It is also noted that the shedding of the negative vortex at  $t = 2T$  seems to induce a local free surface rising and thus leads to the appearance of the sufficiently high pressure region near the curved free surface interface. However, as the shed negative vortex propagates into the downstream of the cylinder, the absolute value of the positive pressure near the free surface seems to decrease. Finally, it is clearly seen that again the near wake is dominated by the presence of positive vorticity as the positive vortex structures represent the regions of the lowest pressure.

Some physical aspects of the mechanism behind vortex shedding can also be addressed using a dynamical system approach based on the proper orthogonal decomposition (POD) technique [see, for example, Dipankar *et al.* (2007) and Deane and Mavriplis (1994)]. In Appendix E, the outline of the POD analysis is given. POD is a statistical technique which allows one to represent coherent structures as a low-description of the flow. In order to better understand the inhibiting influence of the presence of the free surface on the vortex formation and shedding, the POD analysis is employed for the case  $f/f_0 = 2.0$  when (i)  $Fr = 0.4$ ,  $h = 0.5$  and (ii)  $h = \infty$ . It is noted that these extreme cases represent a situation when the presence of the free surface breaks up the flow periodicity such that two flow regimes (the quasi-periodic and non-periodic near wake states) are observed. Following the work of Dipankar *et al.* (2007), the vortex shedding is characterized using POD eigen-modes. The numerical

data is handled by POD over a large domain using the method of snapshots by Sirovich (1987) (see Appendix E for details). Dipankar *et al.* (2007) note that in order to produce the correct statistical picture, it is necessary to remove the effects of early transients. Thus, for the case  $h = \infty$ ,  $f/f_0 = 2.0$  the data is taken from  $t = 100$  to 150. For the case  $Fr = 0.4$ ,  $h = 0.5$ ,  $f/f_0 = 2.0$ , two sets of data are considered with one set produced by taking data from  $t = 20$  to 50 (quasi-periodic state), the other from  $t = 60$  to 100 (non-periodic state). Table 5.6 displays the first ten leading eigenvalues for the considered cases, which were obtained by taking fifty snapshots. The computed eigen-modes for the first four eigenvalues shown in Table 5.6 are displayed in Figure 5.32. Taking an overview of this figure, it is seen that in all cases, the first two eigen-modes seem to accumulate most of the energy and thereby, are sufficient to characterize the vorticity distribution. These eigen-modes suggest that the vortex shedding begins from where the alternate signed vortex structures originate. Dipankar *et al.* (2007) note that when two modes carry most of the energy, the pattern of the vortex shedding can be defined by the phase shift between the eigen-modes. Thus, the vortex shedding begins due to the linear superposition and the pairwise coupling of these two eigen-modes. It is also noted that in the absence of the free surface, the lowest modes are almost symmetric about the near wake centerline as is clearly seen in Figure 5.32(a). For the higher modes, asymmetry about the near wake centerline is observed. On the other hand, Figures 5.32(b) and 5.32(c) indicate that in the presence of the free surface the lowest modes seem to be to prominently asymmetric, i.e., the near wake is seen to be skew symmetric. These figures also show that the near wake is narrowed in the vertical direction when compared to that shown in Figures 5.32(a). These observations suggest that the

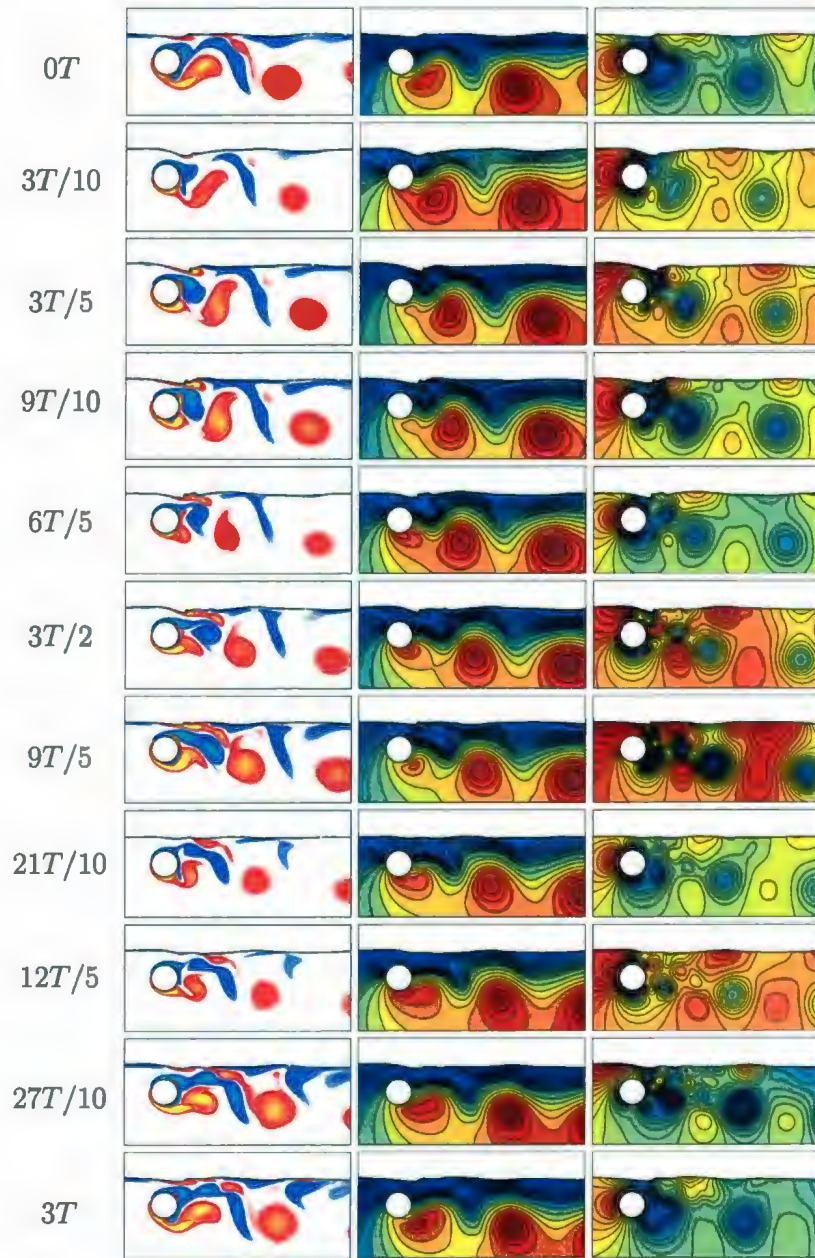


Figure 5.33: The equivorticity patterns (left), the streamline patterns (middle) and the pressure distribution in the near wake (right) over three periods of cylinder oscillation,  $3T$ , at  $R = 200$ :  $A = 0.13$ ,  $f/f_0 = 3.0$ ,  $Fr = 0.4$ ,  $h = 0.5$  ( $T \approx 1.684$ ,  $33.6 \leq t \leq 38.6$ ). The quasi-locked-on  $C(P+S)+S$  mode, per  $3T$ , is observed within  $18T$ .

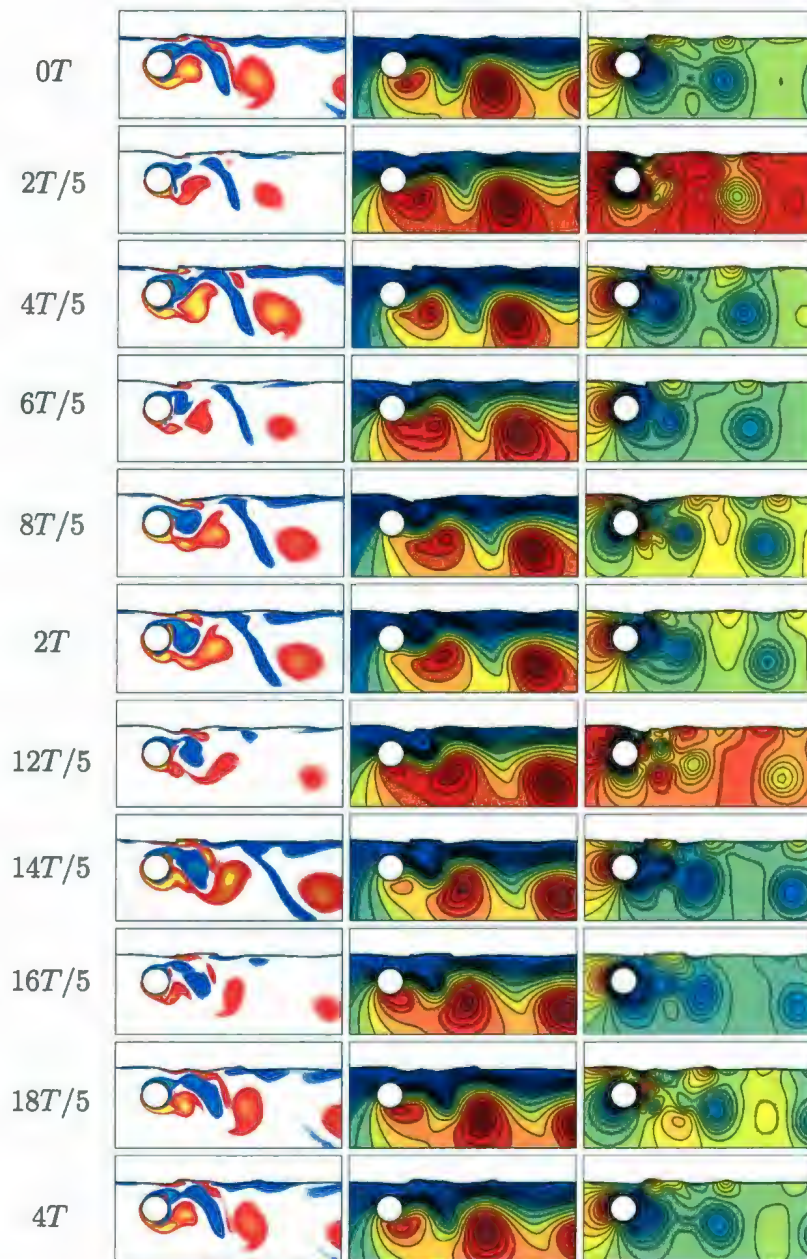


Figure 5.34: The equivorticity patterns (left), the streamline patterns (middle) and the pressure distribution in the near wake (right) over four periods of cylinder oscillation,  $4T$ , at  $R = 200$ :  $A = 0.13$ ,  $f/f_0 = 4.0$ ,  $Fr = 0.4$ ,  $h = 0.5$  ( $T \approx 1.263$ ,  $17.6 \leq t \leq 22.7$ ). The quasi-locked-on  $C(P+S)+S$  mode, per  $4T$ , is observed within  $28T$ .

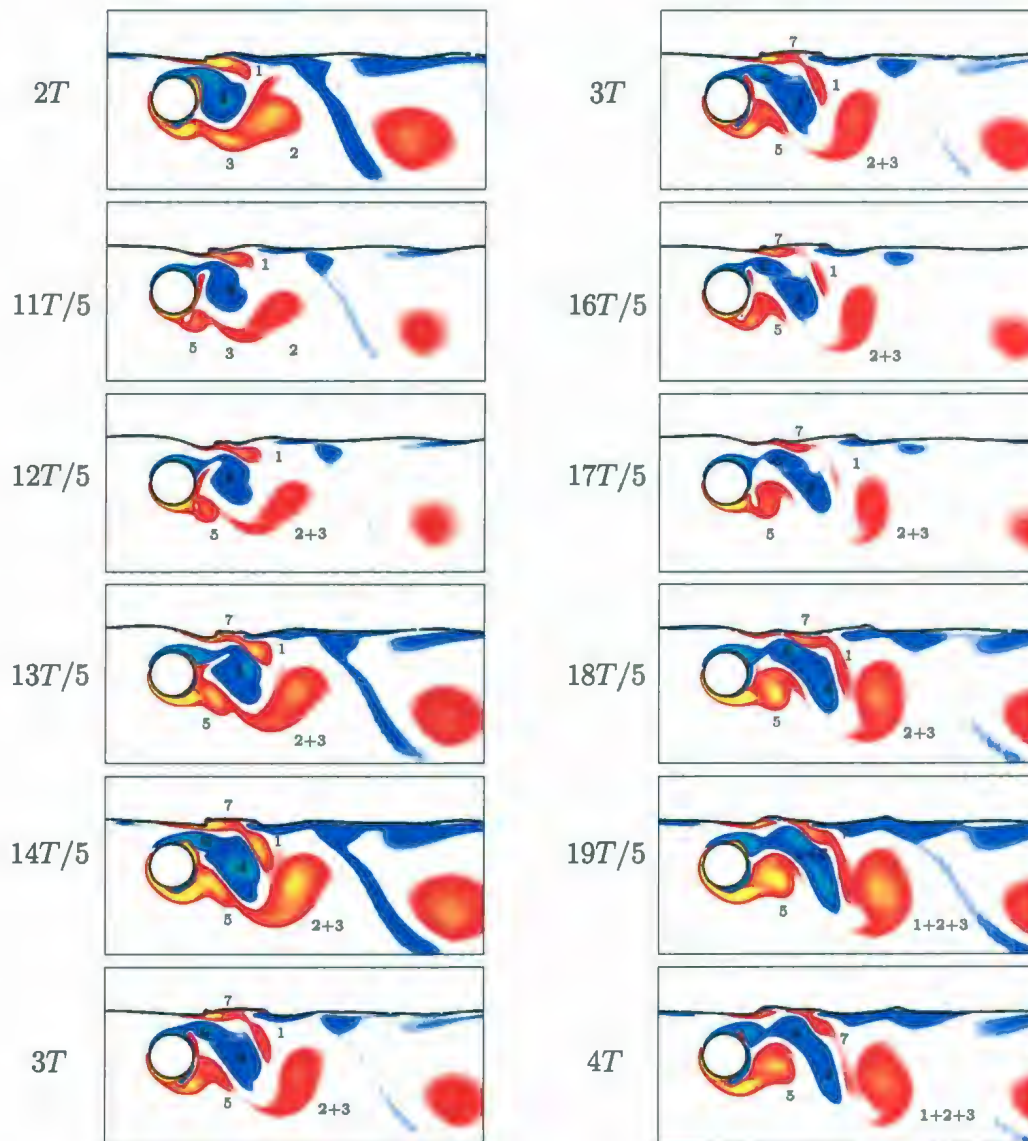


Figure 5.35: The vortex coalescence phenomenon in the quasi-locked-on  $C(P+S)+S$  mode over two periods of cylinder oscillation,  $2T$ , at  $R = 200$ :  $A = 0.13$ ,  $f/f_0 = 4.0$ ,  $h = 0.5$ ,  $Fr = 0.4$  ( $T \approx 1.263$ ,  $20.15 \leq t \leq 22.7$ ).

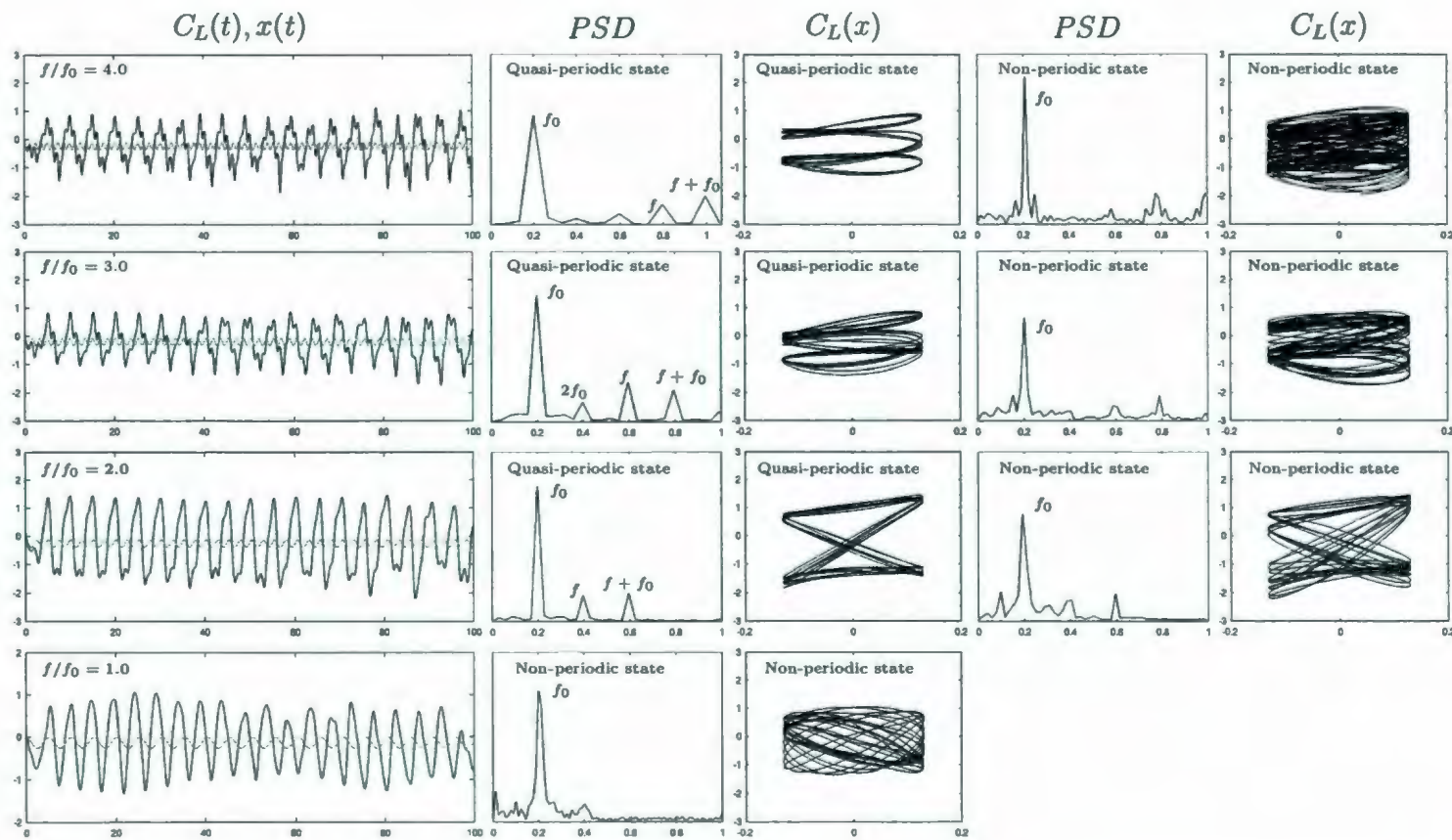


Figure 5.36: The time variation of the lift coefficient,  $C_L$ , (black) and the in-line displacement,  $x(t)$ , (gray); PSD of  $C_L$ ; Lissajous patterns of  $C_L$  at  $R = 200$ :  $A = 0.13$ ,  $1.0 \leq f/f_0 \leq 4.0$ ,  $Fr = 0.4$ ,  $h = 0.75$ .

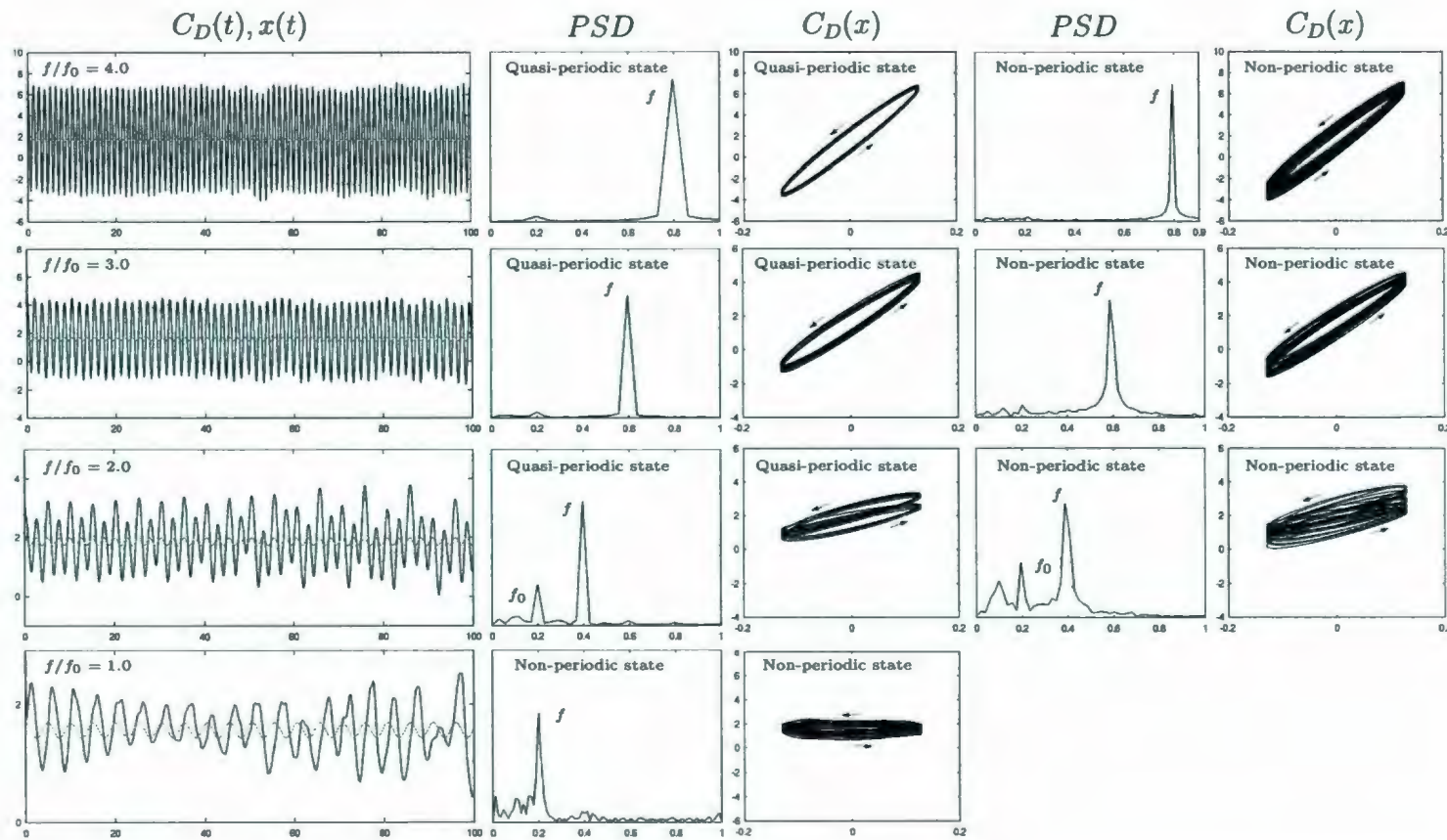


Figure 5.37: The time variation of the drag coefficient,  $C_D$ , (black) and the in-line displacement,  $x(t)$ , (gray); PSD of  $C_D$ ; Lissajous patterns of  $C_D$  at  $R = 200$ :  $A = 0.13$ ,  $1.0 \leq f/f_0 \leq 4.0$ ,  $Fr = 0.4$ ,  $h = 0.75$ .

presence of the free surface seems to bring control in the near wake vortical structures.

The typical equivorticity and streamline patterns, and the pressure distribution in the near wake over three periods of cylinder oscillation,  $3T$ , for the case  $Fr = 0.4$ ,  $h = 0.5$  when  $f/f_0 = 3.0$  are displayed in Figure 5.33 (quasi-periodic state). For this frequency ratio, the vortex shedding mode is designated as quasi-locked-on  $C(P+S)+S$  mode, per  $3T$ , within  $18T$ . This mode is similar to the classical  $C(P+S)$  mode observed for the transversely oscillating cylinder in uniform flow with the only difference that one more vortex is shed from the free surface. Figure 5.33 shows that a pair of co-rotating vortices from the upper side of the cylinder and the elongated positive vortex from the free surface are shed over  $0T \leq t < 3T/5$ . On the other hand, the positive vortex shed from the free surface rapidly decays ( $3T/10 < t < 6T/5$ ). At the same time, a pair of the co-rotating vortices being developed in the positive vortex shedding layer coalesces to form a single large vortex which then lifts up the shed negative vortex close to the free surface where it coalesces with the negative vorticity from the free surface. This negative vortex remains attached to the free surface and tends to diffuse across the interface while propagating into the downstream of the cylinder with the free surface waves. Finally, the positive vortex from the lower side of the cylinder is shed at  $t \approx 9T/10$ . This vortex is immediately reoriented and becomes oval shaped with the major axis laying parallel to the free surface. An examination of the pressure distribution suggests that the shedding of the positive vortex from the free surface is due to the shift of the low pressure into the region above the cylinder ( $t \approx 3T/10$ ). After that, the region of the low pressure seems to shift in the clockwise direction, resulting in the formation of the positive vorticity from the free surface. Similar to the aforementioned case  $f/f_0 = 2.0$ , the highest pressure region associated with

the stagnation seems to switch over between the rear of the cylinder and the region directly above the cylinder. The shift of the highest pressure associated with the stagnation towards the free surface has been observed for the time instants when the pronounced free surface rising occurs in this region. It is also seen that the induced interface curvature enhances the regions of the sufficiently high pressure near the free surface. The lowest pressure is again associated with the centers of the positive vortices, indicating that the near wake is significantly influenced by the presence of the positive vortical structures.

The snapshots in Figure 5.34 display the equivorticity patterns, the streamline patterns and the pressure distribution in the near wake over four periods of cylinder oscillation,  $4T$ , for the case  $Fr = 0.4$ ,  $h = 0.5$  when  $f/f_0 = 4.0$  (quasi-periodic state). For this frequency ratio, the vortex shedding exhibits quasi-locked-on **C(P+S)+S** mode, per  $4T$ , within  $28T$ . Taking an overview of Figure 5.34, it can be seen that a pair of negative vortices and the positive vortex from the free surface are shed at  $t \approx 2T/5$ . The small positive vortex from the free surface rapidly decays over  $2T/5 < t < 6T/5$ . Two co-rotating vortices develop in the lower vortex shedding layer over  $2T/5 < t < 12T/5$ . The positive vorticity layer lifts up the shed negative vortex close to the free surface where it coalesces with the negative vorticity from the free surface. This negative vortex remains attached to the free surface and decays after traveling approximately  $3 \sim 4d$  downstream of the cylinder. Furthermore, two co-rotating vortices being developed in the lower vortex shedding layer and the positive vortex from the free surface coalesce to form a single positive vortex which then envelops the negative vortex being developed from the upper side of the cylinder ( $t \approx 14T/5$ ). At  $t \approx 16T/5$ , the negative vorticity layer cuts through the "envelope"

and thereby, the positive vortex is shed. The pressure distribution shows that the positive vortex from the free surface becomes shed at the time when the low pressure shifts into the region above the cylinder. Moreover, the further shift of the low pressure leads to generation of the secondary vorticity near the free surface interface. Sufficiently high pressure is seen near the free surface as the free surface waves propagate downstream of the cylinder whereas the low pressure is seen to be associated with the shed positive vortices.

Figure 5.35 illustrates the vortex coalescence phenomenon in the quasi-locked-on  $C(P+S)+S$  mode over two periods of cylinder oscillation,  $2T$ , for the case  $h = 0.5$ ,  $Fr = 0.4$  when  $f/f_0 = 4.0$ . In this figure, the positive vortex "1" forms near the surface scar over  $2T \leq t \leq 12T/5$ . Moreover, three positive, "2", "3" and "5", and one negative, "4", vortices develop from the lower and upper sides of the cylinder, respectively ( $2T \leq t \leq 11T/5$ ). The co-rotating vortices "2" and "3" coalesce at  $t = 12T/5$  to form a single positive vortex "2+3". At  $t = 13T/5$ , another positive vortex, "7", starts to develop from the free surface while the vortex "1" tends to coalesce with the vortex "2+3" over  $13T/5 \leq t \leq 14T/5$ . As a result, the negative vortex from the upper side of the cylinder becomes enveloped by the positive vortices "1" and "2+3". However, at  $t = 14T/5$ , the negative vortex "6" starts to form in the upper shear layer. The vortex "6" pushes the vortex "4" and thereby, the positive vortex "2+3" speeds up and separates from the vortex "1" at  $t = 3T$ . At the next time instant,  $t = 16T/5$ , the positive vortex "2+3" sheds into the downstream of the cylinder. On the other hand, the vortex "1" being pushed by the negative vortex "4" catches the propagating positive vortex "2+3" over  $16T/5 \leq t \leq 18T/5$ . This results in the coalescence between the co-rotating vortices "1" and "2+3" at the next time

instant,  $t = 19T/5$ , such that the large positive vortex "1+2+3" forms. It is interesting to note that at  $t = 19T/5$ , the negative vortices "4" and "6" seem to coalesce for a short period of time and they become separated by the growing positive vortex "5" at  $t = 4T$ . It is also noted that the positive vortex "7" remains attached to the vortex "1" over  $17T/5 \leq t \leq 19T/5$  and it becomes detached as the positive vortex "1" completely coalesced with the positive vortex "2+3" ( $t = 4T$ ).

Finally, the case  $h = 0.75$  is considered. Figure 5.36 shows the time variation of the lift coefficient,  $C_L$ , the PSD of  $C_L$  and the Lissajous patterns of  $C_L$  for the case  $Fr = 0.4$ ,  $h = 0.75$ . It is evident that for the smallest frequency ratio,  $f/f_0 = 1.0$ , the trace of the lift coefficient,  $C_L$ , exhibits non-repeatable signatures. This observation is also suggested by the corresponding Lissajous patterns. It is clearly seen that the trajectories of  $C_L(x)$  are non-congruent from cycle to cycle of cylinder oscillation. This indicates large phase variations between the fluctuating lift coefficient,  $C_L$ , and the cylinder motion. Thus, the near wake frequency is not locked-on to the frequency of cylinder oscillation when  $f/f_0 = 1.0$ . On the other hand, for  $f/f_0 \geq 2.0$  the signatures of  $C_L$  suggest that the flow exhibits two regimes. The switching times are  $t \approx 42$  for  $f/f_0 = 2.0, 3.0$  and  $t \approx 37$  for  $f/f_0 = 4.0$ . Figure 5.36 suggests that when  $f/f_0 \geq 2.0$  (quasi-periodic state) the signatures of  $C_L$  exhibit almost periodic patterns over  $2T, 3T$  and  $4T$ , respectively, for  $f/f_0 = 2.0, 3.0, 4.0$ . In all cases, these traces show persistent patterns. Thus, the vortex formation is quasi-locked-on to the cylinder motion when  $f/f_0 \geq 2.0$ . It is also seen that when the switching time is reached, the traces of  $C_L$  become non-repeatable and thereby, show the transition of the wake into the non-periodic state. The corresponding spectra of the lift coefficient, PSD of  $C_L$ , show one well defined peak,  $f_0$ , when  $f/f_0 = 1.0$ ; three well defined peaks,

$f_0$ ,  $f$  and  $f + f_0$ , when  $f/f_0 = 2.0$ ; four well defined peaks,  $f_0$ ,  $2f_0$ ,  $f$  and  $f + f_0$ , when  $f/f_0 = 3.0$  and three well defined peaks,  $f_0$ ,  $f$  and  $f + f_0$ , when  $f/f_0 = 4.0$ . Comparing to the reference case in the absence of the free surface,  $h = \infty$ , it is seen that the effect of the free surface is to enhance the additional frequency,  $f$ , when  $f/f_0 = 2.0, 3.0$ . For each of the frequency ratios,  $1.0 \leq f/f_0 \leq 4.0$ , the dominant peak occurs at  $f_0$  when  $h = 0.75, \infty$ . Thus, the lift coefficient,  $C_L$ , fluctuates with the dominant frequency equal to the natural vortex shedding frequency,  $f_0$ , irrespective of the presence of the free surface. The Lissajous traces,  $C_L(x)$ , exhibit almost congruent shapes with a little shift from cycle to cycle of cylinder oscillation. These observations suggest that when  $f/f_0 \geq 2.0$  the lift coefficient,  $C_L$ , is quasi-phase-locked to the cylinder motion. In addition, at each frequency ratio,  $1.0 \leq f/f_0 \leq 4.0$ , the hysteresis loops of  $C_L(x)$  are essentially confined in the lower half plane again emphasizing the inhibiting influence of the free surface. Considering the last two columns in Figure 5.36, it is evident that in the non-periodic state the lift coefficient,  $C_L$ , fluctuates with  $f_0$  irrespective of the frequency ratio,  $f/f_0$ . In this regime, the traces of  $C_L(x)$  show high phase variations from cycle to cycle of cylinder oscillation and thus indicate the loss of phase-locking between the cylinder motion and the fluctuating  $C_L$ .

The time history of the drag coefficient,  $C_D$ , the PSD of  $C_D$  and the Lissajous patterns of  $C_D$  for the case  $Fr = 0.4$ ,  $h = 0.75$  are displayed in Figure 5.37. It is evident that at  $f/f_0 = 1.0$ , the signatures of  $C_D$  are non-repeatable. On the other hand, when  $f/f_0 \geq 2.0$ , the traces of  $C_D$  exhibit almost periodic patterns over  $2T$  for  $f/f_0 = 2.0$  and over  $T$  for  $f/f_0 = 3.0, 4.0$ . The traces of the drag coefficient,  $C_D$ , show persistent patterns when  $f/f_0 \geq 2.0$ . Thus, the varying of  $f/f_0$  is seen to stabilize the fluctuations of  $C_D$ . It is also seen that as  $f/f_0$  increases, the magnitudes

of the positive and negative peaks of  $C_D$  become larger. Spectra of  $C_D$  suggest the existence of one well defined peak,  $f$ , when  $f/f_0 = 1.0, 3.0, 4.0$  and two well defined peaks,  $f_0$  and  $f$ , when  $f/f_0 = 2.0$ . In all cases, the dominant peak occurs at  $f$ . Taking an overview of the PSD of  $C_D$  in the non-periodic state, it is concluded that even in the non-periodic state, the drag coefficient,  $C_D$ , oscillates with the dominant frequency which equals to  $f$  irrespective of  $f/f_0$ . The traces of  $C_D(x)$  exhibit almost congruent shapes when  $f/f_0 \geq 2.0$  and thereby, indicate the quasi-phase-locking between the fluctuation drag coefficient,  $C_D$ , and the cylinder motion. The hysteresis loops of  $C_D(x)$  are essentially confined in the upper half plane when  $1.0 \leq f/f_0 \leq 4.0$ . Moreover, it is evident that as  $f/f_0$  increases, these loops tend to shift towards the lower half plane. The last column in Figure 5.37 indicates the loss of the phase-locking between the cylinder and  $C_D$  as the wake transition to the non-periodic state occurs. The directions of the hysteresis loops again suggest that in all cases the mechanical energy transfer is from the cylinder to the fluid. It is noted that the amount of transferred energy increases as  $f/f_0$  increases.

For the frequency ratio  $f/f_0 = 2.0$ , the equivorticity and streamline patterns, and the pressure distribution in the near wake over two periods of cylinder oscillation,  $2T$ , for the case  $Fr = 0.4, h = 0.75$  are plotted in Figure 5.38 (quasi-periodic state). In this regime, the vortex shedding exhibits the quasi-locked-on **P+S** mode, per  $2T$ , within  $14T$ . In this figure, the positive vortex and negative vortex develop from the free surface and the upper vortex shedding layer, respectively, over  $0T \leq t < 3T/2$ . The negative vortex sheds at  $t \approx 3T/2$  while the positive vortex from the free surface rapidly weakens due to viscous transport across the interface and thereby, annihilates by  $t \approx 3T/2$ . A pair of co-rotating vortices develops in the lower vortex shedding layer

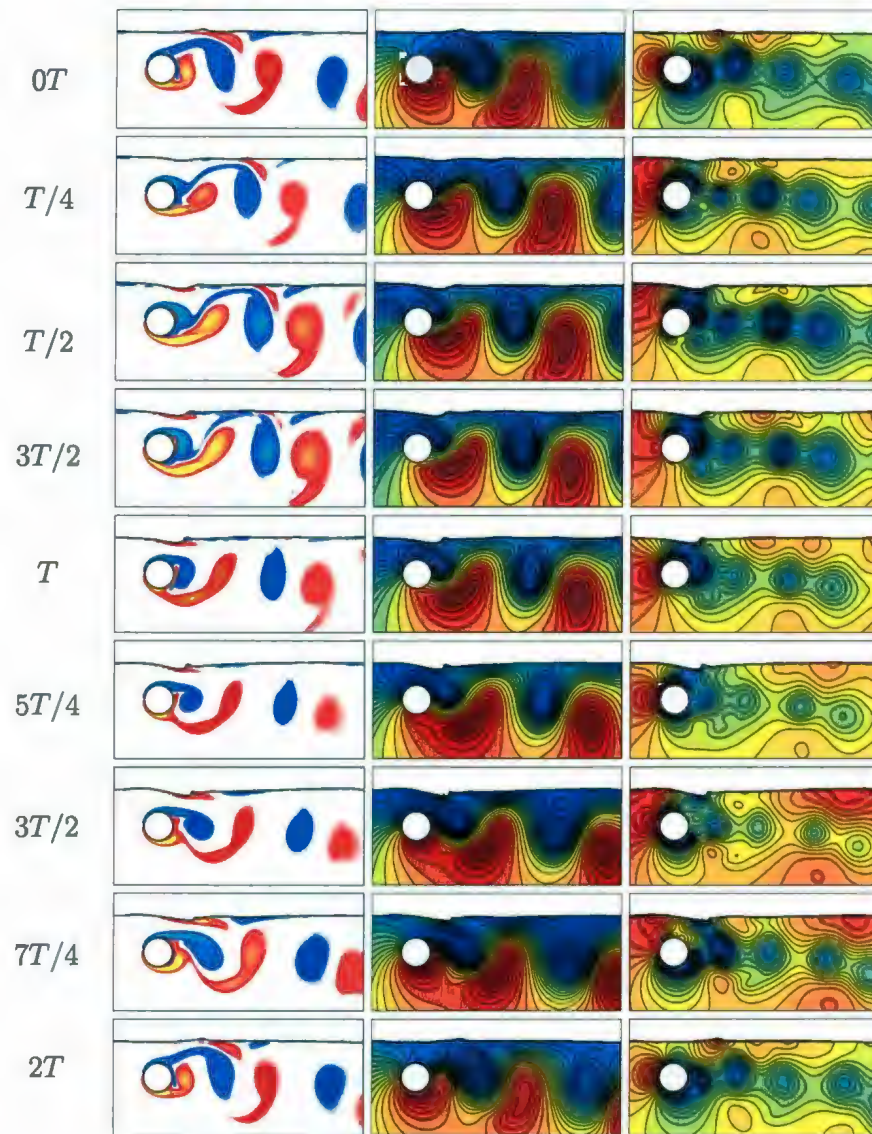


Figure 5.38: The equivorticity patterns (left), the streamline patterns (middle) and the pressure distribution in the near wake (right) over two periods of cylinder oscillation,  $2T$ , at  $R = 200$ :  $A = 0.13$ ,  $f/f_0 = 2.0$ ,  $Fr = 0.4$ ,  $h = 0.75$  ( $T \approx 2.525$ ,  $17.6 \leq t \leq 22.8$ ). The quasi-locked-on P+S mode, per  $2T$ , is observed within  $14T$ .

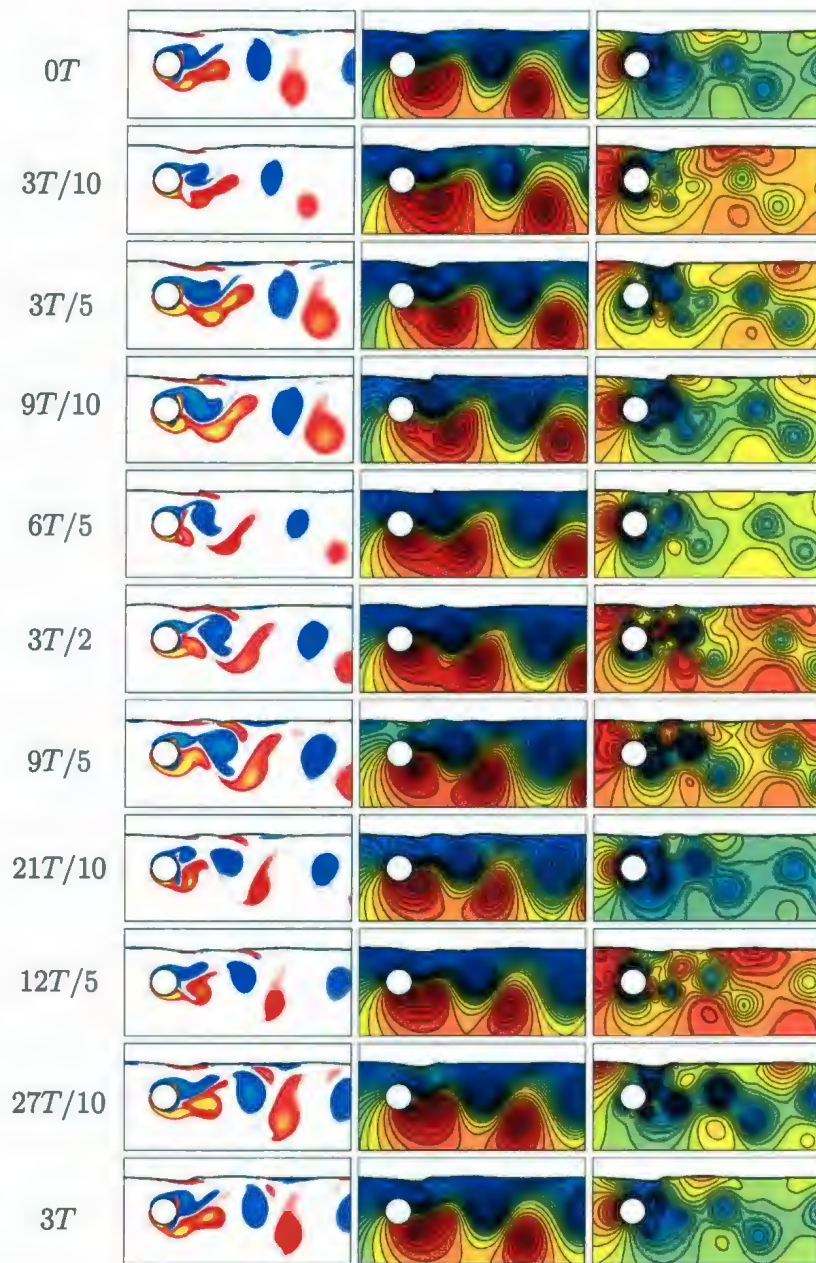


Figure 5.39: The equivorticity patterns (left), the streamline patterns (middle) and the pressure distribution in the near wake (right) over three periods of cylinder oscillation,  $3T$ , at  $R = 200$ :  $A = 0.13$ ,  $f/f_0 = 3.0$ ,  $Fr = 0.4$ ,  $h = 0.75$  ( $T \approx 1.684$ ,  $20.2 \leq t \leq 25.2$ ). The quasi-locked-on  $C(2S)+S$  mode, per  $3T$ , is observed within  $18T$ .

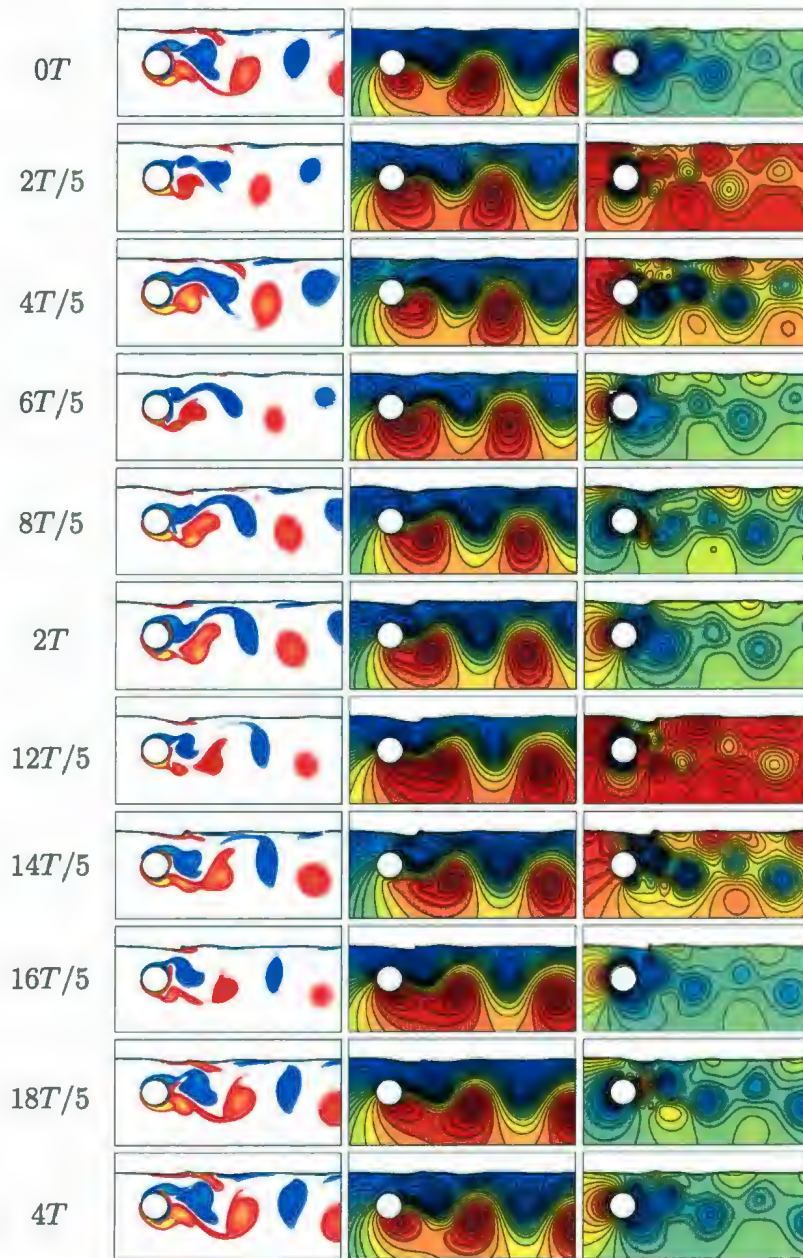


Figure 5.40: The equivorticity patterns (left), the streamline patterns (middle) and the pressure distribution in the near wake (right) over four periods of cylinder oscillation,  $4T$ , at  $R = 200$ :  $A = 0.13$ ,  $f/f_0 = 4.0$ ,  $Fr = 0.4$ ,  $h = 0.75$  ( $T \approx 1.263$ ,  $22.7 \leq t \leq 27.7$ ). The quasi-locked-on  $C(2S)+S$  mode, per  $4T$ , is observed within  $12T$ .

over  $3T/2 \leq t \leq 7T/4$  and then is shed into the downstream of the cylinder at  $t \approx 2T$ . It is interesting to note that both the negative and positive vortices propagating into the near wake of the cylinder are elongated in the transverse direction such that their shapes are similar to that observed at  $h = \infty$ . This indicates that the effect of the free surface weakens as  $h$  increases, as expected. On the other hand, the pressure distribution indicates that even for the large cylinder submergence depth,  $h = 0.75$ , there are still visible regions of the sufficiently high pressure near the curved free surface interface. It is also seen that there is the low pressure region near the surface scar which leads to the development of the positive vorticity near the interface. Figure 5.38 also suggests that the highest pressure in the stagnation seems to switch over between the rear of the cylinder and the region directly above the cylinder when the free surface rises sufficiently in this region.

The plots of Figure 5.39 show the equivorticity patterns, the streamline patterns and the pressure distribution in the near wake over three periods of cylinder oscillation,  $3T$ , for the case  $Fr = 0.4$ ,  $h = 0.75$  when  $f/f_0 = 3.0$  (quasi-periodic state). The vortex shedding mode is designated as quasi-locked-on  $C(2S)+S$  mode, per  $3T$ , within  $18T$ . Taking an overview of the equivorticity plots in Figure 5.39, it is evident that a pair of positive vortices develops and coalesces over  $0T \leq t < 9T/10$  to produce a single large vortex which then sheds at  $t \approx 6T/5$ . At the same time, the positive vortex near the curved free surface interface is being developed. Moreover, the negative vortex from the upper side of the cylinder develops over  $0T \leq t \leq 9T/5$  and then sheds at  $t \approx 21T/10$ . It is interesting to note that this negative vortex interacts with the positive vortex from the free surface and thereby, displaces this positive vortex. As a result, the small positive vortex sheds from the free surface followed by the shedding

of the negative vortex from the upper side of the cylinder ( $t \approx 27T/10$ ). It is seen that both negative and positive vortices propagating into the near wake of the cylinder are elongated in the transverse direction. The pressure plots suggest that again the vortex shedding from the cylinder and from the free surface is due to the shift of the low pressure region. It is also seen that the formation of the positive vortex in the scar area induces sufficiently low pressure. The absolute value of the pressure in the scar region seems to decrease as the free surface is rising. The regions of sufficiently high pressure appear near the rising free surface as free surface waves propagate into the downstream of the cylinder. It can be seen that these regions are largely dissipated near the interface within approximately  $2 \sim 3d$ . An interesting aspect to address here is that, unlike the other cases, the highest pressure region seems to switch over between the stagnation area and front area of the cylinder.

Finally, the equivorticity patterns, the streamline patterns and the pressure distribution in the near wake over four periods of cylinder oscillation,  $4T$ , for the case  $Fr = 0.4$ ,  $h = 0.75$  when  $f/f_0 = 4.0$  are displayed in Figure 5.40 (quasi-periodic state). For this frequency ratio, the vortex shedding mode is quasi-locked-on **C(2S)+S** mode, per  $4T$ , within  $12T$ . This figure indicates that the positive vortex developed in the previous vortex shedding cycle sheds into the downstream of the cylinder at  $t \approx 2T/5$ . On the other hand, two co-rotating vortices develop in the upper vortex shedding layer and then coalesce to form a single large vortex ( $0T \leq t \leq 8T/5$ ). It is seen that at  $f/f_0 = 4.0$  the free surface exhibits pronounced deformations and a large amount of the opposite signed vorticity appears near the interface. The positive vortex from the free surface is shed followed by the development of the negative vortex in the upper vortex shedding layer. On the other hand, the small positive vortex

from the interface annihilates immediately after its shedding. Furthermore, the negative vortex becomes detached at  $t \approx 12T/5$ . Similarly, a pair of co-rotating vortices develops in the lower vortex shedding layer and coalesces over  $6T/5 \leq t \leq 12T/5$  to form a single large vortex which is then shed into the near wake of the cylinder in the next vortex shedding cycle ( $t \approx 2T/5$ ). It is also noted that the propagating negative vortices tend to travel upward and they become more oval shaped as they approach the free surface. An examination of the pressure distribution shown in Figure 5.40 suggests that similar to the aforementioned case  $f/f_0 = 3.0$ , the highest pressure region seems to switch over between the stagnation area and the front area of the cylinder. Moreover, it can be seen again that the formation and the shedding of the positive vortex from the free surface is associated with the presence of the low pressure region near the free surface. The regions of sufficiently high pressure near the curved interface are seen approximately  $1 \sim 2d$  as the free surface waves propagate into the downstream of the cylinder.

| $f/f_0$ | $h = 0.25$   |       | $h = 0.5$   |       | $h = 0.75$   |       | $h = \infty$ |       |
|---------|--|-------|---|-------|--|-------|--------------|-------|
|         | Mode   | $T_0$ | Mode  | $T_0$ | Mode   | $T_0$ | Mode         | $T_0$ |
| 1.0     | non-locked   | -     | C(2S)* (within 5T);<br>non-locked $5T < t < 20T$        | T     | non-locked   | -     | non-locked   | -     |
| 2.0     | non-locked   | -     | C(2S)* (within 14T);<br>non-locked $14T < t < 40T$      | 2T    | (P+S)* (within 14T)<br>non-locked $14T < t < 40T$      | 2T    | 2S           | 2T    |
| 3.0     | C(2S)* (within 20T);<br>non-locked $20T < t < 60T$ | 4T    | [C(P+S)+S]* (within 18T);<br>non-locked $18T < t < 60T$ | 3T    | [C(2S)+S]* (within 18T)<br>non-locked $18T < t < 60T$  | 3T    | non-locked   | -     |
| 4.0     | C(2S)* (within 20T);<br>non-locked $20T < t < 80T$ | 5T    | [C(P+S)+S]* (within 28T);<br>non-locked $28T < t < 80T$ | 4T    | [C(2S)+S]* (within 12T);<br>non-locked $12T < t < 80T$ | 4T    | non-locked   | -     |

Table 5.7: The effect of the free surface inclusion at  $Fr = 0.4$ ,  $h = 0.25, 0.5, 0.75$ , and the frequency ratio,  $f/f_0$ , on flow regimes, vortex shedding modes and their periods,  $T_0$ , at  $R = 200$ ,  $A = 0.13$ ,  $1.0 \leq f/f_0 \leq 4.0$ . The superscript “\*” denotes quasi-locked-on modes.

Figure 5.41 summarizes the effect of the cylinder submergence depth,  $h$  ( $= 0.25, 0.5, 0.75$ ), and the frequency ratio,  $f/f_0$  ( $= 1.0, 2.0, 3.0, 4.0$ ), on the equivorticity

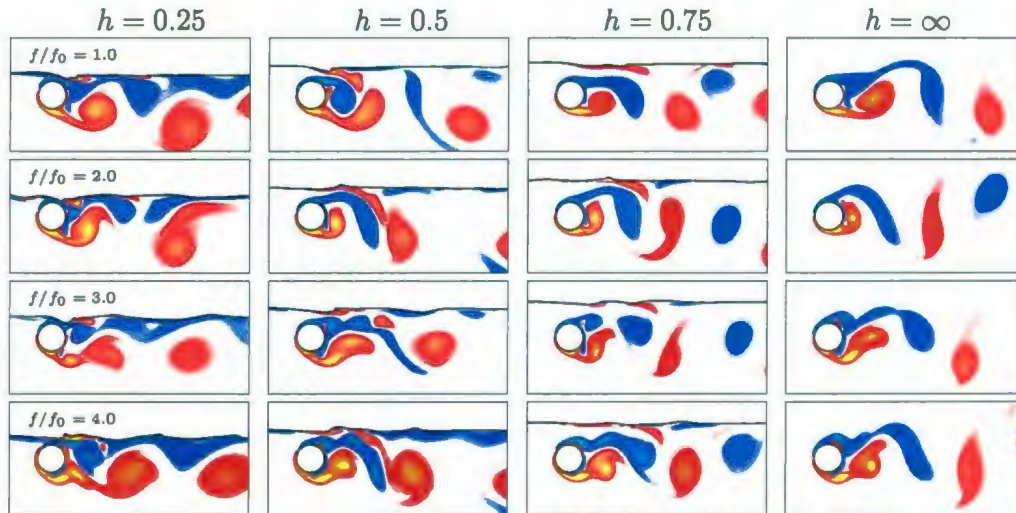


Figure 5.41: The effect of the cylinder submergence depth,  $h$ , and the frequency ratio,  $f/f_0$ , on the equivorticity patterns at  $R = 200$ :  $A = 0.13$ ,  $Fr = 0.4$ . All snapshots are taken at the instant  $x(t) = A$ .

patterns for the case  $R = 200$ ,  $A = 0.13$  when  $Fr = 0.4$ . The reference case  $h = \infty$  is also shown in this figure. The snapshots are taken at the instant  $x(t) = A$ . It is noted that for the periodic/quasi-periodic cases the snapshots are taken over the time interval in which the flow reaches to a periodic/quasi-periodic state. For non-periodic cases, the commonly appearing equivorticity plots at  $x(t) = A$  (within the time interval  $0 < t \leq 100$ ) are shown in Figure 5.41. Figure 5.41 shows that at  $h = 0.25, 0.5, 0.75$  the near wake structure is changed significantly when compared to the reference case  $h = \infty$ . It can be seen that the interface curvature is considerably pronounced and thus, there is a diffusion of the opposite signed vorticity in both the free surface and the fluid flow. This leads to the appearance of the localized wave breaking for smaller cylinder submergence depths,  $h = 0.25, 0.5$ . Moreover, the secondary vorticity from the interface seems to be convected by the free surface

waves into the near wake for all the frequency ratios,  $f/f_0 = 1.0, 2.0, 3.0, 4.0$ , when  $h = 0.25, 0.5, 0.75$ . It is also seen that at  $h = 0.5, 0.75$ , the large amount of positive vorticity develops near the curved free surface. This vorticity tends to coalesce with the near wake vorticity. As a result, the vortex street becomes significantly altered. An interesting aspect to address here is that at  $h = 0.5$ , the coalesced positive vortices from both the free surface and the lower side of cylinder envelop the negative vortex being developed in the upper vortex shedding layer. It is also seen that the previously shed negative vortices seem to be lifted upward and thereby, rapidly diffuse across the interface. When the cylinder submergence depth,  $h$ , is reduced up to 0.25, it is evident, again, that the negative vorticity annihilates due to a strong interaction with the free surface. It is also noted that the negative vortex developing from the upper side of the cylinder becomes severely stretched such that it tends to decay shortly after shedding. It is interesting to note that at  $h = 0.25$ , the significant amount of the positive vorticity is observed for each frequency ratio,  $f/f_0$ , unlike the other cases shown in Figure 5.41. This indicates that at  $h = 0.25$ , the near wake is completely dominated by the presence of the positive vortical structures. Figure 5.41 indicates that at each frequency ratio,  $f/f_0 = 1.0, 2.0, 3.0, 4.0$ , the vortex formation length increases (maximum by  $\approx 136.4\%$ ) as  $h$  decreases from 0.75 to 0.25. An examination of the equivorticity plots in Figure 5.41 suggests that increasing the frequency ratio,  $f/f_0$ , seems to increase the free surface curvature. As a result, with increase in  $f/f_0$ , the positive vortices move faster than the negative ones. This is due to the fact that the convective velocity of the negative vortices decreases as surface curvature increases. Furthermore, the negative vortices seem to decay more rapidly into the downstream due to the viscous transport of the negative vorticity across

the interface as  $f/f_0$  increases. Taking an overview of Figure 5.41, it is also noted that increasing  $f/f_0$  from 2.0 to 4.0 seems to increase the vortex formation length (maximum by  $\approx 140\%$ ) when  $h = 0.25, 0.75$ . It can also be seen from this figure that at the smallest cylinder submergence depth,  $h = 0.25$ , the upper vortex layer becomes largely dissipated as  $f/f_0$  increases from 1.0 to 4.0. Moreover, at  $h = 0.25$ , the amount of positive vorticity seems to increase and thereby, the near wake becomes more dominated by the positive vortical structures as  $f/f_0$  varies.

Tables 5.7-5.12 summarize the effect of the free surface presence for the case  $Fr = 0.4$ ,  $h = 0.25, 0.5, 0.75$  when  $f/f_0 = 1.0, 2.0, 3.0, 4.0$  on the flow regimes, the vortex shedding modes and their periods,  $T_0$ , the fluctuating fluid forces and the mechanical energy transfer,  $E$ . This investigation has shown that when  $Fr = 0.4$ , it is possible to generate distinctly different patterns of the vortex formation than that of classical vortex shedding modes observed for a cylinder subject to transverse oscillations in uniform flow. It is confirmed that the presence of the free surface provides the possibility for quasi-locked-on vortex formation not only from the cylinder but also from the free surface. These new vortex shedding modes are classified based on the terminology of Williamson and Roshko (1988) and are shown in Table 5.7. In the quasi-periodic flow state, the commonly observed vortex shedding modes are **C(2S)** when  $h = 0.25$ ; **C(2S)**, **C(P+S)+S** when  $h = 0.5$  and **C(2S)+S** when  $h = 0.75$ . It is noted that the **C(P+S)+S** and **C(2S)+S** modes are similar, respectively, to the classical **C(P+S)** and **C(2S)** modes with the only exception that one more vortex (from the free surface) is shed downstream of the cylinder over the period of vortex shedding,  $T_0$ . Moreover, unlike the classical vortex shedding modes, the coalescence between the positive vortices from the lower side of the cylinder and the positive vor-

ticity being developed near the curved free surface is observed in  $\mathbf{C(P+S)+S}$  and  $\mathbf{C(2S)+S}$  modes.

Tables 5.8-5.11 show the values of the mean lift and drag coefficients,  $\widehat{C}_L$  and  $\widehat{C}_D$ , and the RMS lift and drag coefficients,  $C_{L,rms}$  and  $C_{D,rms}$ , for the case  $Fr = 0.4$ ,  $h = 0.25, 0.5, 0.75$ . The reference case  $h = \infty$  is also displayed in these tables. In all the tables that follow, “ $\rightarrow$ ” indicates the change in the fluid characteristic as the transition of the fluid from the quasi-periodic state into the non-periodic state occurs. Tables

| $f/f_0 / h$ | 0.25                          | 0.5                           | 0.75                          | $\infty$ |
|-------------|-------------------------------|-------------------------------|-------------------------------|----------|
| 1.0         | -0.7862                       | -0.2031 $\rightarrow$ -0.3323 | -0.1148                       | -0.0028  |
| 2.0         | -0.8080                       | -0.4088 $\rightarrow$ -0.4770 | -0.2283 $\rightarrow$ -0.2972 | -0.0012  |
| 3.0         | -0.8883 $\rightarrow$ -0.9725 | -0.4542 $\rightarrow$ -0.4175 | -0.1803 $\rightarrow$ -0.2487 | -0.0011  |
| 4.0         | -0.8525 $\rightarrow$ -0.8613 | -0.4005 $\rightarrow$ -0.3813 | -0.1932 $\rightarrow$ -0.2459 | -0.0028  |

Table 5.8: The effect of the free surface inclusion at  $Fr = 0.4$ ,  $h = 0.25, 0.5, 0.75$  and the frequency ratio,  $f/f_0$ , on the mean lift coefficient,  $\widehat{C}_L$ , at  $R = 200$ :  $A = 0.13$ ,  $1.0 \leq f/f_0 \leq 4.0$ .

5.8 and 5.9 indicate that the presence of the free surface has important consequences for the values of the mean lift and drag coefficients,  $\widehat{C}_L$  and  $\widehat{C}_D$ . Comparison of the results shown in these tables indicates that for  $h = 0.25, 0.5, 0.75$  and all values of  $f/f_0$ , the values of the mean lift coefficient,  $\widehat{C}_L$ , are decreased significantly when compared to that at  $h = \infty$ . The  $\widehat{C}_L$  varies in the interval between  $-0.9725$  and  $-0.1148$  when the free surface is present whereas the values of  $\widehat{C}_L$  are nearly zero at  $h = \infty$ , as expected. It is interesting to note that  $\widehat{C}_L$  is negative irrespective of the

| $f/f_0 / h$ | 0.25            | 0.5             | 0.75            | $\infty$ |
|-------------|-----------------|-----------------|-----------------|----------|
| 1.0         | 1.4506          | 1.7180 → 1.5712 | 1.5645          | 1.3442   |
| 2.0         | 1.4800          | 1.6714 → 1.6583 | 1.8506 → 1.8390 | 1.6464   |
| 3.0         | 1.4275 → 1.5898 | 1.5531 → 1.4783 | 1.6299 → 1.5290 | 1.3916   |
| 4.0         | 1.4466 → 1.5382 | 1.6092 → 1.5722 | 1.5721 → 1.7117 | 1.4064   |

Table 5.9: The effect of the free surface inclusion at  $Fr = 0.4$ ,  $h = 0.25, 0.5, 0.75$  and the frequency ratio,  $f/f_0$ , on the mean drag coefficient,  $\widehat{C}_D$ , at  $R = 200$ :  $A = 0.13$ ,  $1.0 \leq f/f_0 \leq 4.0$ .

values of  $h$  and  $f/f_0$ . As the cylinder submergence depth,  $h$ , decreases from 0.75 to 0.25, the mean lift coefficient,  $\widehat{C}_L$ , decreases (by a maximum factor of 6.85) for all frequency ratios,  $f/f_0 = 1.0, 2.0, 3.0, 4.0$ . Table 5.8 also suggests that the values of  $\widehat{C}_L$  decrease slightly as the transition of the flow from the quasi-periodic state to the non-periodic state occurs, except for the cases  $f/f_0 = 3.0, 4.0, h = 0.5$ . Furthermore, as  $f/f_0$  increases from 0.1 to 0.4,  $\widehat{C}_L$  seems to decrease (by a maximum factor of 2.14), except for the cases  $f/f_0 = 4.0, h = 0.25$ ;  $f/f_0 = 4.0$  and  $f/f_0 = 3.0$  (non-periodic state),  $h = 0.5$ ;  $f/f_0 = 3.0, h = 0.75$ . On the other hand, Table 5.9 suggests that the presence of the free surface has a slight effect on the values of the mean drag coefficient,  $\widehat{C}_D$ , for all the values of the cylinder submergence depth,  $h = 0.25, 0.5, 0.75$  and the frequency ratio,  $f/f_0 = 1.0, 2.0, 3.0, 4.0$ . More precisely, the values of  $\widehat{C}_D$  increase by a maximum factor of 1.28 when compared to those at  $h = \infty$ , except for the case  $f/f_0 = 2.0, h = 0.25$ . On the other hand, as  $h$  decreases from 0.75 to 0.25, the values of  $\widehat{C}_D$  decrease, in general. At the smallest cylinder submergence depth,  $h = 0.25$ , the values of  $\widehat{C}_D$  seem to increase slightly as the transition of the flow

from the quasi-periodic state to the non-periodic state occurs. In contrast, for larger cylinder submergence depths,  $h = 0.5, 0.75$ , the values of  $\widehat{C}_D$  are decreased slightly when the flow is in non-periodic state, except for the case  $f/f_0 = 4.0, h = 0.75$ . At the larger cylinder submergence depth,  $h = 0.75$ , increasing the frequency ratio,  $f/f_0$ , seems to increase  $\widehat{C}_D$  as  $f/f_0$  increases from 1.0 to 2.0 and to decrease  $\widehat{C}_D$  as  $f/f_0$  increases from 2.0 to 4.0, except  $f/f_0 = 4.0$  (non-periodic state). On the other hand, at  $h = 0.5$ ,  $\widehat{C}_D$  decreases as  $f/f_0$  increases from 1.0 to 3.0, except  $f/f_0 = 2.0$  (non-periodic state), and increases as  $f/f_0$  increases from 3.0 to 4.0. Finally, at the smallest submergence depth,  $h = 0.25$ ,  $\widehat{C}_D$  (i) increases as  $f/f_0$  increases from 1.0 to 2.0, (ii) decreases as  $f/f_0$  increases from 2.0 to 3.0 (except for the non-periodic state) and (iii) increases as  $f/f_0$  increases from 3.0 to 4.0 (except for the non-periodic state).

| $f/f_0 / h$ | 0.25            | 0.5             | 0.75            | $\infty$ |
|-------------|-----------------|-----------------|-----------------|----------|
| 1.0         | 0.8631          | 0.8012 → 0.6878 | 0.6688          | 0.5380   |
| 2.0         | 1.0579          | 0.9792 → 0.9305 | 1.0783 → 1.0855 | 0.9284   |
| 3.0         | 1.0513 → 1.2245 | 0.7555 → 0.6019 | 0.5593 → 0.6756 | 0.4668   |
| 4.0         | 0.9425 → 1.0694 | 0.7027 → 0.6170 | 0.6079 → 0.6882 | 0.5015   |

Table 5.10: The effect of the free surface inclusion at  $Fr = 0.4, h = 0.25, 0.5, 0.75$  and the frequency ratio,  $f/f_0$ , on the RMS lift coefficient,  $C_{L,rms}$ , at  $R = 200: A = 0.13, 1.0 \leq f/f_0 \leq 4.0$ .

Table 5.10 indicates that the presence of the free surface seems to increase the values of the RMS lift coefficient,  $C_{L,rms}$ , by a maximum factor of 2.6. Decreasing the

| $f/f_0 / h$ | 0.25            | 0.5             | 0.75            | $\infty$ |
|-------------|-----------------|-----------------|-----------------|----------|
| 1.0         | 1.5740          | 1.7379 → 1.6651 | 1.6106          | 1.3776   |
| 2.0         | 1.6612          | 1.8481 → 1.8723 | 2.0251 → 2.0413 | 1.9074   |
| 3.0         | 2.0951 → 2.2552 | 2.3674 → 2.3544 | 2.5240 → 2.4739 | 2.6421   |
| 4.0         | 3.2102 → 3.2827 | 3.6797 → 3.6867 | 3.8965 → 3.9289 | 4.2629   |

Table 5.11: The effect of the free surface inclusion at  $Fr = 0.4$ ,  $h = 0.25, 0.5, 0.75$  and the frequency ratio,  $f/f_0$ , on the RMS drag coefficient,  $C_{D,rms}$ , at  $R = 200$ :  $A = 0.13$ ,  $1.0 \leq f/f_0 \leq 4.0$ .

cylinder submergence depth,  $h$ , from 0.75 to 0.25 seems to increase  $C_{L,rms}$  for the cases  $f/f_0 = 1.0, 3.0, 4.0$ , except  $f/f_0 = 3.0, 4.0$  (non-periodic state) and  $h$  decreases from 0.75 to 0.5. On the other hand, for  $f/f_0 = 2.0$ , the values of  $C_{L,rms}$  decrease when  $h$  is reduced from 0.75 to 0.5 and increase when  $h$  is decreased from 0.5 to 0.25. It is noted that at  $h = 0.25, 0.75$ , the values of  $C_{L,rms}$  seem to increase slightly as the transition of the flow from the quasi-periodic state to the non-periodic state occurs. However, at  $h = 0.5$ , the values of  $C_{L,rms}$  decrease when the flow is in the non-periodic state. The increase in the frequency ratio,  $f/f_0$ , seems to increase  $C_{L,rms}$  when  $f/f_0$  increases from 1.0 to 2.0 and to decrease  $C_{L,rms}$  when  $f/f_0$  increases from 2.0 to 4.0, except for the cases  $f/f_0 = 3.0$  (non-periodic state),  $h = 0.25$ ;  $f/f_0 = 4.0$  (non-periodic state),  $h = 0.5$ ;  $f/f_0 = 4.0, h = 0.75, \infty$ . Furthermore, taking an overview of Table 5.11, it is evident that at  $h = 0.25, 0.5, 0.75$  and  $f/f_0 = 1.0$  the values of the RMS drag coefficient,  $C_{D,rms}$ , are increased when compared to those at  $h = \infty$ . However, for  $f/f_0 \geq 2.0$ ,  $C_{D,rms}$  seems to decrease when compared to that at  $h = \infty$ , except  $f/f_0 = 2.0, h = 0.75$ . Decreasing the cylinder submergence

| $f/f_0$ | $h = 0.25$        | $h = 0.5$         | $h = 0.75$        | $h = \infty$ |
|---------|-------------------|-------------------|-------------------|--------------|
| 1.0     | -0.6066           | -0.1130 → -0.4302 | -0.7746           | -0.2759      |
| 2.0     | -0.5033           | -0.3264 → -0.3732 | -0.3602 → -0.3418 | -0.3718      |
| 3.0     | -0.7763 → -0.7458 | -0.5876 → -0.6314 | -0.5607 → -0.5291 | -0.6167      |
| 4.0     | -0.9557 → -0.8964 | -0.8168 → -0.8578 | -0.8590 → -0.8196 | -0.1008      |

Table 5.12: The effect of the free surface inclusion at  $Fr = 0.4$ ,  $h = 0.25, 0.5, 0.75$  and the frequency ratio,  $f/f_0$ , on the total mechanical energy transfer,  $E$ , at  $R = 200$ :  $A = 0.13$ ,  $1.0 \leq f/f_0 \leq 4.0$ .

depth,  $h$ , from 0.75 to 0.25 leads to the decrease in  $C_{D,rms}$  for  $f/f_0 \geq 2.0$ . On the other hand, for  $f/f_0 = 1.0$ , the values of  $C_{D,rms}$  are increased as  $h$  decreases from 0.75 to 0.5 and decreased as  $h$  reduces from 0.5 to 0.25. Table 5.11 also suggests that the values of  $C_{D,rms}$  decrease slightly as the transition of the flow from the quasi-periodic state to the non-periodic state occurs, except for the cases  $f/f_0 = 3.0, 4.0$ ,  $h = 0.25$ ;  $f/f_0 = 2.0, 4.0$ ,  $h = 0.5, 0.75$ . Finally, it is evident that increasing the frequency ratio,  $f/f_0$ , seems to increase the RMS drag coefficient,  $C_{D,rms}$  for each cylinder submergence depth,  $h$ , shown in Table 5.11.

Table 5.12 shows the effect of the cylinder submergence depth,  $h$  ( $= 0.25, 0.5, 0.75$ ), and the frequency ratio,  $f/f_0$  ( $= 1.0, 2.0, 3.0, 4.0$ ), on the total mechanical energy transfer,  $E$ , for the case  $R = 200$ ,  $A = 0.13$  when  $Fr = 0.4$ . The reference case  $h = \infty$  is also shown in Table 5.12. Taking an overview of Table 5.12, it can be seen that the total energy transfer,  $E$ , is negative irrespective of the values of  $h$  and  $f/f_0$  and thereby, the work is always done on the fluid by the cylinder. It is interesting to note

that for the case  $f/f_0 = 1.0$ ,  $h = 0.5$  the absolute value of the total energy transfer,  $E$ , is increased by approximately a factor of 4.0 as the flow transition to the non-periodic state occurs. Thus, when  $f/f_0 = 1.0$ ,  $h = 0.5$  the fluid resistance against the forced motion of the cylinder increases by a factor of 4.0 when the transition of the flow to the non-periodic state occurs. Furthermore, for each of the frequency ratio,  $f/f_0$ , shown in Table 5.12, at the smallest cylinder submergence depth,  $h = 0.25$ , the energy transfer increases (the absolute values of  $E$  are increased) when compared to that at  $h = \infty, 0.75, 0.5$ , except  $f/f_0 = 1.0$ ,  $h = 0.75$ . On the other hand, as  $h$  is reduced from 0.75 to 0.5, the energy transfer,  $E$ , decreases, in general, indicating the loss in the fluid resistance against the forced motion of the cylinder, except when the flow is in the non-periodic state ( $f/f_0 \geq 2.0$ ) and when  $f/f_0 = 3.0$  (quasi-periodic state). Increasing the frequency ratio,  $f/f_0$ , seems to increase the absolute values of the energy transfer,  $E$ , except for the cases  $f/f_0 = 2.0$ ,  $h = 0.25, 0.75$ ;  $f/f_0 = 2.0$  (non-periodic state),  $h = 0.5$ . Thus, the effect of the varying frequency ratio,  $f/f_0$ , seems to increase, in general, the fluid resistance against the forced motion of the cylinder. It is interesting to note that at  $h = 0.25, 0.75$ , there is a slight energy loss as the flow transition to the non-periodic state occurs. On the other hand, at  $h = 0.5$ , the energy slightly increases in the non-periodic state when compared to that in quasi-periodic state for the case when  $f/f_0 \geq 2.0$ .

## 6. Summary, conclusions and recommendations for future work

In this thesis, an accurate computational method is presented for the solution of the problem of uniform viscous incompressible flow past an oscillating horizontal rigid circular cylinder of infinite length located beneath a free surface. The method of solution is based on a finite volume discretization of the special integral form of the two-dimensional unsteady continuity and Navier-Stokes equations (integral form of the FAVOR equations) in their pressure-velocity formulation on a fixed Cartesian grid. A special integral form of the governing equations is derived by extending the Reynolds transport theorem and then applying it to control volumes containing a fluid-body interface. This is done by utilizing, mainly, generalized differentiation. The governing equations are discretized using a finite volume approximation on a staggered grid. The no-slip conditions are implemented on the surface of the cylinder. Well-posed boundary conditions are enforced at the inflow and outflow boundaries since they ensure correct physical development of the flow near the computational domain boundaries. The free slip boundaries are assumed at the top and the bottom of the computational domain. The free surface boundary conditions are applied implicitly by using the two-phase flow technique which treats the fluids in different phases as one fluid with variable material properties. The free surface is discretized with the VOF method in which the volume fraction is used to distinguish between two different fluid phases in the computational domain. The positions of both the free surface and fluid-body interfaces are determined at each time step by using the PLIC algorithm.

---

The advection of the reconstructed free surface with local velocity field is performed by the geometrical area preserving VOF advection algorithm. The combination of the FAVOR and cut cell methods is used to model the motion of the fluid-body interface. Discrete pressure and velocity fields corresponding to the successive time instants are calculated by iterative solution of a preconditioned coupled sparse linear system using the generalized minimal residual method as implemented in Trilinos numerical solver library. The computational model is implemented into the computer program, written in the C++ programming language.

The numerical scheme is verified by applying to the special cases of uniform flow past (i) a stationary cylinder; (ii) a cylinder undergoing forced recti-linear oscillations (oscillations at an angle  $\eta = 60^\circ$  with respect to the free stream, transverse, in-line oscillations); (iii) a cylinder undergoing forced combined transverse and rotational, and combined in-line and rotational oscillations; (iv) a steadily rotating cylinder in the absence of the free surface. The validation of the present numerical model is also presented for uniform flow past (i) a stationary cylinder and (ii) a cylinder undergoing forced translational oscillations in the in-line direction in the presence of the free surface. The comparisons have shown to be in good agreement with previous analytical, experimental and numerical findings for stationary and oscillating circular cylinders in both the absence and presence of the free surface.

The method is applied to study the problem of unsteady, laminar, two-dimensional flow of a viscous incompressible fluid past a cylinder subject to in-line oscillations in uniform flow in the presence of the free surface. The fluid flow is calculated at the Reynolds number of  $R = 200$  and the forcing amplitude  $A = 0.13$  for the range of

frequency ratios  $f/f_0 = 1.0, 2.0, 3.0, 4.0$ . The flow characteristics for Froude numbers  $Fr \approx 0.0$  and  $Fr = 0.2, 0.4$  and for cylinder submergence depths  $h = 0.25, 0.5, 0.75$  are examined. The numerical simulations are also conducted for the case when the free surface is absent ( $h = \infty$ ) under the same oscillation conditions to better understand what differences result from the inclusion of the free surface. The main objectives of this study are (i) to address the alterations of the near wake region, in particular, the flow regimes and the locked-on vortex formation modes, due to the presence of the free surface and (ii) to determine the consequence of the cylinder submergence depth on the fluid forces acting on the cylinder surface. The results are analyzed by means of equivorticity patterns, streamlines and pressure contours in the near wake region as well as the fluid forces. The PSD analysis of the lift coefficient, the near wake vorticity contours and the Lissajous patterns of the lift coefficient are used to define the lock-on modes. The vortex shedding modes are classified following the terminology of Williamson and Roshko (1988). The Lissajous representations of the lift and drag coefficients are also used to demonstrate the mechanism of mechanical energy transfer between the fluid and the cylinder, degree of phase-locking or a loss of lock-on and associated phase shift. The effect of the free surface on the mechanical energy transfer is also explained by using the energy transfer equation (5.1). For selected cases, POD analysis of the vorticity field is used to interpret unsteady near wake structures in terms of POD eigen-modes.

In the view of the analysis and the results provided in Chapter 5, the effect of the Froude number,  $Fr$ , and the cylinder submergence depth,  $h$ , on the flow regimes, the vortex shedding modes and their periods,  $T_0$ , the fluctuating fluid forces as well as the total mechanical energy transfer will now be presented.

## 6.1 Effect of the Froude number, $Fr$ , and the cylinder submergence depth, $h$ , on flow regimes, vortex shedding modes and fluid forces

It has been observed in Chapter 5 that the presence of the free surface at  $h = 0.25, 0.5, 0.75$  alters the flow behaviour in the near wake. Moreover, depending on the Froude number,  $Fr$ , and the cylinder submergence depth,  $h$ , the free surface leads to the breaking up of the near wake vorticity and thereby, the different flow regimes and modes of vortex shedding can be attained.

|          | $Fr \approx 0.0$ |       | $Fr = 0.2$ |       | $Fr = 0.4$   |       |
|----------|------------------|-------|------------|-------|--|-------|
| $h$      | Mode             | $T_0$ | Mode       | $T_0$ | Mode   | $T_0$ |
| 0.25     | non-locked       | -     | non-locked | -     | non-locked   | -     |
| 0.5      | <b>2S</b>        | $T$   | <b>2S*</b> | $T$   | <b>C(2S)*</b> (within $5T$ );<br>non-locked ( $5T < t < 20T$ ) | $T$   |
| 0.75     | <b>2S</b>        | $T$   | <b>2S*</b> | $T$   | non-locked   | -     |
| $\infty$ | non-locked       | -     | non-locked | -     | non-locked   | -     |

Table 6.1: The effect of the Froude number,  $Fr$ , and the cylinder submergence depth,  $h$ , on flow regimes, vortex shedding modes and their periods,  $T_0$ , at  $R = 200$ :  $A = 0.13$ ,  $f/f_0 = 1.0$ . The superscript “\*” denotes quasi-locked-on modes.

Tables 6.1-6.4 show the effect of the Froude number,  $Fr$  ( $\approx 0.0, 0.2, 0.4$ ) and the cylinder submergence depth,  $h$  ( $= 0.25, 0.5, 0.75$ ), on the flow regimes, the vortex shedding modes and their periods,  $T_0$ , for the case  $R = 200$ ,  $A = 0.13$  when  $f/f_0 = 1.0, 2.0$ ,

3.0, 4.0, respectively. These tables also display the results obtained for the reference case  $h = \infty$ . Table 6.1 indicates that when  $f/f_0 = 1.0$  for smaller Froude numbers,  $Fr \approx 0.0$  and  $Fr = 0.2$ , the effect of the presence of the free surface at  $h = 0.5$ , 0.75 is to stabilize the vortex shedding to produce asymmetric locked-on and quasi-locked-on **2S** mode, per  $T$ , respectively. For the highest Froude number,  $Fr = 0.4$

|          | $Fr \approx 0.0$ |       | $Fr = 0.2$    |       | $Fr = 0.4$   |       |
|----------|------------------|-------|---------------|-------|--|-------|
| $h$      | Mode             | $T_0$ | Mode          | $T_0$ | Mode   | $T_0$ |
| 0.25     | non-locked       | -     | non-locked    | -     | non-locked   | -     |
| 0.5      | <b>C(2S)</b>     | $2T$  | <b>2S*</b>    | $2T$  | <b>C(2S)*</b> (within $14T$ );<br>non-locked ( $14T < t < 40T$ ) | $2T$  |
| 0.75     | <b>P+S</b>       | $2T$  | <b>(P+S)*</b> | $2T$  | <b>(P+S)*</b> (within $14T$ );<br>non-locked ( $14T < t < 40T$ ) | $2T$  |
| $\infty$ | <b>2S</b>        | $2T$  | <b>2S</b>     | $2T$  | <b>2S</b>  | $2T$  |

Table 6.2: The effect of the Froude number,  $Fr$ , and the cylinder submergence depth,  $h$ , on flow regimes, vortex shedding modes and their periods,  $T_0$ , at  $R = 200$ :  $A = 0.13$ ,  $f/f_0 = 2.0$ . The superscript “\*” denotes quasi-locked-on modes.

( $f/f_0 = 1.0$ ), two different flow regimes are observed when  $h = 0.5$ : the flow is quasi-periodic (**C(2S)** mode, per  $T$ ), within  $5T$  and then, the flow transition to the non-periodic state occurs ( $5T < t < 20T$ ).

For  $f/f_0 = 2.0$ , as  $h$  decreases from  $\infty$  to 0.75, the vortex shedding mode changes from **2S** mode, per  $2T$ , to **P+S** mode, per  $2T$ , when  $Fr \approx 0.0$  and  $Fr = 0.2$  as shown in Table 6.2. On the other hand, at these Froude numbers,  $Fr \approx 0.0$  and  $Fr = 0.2$ , **2S** mode, per  $2T$ , again persists as  $h$  is decreased from 0.75 to 0.5. Table 6.2 also indicates that increasing the Froude number to 0.4 results in two flow regimes for the

| $h$      | $Fr \approx 0.0$  |       | $Fr = 0.2$ |       | $Fr = 0.4$  |       |
|----------|---|-------|------------|-------|---|-------|
|          | Mode  | $T_0$ | Mode       | $T_0$ | Mode  | $T_0$ |
| 0.25     | non-locked  | -     | non-locked | -     | <b>C(2S)*</b> (within $20T$ );<br>non-locked ( $20T < t < 60T$ )      | $4T$  |
| 0.5      | <b>C(2S)*</b> (within $12T$ );<br>non-locked ( $12T < t < 60T$ )  | $3T$  | non-locked | -     | <b>[C(P+S)+S]*</b> (within $18T$ );<br>non-locked ( $18T < t < 60T$ ) | $3T$  |
| 0.75     | <b>C(P+S)*</b> (within $24T$ );<br>non-locked ( $24T < t < 60T$ ) | $3T$  | non-locked | -     | <b>[C(2S)+S]*</b> (within $18T$ );<br>non-locked ( $18T < t < 60T$ )  | $3T$  |
| $\infty$ | non-locked  | -     | non-locked | -     | non-locked  | -     |

Table 6.3: The effect of the Froude number,  $Fr$ , and the cylinder submergence depth,  $h$ , on flow regimes, vortex shedding modes and their periods,  $T_0$ , at  $R = 200$ :  $A = 0.13$ ,  $f/f_0 = 3.0$ . The superscript "\*" denotes quasi-locked-on modes.

smaller values of cylinder submergence depths,  $h = 0.5, 0.75$ .

Table 6.3 suggests that for the larger frequency ratio,  $f/f_0 = 3.0$ , and  $Fr \approx 0.0$  and  $Fr = 0.4$  decreasing  $h$  from  $\infty$  to  $0.25$  seems to stabilize the flow behaviour for a short period of time such that the near wake vorticity produces quasi-locked-on modes of vortex shedding and then, the transition of the near wake to the non-periodic state is observed, except  $h = 0.25$ ,  $Fr \approx 0.0$ . An interesting aspect to address here is that as  $Fr$  is increased to  $0.4$ , different modes of vortex shedding, **C(P+S)+S** and **C(2S)+S**, persist in which an additional single positive vortex (from the free surface) is shed over  $3T$ . Another interesting point to note is that at this frequency ratio,  $f/f_0 = 3.0$ , the effect of the smallest cylinder submergence depth,  $h = 0.25$ , and the highest Froude number,  $Fr = 0.4$ , is to produce two flow regimes: the vortex shedding exhibits quasi-locked-on **C(2S)** mode, per  $4T$ , within  $20T$  and then, the flow behaviour tends to be non-periodic ( $20T < t < 60T$ ). This phenomenon is not observed for the smaller frequency ratios,  $f/f_0 \leq 2.0$ . Table 6.3 also suggests for the

| $h$      | $Fr \approx 0.0$  |       | $Fr = 0.2$ |       | $Fr = 0.4$  |       |
|----------|---|-------|------------|-------|---|-------|
|          | Mode  | $T_0$ | Mode       | $T_0$ | Mode  | $T_0$ |
| 0.25     | <b>C(2S)*</b>   | $5T$  | non-locked | -     | <b>C(2S)*</b> (within $20T$ );<br>non-locked ( $20T < t < 80T$ )      | $5T$  |
| 0.5      | <b>2P*</b> (within $20T$ );<br>non-locked ( $20T < t < 80T$ ) | $4T$  | non-locked | -     | <b>[C(P+S)+S]*</b> (within $28T$ );<br>non-locked ( $28T < t < 80T$ ) | $4T$  |
| 0.75     | <b>C(P+S)</b>   | $4T$  | non-locked | -     | <b>[C(2S)+S]*</b> (within $12T$ );<br>non-locked ( $12T < t < 80T$ )  | $4T$  |
| $\infty$ | non-locked  | -     | non-locked | -     | non-locked  | -     |

Table 6.4: The effect of the Froude number,  $Fr$ , and the cylinder submergence depth,  $h$ , on flow regimes, vortex shedding modes and their periods,  $T_0$ , at  $R = 200$ :  $A = 0.13$ ,  $f/f_0 = 4.0$ . The superscript “\*” denotes quasi-locked-on modes.

case  $Fr = 0.2$ , the flow is non-periodic irrespective of the presence of the free surface.

For the higher frequency ratio,  $f/f_0 = 4.0$ , the flow behaviour is very similar to the aforementioned case  $f/f_0 = 3.0$ . Table 6.4 indicates that for the case  $Fr = 0.2$ , the flow is non-periodic irrespective of the presence of the free surface. On the other hand, the presence of the free surface seems to produce two flow regimes, except for the cases  $h = 0.25, 0.75, Fr \approx 0.0$ . Furthermore, a period increase is observed for Froude numbers  $Fr \approx 0.0$  and  $Fr = 0.4$  as  $h$  is decreased from 0.5 to 0.25. It is also noted that the increase in the Froude number,  $Fr$ , seems to begin the vortex shedding from the free surface. In fact, when  $h = 0.5, 0.75, Fr = 0.4$  one more vortex (the positive vortex from the free surface) sheds into the downstream of the cylinder unlike the other cases shown in Table 6.4. Taking an overview of Table 6.4, the coalescence of vortices seems to be more pronounced as  $Fr$  increases.

Figures 6.1-6.4 summarize the effect of the Froude number,  $Fr$  ( $\approx 0.0$  and  $0.2, 0.4$ ), and the cylinder submergence depth,  $h$  ( $= 0.25, 0.5, 0.75$ ), on the equivorticity pat-

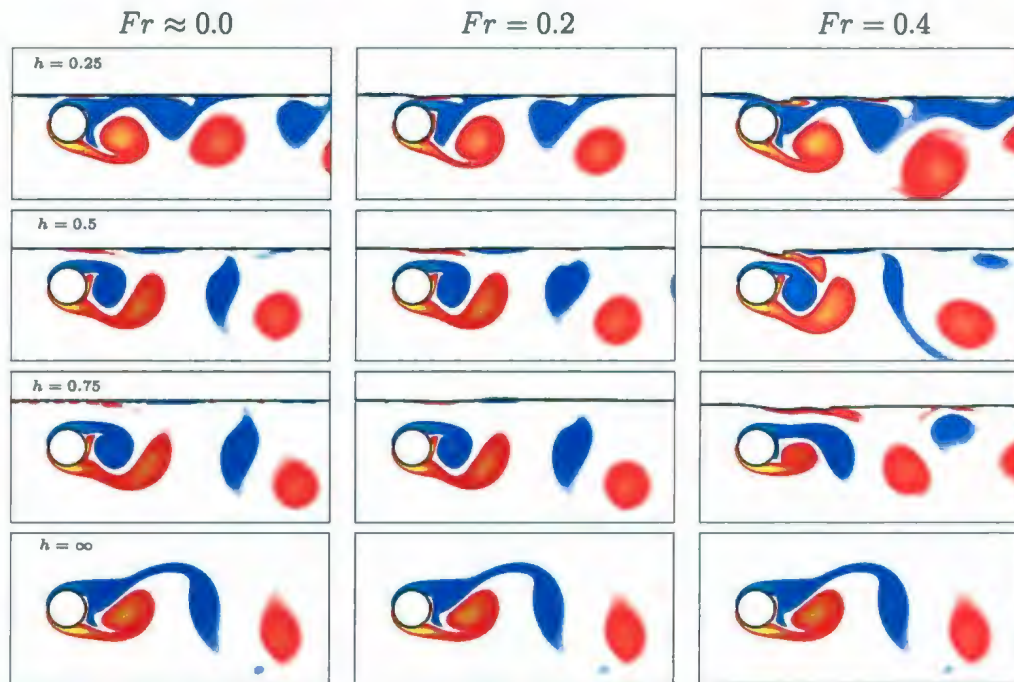


Figure 6.1: The effect of the Froude number,  $Fr$ , and the cylinder submergence depth,  $h$ , on the equivorticity patterns at  $R = 200$ :  $A = 0.13$ ,  $f/f_0 = 1.0$ . All snapshots are taken at the instant  $x(t) = A$ .

terns for the case  $R = 200$ ,  $A = 0.13$  when  $f/f_0 = 1.0, 2.0, 3.0, 4.0$ . The reference case  $h = \infty$  is also shown in these figures. The snapshots are taken at the instant  $x(t) = A$ . For the periodic/quasi-periodic cases the snapshots are taken over the time interval in which the flow reaches to a periodic/quasi-periodic state. For non-periodic cases, the commonly appearing equivorticity plots at  $x(t) = A$  (within the time interval  $0 < t \leq 100$ ) are shown in Figures 6.1-6.4. Figure 6.1 corresponds to the case when  $f/f_0 = 1.0$  and shows the changes in the near wake behaviour and the free surface evolution as  $Fr$  increases from 0.0 to 0.4 and  $h$  decreases from  $\infty$  to 0.25. It is seen that at larger cylinder submergence depths,  $h = 0.5, 0.75$ , and smaller Froude

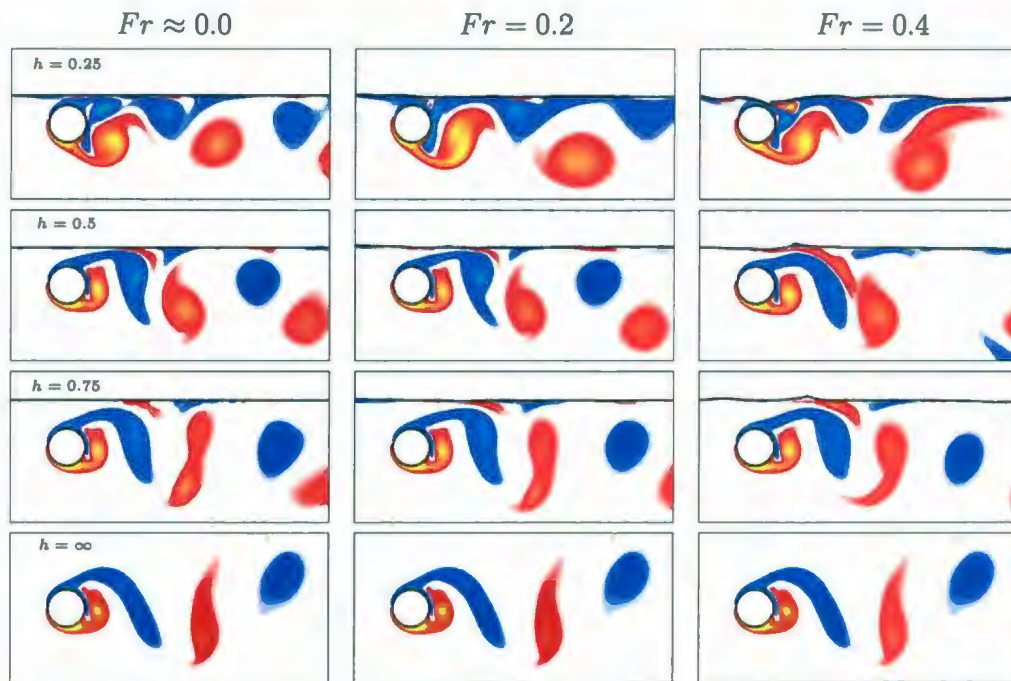


Figure 6.2: The effect of the Froude number,  $Fr$ , and the cylinder submergence depth,  $h$ , on the equivorticity patterns at  $R = 200$ :  $A = 0.13$ ,  $f/f_0 = 2.0$ . All snapshots are taken at the instant  $x(t) = A$ .

numbers,  $Fr \approx 0.0$  and  $Fr = 0.2$ , the near wake behaviour is not too dissimilar to that from the reference case  $h = \infty$ . However, unlike the case when the free surface is absent, there is some diffusion of the opposite signed vorticity across the interface and the near wake seems to be skew symmetric. On the other hand, when the cylinder is submerged very close to the free surface,  $h = 0.25$ , the near wake is changed significantly. At this cylinder submergence depth,  $h = 0.25$ , the rapid diffusion of the negative vorticity across the interface is observed and thereby, the near wake is dominated by positive vortex structures. It is also noted that for Froude numbers,  $Fr \approx 0.0$  and  $Fr = 0.2$ , only slight surface curvature is noted in Figure 6.1. For the

larger Froude number of 0.4, there is a marked difference in the near wake. Here, the free surface curvature appears to be considerably pronounced and the induced surface curvature leads to a viscous transport of the opposite signed vorticity in both the free surface and the fluid flow, with the localized wave breaking noted for smaller cylinder submergence depths,  $h = 0.25, 0.5$ . This secondary vorticity is then convected by the free surface waves into the downstream of the cylinder. Taking an overview of Figure 6.1, it is seen that at  $h = 0.75$  there is a decrease in the vortex formation length (maximum by 110%) as the Froude number,  $Fr$ , increases from 0.0 to 0.4. On the other hand, at  $h = 0.25, 0.5$ , the vortex formation length remains almost the same as  $Fr$  increases.

The case when  $f/f_0 = 2.0$  is displayed in Figure 6.2. This figure clearly shows the rise in the level of surface deformations when the Froude number,  $Fr$ , increases. It is seen that as  $h$  decreases from 0.75 to 0.5, the near wake shows a similar behaviour when compared to that at  $h = \infty$  for each of the Froude numbers,  $Fr$ , displayed in Figure 6.2. On the other hand, it is evident that the larger amount of the positive vorticity develops near the curved free surface as  $Fr$  increases. At the highest Froude number,  $Fr = 0.4$ , this secondary vorticity tends to coalesce with the near wake vorticity, causing the wake to become much more asymmetric downstream. A remarkable difference in the near wake behaviour is noted when the cylinder becomes close to the free surface interface ( $h = 0.25$ ). At this cylinder submergence depth,  $h = 0.25$ , the near wake is very dissimilar to that observed at larger cylinder submergence depths,  $h = 0.5, 0.75$ . Again it is seen that the negative vorticity annihilates due to a strong interaction with the free surface and the near wake becomes dominated by the positive vorticity. It is also seen that as  $h$  decreases from 0.75 to 0.5, the vortex formation

6.1. Effect of the Froude number,  $Fr$ , and the cylinder submergence depth,  $h$ , on flow regimes, vortex shedding modes and fluid forces 252

length remains almost the same for all Froude numbers,  $Fr \approx 0.0$  and  $Fr = 0.2, 0.4$ . However, there is a significant increase in the vortex formation length (maximum by 166.7%) as  $h$  decreases from 0.5 to 0.25 for each Froude number,  $Fr$ , shown in Figure 6.2. On the other hand, at  $h = 0.25$ , the vortex formation length remains almost the same irrespective of the Froude number,  $Fr$ .

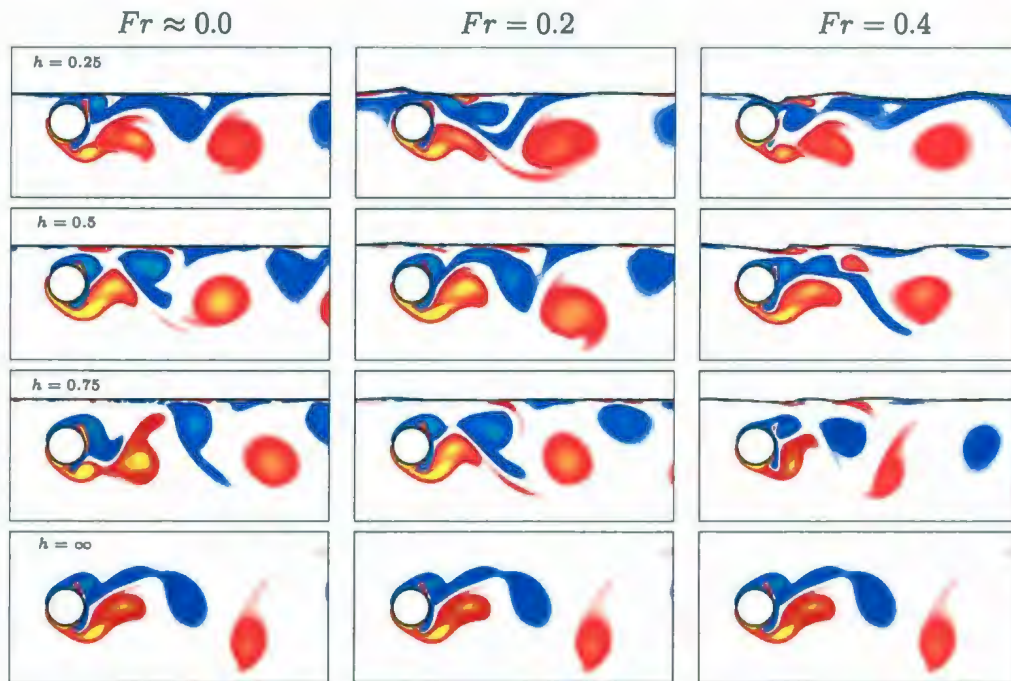


Figure 6.3: The effect of the Froude number,  $Fr$ , and the cylinder submergence depth,  $h$ , on the equivorticity patterns at  $R = 200$ :  $A = 0.13$ ,  $f/f_0 = 3.0$ . All snapshots are taken at the instant  $x(t) = A$ .

The plots in Figure 6.3 correspond to the case  $f/f_0 = 3.0$ . At this frequency ratio,  $f/f_0 = 3.0$ , the near wake is considerably different from the previous cases, showing a complex flow behaviour. Here, surface distortion becomes substantial and, when

$Fr = 0.4$ , the upper vortex shedding layer seems to dissipate largely downstream of the cylinder. As the cylinder submergence depth,  $h$ , is reduced from  $\infty$  to 0.25, the shape and the strength of the vortices become altered such that the positive vortices traveling downstream of the cylinder become more oval shaped with their major axis lying almost parallel to the free surface. On the other hand, the negative vortices seem to be reoriented and elongated such that their major axis is lying under a sufficiently large angle with respect to the free surface. As the Froude number,  $Fr$ , increases, the vortex formation length seems to decrease ( $\approx 90\%$ ) when  $h = 0.75$  and increase ( $\approx 14.3\%$ ) when  $h = 0.5$ . The small scale wave breaking is noted at the highest Froude number,  $Fr = 0.4$ , as the cylinder approaches the free surface ( $h = 0.25, 0.5$ ).

Figure 6.4 indicates significant deformations of the free surface when  $f/f_0 = 4.0$ . For this frequency ratio,  $f/f_0 = 4.0$ , the localized wave breaking occurs even for smaller Froude number,  $Fr = 0.2$ , unlike the previous cases. This situation is best illustrated by the equivorticity plot taken for  $Fr = 0.2$ ,  $h = 0.25$ . It is also seen that for each Froude number,  $Fr$ , the vortex formation length seems to increase (maximum by  $\approx 146.15\%$ ), in general, as the cylinder submergence depth,  $h$ , decreases from 0.75 to 0.25. Moreover, the larger amount of the positive vorticity develops near the curved free surface as  $Fr$  increases and  $h$  decreases. At the highest Froude number,  $Fr = 0.4$ , this secondary vorticity tends to coalesce with the near wake vorticity and thereby, causes the asymmetry of the near wake downstream. At the smallest cylinder submergence depth,  $h = 0.25$ , there is a marked difference in the downstream wake, comparing to the cases of larger cylinder submergence depths,  $h = 0.5, 0.75$ . Again it is seen that the negative vorticity annihilates due to a strong interaction with the free surface and the near wake becomes dominated by the positive vorticity. Moreover,

similar to the aforementioned case when  $f/f_0 = 3.0$ , at  $h = 0.25$ , the upper vortex shedding layer tends to dissipate largely downstream of the cylinder as  $Fr$  increases.

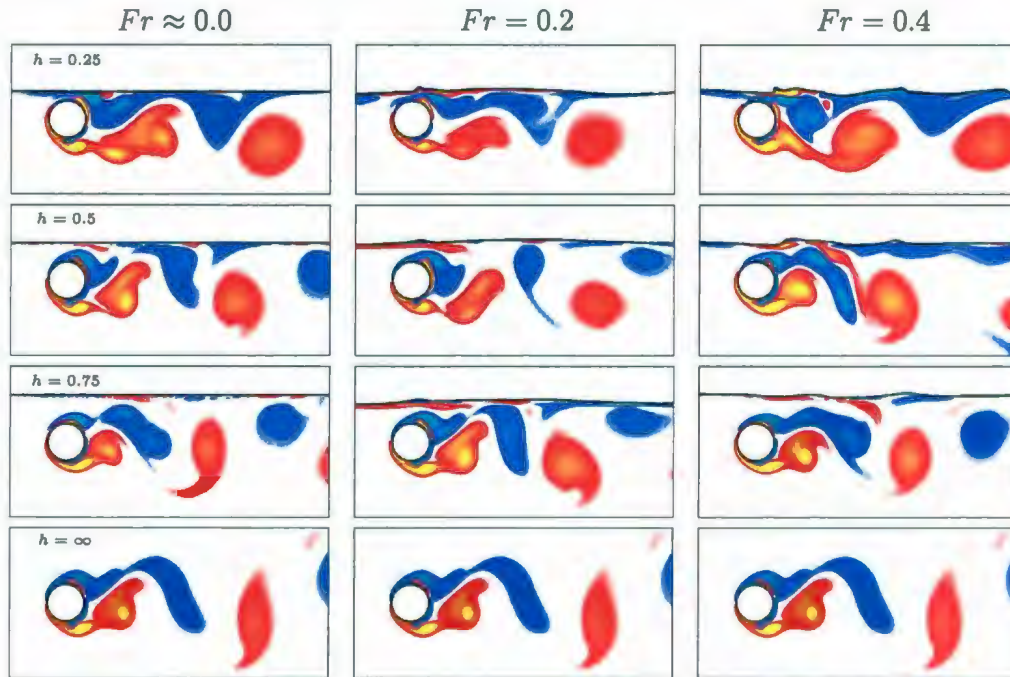


Figure 6.4: The effect of the Froude number,  $Fr$ , and the cylinder submergence depth,  $h$ , on the equivorticity patterns at  $R = 200$ :  $A = 0.13$ ,  $f/f_0 = 4.0$ . All snapshots are taken at the instant  $x(t) = A$ .

Tables 6.5 and 6.6 summarize the effect of the Froude number,  $Fr$  ( $= 0.2, 0.4$ ), and the cylinder submergence depth,  $h$  ( $= 0.25, 0.5, 0.75$ ), on the mean lift and drag coefficients,  $\widehat{C}_L$  and  $\widehat{C}_D$ , for the case  $R = 200$ ,  $A = 0.13$  when  $1.0 \leq f/f_0 \leq 4.0$ . The results for the reference case  $h = \infty$  are also displayed in these tables. It can be seen that in all cases shown in Table 6.5 the presence of the free surface has a significant effect on the mean lift coefficient,  $\widehat{C}_L$ . At the smallest cylinder

|             |          | $Fr = 0.2$ |        |       | $Fr = 0.4$      |                 |                 |
|-------------|----------|------------|--------|-------|-----------------|-----------------|-----------------|
| $f/f_0 / h$ | $\infty$ | 0.25       | 0.5    | 0.75  | 0.25            | 0.5             | 0.75            |
| 1.0         | -0.003   | -0.350     | 0.161  | 0.167 | -0.786          | -0.203 → -0.332 | -0.115          |
| 2.0         | -0.001   | -0.590     | -0.028 | 0.186 | -0.808          | -0.409 → -0.477 | -0.228 → -0.297 |
| 3.0         | -0.001   | -0.709     | 0.004  | 0.152 | -0.888 → -0.973 | -0.454 → -0.418 | -0.180 → -0.249 |
| 4.0         | -0.003   | -0.536     | 0.030  | 0.141 | -0.853 → -0.861 | -0.401 → -0.381 | -0.193 → -0.246 |

Table 6.5: The effect of the Froude number,  $Fr$ , and the cylinder submergence depth,  $h$ , on the mean lift coefficient,  $\widehat{C}_L$ , at  $R = 200$ :  $A = 0.13$ ,  $1.0 \leq f/f_0 \leq 4.0$ .

submergence depth,  $h = 0.25$ , the values of  $\widehat{C}_L$  decrease (by a maximum factor of 2.0) as the Froude number,  $Fr$ , increases. It is also seen that at  $h = 0.25$ ,  $\widehat{C}_L$  is negative irrespective of the values of  $Fr$ . For the larger cylinder submergence depth,  $h = 0.5$ , the increase in  $Fr$  seems to change the sign of  $\widehat{C}_L$  from positive to negative, except for the case  $f/f_0 = 2.0$ . Moreover, at  $h = 0.5$ ,  $Fr = 0.4$  the absolute values of  $\widehat{C}_L$  are increased significantly when compared to those obtained at the smaller Froude number,  $Fr = 0.2$ . It should be noted that the increasing of the Froude number,  $Fr$ , dramatically affects  $\widehat{C}_L$  for the case  $f/f_0 = 3.0$ ,  $h = 0.5$  by shifting its value from 0.004 to  $-0.454$  in the quasi-periodic state and to  $-0.418$  in the non-periodic state. Further, at the largest cylinder submergence depth,  $h = 0.75$ , the values of  $\widehat{C}_L$  seem to change the sign from positive to negative as the Froude number,  $Fr$ , increases from 0.2 to 0.4. Comparing the results for  $h = 0.75$ ,  $Fr = 0.2$  and  $h = 0.75$ ,  $Fr = 0.4$  it is seen that the absolute values of  $\widehat{C}_L$  increase slightly as  $Fr$  increases, except for the smallest frequency ratio,  $f/f_0 = 1.0$ . Table 6.5 also shows that decreasing the cylinder submergence depth,  $h$ , from 0.75 to 0.25 leads to the decrease in  $\widehat{C}_L$  for each of Froude numbers,  $Fr = 0.2, 0.4$ . Taking an overview of Table 6.6, it is evident

|             |          | $Fr = 0.2$ |       |       | $Fr = 0.4$    |               |               |
|-------------|----------|------------|-------|-------|---------------|---------------|---------------|
| $f/f_0 / h$ | $\infty$ | 0.25       | 0.5   | 0.75  | 0.25          | 0.5           | 0.75          |
| 1.0         | 1.344    | 1.495      | 1.684 | 1.514 | 1.451         | 1.718 → 1.571 | 1.565         |
| 2.0         | 1.646    | 1.551      | 1.853 | 1.823 | 1.480         | 1.671 → 1.658 | 1.851 → 1.839 |
| 3.0         | 1.392    | 1.885      | 1.730 | 1.623 | 1.428 → 1.590 | 1.553 → 1.478 | 1.630 → 1.529 |
| 4.0         | 1.406    | 1.612      | 1.582 | 1.570 | 1.447 → 1.539 | 1.610 → 1.573 | 1.573 → 1.712 |

Table 6.6: The effect of the Froude number,  $Fr$ , and the cylinder submergence depth,  $h$ , on the mean drag coefficient,  $\widehat{C}_D$ , at  $R = 200$ :  $A = 0.13$ ,  $1.0 \leq f/f_0 \leq 4.0$ .

that the presence of the free surface has a slight effect on the mean drag coefficient,  $\widehat{C}_D$ , when compared to the reference case  $h = \infty$ . Increasing the Froude number,  $Fr$ , seems to decrease slightly the values of  $\widehat{C}_D$  (by a maximum factor of 1.31) when  $h = 0.25$ . On the other hand, for the larger cylinder submergence depth,  $h = 0.5$ , the increase in the Froude number,  $Fr$ , seems to (i) decrease the values of  $\widehat{C}_D$  for  $f/f_0 = 2.0, 3.0$ ; (ii) increase the values of  $\widehat{C}_D$  for  $f/f_0 = 1.0, 4.0$  when the flow is in the quasi-periodic state and (iii) decrease the values of  $\widehat{C}_D$  for  $f/f_0 = 1.0, 4.0$  when the transition of the flow into the non-periodic state occurs. For the largest depth of the cylinder submergence,  $h = 0.75$ , the values of  $\widehat{C}_D$  seem to be increased, except for the case  $f/f_0 = 3.0$  (non-periodic state), as  $Fr$  increases. As  $h$  decreases, for the smallest frequency ratio,  $f/f_0 = 1.0$ ,  $\widehat{C}_D$  increases as  $h$  decreases from 0.75 to 0.5 and decreases as  $h$  is reduced from 0.5 to 0.25 for each of Froude numbers,  $Fr = 0.2, 0.4$ . For  $f/f_0 = 2.0$  and  $Fr = 0.2, 0.4$ , the effect of the decrease in  $h$  (from 0.75 to 0.25) is to decrease the values of  $\widehat{C}_D$ , except for the case  $Fr = 0.2$  as  $h$  reduces from 0.75 to 0.5. Furthermore, for  $f/f_0 = 3.0, 4.0$ , the mean drag coefficient,  $\widehat{C}_D$ , increases when  $Fr = 0.2$  and decreases, in general, when  $Fr = 0.4$ .

Tables 6.7 and 6.8 show the effect of the Froude number,  $Fr$  ( $= 0.2, 0.4$ ), and the cylinder submergence depth,  $h$  ( $= 0.25, 0.5, 0.75$ ), on the RMS lift and drag coefficients,  $C_{L,rms}$  and  $C_{D,rms}$ , for the case  $R = 200$ ,  $A = 0.13$  when  $1.0 \leq f/f_0 \leq 4.0$ . The results for the reference case  $h = \infty$  are also displayed in these tables. It is clear that

|             |          | $Fr = 0.2$ |       |       | $Fr = 0.4$    |               |               |
|-------------|----------|------------|-------|-------|---------------|---------------|---------------|
| $f/f_0 / h$ | $\infty$ | 0.25       | 0.5   | 0.75  | 0.25          | 0.5           | 0.75          |
| 1.0         | 0.538    | 0.665      | 0.937 | 0.801 | 0.863         | 0.801 → 0.688 | 0.669         |
| 2.0         | 0.928    | 0.792      | 1.212 | 1.202 | 1.058         | 0.979 → 0.931 | 1.078 → 1.086 |
| 3.0         | 0.467    | 1.872      | 1.129 | 0.826 | 1.051 → 1.225 | 0.756 → 0.602 | 0.559 → 0.676 |
| 4.0         | 0.502    | 1.914      | 1.269 | 0.967 | 0.943 → 1.069 | 0.703 → 0.617 | 0.608 → 0.688 |

Table 6.7: The effect of the Froude number,  $Fr$ , and the cylinder submergence depth,  $h$ , on the RMS lift coefficient,  $C_{L,rms}$ , at  $R = 200$ :  $A = 0.13$ ,  $1.0 \leq f/f_0 \leq 4.0$ .

for all Froude numbers shown in Table 6.7, the RMS lift coefficient,  $C_{L,rms}$ , increases when compared to that observed at  $h = \infty$ , except for the case  $f/f_0 = 2.0$ ,  $h = 0.25$ . This table also indicates that as the Froude number increases from 0.2 to 0.4, the values of  $C_{L,rms}$  decrease at  $h = 0.5, 0.75$ . On the other hand,  $C_{L,rms}$  increases for  $f/f_0 = 1.0, 2.0$  and decreases for  $f/f_0 = 3.0, 4.0$  when  $h = 0.25$  as  $Fr$  increases. For the smallest frequency ratio,  $f/f_0 = 1.0$ , decreasing the cylinder submergence depth,  $h$ , from 0.75 to 0.25 seems to increase the values of  $C_{L,rms}$  when  $Fr = 0.2, 0.4$ , except for the case when  $Fr = 0.2$  and  $h$  is reduced from 0.5 to 0.25. An interesting trend in the  $C_{L,rms}$  behaviour is observed for  $f/f_0 = 2.0$ . It is seen that when  $Fr = 0.2$ ,  $C_{L,rms}$  increases as  $h$  decreases from 0.75 to 0.5 and decreases as  $h$  is reduced from 0.5 to 0.25. In contrast, when  $Fr = 0.4$ ,  $C_{L,rms}$  decreases as  $h$  reduces from 0.75 to 0.5 and increases as  $h$  decreases from 0.5 to 0.25. For the larger frequency ratios,  $f/f_0 = 3.0$ ,

4.0, the values of  $C_{L,rms}$  seem to increase for each of Froude numbers,  $Fr = 0.2, 0.4$ , as  $h$  decreases from 0.75 to 0.25, except for the case  $Fr = 0.4$  (non-periodic state) and  $h$  reduces from 0.75 to 0.5. Taking an overview of Table 6.8, it can be seen that the

|             |          | $Fr = 0.2$ |       |       | $Fr = 0.4$    |               |               |
|-------------|----------|------------|-------|-------|---------------|---------------|---------------|
| $f/f_0 / h$ | $\infty$ | 0.25       | 0.5   | 0.75  | 0.25          | 0.5           | 0.75          |
| 1.0         | 1.378    | 1.639      | 1.737 | 1.567 | 1.574         | 1.738 → 1.665 | 1.611         |
| 2.0         | 1.907    | 2.362      | 2.247 | 2.133 | 1.661         | 1.848 → 1.872 | 2.025 → 2.041 |
| 3.0         | 2.642    | 3.396      | 3.003 | 2.756 | 2.095 → 2.255 | 2.367 → 2.354 | 2.524 → 2.474 |
| 4.0         | 4.263    | 3.550      | 3.325 | 3.488 | 3.210 → 3.283 | 3.680 → 3.687 | 3.897 → 3.929 |

Table 6.8: The effect of the Froude number,  $Fr$ , and the cylinder submergence depth,  $h$ , on the RMS drag coefficient,  $C_{D,rms}$ , at  $R = 200$ :  $A = 0.13$ ,  $1.0 \leq f/f_0 \leq 4.0$ .

RMS drag coefficient,  $C_{D,rms}$ , varies significantly when compared to the case  $h = \infty$ . More precisely, the values of  $C_{D,rms}$  (i) increase for  $f/f_0 = 1.0, 2.0, 3.0$ ,  $h = 0.25, 0.5, 0.75$ ,  $Fr = 0.2$ ; (ii) decrease for  $f/f_0 = 4.0$ ,  $h = 0.25, 0.5, 0.75$ ,  $Fr = 0.2$ ; (iii) increase for  $f/f_0 = 1.0$ ,  $h = 0.25, 0.5, 0.75$ ,  $Fr = 0.4$ ; (iv) decrease for  $f/f_0 = 2.0$ ,  $h = 0.25, 0.5$ ,  $Fr = 0.4$ ; (v) increase for  $f/f_0 = 2.0$ ,  $h = 0.75$ ,  $Fr = 0.4$ ; (vi) decrease for  $f/f_0 = 3.0, 4.0$ ,  $h = 0.25, 0.5, 0.75$ ,  $Fr = 0.4$ . This table indicates that as  $Fr$  increases, the values of  $C_{D,rms}$  decrease at the smallest cylinder submergence depth,  $h = 0.25$ . For larger cylinder submergence depths,  $h = 0.5, 0.75$ ,  $C_{D,rms}$  increases for  $f/f_0 = 1.0, 4.0$ , except for the case  $f/f_0 = 1.0$ ,  $h = 0.5$ ,  $Fr = 0.4$  (non-periodic state) as  $Fr$  increases. In contrast, for  $f/f_0 = 2.0, 3.0$ ,  $h = 0.5, 0.75$ , the values of  $C_{D,rms}$  decrease as  $Fr$  increases. Furthermore, for  $f/f_0 = 1.0$ , the values of  $C_{D,rms}$  seem to increase as  $h$  decreases from 0.75 to 0.5 and to decrease as  $h$  reduces from 0.5 to 0.25 for each of Froude numbers,  $Fr = 0.2, 0.4$ . An interesting trend in the

|             |          | $Fr = 0.2$ |        |        | $Fr = 0.4$      |                 |                 |
|-------------|----------|------------|--------|--------|-----------------|-----------------|-----------------|
| $f/f_0 / h$ | $\infty$ | 0.25       | 0.5    | 0.75   | 0.25            | 0.5             | 0.75            |
| 1.0         | -0.276   | -0.469     | -0.210 | -0.319 | -0.607          | -0.113 → -0.430 | -0.775          |
| 2.0         | -0.372   | -1.524     | -0.764 | -0.702 | -0.503          | -0.326 → -0.373 | -0.360 → -0.342 |
| 3.0         | -0.617   | -2.588     | -1.647 | -1.326 | -0.776 → -0.746 | -0.588 → -0.631 | -0.561 → -0.530 |
| 4.0         | -0.101   | -2.983     | -1.794 | -1.345 | -0.956 → -0.896 | -0.818 → -0.858 | -0.859 → -0.820 |

Table 6.9: The effect of the Froude number,  $Fr$ , and the cylinder submergence depth,  $h$ , on the total mechanical energy transfer,  $E$ , at  $R = 200$ :  $A = 0.13$ ,  $1.0 \leq f/f_0 \leq 4.0$

$C_{D,rms}$  behaviour is observed for the higher frequency ratios,  $f/f_0 = 2.0, 3.0$ . It is evident that for  $f/f_0 = 2.0, 3.0$ ,  $C_{D,rms}$  increases when  $Fr = 0.2$  and decreases when  $Fr = 0.4$  as  $h$  reduces from 0.75 to 0.25. Finally, for  $f/f_0 = 4.0$ , the decrease in  $h$  leads to the (i) decrease in  $C_{D,rms}$  when  $Fr = 0.2$  and  $h$  reduces from 0.75 to 0.5; (ii) increase in  $C_{D,rms}$  when  $Fr = 0.2$  and  $h$  reduces from 0.5 to 0.25 and (iii) decrease in  $C_{D,rms}$  when  $Fr = 0.4$  and  $h$  reduces from 0.75 to 0.25.

Table 6.9 shows the effect of the Froude number,  $Fr$  ( $= 0.2, 0.4$ ), and the cylinder submergence depth,  $h$  ( $= 0.25, 0.5, 0.75$ ), on the total mechanical energy transfer,  $E$ , for the case  $R = 200$ ,  $A = 0.13$  when  $1.0 \leq f/f_0 \leq 4.0$ . The reference case  $h = \infty$  is also shown in this table. It is clearly seen that the overall energy transfer,  $E$ , is always negative. Therefore, for all cases, the negative energy is delivered from the cylinder to the fluid and thereby, the fluid produces a resistance against the forced motion of the cylinder. Taking an overview of Table 6.9, it is seen that the effect of the increasing  $Fr$  from 0.2 to 0.4 is to increase the total energy transfer,  $E$ , (i.e., to increase the absolute values of  $E$ ) when  $f/f_0 = 1.0$ , except for the case  $Fr = 0.4$ ,  $h = 0.5$  (quasi-periodic state), and to decrease the energy transfer,  $E$ , when  $f/f_0 \geq 2.0$ . This

indicates that for the smallest frequency ratio,  $f/f_0 = 1.0$ , the fluid resistance against the forced motion of the cylinder increases (by a maximum factor of 2.0) as  $Fr$  varies. In contrast, for the higher frequency ratios,  $f/f_0 \geq 2.0$ , the fluid resistance against the forced motion of the cylinder seems to decrease (by a maximum factor of 3.0) as  $Fr$  varies. Table 6.9 also indicates that for  $Fr = 0.2$  the absolute values of the total energy transfer,  $E$ , significantly increase, except for the case  $f/f_0 = 1.0$ ,  $h = 0.5$  as  $h$  decreases from  $\infty$  to 0.25. On the other hand, for the higher Froude number of 0.4, the absolute values of the total energy transfer,  $E$ , decrease as  $h$  decreases from  $\infty$  to 0.75, except  $f/f_0 = 1.0$ , 4.0, and increase as  $h$  decreases further to 0.25, except for the cases  $f/f_0 = 1.0$ ,  $f/f_0 = 2.0$  (quasi-periodic state),  $f/f_0 = 4.0$  (quasi-periodic state) when  $h = 0.5$ .

## 6.2 Overview of distinctive flow features and vortex shedding modes

In this thesis, the numerical simulations of unsteady, laminar, two-dimensional flow of a viscous incompressible fluid past a cylinder subject to in-line oscillations in uniform flow in the presence of the free surface are performed for the first time. Overall, this investigation has shown that when the free surface is present, both the near wake structure and the free surface deformations are very sensitive to the Froude number,  $Fr$ , and to the cylinder submergence depth,  $h$ . For smaller Froude numbers,  $Fr \approx 0.0$  and  $Fr = 0.2$ , the surface deformations are minimal and they become substantial as  $Fr$  increases. As  $Fr$  increases to 0.4 and  $h$  decreases to 0.25, the localized interface

sharpening and wave breaking occur. This yields to introduction of a substantial quantity of opposite signed vorticity from the free surface which interacts with the upper vorticity shedding layer through diffusion and thereby, substantially changes the wake evolution. These findings are in accord with that of Reichl *et al.* (2005) for uniform flow past the cylinder in the presence of the free surface for the case  $R = 180$ ,  $0 \leq Fr \leq 0.7$  and  $0.1 \leq h \leq 0.5$ . Reichl *et al.* (2005) suggest that the sharpening of the interface is presumably due to the local Froude number in the region directly above the cylinder,  $Fr|_L$ . The local Froude number,  $Fr|_L$ , generally becomes considerably higher than the global Froude number,  $Fr$ , for the small cylinder submergence depth,  $h$ , and thereby, a sharpened scar occurs in the region where  $Fr|_L \rightarrow 1$ . When this happens, the accelerated fluid in a scar region interacts with the slower fluid from above the positive vortices and thereby, a shift from a surface scar to a localized wave breaking occurs. Moreover, it has also been observed that for small depths of the cylinder submergence,  $h = 0.25, 0.5$ , the negative vortices seem to decay rapidly into the downstream due to the viscous transport of the negative vorticity across the interface. Hence, the negative vorticity is being removed from the fluid by diffusion and cross-annihilation. Furthermore, this investigation shows that the upper vortex shedding layer from the cylinder surface induces a strong time-dependant surface curvature, which, in turn, introduces substantial positive vorticity near the curved interface. This vorticity interacts with the upper vortex shedding layer through diffusion and cross-annihilation and thereby, significantly alters the near wake evolution. Moreover, the induced surface curvature allows easier entry of the secondary vorticity appearing near the free surface into the near wake. As a consequence, the upper vortex shedding layer becomes weaker as it contains less vorticity

than the lower vortex shedding layer and thus the wake evolution is being dominated by the positive vortex structures. This results in an asymmetry in the near wake and thereby, the absolute instability is being at least partially suppressed. As a result, the vortex formation and shedding become weaker over subsequent cycles and thus at certain  $Fr-h$  combinations the transition of the near wake from the quasi-locked-on state to the non-locked-on state occurs. It is noted that similar phenomena have been reported in the numerical work by Reichl *et al.* (2005) and the experimental work of Sheridan *et al.* (1995, 1997) for the case of uniform flow past a stationary cylinder in the presence of the free surface, and the experimental study by Cetiner and Rockwell (2001) for the case of cylinder subject to in-line oscillations in uniform flow in the presence of the free surface. In fact, the works of Reichl *et al.* (2005) and Sheridan *et al.* (1995, 1997) ( $0 < h \leq 0.75$ ,  $5990 \leq R \leq 9120$  and  $0.47 \leq Fr \leq 0.72$ ) have shown that at certain  $Fr-h$  combinations, the presence of the free surface causes a switching between the near wake states. These studies found that the near wake spontaneously changes from one state to another in a pseudo-periodic manner. In the work by Cetiner and Rockwell (2001), the uniform flow past the cylinder subject to in-line oscillations is considered at  $R = 917, 2075$ ,  $Fr \rightarrow 0.07, 0.158$ ,  $A = 0.96$ ,  $f/f_0 = 0.44, 1.0$  and  $h = 0.06, 0.19, 11.23$ . It has been observed that for certain  $Fr-h$  combinations the vortex shedding exhibits locked-on (or quasi-locked-on) states at least over several cycles of cylinder oscillations and then, the transition to the non-locked-on state occurs.

One of the most interesting findings of this thesis is that it seems to be possible to generate distinctly different patterns of the vortex formation than that of classical vortex shedding modes observed for a cylinder subject to transverse oscillations in

uniform flow, provided that the cylinder is located sufficiently close to the free surface and the Froude number is high. Moreover, it is shown that the presence of the free surface provides the possibility for quasi-locked-on vortex formation not only from the cylinder but also from the free surface. These observations agree with that of Cetiner and Rockwell (2001). In Table 6.10, these new vortex formation modes are briefly summarized.

| Mode            | Description  |
|-----------------|--|
| <b>C(P+S)+S</b> | Similar to the classical <b>C(P+S)</b> mode with the only difference that one more single vortex is shed from the free surface over the period of vortex shedding, $T_0$ |
| <b>C(2S)+S</b>  | Similar to the classical <b>C(2S)</b> mode with the only difference that one more single vortex is shed from the free surface over the period of vortex shedding, $T_0$  |

Table 6.10: The new vortex shedding modes (and their descriptions) observed in the present thesis.

The quasi-locked-on **C(P+S)+S** and **C(2S)+S** modes shown in Table 6.10 have been observed for  $f/f_0 = 3.0$  over  $3T$  (within  $18T$ ) and for  $f/f_0 = 4.0$  over  $4T$  (within  $28T$  and  $12T$ ) at  $h = 0.5, 0.75$ , respectively, when  $Fr = 0.4$ . The other observed vortex shedding modes are as follows. For the limiting case  $Fr \approx 0.0$ , three basic quasi-locked-on asymmetric vortex shedding modes, **2S**, **2P** and **P+S**, and two locked-on asymmetric vortex shedding modes, **2S** and **P+S** have been observed. The quasi-locked-on asymmetric **2S** mode occurs over  $5T$ , for  $f/f_0 = 4.0$  at  $h = 0.25$  and over  $3T$  (within  $12T$ ) for  $f/f_0 = 3.0$  at  $h = 0.5$  when  $Fr \approx 0.0$ . The quasi-locked-on asymmetric **2P** mode occurs over  $4T$  (within  $20T$ ) for  $f/f_0 = 4.0$  at  $h = 0.5$ ,  $Fr \approx 0.0$ . The quasi-locked-on asymmetric **P+S** mode occurs over  $3T$  (within  $24T$ )

for  $f/f_0 = 3.0$  at  $h = 0.75$  when  $Fr \approx 0.0$ . On the other hand, the locked-on asymmetric **2S** mode occurs over  $T$ , for  $f/f_0 = 1.0$  at  $h = 0.5, 0.75$  and over  $2T$ , for  $f/f_0 = 2.0$  at  $h = 0.5$  when  $Fr \approx 0.0$ . The locked-on asymmetric **P+S** mode occurs over  $2T$  for  $f/f_0 = 2.0$  and over  $4T$  for  $f/f_0 = 4.0$  when  $h = 0.75, Fr \approx 0.0$ . It is also noted that for this Froude number,  $Fr \approx 0.0$ , the coalescence between the vortices in the vortex shedding layers appears for the high frequency ratios,  $f/f_0 = 2.0$  at  $h = 0.5$ ;  $f/f_0 = 3.0$  at  $h = 0.5, 0.75$  and  $f/f_0 = 4.0$  at  $h = 0.25, 0.75$ . Further, at moderate Froude number of 0.2, the vortex shedding exhibits quasi-locked-on asymmetric **2S** mode over  $T$  for  $f/f_0 = 1.0, h = 0.5, 0.75$ , and over  $2T$  for  $f/f_0 = 2.0, h = 0.5$ . The quasi-locked-on asymmetric **P+S** mode over  $2T$  has been observed for  $f/f_0 = 2.0, h = 0.75, Fr = 0.2$ . Finally, at the highest Froude number  $Fr = 0.4$ , the vortex shedding modes are the quasi-locked-on asymmetric **2S** mode over  $4T$  (within  $20T$ ) and over  $5T$  (within  $20T$ ), respectively, for  $f/f_0 = 3.0, 4.0$  at  $h = 0.25$ ; over  $T$  (within  $5T$ ) and over  $2T$  (within  $14T$ ), respectively, for  $f/f_0 = 1.0, 2.0$  at  $h = 0.5$  and quasi-locked-on asymmetric **P+S** mode over  $2T$  (within  $14T$ ) for  $f/f_0 = 2.0$  at  $h = 0.75$ . At this Froude number,  $Fr = 4.0$ , the coalescence between the vortices in the vortex shedding layers appears for  $f/f_0 = 3.0, 4.0$  at  $h = 0.25$  and  $f/f_0 = 1.0, 2.0$  at  $h = 0.5$ .

### 6.3 Practical significance of the present results

Flow induced forces play an important role in the design of variety of engineering structures. Representative structures having a cylindrical shape include towing cables

inclined at a shallow angle with respect to the free surface and thereby approximating a horizontal orientation. Rapidly deployable cable systems with instrumentation dropped from an aircraft through a free surface may be oriented horizontally beneath the free surface during the initial stages of deployment. Furthermore, many offshore platforms have horizontal, cylindrically shaped members. The unsteady forces acting on all of these configurations can be approximated by a horizontal cylinder placed in a steady uniform stream in the presence of the free surface.

Control of vortex shedding leads to reduction in the unsteady forces acting on the bluff body and can reduce its vibrations. Flow control may be accomplished by controlling the boundary layer separation and/or the structure of shear layer in the wake. In this thesis, the separation control is achieved by subjecting the cylinder to harmonic oscillations. Precisely, the problem of uniform viscous incompressible flow past an oscillating horizontal rigid circular cylinder of infinite length located beneath a free surface is considered. The present investigation has shown that for the cylindrical structures, the presence of the free surface markedly influences the mean values of both the lift and drag forces. Moreover, the presence of the free surface seems to destabilize, in general, the locked-on states of the vortex shedding. These observations suggest that the free surface could be used to bring control in the near wake vortical structures. Specifically, the free surface alters the nature of the forcing function associated with self-excited vibration and thus the conditions for onset of self-excited vibration can be altered as well. The important consequence of this is that for the cylindrical configurations submerged under the free surface, the design criteria based on the cylinder in the absence of the free surface will be, in general, in error.

## 6.4 Future work

One area of future work is in implementation of a higher order scheme for the temporal discretization. It is hoped that the temporal accuracy of the VOF methods could be improved by using multi-step methods such as Adams-Bashford method, Adams-Moulton method, Gear's method and others. Promising results have already obtained by other researchers for simple flows [see, for example, Li *et al.* (2004)].

Another area of future work is in reducing computational time required to perform simulations. Reducing computational time is necessary as the large time simulations of free surface flows with moving rigid bodies are computationally very expensive. Computation time can be greatly reduced by parallelizing the code so that it can be run on a distributed-memory high performance cluster of parallel processors. The parallelization of the code can be implemented without the need for any fundamental changes to the structure of the code. This is due to the fact that the code is written in modular form with extensive use of array algebra and other parallel data structures such as Trilinos library. It is noted that running the code in parallel will also allow using high resolution grids which will improve stability of computations as the free surface will be resolved more accurately.

Finally, an interesting direction would be to implement surface tension and test the ability of the method to model micro gravity flows. The modeling of surface tension in numerical simulation of interfacial flows is a big challenge. One of the issues in the numerical modeling of surface tension is the production of unphysical vortical flows so-called "spurious" or "parasitic" currents which are due to the imbalance between

---

stresses in the interfacial region. The main source for the occurrence of the currents is the discretization errors such as those used to calculate the interface curvatures. The currents cause the vibration of a phase interface, producing unphysical results and solver breakdowns. In this thesis, an attempt to model surface tension has been made. The relatively simple approaches such as described in Gerrits (2001) and Prosperetti and Tryggvason (2007) have been used to model surface tension. In all of the cases, vibration of the free surface and thus a numerical breakdown are observed. It is believed that more sophisticated approaches involving spline interpolants must be used to compute interface curvatures accurately. In this regard, the method of Ginzburg and Wittum (2001) seems to be a promising technique for a future development.

# Bibliography

---

- Akyildiz, H. and Ünal, N. E. (2006). Sloshing in a three-dimensional rectangular tank: Numerical simulation and experimental validation. *Ocean Engineering*, 33(16):2135-2149.
- Al-Mdallal, Q. M. (2004). *Analysis and computation of the cross-flow past an oscillating cylinder with two degrees of freedom*. Ph.D. thesis, Memorial University of Newfoundland.
- Al-Mdallal, Q. M., Lawrence, K. P. and Kocabiyik, S. (2007). Forced streamwise oscillations of a circular cylinder: Locked-on modes and resulting fluid forces. *Journal of Fluids and Structures*, 23(5):681-701.
- Anagnostopoulos, P. (1997). Computer-aided flow visualization and vorticity balance in the laminar wake of a circular cylinder. *Journal of Fluids and Structures*, 11(1):33-72.
- Anagnostopoulos, P. (2000). Numerical study of the flow past a cylinder excited transversely to the incident stream. Part 1: Lock-in zone, hydrodynamic forces and wake geometry. *Journal of Fluids and Structures*, 14:819-851.
- Anagnostopoulos, P. (2002). *Flow-Induced Vibrations in Engineering Practice*. International Series on Advances in Fluid Mechanics, Vol. 31. WIT Press, UK.
- Anderson, C. R. and Reider, M. B. (1996). A high order explicit method for the computation of flow about a circular cylinder. *Journal of Computational Physics*, 125(1):207-224.
- Armenio, V. (1997). An improved MAC method (SIMAC) for unsteady high-Reynolds free surface flows. *International Journal for Numerical Methods in Fluids*, 24(2):185-214.
- Aulisa, E., Manservigi, S. and Scardovelli, R. (2003a). A mixed markers and volume-of-fluid method for the reconstruction and advection of interfaces in two-phase and free-boundary flows. *Journal of Computational Physics*, 188(2):611-639.
- Aulisa, E., Manservigi, S., Scardovelli, R. and Zaleski, S. (2003b). A geometrical area-preserving volume-of-fluid advection method. *Journal of Computational Physics*, 192(1):355-364.

- Badr, H. M. and Dennis, S. C. R. (1985). Time-dependent viscous flow past an impulsively started rotating and translating circular cylinder. *Journal of Fluid Mechanics*, 158:447-488.
- Bearman, P. W. (1984). Vortex shedding from oscillating bluff bodies. *Annual Review of Fluid Mechanics*, 16:195-222.
- Bénard, H. (1908a). Formation of centers of circulation behind a moving obstacle (in French). *Comptes Rendus Academie des Sciences*, 147:839-842 (Hist., Exp. FV, 1, 3, 5).
- Bénard, H. (1908b). A cinematographic study of eddies and ripples produced by towed obstacle (in French). *Comptes Rendus Academie des Sciences*, 147:970-972 (Hist., Exp. FV, 1, 3, 5).
- Biausser, B., Guignard, S., Marcer, R. and Fraunié, P. (2004). 3D two phase flows numerical simulations by SL-VOF method. *International Journal of Numerical Methods in Fluids*, 45(6):581-604.
- Blackburn, H. M. and Henderson, R. D. (1999). A study of two-dimensional flow past an oscillating cylinder. *Journal of Fluid Mechanics*, 385:255-286.
- Braza, M., Chassaing, P. and Ha Minh, H. (1986). Numerical study and physical analysis of the pressure and velocity fields in the near wake of a circular cylinder. *Journal of Fluid Mechanics*, 165:79-130.
- Brent, R. P. (1973). *Algorithms for Minimization without Derivatives*. Prentice-Hall, New Jersey.
- Carberry, J. (2002). *Wake states of a submerged oscillating cylinder and of a cylinder beneath a free surface*. Ph.D. thesis, Monash University, Australia.
- Carberry, J., Sheridan, J. and Rockwell, D. (2001). Stationary and oscillating cylinders in the presence of a free surface. *Proceedings of the 14<sup>th</sup> Australasian fluid mechanics conference*. Adelaide, Australia.
- Carberry, J., Sheridan, J. and Rockwell, D. (2004). Cylinder oscillations beneath a free surface. *European Journal of Mechanics- B/Fluids*, 23(1):81-88.

- Cetiner, O. and Rockwell, D. (2001a). Streamwise oscillations of a cylinder in a steady current. Part 1. Locked-on states of vortex formation and loading. *Journal of Fluid Mechanics*, 427:1-28.
- Cetiner, O. and Rockwell, D. (2001b). Streamwise oscillations of a cylinder in steady current. Part 2. Free-surface effects on vortex formation and loading. *Journal of Fluid Mechanics*, 427:29-59.
- Coutanceau, M. and Menard, C. (1985). Influence of rotation on the near-wake development behind an impulsively started circular cylinder. *Journal of Fluid Mechanics*, 158:399-446.
- Deane, A. E. and Mavriplis, C. (1994). Low-dimensional description of the dynamics in separated flow past thick airfoils. *American Institute of Aeronautics and Astronautics Journal*, 32:1222-1227.
- De Palma, P., Tullio, M. D., Pascazio, G. and Napolitano, M. (2006). An immersed-boundary method for compressible viscous flows. *Computers and Fluids*, 35(7):693-702.
- Dipankar, A., Sengupta, T. K. and Talla, S. B. (2007). Suppression of vortex shedding behind a circular cylinder by another control cylinder at low Reynolds numbers. *Journal of Fluid Mechanics*, 573:171-190.
- Dirac, P. A. M. (1947). *The Principles of Quantum Mechanics*, 3<sup>rd</sup> Edition. Oxford University Press, London.
- Farassat, F. (1996). *Introduction to generalized functions with applications in aerodynamics and aeroacoustics*. NASA Technical Paper No. 3428. Langley Research Center, Hampton, Virginia.
- Farell, C. (1981). Flow around fixed circular cylinders: Fluctuating loads. *Journal of the Engineering Mechanics Division*, 107(3):565-588.
- Fekken, G. (2004). *Numerical simulation of free-surface flow with moving rigid bodies*. Ph.D. thesis, University of Groningen.
- Flemming, F. and Williamson, C. H. K. (2005). Vortex-induced vibrations of a pivoted cylinder. *Journal of Fluid Mechanics*, 522:215-252.

- Floryan, J. M. and Rasmussen, H. (1989). Numerical analysis of viscous flows with free surfaces. *Applied Mechanics Reviews*, 42(12):323-341.
- Forsythe, G. E., Malcolm, M. A., and Moler, C. B. (1977). *Computer Methods for Mathematical Computations*. Prentice-Hall, Englewood Cliffs.
- Gad-el-Hak, M. and Bushnell, D. M. (1991). Separation control: review. *Journal of Fluids Engineering*, 113:5-30.
- Gerrard, J. H. (1997). Numerical study of the instabilities in the near wake of a circular cylinder at low Reynolds number. *Journal of Fluids and Structures*, 11(3):271-291.
- Gerrits, J. (2001). *Dynamics of liquid-filled spacecraft*. Ph.D. thesis, University of Groningen.
- Ginzburg, I. and Wittum, G. (2001). Two-phase flows on interface refined grids modeled with VOF, staggered finite volumes, and spline interpolants. *Journal of Computational Physics*, 166(2):302-335.
- Glowinski, R. and Kuznetsov, Y. (2007). Distributed Lagrange multipliers based on fictitious domain method for second order elliptic problems. *Computer Methods in Applied Mechanics and Engineering*, 196(8):1498-1506.
- Glowinski, R., Pan, T.-W. and Périaux, J. (1997). *A Lagrange Multiplier/Fictitious Domain Method for the Numerical Simulation of Incompressible Viscous Flow Around Moving Rigid Bodies (I): The Case where the Rigid Body Motions are Known a Priory*. Serie I: Mathematical Problems in Mechanics, Vol. 324, pp. 361-369. Comptes-Rendus de l'Académie des Sciences de Paris, Paris.
- Gresho, P. M. and Sani, R. L. (1998). *Incompressible Flow and the Finite Element Method*. John Wiley and Sons, Inc., New York.
- Griebel, M., Dornseifer, T. and Neunhoffer, T. (1998). *Numerical Simulations in Fluid Dynamics. A Practical Introduction*. Society for Industrial and Applied Mathematics, Philadelphia.
- Griffin, O. and Hall, M. (1991). Review-vortex shedding lock-on and flow control in bluff body wakes. *Journal of Fluids Engineering*, 113:526-537.

- Gubanov, O. (2006). *Design of CFD code using high level programming paradigms: Free surface flows with arbitrarily moving rigid bodies*. M.Sc. thesis, Memorial University of Newfoundland.
- Guilmineau, E. and Queutey, P. (2002). A numerical simulation of vortex shedding from an oscillating circular cylinder. *Journal of Fluids and Structures*, 16(6):773-794.
- Harlow, F. H. and Welsh, J. E. (1965). Numerical calculation of time-dependent viscous incompressible flow of fluid with free surface. *Physics of Fluids*, 8(12):2182-2189.
- Harvie, D. J. E. and Fletcher, D. F. (2000). A new volume of fluid advection algorithm: the stream scheme. *Journal of Computational Physics*, 162(1):1-32.
- He, J.-W., Glowinski, R., Metcalfe, R., Nordlander, A. and Periaux, J. (2000). Active control and drag optimization for flow past a circular cylinder. I. Oscillatory cylinder rotation. *Journal of Computational Physics*, 163:83-117.
- Henderson, R. D. (1995). Details of the drag curve near the onset of vortex shedding. *Physics of Fluids*, 7(9):2102-2104.
- Henderson, R. D. (1997). Nonlinear dynamics and pattern formation in turbulent wake transition. *Journal of Fluid Mechanics*, 352:65-112.
- Hirt, C. W. (1992). *Volume-fraction techniques: Powerful tools for flow modeling*. Technical Report No. FSI-92-00-02. Flow Science Inc., Los Alamos, New Mexico.
- Hirt, C. W. (1993). Volume-fraction techniques: powerful tools for wind engineering. *Journal of Wind Engineering and Industrial Aerodynamics*, 46-47:327-338.
- Hirt, C. W. and Nichols, B. D. (1981). Volume of fluid (VOF) method for the dynamics of free boundaries. *Journal of Computational Physics*, 39:201-225.
- Hirt, C. W. and Sicilian, J. M. (1985). *A porosity technique for the definition of obstacles in rectangular cell meshes*. Flow Science, Inc., Los Alamos, New Mexico.
- Ho, L. W. (1989). *A Legendre spectral element method for simulation of incompressible*

- unsteady free surface flows*. Ph.D. thesis, Massachusetts Institute of Technology.
- Hu, X. Y., Khoo, B. C., Adams, N. A. and Huang, F. L. (2006). A conservative interface method for compressible flows. *Journal of Computational Physics*, 219(2):553-578.
- Jacqmin, D. (1999). Calculation of two-phase Navier-Stokes flows using phase-field modeling. *Journal of Computational Physics*, 115(1):96-127.
- Justesen, P. (1991). A numerical study of oscillating flow around a circular cylinder. *Journal of Fluid Mechanics*, 222:157-196.
- Karanth, D., Rankin, G. W. and Sridhar, K. (1995). Computational study of flow past a cylinder with combined in-line and transverse oscillation. *Computational Mechanics*, 16:1-10.
- Kármán, T. von. (1911). Über den mechanismus des widerstandes, den ein bewegter körper in einer flüssigkeit erfährt. 1. Teil. *Göttinger Nachrichten Math-Phys. Klasse 1911*, 509.
- Kármán, T. von. (1912). Über den mechanismus des widerstandes, den ein bewegter körper in einer flüssigkeit erfährt. 2. Teil. *Göttinger Nachrichten Math-Phys. Klasse 1912*, 547.
- Karniadakis, G. E., Israeli, M. and Orszag, S. A. (1991). High-order splitting methods for the incompressible Navier-Stokes equations. *Journal of Computational Physics*, 97:414-443.
- Kim, J., Kim, D. and Choi, H. (2001). An immersed-boundary finite-volume method for simulations of flow in complex geometries. *Journal of Computational Physics*, 171(1):132-150.
- King, R. (1977). A review of vortex shedding research and its applications. *Ocean Engineering*, 4:141-172.
- Kirkpatrick, M. P., Armfield, S. W. and Kent, J. H. (2003). A representation of curved boundaries for the solution of the Navier-Stokes equations on a staggered three-dimensional Cartesian grid. *Journal of Computational Physics*, 184(1):1-36.

- Kleefsman, K. M. T. (2005). *Water impact loading on offshore structures. A numerical study*. Ph.D. thesis, University of Groningen.
- Kothe, D. B. and Mjolsness, R. C. (1992). Ripple: a new model for incompressible flows with free surfaces. *American Institute of Aeronautics and Astronautics Journal*, 30(11):2694-2700.
- Kravchenko, A. G., Moin, P. and Shariff, K. (1999). B-spline method and zonal grids for simulations of complex turbulent flows. *Journal of Computational Physics*, 151(2):757-789.
- Ku, H.-C. (1995). Solution of flow in complex geometries by the pseudospectral element method. *Journal of Computational Physics*, 117(2):215-227.
- Leonard, B. P. (1979). A stable and accurate convective modelling procedure based on quadratic upstream interpolation. *Computer Methods in Applied Mechanics and Engineering*, 19:59-98.
- Levy, S. (1999). *Two-Phase Flow in Complex Systems*. John Wiley and Sons, Inc., New York.
- Li, T., Troch, P. and De Rouck, J. (2004). Wave overtopping over a sea dike. *Journal of Computational Physics*, 198(2):686-726.
- Li, Y., Shock, R., Zhang, R. and Chen, H. (2004). Numerical study of flow past an impulsively started cylinder by the lattice-Boltzmann method. *Journal of Fluid Mechanics*, 519:273-300.
- Lin, P. (2007). A fixed-grid model for simulation of a moving body in free surface flows. *Computers and Fluids*, 36(3):549-561.
- Liu, C., Zheng, X. and Sung, C. H. (1998). Preconditioned multigrid methods for unsteady incompressible flows. *Journal of Computational Physics*, 139(1):35-57.
- Longuet-Higgins, M. S. (1992). Capillary rollers and bores. *Journal of Fluid Mechanics*, 240:659-679.
- Meneghini, J. R. and Bearman, P. W. (1995). Numerical simulation of high amplitude oscillatory flow about a circular cylinder. *Journal of Fluids and Structures*,

9:435-455.

- Nair, M. T., Sengupta, T. K. and Chauhan, U. S. (1998). Flow past rotating cylinders at high Reynolds numbers using higher order upwind scheme. *Computers and Fluids*, 27(1):47-70.
- Naudascher, E. and Rockwell, D. (1993). *Flow-Induced Vibrations. An Engineering Guide*. Advanced Series on Coastal Engineering. A.A. Balkema Publishers, The Netherlands.
- Noh, W. F. and Woodward, P. R. (1976). *SLIC (simple line interface calculation)*, Springer Lecture Notes in Physics, Vol. 59, pp. 330-340(Edited by A.I. van de Vooren and P.J. Zandbergen). Springer-Verlag, Germany.
- Norberg, C. (2003). Fluctuating lift on a circular cylinder: review and new measurements. *Journal of Fluids and Structures*, 17:57-96.
- Ongoren, A. and Rockwell, D. (1988a). Flow structure from an oscillating cylinder. Part 1. Mechanisms of phase shift and recovery in the near wake. *Journal of Fluid Mechanics*, 191:197-223.
- Ongoren, A. and Rockwell, D. (1988b). Flow structure from an oscillating cylinder. Part 2. Mode competition in the near wake. *Journal of Fluid Mechanics*, 191:225-245.
- Osher, S. and Fedkiw, R. (2003). *Level Set Methods and Dynamic Implicit Surfaces*. Applied Mathematical Sciences, Vol. 153. Springer-Verlag, New York.
- Osher, S. and Sethian, J. A. (1988). Fronts propagating with curvature dependent speed: algorithms based on Hamilton-Jacobi formulations. *Journal of Computational Physics*, 79:12-49.
- Pan, X.-Q., Shen, Q., Chen, X.-J. and Sun, H.-C. (2006). Hydrodynamic optimization of performance of blunt ships. *Journal of Hydrodynamics*, 18(3):337-342.
- Panton, R. L. (1996). *Incompressible Flow*, 2<sup>nd</sup> Edition. John Wiley and Sons, Inc., New York.
- Park, J. Y., Kwon, K. Y. and Choi, H. C. (1998). Numerical solutions of flow past a

- circular cylinder at Reynolds numbers up to 160. *Korean Society of Mechanical Engineers (KSME) International Journal*, 12:1200-1205.
- Patankar, S. V. (1980). *Numerical Heat Transfer and Fluid Flow*. Hemisphere Publishing Corporation, Washington.
- Peskin, C. S. (2002). The immersed boundary method. *Acta Numerica*:479-517.
- Pilliod, J. E., Jr. and Puckett, E. G. (2004). Second-order accurate volume-of-fluid algorithms for tracking material interfaces. *Journal of Computational Physics*, 199(2):465-502.
- Ploumhans, P. and Winckelmans, G. S. (2000). Vortex methods for high-resolution simulations of viscous flow past bluff bodies of general geometry. *Journal of Computational Physics*, 165(2):354-406.
- Poncet, P. (2004). Topological aspects of three-dimensional wakes behind rotary oscillating cylinders. *Journal of Fluid Mechanics*, 517:27-53.
- Posdziech, O. and Grundmann, R. (2001). Numerical simulation of the flow around an infinitely long circular cylinder in the transition regime. *Theoretical and Computational Fluid Dynamics*, 15(2):121-141.
- Prosperetti, A. and Tryggvason, G. (2007). *Computational Methods for Multiphase Flow*. Cambridge University Press, Cambridge.
- Ramière, I., Angot, P. and Belliard, M. (2007). A fictitious domain approach with spread interface for elliptic problems with general boundary conditions. *Computer Methods in Applied Mechanics and Engineering*, 196(4-6):766-781.
- Reichl, P. (2001). *Flow past a cylinder close to a free surface*. Ph.D. thesis, Monash University.
- Reichl, P., Hourigan, K. and Thompson, M. (2003). The unsteady wake of a circular cylinder near a free surface. *Flow, Turbulence and Combustion*, 71:347-359.
- Reichl, P., Hourigan, K. and Thompson, M. C. (2005). Flow past a cylinder close to a free surface. *Journal of Fluid Mechanics*, 533:269-296.

- Rider, W. J. and Kothe, D. B. (1998). Reconstructing volume tracking. *Journal of Computational Physics*, 141(2):112-152.
- Rockwell, D. (1998). Vortex-body interactions. *Annual Review of Fluid Mechanics*, 30:199-229.
- Rood, E. P. (1995). *Vorticity Interactions with a Free Surface*. Fluid Vorticities (Edited by S. I. Green). Kluwer Academic, The Netherlands.
- Rudman, M. (1997). Volume-tracking methods for interfacial flow calculations. *International Journal for Numerical Methods in Fluids*, 24(7):671-691.
- Sala, M., Heroux, M. A. and Day, D. M. (2004). *Trilinos tutorial*. Sandia Report No. SAND2004-2189. Sandia National Laboratories, Albuquerque, New Mexico.
- Sarpkaya, T. (1996). Vorticity, free surface and surfactants. *Annual Review of Fluid Mechanics*, 28:83-128.
- Sarpkaya, T. (2004). A critical review of the intrinsic nature of vortex-induced vibrations. *Journal of Fluids and Structures*, 19:389-447.
- Scardovelli, R. and Zaleski, S. (2003). Interface reconstruction with least-square fit and split Eulerian-Lagrangian advection. *International Journal for Numerical Methods in Fluids*, 41(3):251-274.
- Schwartz, L. (n.d.). *Théories des Distributions*. Vol. 2, 1<sup>st</sup> Edition, Actualities Scientifiques et Industrielles.
- Schwartz, L. (1950). *Théories des Distributions*. Vol. 1, 1<sup>st</sup> Edition, Actualities Scientifiques et Industrielles. Hermann and Cie, France.
- Sethian, J. A. and Smereka, P. (2003). Level set methods for fluid interfaces. *Annual Review of Fluid Mechanics*, 35:341-372.
- Sheridan, J., Lin, J.-C. and Rockwell, D. (1995). Metastable states of a cylinder wake adjacent to a free surface. *Physics of Fluids*, 7(9):2099-2101.
- Sheridan, J., Lin, J.-C. and Rockwell, D. (1997). Flow past a cylinder close to a free surface. *Journal of Fluid Mechanics*, 330:1-30.

- Shyy, W., Udaykumar, H. S., Rao, M. M. and Smith, R. W. (1996). *Computational Fluid Dynamics With Moving Boundaries*. Series in computational and physical processes in mechanics and thermal sciences. Taylor and Francis, Washington.
- Sirovich, S. (1987). Turbulence and the dynamics of coherent structures. I - Coherent structures. II - Symmetries and transformations. III - Dynamics and scaling. *Quarterly of Applied Mathematics*, 45:561-590.
- Strouhal, V. (1878). Über eine besondere art der tonerregung. *Annalen der Physik und Chemie*, 5:216-251.
- Su, S.-W., Lai, M.-C. and Lin, C.-A. (2007). An immersed boundary technique for simulating complex flows with rigid boundary. *Computers and Fluids*, 36(2):313-324.
- Sumer, B. M. and Fredsøe, J. (1997). *Hydrodynamics Around Cylindrical Structures*. Advanced Series on Coastal Engineering, Vol. 12. World Scientific Publishing Company, UK.
- Sussman, M. and Puckett, E. G. (2000). A coupled level set and volume-of-fluid method for computing 3D and axisymmetric incompressible two-phase flows. *Journal of Computational Physics*, 162(2):301-337.
- Taha, T. and Cui, Z. F. (2004). Hydrodynamics of slug flow inside capillaries. *Chemical Engineering Science*, 59(6):1181-1190.
- Takada, N. and Tsutahara, M. (1998). Evolution of viscous flow around a suddenly rotating circular cylinder in the lattice-Boltzmann method. *Computers and Fluids*, 27(7):807-828.
- Takewaki, H. and Yabe, T. (1987). The cubic-interpolated Pseudo particle (cip) method: application to nonlinear and multi-dimensional hyperbolic equations. *Journal of Computational Physics*, 70(2):355-372.
- Thompson, M. C., Leweke, T. and Williamson, C. H. K. (2001). The physical mechanism of transition in bluff body wakes. *Journal of Fluids and Structures*, 15(3):607-616.
- Troch, P., De Rouck, J. and Schüttrumpf, H. (2002). *Numerical simulation of wave*

- overtopping over a smooth imperiable sea dike.* Advances in Fluid Mechanics IV, Vol. 32. WIT Press, UK.
- Tseng, Y.-H. and Ferziger, J. H. (2003). A ghost-cell immersed boundary method for flow in complex geometry. *Journal of Computational Physics*, 192(2):593-623.
- Tsukiyama, H., Tajima, Y., Yao, M. and Arai, H. (1993). Solution method for the time transient moving boundary problems using generalized porous media technique-FAVORITE (FAVOR ImitaTE) program. *Journal of Wind Engineering and Industrial Aerodynamics*, 46-47:381-391.
- Udaykumar, H. S., Kan, H.-C., Shyy, W. and Tran-Son-Tay, R. (1997). Multi-phase dynamics in arbitrary geometries on fixed Cartesian grids. *Journal of Computational Physics*, 137(2):366-405.
- Udaykumar, H. S., Mittal, R., Rampunggoon, P. and Khanna, A. (2001). A sharp interface Cartesian grid method for simulating flows with complex moving boundaries. *Journal of Computational Physics*, 174(1):345-380.
- Veeramani, C., Mineev, P. D. and Nandakumar, K. (2007). A fictitious domain formulation for flows with rigid particles: A non-Lagrange multiplier version. *Journal of Computational Physics*, 224(2):867-879.
- Versteeg, H. K. and Malalasekera, W. (1995). *An Introduction to Computational Fluid Dynamics. The Finite Volume Method.* Longman Scientific and Technical, UK.
- Wan, D. and Turek, S. (2007). An efficient multigrid-FEM method for the simulation of solid-liquid two-phase flows. *Journal of Computational and Applied Mathematics*, 203(2):561-580.
- Warburton, T. C. and Karniadakis, G. E. (1997). Spectral simulations of flow past a cylinder close to a free-surface. *Proceedings of the 1997 American Society of Mechanical Engineers (ASME) fluids engineering division summer meeting* (p. 1-8). Vancouver, Canada.
- Wen, C.-Y. and Lin, C.-Y. (2001). Two-dimensional vortex shedding of a circular cylinder. *Physics of Fluids*, 13(3):557-560.

- White, F. M. (1998). *Fluid Mechanics*, 4<sup>th</sup> Edition. McGraw-Hill College, UK.
- Williamson, C. H. K. (1996). Vortex dynamics in the cylinder wake. *Annual Review of Fluid Mechanics*, 28:477-539.
- Williamson, C. H. K. and Govardhan, R. (2004). Vortex-induced vibrations. *Annual Review of Fluid Mechanics*, 36:413-455.
- Williamson, C. H. K. and Roshko, A. (1988). Vortex formation in the wake of an oscillating cylinder. *Journal of Fluids and Structures*, 2:355-381.
- Wu, J., Sheridan, J., Welsh, M. C. and Hourigan, K. (1996). Three-dimensional vortex structures in a cylinder wake. *Journal of Fluid Mechanics*, 312:201-222.
- Yan, B. (1998). Oscillatory flow beneath a free surface. *Fluid Dynamics Research*, 22(1):1-23.
- Yan, B. (2000). Unsteady viscous flow about a submerged circular cylinder with a steady current. *Fluid Dynamics Research*, 26(2):69-94.
- Yan, B. and Riley, N. (1996). Boundary-layer flow around a submerged circular cylinder induced by free-surface travelling waves. *Journal of Fluid Mechanics*, 316:241-257.
- Ye, T., Mittal, R., Udaykumar, H. S. and Shyy, W. (1999). An accurate Cartesian grid method for viscous incompressible flows with complex immersed boundaries. *Journal of Computational Physics*, 156(2):209-240.
- Youngs, D. L. (1987). *An interface tracking method for a 3D Eulerian hydrodynamics code*. Technical Report No. AWRE/44/92/35. Atomic Weapons Research Establishment, Los Alamos National Laboratory.
- Zdravkovich, M. M. (1997). *Flow Around Circular Cylinders*. Vol. 1. Fundamentals. Oxford University Press, USA.
- Zhang, J. and Dalton, C. (1998). A three-dimensional simulation of a steady approach flow past a circular cylinder at low Reynolds number. *International Journal of Numerical Methods in Fluids*, 26(9):1003-1022.

- 
- Zhu, Q., Lin, J.-C., Unal, M. F. and Rockwell, D. (2000). Motion of a cylinder adjacent to a free-surface: flow patterns and loading. *Experiments in Fluids*, 28:559-575.
- Zhu, R. Q. and Wu, Y. S. (2004). Sloshing simulation of viscous liquid coupled with elastic structures. Hydrodynamics VI: Theory and Applications. *Proceedings of the 6<sup>th</sup> International Conference on Hydrodynamics* Edited by Cheng, L., Yeow, K. (p. 181-189). Perth, Western Australia.

## A. Integral form of the FAVOR equations versus differential form of the FAVOR equations

Figure 2.2 summarizes derivation of the differential and integral forms of the FAVOR equations.

*Differential form of the FAVOR equations:*

Step 1. Consider the general continuity and Navier-Stokes equations in their differential form

$$\frac{\partial \rho}{\partial t^*} + \nabla \cdot \rho \vec{u}^* = 0, \quad (\text{A.1})$$

$$\frac{\partial \rho \vec{u}^*}{\partial t^*} + (\rho \vec{u}^* \cdot \nabla) \vec{u}^* = -\nabla p^* + \nabla \cdot (\mu \nabla \vec{u}^*) + \rho \vec{F}^*. \quad (\text{A.2})$$

Step 2. Equations (A.1) and (A.2) can be extended to the entire control volume,  $V^*$ , by multiplying these equations with the Heaviside unit step function as follows

$$H \frac{\partial \rho}{\partial t^*} + H \nabla \cdot \rho \vec{u}^* = 0, \quad (\text{A.3})$$

$$H \frac{\partial \rho \vec{u}^*}{\partial t^*} + H (\rho \vec{u}^* \cdot \nabla) \vec{u}^* = -H \nabla p^* + H \nabla \cdot (\mu \nabla \vec{u}^*) + H \rho \vec{F}^*, \quad (\text{A.4})$$

where the Heaviside unit step function is defined as

$$H = \begin{cases} 1, & \text{in the fluid,} \\ 0, & \text{in the solid body.} \end{cases} \quad (\text{A.5})$$

Step 3. The Heaviside unit step function is moved into the time and spatial derivatives

in equations (A.1) and (A.2) to yield *Hirt and Sicilian's porosity equations*

$$\frac{\partial H}{\partial t^*} + \nabla \cdot (H\vec{u}^*) = 0, \quad (\text{A.6})$$

$$\frac{\partial(H\vec{u}^*)}{\partial t^*} + \nabla \cdot (H\vec{u}^*\vec{u}^*) = -\frac{1}{\rho}H\nabla p^* + \nu\nabla \cdot H\nabla\vec{u}^* + H\vec{F}^*, \quad (\text{A.7})$$

after making use of the fact that the incompressible Newtonian fluid density,  $\rho$ , is constant.

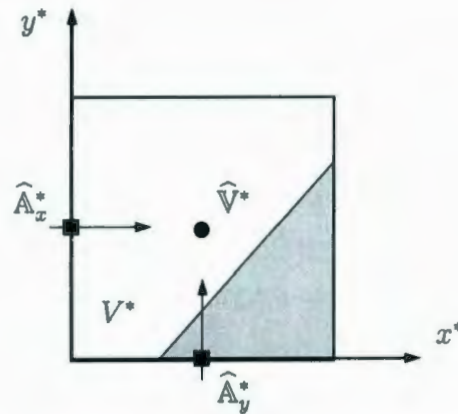


Figure A.1: Location of  $\hat{A}_x^*$ ,  $\hat{A}_y^*$  and  $\hat{V}^*$  within the computational cell,  $V^*$ . The solid body is shown in gray.

Step 4. Equations (A.6) and (A.7) can be reformulated using fractional area and volume porosity functions based on the FAVOR method to yield the *differential form of the FAVOR equations*

$$\frac{\partial \hat{V}^*}{\partial t^*} + \frac{\partial(u^*\hat{A}_x^*)}{\partial x^*} + \frac{\partial(v^*\hat{A}_y^*)}{\partial y^*} = 0, \quad (\text{A.8})$$

$$\frac{\partial u^*}{\partial t^*} + \frac{1}{\hat{V}^*} \left( u^*\hat{A}_x^* \frac{\partial u^*}{\partial x^*} + v^*\hat{A}_y^* \frac{\partial u^*}{\partial y^*} \right) = F_1^* - \frac{1}{\rho} \frac{\partial p^*}{\partial x^*} + \nu \nabla^2 u^*, \quad (\text{A.9})$$

$$\frac{\partial v^*}{\partial t^*} + \frac{1}{\hat{V}^*} \left( u^*\hat{A}_x^* \frac{\partial v^*}{\partial x^*} + v^*\hat{A}_y^* \frac{\partial v^*}{\partial y^*} \right) = F_2^* - \frac{1}{\rho} \frac{\partial p^*}{\partial y^*} + \nu \nabla^2 v^*. \quad (\text{A.10})$$

The fractional areas in  $x^*$ - and  $y^*$ -directions,  $\widehat{A}_x^*$  and  $\widehat{A}_y^*$ , and the fractional volume,  $\widehat{V}^*$ , open to flow within the computational cell,  $V^*$ , are defined as unknown variables. The fractional volume,  $\widehat{V}$ , is located in the center of the computational cell,  $V^*$ , and the fractional areas  $\widehat{A}_x^*$ ,  $\widehat{A}_y^*$  are located in the face centers of the computational cell boundaries,  $S_x^*$  and  $S_y^*$ , respectively, as shown in Figure A.1. They are defined by

$$\widehat{V}^* = \lim_{V^* \rightarrow 0} \bar{V}^*, \quad \widehat{A}_x^* = \lim_{S_x^* \rightarrow 0} \bar{A}_x^*, \quad \widehat{A}_y^* = \lim_{S_y^* \rightarrow 0} \bar{A}_y^* \quad (\text{A.11})$$

where

$$\bar{V}^* = \frac{1}{V^*} \int_{V^*} H \, dV^*, \quad \bar{A}_x^* = \frac{1}{S_x^*} \int_{S_x^*} H \, dS^*, \quad \bar{A}_y^* = \frac{1}{S_y^*} \int_{S_y^*} H \, dS^* \quad (\text{A.12})$$

and the Heaviside unit step function,  $H$ , is defined by equation (A.5). It is noted that in equation (A.12),  $\bar{V}^*$  and  $\bar{A}_x^*$ ,  $\bar{A}_y^*$  are the fractional volume and areas, respectively, open to flow within the computational cell,  $V^*$  [see Hirt and Sicilian (1985) for details].

*Integral form of the FAVOR equations:*

Step 1. Consider the law of conservation of mass and the Newton's second law of motion,

$$\frac{d}{dt^*} \int_{V^*(t^*)} \rho \, dV^* = 0, \quad (\text{A.13})$$

and

$$\frac{d}{dt^*} \int_{V^*(t^*)} \rho \vec{u}^* \, dV^* = \int_{V^*} \rho \vec{F}^* \, dV^* + \int_{S^*} \vec{\sigma} \cdot \vec{n} \, dS^*, \quad (\text{A.14})$$

respectively.

Step 2. Equations (A.13) and (A.14) can be written for an arbitrary rectangular control volume,  $V^*$ , with the surface,  $S^*$ , containing a fluid-body interface (see Figure

A.2) by using the generalized transport theorem,

$$\frac{d}{dt^*} \int_{V^*(t^*)} P dV^* = \frac{d}{dt^*} \int_{V^*} P dV^* + \int_{A^*} (\vec{n} \cdot \vec{u}^*) P dS^*. \quad (\text{A.15})$$

It is noted that a control volume boundary,  $S^*$ , is composed of left,  $S_1^*$ , right,  $S_2^*$ , top,  $S_3^*$ , and bottom,  $S_0^*$ , pieces, i.e.,  $S^* = S_0^* \cup S_1^* \cup S_2^* \cup S_3^*$  as shown in Figure A.2(a).

The volume and areas open to flow are defined as

$$V^* = \int_{V^*} H dV^*, \quad A^* = \int_{S^*} H dS^*, \quad (\text{A.16})$$

respectively (see Figure A.2(b)), where the Heaviside unit step function,  $H$ , is defined by equation (A.5).

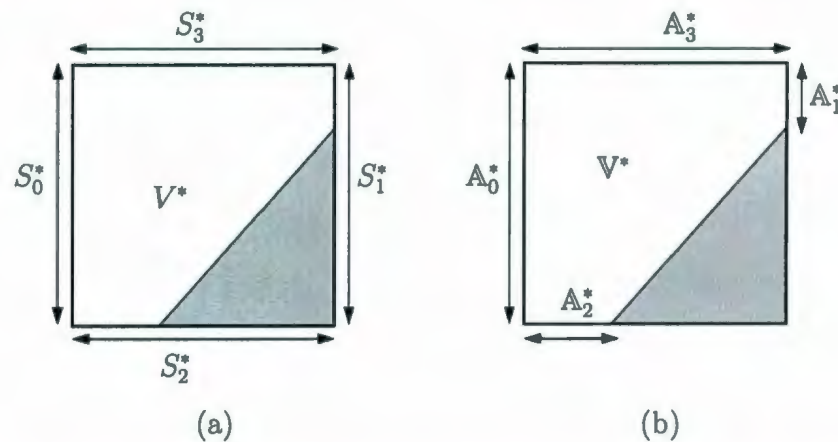


Figure A.2: Typical computational cell,  $V^*$ , containing a fluid-body interface, (b) typical computational cell,  $V^*$ , which includes areas,  $A_i^*$  ( $i = 0, 1, 2, 3$ ) and volume,  $V^*$ , open to flow within  $V^*$ . The solid body is shown in gray.

Step 3. Step 2 yields the integral form of the continuity and Navier-Stokes equations which are valid for a control volume containing a fluid-body interface (integral form

of the FAVOR equations), in the form

$$\frac{d}{dt^*} \int_{V^*} \rho \, dV^* + \int_{A^*} (\rho \vec{u}^* \cdot \vec{n}) \, dS^* = 0, \quad (\text{A.17})$$

$$\frac{d}{dt^*} \int_{V^*} \rho \vec{u}^* \, dV^* + \int_{A^*} (\vec{n} \cdot \vec{u}^*) \rho \vec{u}^* \, dS^* = - \int_{A^* \cup I^*} p^* \vec{n} \, dS^* + \int_{A^* \cup I^*} \vec{n} \cdot \mu \nabla \vec{u}^* \, dS^* + \int_{V^*} \rho \vec{F}^* \, dV^*, \quad (\text{A.18})$$

respectively. For the two-dimensional flow of incompressible Newtonian fluid, the integral form of the FAVOR equations can be written as

$$\frac{dV^*}{dt^*} + \int_{A^*} (\vec{n} \cdot \vec{u}^*) \, dS^* = 0, \quad (\text{A.19})$$

and

$$\frac{d}{dt^*} \int_{V^*} \vec{u}^* \, dV^* + \int_{A^*} (\vec{n} \cdot \vec{u}^*) \vec{u}^* \, dS^* = - \frac{1}{\rho} \int_{A^* \cup I^*} p^* \vec{n} \, dS^* + \nu \int_{A^* \cup I^*} \vec{n} \cdot \nabla \vec{u}^* \, dS^* + \int_{V^*} \vec{F}^* \, dV^*, \quad (\text{A.20})$$

respectively.

Integral form of the FAVOR equations (2.32) and (2.42) can be derived from the differential form of the FAVOR equations (2.3)-(2.5) as follows. Equation (2.3) can be rewritten as

$$\frac{\partial \widehat{V}^*}{\partial t^*} + \frac{\partial (u^* \widehat{A}_x^*)}{\partial x^*} + \frac{\partial (v^* \widehat{A}_y^*)}{\partial y^*} = \frac{\partial \widehat{V}^*}{\partial t^*} + \nabla \cdot \overrightarrow{(u^* \widehat{A}^*)}, \quad (\text{A.21})$$

where  $\overrightarrow{(u^* \widehat{A}^*)} = (u^* \widehat{A}_x^*, v^* \widehat{A}_y^*, 0)$ . Integration of equation (A.21) over the computational cell,  $V^*$ , shown in Figures A.2 and A.1, yields

$$\int_{V^*} \frac{\partial \widehat{V}^*}{\partial t^*} \, dV^* + \int_{V^*} \nabla \cdot \overrightarrow{(u^* \widehat{A}^*)} \, dV^* = 0. \quad (\text{A.22})$$

The first integral on the left hand side of equation (A.22) can be rewritten as

$$\int_{V^*} \frac{\partial \widehat{V}^*}{\partial t^*} dV^* = \frac{d}{dt^*} \int_{V^*} \widehat{V}^* dV^* = \frac{d}{dt^*} \int_{V^*} H dV^* = \frac{dV^*}{dt^*} \quad (\text{A.23})$$

after making use of equation (A.11). The second integral on the left hand side of equation (A.22) can be rewritten as

$$\begin{aligned} \int_{V^*} \nabla \cdot \overrightarrow{(u^* \widehat{A}^*)} dV^* &= \int_{S^*} \vec{n} \cdot \overrightarrow{(u^* \widehat{A}^*)} dS^* \\ &= \int_{S_0^*} uH dS^* - \int_{S_1^*} uH dS^* + \int_{S_2^*} vH dS^* - \int_{S_3^*} vH dS^* \\ &= \int_{A_0^*} u dS^* - \int_{A_1^*} u dS^* + \int_{A_2^*} v dS^* - \int_{A_3^*} v dS^* \\ &= \int_{A^*} \vec{n} \cdot \vec{u}^* dS^*, \end{aligned} \quad (\text{A.24})$$

after making use of equation (A.11) (see Figures A.2 and A.1). Thus,

$$\int_{V^*} \frac{\partial \widehat{V}^*}{\partial t^*} dV^* + \int_{V^*} \nabla \cdot \overrightarrow{(u^* \widehat{A}^*)} dV^* = \frac{dV^*}{dt^*} + \int_{A^*} \vec{n} \cdot \vec{u}^* dS^*. \quad (\text{A.25})$$

Equation (A.25) coincides with equation (2.32).

The momentum equations (2.4) and (2.5) can be rewritten, respectively, as

$$\widehat{V}^* \frac{\partial u^*}{\partial t^*} + \overrightarrow{(u^* \widehat{A}^*)} \cdot \nabla u^* = \widehat{V}^* F_1^* - \frac{\widehat{V}^*}{\rho} \frac{\partial p^*}{\partial x^*} + \widehat{V}^* \nu \nabla^2 u^*, \quad (\text{A.26})$$

$$\widehat{V}^* \frac{\partial v^*}{\partial t^*} + \overrightarrow{(u^* \widehat{A}^*)} \cdot \nabla v^* = \widehat{V}^* F_2^* - \frac{\widehat{V}^*}{\rho} \frac{\partial p^*}{\partial y^*} + \widehat{V}^* \nu \nabla^2 v^*. \quad (\text{A.27})$$

Integration of equation (A.26) over the computational cell,  $V^*$ , shown in Figures A.2

and A.1, yields

$$\int_{V^*} \widehat{V}^* \frac{\partial u^*}{\partial t^*} dV^* + \int_{V^*} \overrightarrow{(u^* \widehat{A}^*)} \cdot \nabla u^* dV^* = \int_{V^*} \widehat{V}^* F_1^* dV^* - \int_{V^*} \frac{\widehat{V}^*}{\rho} \frac{\partial p^*}{\partial x^*} dV^* + \int_{V^*} \widehat{V}^* \nu \nabla^2 u^* dV^*. \quad (\text{A.28})$$

Consider the integrals on the left hand side of equation (A.28). The unsteady term can be written as

$$\begin{aligned} \int_{V^*} \widehat{V}^* \frac{\partial u^*}{\partial t^*} dV^* &= \int_{V^*} \frac{\partial \widehat{V}^* u^*}{\partial t^*} dV^* - \int_{V^*} u^* \frac{\partial \widehat{V}^*}{\partial t^*} dV^* \\ &= \frac{\partial}{\partial t^*} \int_{V^*} \widehat{V}^* u^* dV^* - \int_{V^*} u^* \frac{d\widehat{V}^*}{dt^*} dV^* \\ &= \frac{\partial}{\partial t^*} \int_{V^*} H u^* dV^* - \int_{V^*} u^* \frac{d\widehat{V}^*}{dt^*} dV^* \\ &= \frac{d}{dt^*} \int_{V^*} u^* dV^* - \int_{V^*} u^* \frac{d\widehat{V}^*}{dt^*} dV^*, \end{aligned} \quad (\text{A.29})$$

after making use of equation (A.11).

The convection term in equation (A.28) can be rewritten as follows

$$\int_{V^*} \overrightarrow{(u^* \widehat{A}^*)} \cdot \nabla u^* dV^* = \int_{V^*} \nabla \cdot u^* \overrightarrow{(u^* \widehat{A}^*)} dV^* - \int_{V^*} u^* \nabla \cdot \overrightarrow{(u^* \widehat{A}^*)} dV^*. \quad (\text{A.30})$$

On the other hand,

$$\nabla \cdot \overrightarrow{(u^* \widehat{A}^*)} = -\frac{d\widehat{V}^*}{dt^*}, \quad (\text{A.31})$$

where equation (A.31) follows from the continuity equation (A.21). Thus, equation (A.30) can be written as

$$\int_{V^*} \overrightarrow{(u^* \widehat{A}^*)} \cdot \nabla u^* dV^* = \int_{V^*} \nabla \cdot u^* \overrightarrow{(u^* \widehat{A}^*)} dV^* + \int_{V^*} u^* \frac{d\widehat{V}^*}{dt^*} dV^*. \quad (\text{A.32})$$

The first integral on the right hand side of equation (A.32) can be written as

$$\begin{aligned}
 \int_{V^*} \nabla \cdot \overline{u^* \widehat{\mathbf{A}}^*} dV^* &= \int_{S^*} \vec{n} \cdot \overline{u^* \widehat{\mathbf{A}}^*} dS^* \\
 &= \int_{S_0^*} u^* u^* H dS^* - \int_{S_1^*} u^* u^* H dS^* \\
 &\quad + \int_{S_2^*} u^* v^* H dS^* - \int_{S_3^*} u^* v^* H dS^* \\
 &= \int_{\Lambda_0^*} u^* u^* dS^* - \int_{\Lambda_1^*} u^* u^* dS^* + \int_{\Lambda_2^*} u^* v^* dS^* - \int_{\Lambda_3^*} u^* v^* dS^* \\
 &= \int_{\Lambda^*} (\vec{n} \cdot \vec{u}^*) u^* dS^*.
 \end{aligned} \tag{A.33}$$

Now, consider the integrals on the right hand side of equation (A.28). The volumetric force can be represented as

$$\int_{V^*} \widehat{\mathbf{V}}^* F_1^* dV^* = \int_{V^*} H F_1^* dV^* = \int_{V^*} F_1^* dV^*. \tag{A.34}$$

The pressure and diffusive terms become

$$\int_{V^*} \frac{\widehat{\mathbf{V}}^*}{\rho} \frac{\partial p^*}{\partial x^*} dV^* = \frac{1}{\rho} \int_{V^*} H \frac{\partial p^*}{\partial x^*} dV^*, \tag{A.35}$$

and

$$\int_{V^*} \widehat{\mathbf{V}}^* \nu \nabla^2 u^* dV^* = \nu \int_{V^*} H \nabla^2 u^* dV^*, \tag{A.36}$$

respectively. Finally, substitution of equations (A.29), (A.32)-(A.36) into equation (A.28) yields

$$\frac{d}{dt^*} \int_{V^*} u^* dV^* + \int_{\Lambda^*} (\vec{n} \cdot \vec{u}^*) u^* dS^* = \int_{V^*} F_1^* dV^* - \frac{1}{\rho} \int_{V^*} H \frac{\partial p^*}{\partial x^*} dV^* + \nu \int_{V^*} H \nabla^2 u^* dV^*. \tag{A.37}$$

Similarly, equation (A.28) can be integrated over the computational cell,  $V^*$ , shown in Figures A.2 and A.1, to yield the form

$$\frac{d}{dt^*} \int_{V^*} v^* dV^* + \int_{A^*} (\vec{n} \cdot \vec{u}^*) v^* dS^* = \int_{V^*} F_2^* dV^* - \frac{1}{\rho} \int_{V^*} H \frac{\partial p^*}{\partial y^*} dV^* + \nu \int_{V^*} H \nabla^2 v^* dV^*. \quad (\text{A.38})$$

Equations (A.37) and (A.38) can be written in the vector form as

$$\frac{d}{dt^*} \int_{V^*} \vec{u}^* dV^* + \int_{A^*} (\vec{n} \cdot \vec{u}^*) \vec{u}^* dS^* = -\frac{1}{\rho} \int_{V^*} H \nabla p^* dV^* + \nu \int_{V^*} H \nabla \cdot (\nabla \vec{u}^*) dV^* + \int_{V^*} \vec{F}^* dV^*. \quad (\text{A.39})$$

The pressure term in equation (A.39) can be rewritten as

$$\begin{aligned} \frac{1}{\rho} \int_{V^*} H \nabla p^* dV^* &= \frac{1}{\rho} \int_{V^*} \nabla H p^* dV^* - \frac{1}{\rho} \int_{V^*} p^* \nabla H dV^* \\ &= \frac{1}{\rho} \int_{S^*} H p^* \vec{n} dS^* + \frac{1}{\rho} \int_{V^*} p^* \vec{n} \delta dV^* \\ &= \frac{1}{\rho} \int_{A^*} p^* \vec{n} dS^* + \frac{1}{\rho} \int_{I^*} p^* \vec{n} dS^* \frac{1}{\rho} \int_{V^*} H \nabla p^* dV^* \\ &= \frac{1}{\rho} \int_{A^* \cup I^*} p^* \vec{n} dS^*, \end{aligned} \quad (\text{A.40})$$

after making use of equation (2.25). Similarly, the diffusion term in equation (A.39)

can be written as

$$\begin{aligned} \nu \int_{V^*} H \nabla \cdot (\nabla \vec{u}^*) dV^* &= \nu \int_{V^*} \nabla \cdot (H \nabla \vec{u}^*) dV^* - \nu \int_{V^*} \nabla H \cdot \nabla \vec{u}^* dV^* \\ &= \nu \int_{S^*} \vec{n} \cdot (H \nabla \vec{u}^*) dS^* + \nu \int_{V^*} \vec{n} \delta \cdot \nabla \vec{u}^* dV^* \\ &= \nu \int_{A^*} \vec{n} \cdot \nabla \vec{u}^* dS^* + \nu \int_{I^*} \vec{n} \cdot \nabla \vec{u}^* dV^* \\ &= \nu \int_{A^* \cup I^*} \vec{n} \cdot \nabla \vec{u}^* dV^* \end{aligned} \quad (\text{A.41})$$

after making use of equation (2.25). Substitution of equations (A.40) and (A.41) into equation (A.39) yields the form

$$\frac{d}{dt^*} \int_{V^*} \vec{u}^* dV^* + \int_{A^*} (\vec{n} \cdot \vec{u}^*) \vec{u}^* dS^* = -\frac{1}{\rho} \int_{A^* \cup I^*} p^* \vec{n} dS^* + \nu \int_{A^* \cup I^*} \vec{n} \cdot \nabla \vec{u}^* dS^* + \int_{V^*} \vec{F}^* dV^*. \quad (\text{A.42})$$

Equation (A.42) coincides with equation (2.42).

## B. Generalized functions and generalized differentiation

The underlying concept of Schwartz's theory of distributions (or generalized functions) is to consider only values of specific operations of symbolic or ideal functions on certain classes of functions but never values of the function itself. For example, Dirac (1947) introduced the delta function  $\delta(x^*)$  by its shifting property

$$\int_{-\infty}^{\infty} \widehat{\phi}(x^*) \delta(x^*) dx^* = \widehat{\phi}(0) \quad (\text{B.1})$$

in which  $\delta$  is regarded as a symbol representing an integration, defined at least for all functions  $\widehat{\phi}(x^*)$ , continuous on a neighbourhood of origin, which maps each  $\widehat{\phi}(x^*)$  into the value  $\widehat{\phi}(0)$ . Symbols such as  $\delta$  when regarded as specifying operations on certain classes of functions (rather than as standing for pointwise specified function  $\delta(x^*)$ ) are referred as a generalized function. The properties of generalized functions are established rigorously in Schwartz (1950, 1951). It is shown from classical Lebesgue integration theory that the Dirac  $\delta$  function cannot be an ordinary function. Here, a locally Lebesgue integrable function  $f(x^*)$  is considered as an ordinary function that has a finite integral over any bounded region  $\Omega \in \mathbb{R}^n$ , where  $\mathbb{R}^n$  is the  $n$ -dimensional real space

$$\int_{\Omega} f(x^*) dx^* \leq \int_{\Omega} |f(x^*)| dx^*. \quad (\text{B.2})$$

Thus, to include the Dirac delta function in mathematics, one must think of an ordinary function  $f(x^*)$  differently. Conventionally, one can think of ordinary or generalized function  $f(x^*)$  as a set of ordered pairs  $(x^*, f(x^*))$ . These numbers are

produced by

$$F[\widehat{\phi}] = \int_{-\infty}^{\infty} f(x^*)\widehat{\phi}(x^*) dx^*, \quad (\text{B.3})$$

where the function  $\widehat{\phi}(x^*)$  is a test function. The test function space  $D \in \mathbb{R}^n$  is a space of all infinitely differentiable functions with bounded support. The support of a function  $\widehat{\phi}(x^*)$  is the closure of the set on which  $\widehat{\phi}(x^*) \neq 0$

$$\text{supp } \widehat{\phi} = \{\widehat{\phi} \mid \widehat{\phi} \in D, \widehat{\phi} \neq 0\}. \quad (\text{B.4})$$

For a fixed function  $f(x^*)$ , equation (B.3) is a mapping of the test function space into real or complex numbers. Such a mapping is called a functional which is denoted by square brackets (e.g.,  $F[\widehat{\phi}]$  and  $\delta[\widehat{\phi}]$ ). Therefore, a function  $f(x^*)$  can now be described by a number of its functional values over a given space of test functions. For any given ordinary function  $f(x^*)$ , the functional  $F[\widehat{\phi}]$  is linear and continuous. Schwartz noted that not all continuous linear functionals on space  $D$  are generated by ordinary functions through equation (B.3). For example, the continuous and linear functional  $\delta[\widehat{\phi}] = \widehat{\phi}(0)$  on space  $D$  cannot be generated by an ordinary function. However, this functional has the shifting property that the Dirac  $\delta$  function requires and no ordinary function has the shifting property, given by equation (B.1). Therefore, this approach introduces the  $\delta$  function rigorously into mathematics. Thus, the generalized functions can be viewed as continuous linear functionals on space  $D$ . This means that the ordinary functions can be seen as the regular generalized functions, whereas all other generalized functions (such as the Dirac  $\delta$  function) are seen as singular generalized functions. In general, singular generalized functions are not defined pointwise but they define a functional when they are multiplied by a test function and appear under an integral sign. Thus, when a singular generalized function appears in

an expression, it is always in an intermediate stage in the solution of a real physical problem. In what follows, one of the properties of the Dirac  $\delta$  function is stated. The concept of generalized differentiation is also introduced. Generalized differentiation is the most important concept in generalized function theory and the extension of the Reynolds transport theorem utilizes mainly this concept.

*Property of the Dirac  $\delta$  function.* The most powerful property of the Dirac  $\delta$  function is that the integration of the product of any regular generalized function  $f(\vec{x}^*)$  and  $\delta(\phi)$  over  $\mathbb{R}$  reduces to the integration of  $f(\vec{x}^*)$  over the boundary of the region,  $\phi = 0$ ,

$$\int_{\mathbb{R}} f(\vec{x}^*) \delta(\phi) dV^* = \int_{\phi=0} f(\vec{x}^*) dS^* \quad (\text{B.5})$$

[see Farassat (1996) for details].

*Generalized differentiation.* Let  $f(x^*)$  be a piecewise smooth singular generalized function defined on the interval  $[a, b]$  with the discontinuity at  $x_0^* \in [a, b]$  and a jump at this point defined by  $\Delta f = f(x_{0+}^*) - f(x_{0-}^*)$ . Let  $\hat{\phi} \in D$  and  $x_0^* \in \hat{\phi}(x^*)$ . If  $F[\hat{\phi}]$  is the functional representing  $f(x^*)$  given by equation (B.3), then  $\text{supp } \hat{\phi} = [a, b]$ , and the generalized derivative can be defined as

$$F'[\hat{\phi}] = -F[\hat{\phi}'] = - \int_a^b f(x^*) \hat{\phi}' dx^* = \int_a^b f'(x^*) \hat{\phi}(x^*) dx^* + \Delta f \hat{\phi}(x_0^*). \quad (\text{B.6})$$

## C. Surface force term in the incompressible Navier-Stokes equations

In continuum mechanics, surface forces acting on a material volume  $V^*(t^*)$  are modeled with stress tensor  $\bar{\sigma}$ . External surface force  $\vec{F}_s^*$  acting on  $V^*(t^*)$  is computed as the surface integral over the boundary of a material volume,  $\partial V^*(t^*)$ , as

$$\vec{F}_s^* = \int_{V^*(t^*)} \bar{\sigma} \cdot \vec{n} \, dS^*. \quad (\text{C.1})$$

For Newtonian fluids, stress tensor consists of the pressure and viscous contributions

$$\bar{\sigma} = -p^* \bar{I} + \mu (\nabla \vec{u}^* + (\nabla \vec{u}^*)^T). \quad (\text{C.2})$$

However, majority of fluid mechanics textbooks utilize the differential form of the incompressible Navier-Stokes equations, in which surface forces are represented by

$$\bar{\sigma}' = -p^* \bar{I} + \mu \nabla \vec{u}^*. \quad (\text{C.3})$$

Equation (C.3) can be deduced from equation (C.2) in the following manner. First, equation (C.1) is rewritten as

$$\vec{F}_s^* = \int_{V^*(t^*)} \nabla \cdot \bar{\sigma} \, dV^*, \quad (\text{C.4})$$

after making use of the divergence theorem. Next, the divergence of the stress tensor is calculated as

$$\nabla \cdot \bar{\sigma} = -\nabla p^* + (\nabla \cdot \mu \nabla \vec{u}^* + \nabla(\nabla \cdot \vec{u}^*)). \quad (\text{C.5})$$

This is done by making use of equation (C.2). The last term in equation (C.5) contains the velocity divergence,  $\nabla \cdot \vec{u}^*$ , which is zero for incompressible fluids. Thus,

$$\nabla \cdot \bar{\sigma} = -\nabla p^* + \nabla \cdot \mu \nabla \vec{u}^*. \quad (\text{C.6})$$

Substitution of equation (C.6) into equation (C.4) yields

$$\vec{F}_s^* = \int_{V^*(t^*)} (-\nabla p^* + \nabla \cdot \mu \nabla \vec{u}^*) dV^*. \quad (\text{C.7})$$

Finally, the divergence theorem is used to express equation (C.7) in the form

$$\vec{F}_s^* = \int_{\partial V^*(t^*)} \left( -p^* \bar{I} + \mu \nabla \vec{u}^* \right) \cdot \vec{n} dS^* = \int_{V^*(t^*)} \bar{\sigma}' \cdot \vec{n} dS^*. \quad (\text{C.8})$$

## D. Invariance of the governing equations in non-inertial frame of reference

The incompressible continuity and Navier-Stokes equations satisfy a special invariance in the non-inertial frame of reference,  $\widehat{X} = \{\widehat{x}^*, \widehat{t}^*\}$ , that is moving in the  $x^*$ - and  $y^*$ -directions (but is not rotating) with respect to the inertial frame of reference,  $X = \{\bar{x}^*, t^*\}$ , [see, for example, Panton (1996)]. Here,  $\bar{x}^* = (x^*, y^*, 0)$ ,  $\widehat{x}^* = (\widehat{x}^*, \widehat{y}^*, 0)$  and the origin of the non-inertial frame of reference,  $\widehat{X}$ , moves with an arbitrary velocity  $\widehat{v}^* = (v_1^*, v_2^*, 0)$ . The spatial coordinates and velocities in inertial,  $X$ , and non-inertial,  $\widehat{X}$ , frames of reference are related as

$$\widehat{x}^* = \bar{x}^* - \int_0^{t^*} \widehat{v}^*(t') dt', \quad \widehat{u}^* = \bar{u}^* - \widehat{v}^*, \quad \widehat{t}^* = t^*. \quad (\text{D.1})$$

The partial derivatives in inertial,  $X$ , and non-inertial,  $\widehat{X}$ , frames of reference can be related as follows

$$\frac{\partial}{\partial \bar{x}^*} = \frac{\partial}{\partial \widehat{x}^*}, \quad \frac{\partial}{\partial t^*} = \frac{\partial}{\partial \widehat{t}^*} - \widehat{v}^* \frac{\partial}{\partial \widehat{x}^*}, \quad (\text{D.2})$$

after making use of the fact that  $\widehat{v}^*$  is constant in space and using equation (D.1).

Equations (2.32) and (2.42) coincide with equations (2.8) and (2.9) in the fluid. Thus, it is sufficient to show that equations (2.8) and (2.9) are invariant in the non-inertial frame of reference,  $\widehat{X}$ . Consider the differential form of equations (2.8) and (2.9),

$$\frac{\partial \rho}{\partial t^*} + \nabla \cdot \rho \bar{u}^* = 0, \quad (\text{D.3})$$

$$\frac{\partial \rho \bar{u}^*}{\partial t^*} + (\rho \bar{u}^* \cdot \nabla) \bar{u}^* = -\nabla p^* + \nabla \cdot (\mu \nabla \bar{u}^*) + \rho \bar{F}^*. \quad (\text{D.4})$$

Equation (D.3) can be rewritten in the non-inertial frame of reference,  $\widehat{X}$ , as

$$\frac{\partial \rho}{\partial t^*} + \frac{\partial u^*}{\partial x^*} + \frac{\partial v^*}{\partial y^*} = \frac{\partial \rho}{\partial \widehat{t}^*} - \widehat{v}^* \frac{\partial \rho}{\partial \widehat{x}^*} + \frac{\partial (\widehat{u}^* + v_1^*)}{\partial \widehat{x}^*} + \frac{\partial (\widehat{v}^* + v_2^*)}{\partial \widehat{y}^*}. \quad (\text{D.5})$$

This is done after making use of equation (D.2). For Newtonian fluids ( $\rho$  is constant), equation (D.5) can be rewritten as

$$\frac{\partial \rho}{\partial t^*} + \frac{\partial u^*}{\partial x^*} + \frac{\partial v^*}{\partial y^*} = \frac{\partial \rho}{\partial \widehat{t}^*} + \frac{\partial \widehat{u}^*}{\partial \widehat{x}^*} + \frac{\partial \widehat{v}^*}{\partial \widehat{y}^*} = 0. \quad (\text{D.6})$$

It is seen that equation (D.3) coincides with equation (D.6).

Consider the momentum equation (D.4). This equation can be written in the componentwise form as

$$\frac{\partial \rho u^*}{\partial t^*} + u^* \frac{\partial \rho u^*}{\partial x^*} + v^* \frac{\partial \rho u^*}{\partial y^*} = -\frac{\partial p^*}{\partial x^*} + \mu \left( \frac{\partial^2 u^*}{\partial x^{*2}} + \frac{\partial^2 u^*}{\partial y^{*2}} \right) + \rho F_1^*, \quad (\text{D.7})$$

$$\frac{\partial \rho v^*}{\partial t^*} + u^* \frac{\partial \rho v^*}{\partial x^*} + v^* \frac{\partial \rho v^*}{\partial y^*} = -\frac{\partial p^*}{\partial y^*} + \mu \left( \frac{\partial^2 v^*}{\partial x^{*2}} + \frac{\partial^2 v^*}{\partial y^{*2}} \right) + \rho F_2^*. \quad (\text{D.8})$$

In what follows, only equation (D.7) is considered. Equation (D.8) follows a similar approach. The unsteady, convective, pressure and diffusive terms in equation (D.7) can be rewritten in the non-inertial frame of reference,  $\widehat{X}$ , as

$$\frac{\partial \rho u^*}{\partial t^*} = \frac{\partial \rho \widehat{u}^*}{\partial \widehat{t}^*} + \frac{\partial \rho v_1^*}{\partial \widehat{t}^*} - v_1^* \frac{\partial \rho \widehat{u}^*}{\partial \widehat{x}^*} - v_2^* \frac{\partial \rho \widehat{u}^*}{\partial \widehat{y}^*}, \quad (\text{D.9})$$

$$u^* \frac{\partial \rho u^*}{\partial x^*} = \widehat{u}^* \frac{\partial \rho \widehat{u}^*}{\partial \widehat{x}^*} + v_1^* \frac{\partial \rho \widehat{u}^*}{\partial \widehat{x}^*}, \quad v^* \frac{\partial \rho u^*}{\partial y^*} = \widehat{v}^* \frac{\partial \rho \widehat{u}^*}{\partial \widehat{y}^*} + v_2^* \frac{\partial \rho \widehat{u}^*}{\partial \widehat{y}^*}, \quad (\text{D.10})$$

$$\frac{\partial p^*}{\partial x^*} = \frac{\partial p^*}{\partial \widehat{x}^*}, \quad \frac{\partial^2 u^*}{\partial x^{*2}} = \frac{\partial^2 \widehat{u}^*}{\partial \widehat{x}^{*2}}, \quad \frac{\partial^2 u^*}{\partial y^{*2}} = \frac{\partial^2 \widehat{u}^*}{\partial \widehat{y}^{*2}}, \quad (\text{D.11})$$

after making use of equations (D.1) and (D.2). Substitution of equations (D.9)-(D.11) into (D.7) yields

$$\frac{\partial \rho \widehat{u}^*}{\partial \widehat{t}^*} + \widehat{u}^* \frac{\partial \rho \widehat{u}^*}{\partial \widehat{x}^*} + \widehat{v}^* \frac{\partial \rho \widehat{u}^*}{\partial \widehat{y}^*} = -\frac{\partial p^*}{\partial \widehat{x}^*} + \mu \frac{\partial^2 \widehat{u}^*}{\partial \widehat{x}^{*2}} + \frac{\partial^2 \widehat{u}^*}{\partial \widehat{y}^{*2}} + \rho \widehat{F}_1^*, \quad (\text{D.12})$$

where

$$\widehat{F}_1^* = F_1^* - a_1^*, \quad a_1^* = \frac{\partial v_1^*}{\partial t^*}. \quad (\text{D.13})$$

Similarly, equation (D.8) takes the form

$$\frac{\partial \rho \widehat{v}^*}{\partial \widehat{t}^*} + \widehat{u}^* \frac{\partial \rho \widehat{v}^*}{\partial \widehat{x}^*} + \widehat{v}^* \frac{\partial \rho \widehat{v}^*}{\partial \widehat{y}^*} = -\frac{\partial p^*}{\partial \widehat{x}^*} + \mu \frac{\partial^2 \widehat{v}^*}{\partial \widehat{x}^{*2}} + \frac{\partial^2 \widehat{v}^*}{\partial \widehat{y}^{*2}} + \rho \widehat{F}_2^*, \quad (\text{D.14})$$

where

$$\widehat{F}_2^* = F_2^* - a_2^*, \quad a_2^* = \frac{\partial v_2^*}{\partial t^*}. \quad (\text{D.15})$$

Here,  $a_1^*$  and  $a_2^*$  are the  $x^*$ - and  $y^*$ -components of the acceleration of the non-inertial frame of reference,  $\widehat{X}$ ,  $\vec{a}^* = (a_1^*, a_2^*, 0)$ , respectively. It is seen that equations (D.7) and (D.8) coincide with equations (D.12) and (D.14).

## E. Proper orthogonal decomposition

In this appendix, the outline of the proper orthogonal decomposition (POD) analysis is given. In POD method, the sampled data (for example, vorticity field,  $\zeta$ ) is represented as a vector-valued function

$$\zeta = \begin{pmatrix} \zeta_1(\vec{x}_1) & \zeta_2(\vec{x}_1) & \dots & \zeta_M(\vec{x}_1) \\ \zeta_1(\vec{x}_2) & \zeta_2(\vec{x}_2) & \dots & \zeta_M(\vec{x}_2) \\ \vdots & \vdots & \ddots & \vdots \\ \zeta_1(\vec{x}_N) & \zeta_2(\vec{x}_2) & \dots & \zeta_M(\vec{x}_N) \end{pmatrix} \quad (\text{E.1})$$

using a time series,  $\zeta_t(\vec{x})$ , obtained from a numerical simulation or an experiment. Here,  $t$  is time;  $\vec{x}$  denotes a position in space;  $N$  is the number of positions in the spatial domain and  $M$  is the number of samples taken in time. A suitable POD basis  $\Phi = (\varphi_1, \dots, \varphi_N)$  can be obtained by solving the eigenvalue problem

$$C\Phi = \lambda\Phi. \quad (\text{E.2})$$

Then, the solution  $\zeta_t(\vec{x})$  can be expressed by a linear combination of the eigenfunctions as

$$\tilde{\zeta}_k(\vec{x}) = \sum_{k=1}^K a_k(t)\varphi_k(\vec{x}), \quad K < N \quad (\text{E.3})$$

using the POD modes. Here,  $C(\vec{x}, \vec{x}') = \langle \zeta(\vec{x}), \zeta(\vec{x}') \rangle$  is the time-averaged correlation matrix;  $K$  is the number of modes used for truncation and  $a_k$  are modal coefficients that can be determined by projection of the ensemble of data onto the POD modes. Sirovich (1987) has shown that when the number of collected time samples is smaller than the space discretization, the eigenfunctions can be represented as linear combi-

nations of the snapshots by

$$\varphi(\vec{x}) = \sum_{i=1}^M b_i \zeta_i(\vec{x}). \quad (\text{E.4})$$

Substituting equation (E.4) into equation (E.2) results in

$$CB = \lambda B, \text{ where } C_{i,j} = \frac{1}{N} \sum_{k=1}^N \zeta_i(\vec{x}_k) \zeta_j(\vec{x}_k). \quad (\text{E.5})$$

Hence, the POD eigenvalue problem (E.5) is solved and the POD eigenfunctions are determined as a combination of eigenvectors and the snapshots. The coefficients of POD eigenfunctions are calculated by conducting the orthogonal projection of the data onto the set of POD basis functions.







